



HAL
open science

Study of Antiproton-proton Annihilation Reactions and Experimental Contribution to Hadron Polarimetry

Ying Wang

► **To cite this version:**

Ying Wang. Study of Antiproton-proton Annihilation Reactions and Experimental Contribution to Hadron Polarimetry. High Energy Physics - Phenomenology [hep-ph]. Université Paris-Saclay, 2017. English. NNT : 2017SACLS142 . tel-01756830

HAL Id: tel-01756830

<https://theses.hal.science/tel-01756830>

Submitted on 3 Apr 2018

HAL is a multi-disciplinary open access archive for the deposit and dissemination of scientific research documents, whether they are published or not. The documents may come from teaching and research institutions in France or abroad, or from public or private research centers.

L'archive ouverte pluridisciplinaire **HAL**, est destinée au dépôt et à la diffusion de documents scientifiques de niveau recherche, publiés ou non, émanant des établissements d'enseignement et de recherche français ou étrangers, des laboratoires publics ou privés.

NNT : 2017SACLS142

THÈSE DE DOCTORAT
DE
L'UNIVERSITÉ PARIS-SACLAY
PRÉPARÉE À
L'UNIVERSITÉ PARIS-SUD

ECOLE DOCTORALE N°576

Particules hadrons énergie et noyau : Instrumentation, Image, Cosmos et Simulation
(PHENIICS)

Spécialité de Doctorat : Physique Hadronique

Par

Mme Ying Wang

Etude des réactions d'annihilation proton-antiproton et contribution expérimentale à
la polarimétrie hadronique

Thèse présentée et soutenue à Orsay, le 7 Juillet 2017:

Composition du Jury :

Mme Tiina SUOMIJÄRVI	Professeur	IPN Orsay,	Président
M. Frank MAAS	Professeur	HIM Mainz,	Rapporteur
M. Marco MAGGIORA	Professeur	Univ. de Turin,	Rapporteur
Mme Dominique MARCHAND	Chargée de Recherche	IPN Orsay,	Co-directeur de thèse
M. Nikolay PISKUNOV	Chercheur	VBLHE Dubna,	Examineur
Mme Egle TOMASI-GUSTAFSSON	Ingénieure-Chercheuse	CEA, Irfu,	Directeur de thèse

Study of antiproton-proton annihilation
reactions and experimental contribution to
hadron polarimetry

Ms. Ying Wang

July 7, 2017

Acknowledgements

Since the 15th September 2014, 3 years have almost passed. If look back, it usually seems really faster than we thought at the beginning. During the past 3 years, I met many people, and they helped and taught me a lot. Here I would like to thank all of them, and without them I would not be the same as today.

I thank the Directorate of the Institut de Physique Nucléaire d'Orsay for offering me the hospitality and the possibility to work in very good conditions, as a scholar of the China Scholarship Council.

I would like to thank all the members of the defence committee for accepting to evaluate my work: Professor Tiina Suomijärvi who chaired the committee, Professor Frank Maas and Professor Marco Maggiora for their reports and for very comprehensive and helpful comments, and Professor Nikolay Piskunov for the very enlightening questions.

Especially I would like to thank my supervisors, Dr. Egle Tomasi-Gustafsson and Dr. Dominique Marchand. I did not initially plan to come to France, but the coincidence made the decision for me. Reviewing the 3 years, I have to say I thank this coincidence. Dr. Tomasi-Gustafsson, who is a strong female model, from her I did not only learn physics and the research skills, but also learned to be tough to the difficulties. She led me to the hadronic physics and to the polarization experiment. She can always explain the problem in a more comprehensible and physical way. Dr. Marchand, helped me a lot in my daily life. I remember the first day she picked me from the airport with the "Welcome" sign in her hand. During the following 3 years, she gave me countless help in almost all the aspects. From her I also learned the optimistic spirit.

I am grateful to the colleagues of the institute. I also would like to thank my friends, for helping me to prepare and manage different aspects of the defence.

There are also other very important people that I would like to thank. First I would like to thank Professor Xie Yuehong, even though he won't see this manuscript, who gave me the confidence and encouraged me to step to this field. Second I would like to thank Dr. Sun Fei. We have known each other for 10 years through the college till now, and I hope the friendship will last long. Without her support and company I would not be able to get through the tough time.

I wish to thank the people from PANDA group in Mainz, and the people from ALPOM2 group in Dubna, also the people from JLab group in the laboratory. From them I also learned a lot and received a lot of help.

Last, I would like to thank my family.

II

Sincere thanks to all the people I have met during the past 3 years. These 3 years, I have grown up a lot in both mental and physical sides with all your help or affect.

Résumé

Ce travail de thèse est dédié à l'étude de la structure interne des nucléons. Il s'inscrit dans le cadre de la physique hadronique et comprend deux parties, une phénoménologique et une expérimentale, liées aux mesures des facteurs de forme électromagnétiques des hadrons respectivement dans les régions temps et espace. La structure électromagnétique du nucléon, liée à la dynamique interne des courants électrique et magnétique, apporte des contraintes sur les modèles des nucléons et se paramétrise en terme de facteurs de forme.

Partie 1 : étude phénoménologique de l'annihilation $\bar{p}p$ en une paire de mésons légers

Un programme expérimental de mesure des facteurs de forme électromagnétiques (EM) du proton dans la région temps est prévu auprès du futur complexe accélérateur FAIR (Facility for Antiproton and Ion Research) à Darmstadt, Allemagne, avec le détecteur à large acceptation PANDA (anti-Proton ANnihilation at DARMstadt) via les réactions d'annihilation $\bar{p}p \rightarrow e^+e^-$ et $\bar{p}p \rightarrow \mu^+\mu^-$ dans le domaine en énergie $2.25(1.5) \leq \sqrt{s}(p_{Lab}) \leq 5.47(15) \text{ GeV}(\text{GeV}/c)$ ¹. $\sqrt{s}(p_{Lab})$ est l'énergie totale dans le système du centre de masse (l'impulsion du faisceau dans le système du laboratoire). Dans de telles réactions, la difficulté majeure est d'extraire le signal d'intérêt du large bruit de fond issu des voies hadroniques, principalement la production d'une paire de pions chargés. La production d'une paire de mésons légers dans l'annihilation $\bar{p}p$ est l'un des sujets de cette thèse.

Le but est double : mieux évaluer le bruit de fond hadronique et améliorer notre connaissance sur la structure interne des hadrons car une telle réaction contient par elle-même des informations utiles sur le contenu en quarks des hadrons. Un modèle de mésons effectif a été développé pour évaluer la section efficace d'annihilation $\bar{p}p$ en une paire de mésons légers dans le domaine en énergie correspondant à l'expérience PANDA.

• **Chapitre 1** : ce chapitre introduit les projets au complexe accélérateur FAIR et le programme de physique prévu avec le détecteur PANDA. Après une revue bibliographique des expériences et des modèles liés à l'annihilation $\bar{p}p$ en une paire de pions chargés, les relations entre les variables cinématiques sont dérivées dans les systèmes du laboratoire et du centre de masse. Sur la base de la revue de la littérature associée, les sections efficaces et les distributions angulaires nécessaires aux études de faisabilité des mesures des facteurs de forme EM du proton dans

¹Nous utilisons les unités naturelles, $\hbar = c = 1$.

la région temps sont collectées. Pour accroître le nombre de données dans le domaine d'intérêt pour PANDA, on considère aussi la diffusion élastique pion-proton liés par symétrie de croisement et les expressions des relations entre les réactions d'annihilation et de diffusion sont dérivées.

• **Chapitre 2 :** un modèle de Lagrangien effectif basé sur les diagrammes de Feynman est développé pour calculer la section efficace différentielle pour la réaction $\bar{p}p \rightarrow \pi\pi$. On considère l'échange du nucléon et du Δ dans les voies t et u et du méson ρ dans l'état s . Les amplitudes de cette réaction dépendent de deux variables cinématiques indépendantes. Le rôle relatif de ces amplitudes varie avec la région cinématique. A l'avant la contribution dominante est l'échange du nucléon tandis que le Δ^{++} contribue principalement à l'arrière. On néglige la différence de masses entre le proton et le neutron ainsi qu'entre les différents états de charge des pions et des isobars de la résonance Δ . La diffusion à $\cos\theta = 0$ est sensible à l'échange de mésons vecteurs dans la voie s . Nous nous limitons à la contribution du méson ρ . Les amplitudes correspondant aux diagrammes considérés sont calculées analytiquement en suivant les règles de Feynman. Les traces ont été calculées et/ou vérifiées à l'aide du program FORM et les expressions obtenues ont été simplifiées avec *MATHEMATICA*. D'autres calculs de graphes ont été réalisés à l'aide des logiciels C++ et ROOT. Pour la première fois, pour prendre en compte la nature composite des hadrons en interaction, un facteur de forme logarithmique est introduit à la place d'autres fonctions utilisées dans la littérature.

Les effets de l'interaction forte dans l'état initial, entre les antiprotons et les protons, provenant de l'échange de mésons vecteurs et (pseudo) scalaires sont essentiels. La plus simple structure que nous pouvons considérer pour un méson est un monopôle et pour un baryon un dipôle. L'étude de différentes paramétrisations de facteurs de forme a montré que, dans la région d'énergie intermédiaire, la forme logarithmique est préférable pour tenir compte de la nature composite des baryons en interaction.

La comparaison de toutes les données existantes de production de pions chargés avec les prédictions des distributions angulaires et de dépendances obtenues avec notre modèle sont présentées dans le domaine en énergie

$3.362(5) \leq \sqrt{s}(p_{Lab}) \leq 4.559(15) \text{ GeV} (\text{GeV}/c)$. La dépendance en énergie est aussi discutée et comparée avec la règle de comptage des quarks à 90° dans le système du centre de masse. La stabilité de notre modèle a également été testée en variant la valeur des paramètres de $\pm 10\%$. En utilisant la symétrie de croisement nous avons appliqué notre modèle à la diffusion élastique πp . Les données sont en générale bien reproduites. En appliquant la symétrie SU(3) nous avons reproduit les données existantes sur la production d'une paire de kaons chargés. En intégrant les distributions angulaires résultant de notre modèle, on donne des valeurs de sections efficaces totales dans le domaine d'intérêt pour l'expérience PANDA. Quatre paramètres sont suffisants pour reproduire les données considérées.

• **Chapitre 3 :** bien que la réaction $\bar{p}p \rightarrow \pi^0\pi^0$ ait une section efficace dix fois plus faible que la production d'une paire de pions chargés, elle représente aussi un bruit de fond important pour les voies finales électromagnétiques et contient également des informations sur le mécanisme de la réaction régi par la chromodynamique quantique. Pour décrire cette réaction, nous avons étendu le formalisme utilisé précédemment dans le cadre de notre modèle de Lagrangien effectif en adaptant le mécanisme de réaction. Pour adapter notre modèle à la production de mésons neutres identiques, les diagrammes de Feynman ont été symétrisés dans les voies t et s et, dans la voie s , la particule échangée est un méson de moment angulaire pair, f_0 ou f_2 , car deux mésons identiques doivent être dans une onde relative paire.

Un terme exponentiel a été introduit au niveau du paramètre du facteur de forme logarithmique pour compenser un excès de section efficace dans la région de basse énergie. Notre modèle étendu reproduit de manière satisfaisante les données de sections efficaces différentielles obtenues dans l'expérience E835 (FERMILAB, USA) dans le domaine d'énergie $2.911 \leq \sqrt{s} \leq 3.68 \text{ GeV}$. Les mésons π^0 et η sont tous deux pseudo-scalaires. Les mésons η et π^0 font partie du même multiplet et sont liés par les symétries du modèle en quark. Nous utilisons cette propriété pour appliquer notre modèle aux réactions $\bar{p}p \rightarrow \eta\eta$ et $\bar{p}p \rightarrow \eta\pi^0$.

Il est nécessaire d'adapter les cinématiques et les masses en conséquence. Dans le cas de l'état final $\eta\pi^0$, qui n'est pas symétrique, il suffit d'introduire un angle de mélange au méson η . En appliquant la symétrie SU(3) et en tenant compte de la différence de cinématiques due aux masses, sans réajustement des paramètres, les distributions angulaires des réactions $\eta\eta$ et $\eta\pi^0$ dans le domaine en énergie $2.911 \leq \sqrt{s} \leq 3.617 \text{ GeV}$ sont bien reproduites.

Partie 2 : contribution à l'expérience ALPOM2 : mesure des pouvoirs d'analyse protons et neutrons

L'effort expérimental pour mesurer précisément le rapport $\frac{G_E}{G_M}$ entre les facteurs de forme EM du proton dans la région espace repose, depuis une vingtaine d'années, sur la méthode dite de polarisation du nucléon de recul dans la diffusion élastique électron polarisé - proton qu'on réalise au Jefferson Laboratory (Newport News, VA, USA). Ce programme expérimental sera très prochainement étendu jusqu'à des quadri-moments transférés au carré de 10 GeV^2 pour le proton et sera également appliqué au neutron. Cette méthode requiert de mesurer très précisément la polarisation de la particule de recul, le proton ou le neutron. Dans le cadre de la conception et de l'optimisation des polarimètres dans la région du GeV , il est essentiel, pour limiter la durée des prises de données, d'optimiser l'efficacité et le pouvoir d'analyse, quantités combinées dans la figure de mérite associée à chaque polarimètre. Dans ce contexte j'ai contribué à l'expérience ALPOM2 (JINR Dubna, Russia), la seule capable actuellement de mesurer des pouvoirs d'analyse pour des protons et des neutrons dans le domaine en impulsion d'intérêt pour les expériences réalisées au Jefferson Laboratory et permettant de considérer différents types de cible.

Dans le cadre de l'expérience ALPOM2, les faisceaux de protons et neutrons polarisés d'impulsion 3.00, 3.75 et 4.20 GeV/c sont obtenus par cassure du faisceau de deutons polarisés d'énergie jusqu'à 13 GeV délivré par le Nuclotron et on détecte les fragments chargés issus de la collision avec les cibles de C , CH_2 , CH et Cu . Pour les neutrons, dans le domaine d'impulsion entre 1 et 6 GeV/c , deux processus sont à considérer pour déterminer les pouvoirs d'analyse : la diffusion élastique $\vec{n}+p \rightarrow \vec{n}+p$ et la réaction avec échange de charge $\vec{n}+p \rightarrow p+\vec{n}$. En comparant les figures de mérite associés à chacun de ces processus, il apparaît que la réaction avec échange de charge est plus efficace pour la polarimétrie à haute énergie, au-delà de 4.8 GeV/c . Le dispositif expérimental et les résultats préliminaires sont présentés.

• **Chapitre 4** : ce chapitre présente un historique des méthodes de mesures des facteurs de forme EM des nucléons, depuis la méthode traditionnelle de Rosenbluth à la méthode de double polarisation proposée par Akhiezer et Rekalov. Dans l'approximation de Born, échange d'un photon virtuel, les extractions des facteurs de forme, dans les régions temps et espace, sont discutées. Dans la région temps, accessible expérimentalement par réaction d'annihilation auprès de collisionneurs électrons - positrons ou antiprotons - protons, les facteurs de forme sont complexes et les phénomènes de polarisation sont particulièrement importants. Dans la région espace, accessible expérimentalement par diffusion élastique, la contribution du terme électrique est inversement proportionnelle au quadri-moment transféré carré Q^2 . En utilisant la méthode de séparation de Rosenbluth, à grand Q^2 , ceci conduit à une grande incertitude sur le facteur de forme électrique. La méthode de double polarisation consiste à faire diffuser élastiquement un faisceau d'électrons polarisés sur une cible d'hydrogène non polarisée. La mesure du rapport G_E/G_M des facteurs de forme EM s'obtient en mesurant le rapport des composantes de polarisation transverse et longitudinale du proton de recul. Par cette méthode, les erreurs systématiques sont réduites et cela rend possible la détermination précise du rapport des facteurs de forme EM jusqu'à des grands Q^2 . Cette méthode est particulièrement intéressante pour le neutron car le facteur de forme électrique est petit.

• **Chapitre 5** : au Jefferson Laboratory, les expériences basées sur la méthode de double polarisation requièrent de mesurer les composantes de polarisations de protons et de neutrons de plusieurs GeV . Expérimentalement, il s'agit de mesurer dans un polarimètre hadronique de plan focal l'asymétrie azimutale de la diffusion secondaire des nucléons de recul sur une cible riche en hydrogène. La première étape pour optimiser la polarimétrie protons et neutrons est de réaliser l'expérience ALPOM2.

Dans le cas des neutrons, deux réactions permettent la mesure du pouvoir d'analyse : la réaction élastique et la réaction avec échange de charge, c'est-à-dire où le neutron est diffusé vers l'arrière. Les figures de mérite associées à ces deux réactions ont été calculées et comparées. Un modèle de pôles a été utilisé pour estimer

les sections efficaces et les données de pouvoirs d'analyse disponibles ont été collectées pour l'évaluation de l'expérience ALPOM2. La conclusion est que la réaction avec échange de charge est recommandée pour des impulsions supérieures à 4.8 GeV/c .

• **Chapitre 6 :** ce chapitre présente le dispositif expérimental de l'expérience ALPOM2 et les résultats préliminaires des analyses des prises de données de novembre 2016 et février 2017.

Les faisceaux polarisés de protons et de neutrons sont obtenus par cassure des deutons polarisés. Les deutons polarisés sont produits par une nouvelle source d'ions polarisés (CIPIOS) établie au Nuclotron. Il est attendu que la source CIPIOS délivre des faisceaux de deutons polarisés de haute qualité avec une intensité de 5 mA et d'énergie jusqu'à 6.5 $GeV/nuc\ell\grave{e}on$. Après la source, un accélérateur linéaire de type Alvarez DTL (Drift Tube Linac) LU-20 est utilisé pour comme injecteur pour le Nuclotron, un synchrotron supraconducteur. La mesure précise de la polarisation du faisceau de deutons est essentielle car elle intervient directement dans la détermination du pouvoir d'analyse. Dans ce but, plusieurs polarimètres de faisceaux sont placés sur la ligne. Ils permettent aussi de contrôler d'éventuelles dépolariation du faisceau durant les phases de transmission et d'accélération. Durant l'expérience ALPOM2, on utilise principalement le polarimètre de haute énergie F3 car son information est enregistrée en ligne avec les données, pour chaque paquet de faisceau, assurant un contrôle relatif continu de la polarisation du faisceau. Les protons polarisés sont produits par cassure des noyaux de deutérium diffusés sur une cible de CH_2 puis les protons sont séparés des neutrons et des deutons par un aimant dipolaire. Les neutrons sont produits par cassure du deutérium lors de l'interaction avec une cible de carbone, les protons et les deutons sont déviés magnétiquement.

Le dispositif ALPOM2 dérive d'une mise à niveau de l'expérience ALPOM. Un calorimètre hadronique a été ajouté en aval de la ligne faisceau afin de sélectionner les événements par leur dépôt d'énergie. En outre, comme le pouvoir d'analyse devient de plus en plus petit quand l'impulsion augmente, ce calorimètre est aussi utilisé pour identifier les particules chargées aux petits angles, ce qui a pour effet d'accroître la précision sur le pouvoir d'analyse. Les détecteurs de l'expérience ALPOM2 sont principalement des scintillateurs et des chambres à dérive. Les scintillateurs servent de *trigger* et les chambres à dérive enregistrent les trajectoires des particules. Pendant les mesures de novembre 2016 et février 2017, des données ont été acquises pour des protons et des neutrons polarisés à trois valeurs d'impulsion, 3.00, 3.75 et 4.20 GeV/c sur des cibles de C , CH , CH_2 et Cu . L'analyse et les résultats préliminaires obtenus pour la cible CH_2 sont présentés et comparés aux résultats précédents. Pour le proton, les résultats sont en accord avec ceux obtenus lors des précédentes campagnes de mesure. Pour le neutron les mesures de pouvoirs d'analyse réalisées à Dubna jusqu'à une impulsion de 4.2 GeV/c sont les premières données obtenues sur des cibles complexes, plus lourdes que l'hydrogène.

Abstract

This thesis work, in the framework of hadron physics, reports on a phenomenological and an experimental study dedicated to the nucleon internal structure, both related to hadron electromagnetic form factor measurements in the time-like and in the space-like regions.

At the future Facility for Antiproton and Ion Research (FAIR) in Darmstadt, Germany, an experimental program aiming to determine the proton electromagnetic form factors in the time-like region is planned at the PANDA (anti-Proton Annihilation at Darmstadt) large acceptance detector through the annihilation reactions $\bar{p}p \rightarrow e^+e^-$ and $\bar{p}p \rightarrow \mu^+\mu^-$ in the energy range $2.25(1.5) \leq \sqrt{s}(p_L) \leq 5.47(15)$ GeV $(\text{GeV}/c)^2$, where $\sqrt{s}(p_L)$ is the total energy in the center of mass system (the antiproton beam momentum in laboratory frame). In such reactions, the main difficulty will be to extract the signal of interest from the huge background coming from hadronic channels, mainly charged pion pair production. Meson pair production in $\bar{p}p$ annihilation is one of the subjects of this thesis. The goal is two-fold: to better evaluate the hadronic background and to improve our knowledge on the hadron internal structure as such reaction contains by itself useful information on the hadron quark content. An effective meson model has been developed to evaluate the cross section of $\bar{p}p$ annihilation into light meson pairs, in the energy domain relevant to the PANDA experiment. A logarithmic form factor is introduced to account for the composite nature of the interacting hadrons. A comparison with the data for charged pion pair production and predictions for angular distributions and energy dependence are presented in the range $3.362(5) \leq \sqrt{s}(p_L) \leq 4.559(10.1)$ GeV (GeV/c) . The model is applied to πp elastic scattering, using crossing symmetry, and to charged kaon pair production, on the basis of SU(3) symmetry. The model is extended to different neutral channels $\pi^0\pi^0, \eta\eta, \eta\pi^0$. The results are presented and successfully compared to the data.

In the space-like region, the experimental effort, dedicated to precise measurements of the proton electromagnetic form factor ratio with the recoil polarization method in electron-proton elastic scattering at Jefferson Laboratory (JLab-Newport News, VA, USA), will be pursued up to higher momentum transfer squared, above 10 GeV², and will be also applied to neutron. This method requires an accurate measurement of the polarization of the recoil particle, the proton or the neutron. In order to design and optimize the polarimetry in the GeV region, the determination of the efficiency and the analyzing powers, that combine into the Figure of Merit, is mandatory to conceive a polarimeter, as polarization experiments are very lengthy. In this context I contributed to the ALPOM2 experiment (JINR Dubna, Russia), the only experiment right now able to measure proton and neutron analyzing powers in the momentum range of interest for JLab experiments and allowing to consider different types of target. Experimentally, in the framework of ALPOM2, from the Nuclotron polarized deuteron beam (up to 13 GeV energy), polarized proton and

²We use natural units, $\hbar = c = 1$, but in the expression of the momentum c is kept.

neutron beams at 3.0, 3.75 and 4.2 GeV/ c were obtained by deuteron break-up and the charged fragments from the collisions with C , CH_2 , CH and Cu targets were measured. For neutrons, in the range from 1 to 6 GeV/ c , two processes have been considered to determine the analyzing power: the elastic scattering $\vec{n} + p \rightarrow \vec{n} + p$ and the charge exchange reaction $\vec{n} + p \rightarrow p + \vec{n}$. From the comparison of the Figure of Merit associated to each of these two processes, the charge exchange reaction appears to be more efficient for polarimetry at high energy. Neutron analyzing powers for the charge exchange reaction on CH , and Cu targets have been measured up to 4.2 GeV/ c for the first time. For the proton, more precise analyzing power data have been obtained. The experimental results obtained from a preliminary analysis are presented.

Contents

I	Light meson productions in $\bar{p}p$ annihilation	9
1	Annihilation of $\bar{p}p$ into light mesons	11
1.1	Introduction	11
1.2	Kinematics of $\bar{p} + p \rightarrow \pi^- + \pi^+$	15
1.3	Existing experimental data for $\bar{p} + p \rightarrow \pi^- + \pi^+$	19
1.3.1	Differential cross sections	19
1.3.2	Total cross sections	24
1.3.3	High energy region	25
1.3.4	Low energy region	25
1.3.5	Polarized experiments	26
1.3.6	Central collisions	26
1.4	Relation with the crossed processes	27
2	Calculation of $\bar{p}p$ annihilation into charged light meson pairs	31
2.1	Introduction	31
2.2	Formalism for $\bar{p} + p \rightarrow \pi^- + \pi^+$	34
2.2.1	Derivation of the invariant cross section	34
2.2.2	Calculation of the matrix element	35
2.2.3	t -channel neutron exchange	37
2.2.4	t -channel Δ^0 exchange	38
2.2.5	u -channel Δ^{++} exchange	40
2.2.6	s -channel ρ meson exchange	41
2.2.7	The interferences	43
2.2.7.1	The $\Delta^0 - N$ interference	43
2.2.7.2	The $\Delta^{++} - N$ interference	44
2.2.7.3	The $\Delta^{++} - \Delta^0$ interference	44
2.2.7.4	The $N - \rho$ interference	44
2.2.7.5	The $\Delta^0 - \rho$ interference	44
2.2.7.6	The $\Delta^{++} - \rho$ interference	44
2.2.8	Form factors at vertices	45
2.2.8.1	Angular and energy dependencies of different form factors and Regge factors	45
2.2.8.2	The ρNN form factor	47

2.3	Results and comparison with the data	49
2.3.1	Angular distributions	50
2.3.2	Energy dependence	55
2.3.3	Total cross section	56
2.4	Comparison with the existing data on $\bar{p} + p \rightarrow K^- + K^+$	58
2.5	Summary	59
3	Annihilation into neutral light meson pairs	61
3.1	Introduction	61
3.2	Calculation of the matrix element	61
3.2.1	s -exchange of neutral scalar mesons: the f_0 contribution	62
3.2.2	The f_0 interferences	64
3.2.2.1	The $N - f_0$ interference	64
3.2.2.2	The $\Delta - f_0$ interference	64
3.2.3	s -exchange of neutral scalar mesons: the f_2 contribution	65
3.2.4	The f_2 interferences	67
3.2.4.1	The $f_0 - f_2$ interference	67
3.2.4.2	The $N - f_2$ interference	67
3.2.4.3	The $\Delta - f_2$ interference	67
3.2.5	The total contribution	68
3.3	Results for $\bar{p} + p \rightarrow \pi^0 + \pi^0$	68
3.4	Results for $\bar{p} + p \rightarrow \eta + \eta$ and $\bar{p} + p \rightarrow \eta + \pi^0$	73
II	Proton and neutron analyzing power measurements	77
4	Introduction on electromagnetic form factors	79
4.1	Form factors in the time-like region	81
4.2	Form factors in the space-like region	82
5	Calculation of cross sections, analyzing powers, efficiency and figure of merit	87
5.1	Performance of a polarimeter	88
5.1.1	Kinematics of np scattering	89
5.1.2	Angular distributions of np scattering	91
5.1.3	Analyzing powers	95
5.2	Calculation of polarimeter efficiency and maximum figure of merit	97
6	The ALPOM2 Experiment at Nuclotron accelerator of the Joint Institute for Nuclear Research	101
6.1	Introduction	101
6.2	Short presentation of the Joint Institute for Nuclear Research	101
6.3	Description of the experiment	104
6.3.1	The experimental setup	105

6.3.1.1	The beam	105
6.3.1.2	On-line beam polarimeters	112
6.3.1.3	Deuteron breakup	115
6.3.2	Setup for the test run	116
6.3.2.1	Drift Chamber	116
6.3.2.2	Track reconstruction	118
6.3.2.3	Polarimeter target	119
6.3.2.4	Hadron calorimeter	120
6.3.3	Online data acquisition system and analysis	125
6.4	Extraction of analyzing powers	130
6.5	Summary of experimental results	136
7	Conclusion	139
A	Collection of experimental data	143
A.1	Charged meson pair production	144
A.2	Neutral meson pair production	149
A.3	Table of acronyms	160

List of Figures

1.1	Illustration of the FAIR Accelerator Complex, including the four collaborations: APPA (Atomic Physics, Plasma and Applied sciences), CBM (Compressed Baryonic Matter experiment), NuSTAR (Nuclear structure, Astrophysics and Reactions) and PANDA (Antiproton annihilation at Darmstadt).	12
1.2	Scheme of the reaction (1.1) in the Lab and CM systems.	16
1.3	Energy of the π^\pm meson as a function of the emission angle for $p_L = 1.9 \text{ GeV}/c$ in Lab system. The black points are the events from the FTF generator and the solid line is the result of Eq. (1.7). The red(green) line corresponds to $\varepsilon^{L(+)}(\varepsilon^{L(-)})$	17
1.4	Energy of π^+ -meson as a function of the energy of π^- -meson for incident momentum $p_L=1.9 \text{ GeV}/c$ in Lab system. The black points are the events from the FTF generator and the solid red line is the calculation of kinematics.	17
1.5	Correlation between the angles of the π^\pm -mesons for incident momentum $p_L=1.9 \text{ GeV}/c$. The black points are the events from the FTF generator. The blue line represents a π^- moving forward (π^+ moving backward), the red line is for the opposite. The green line shows the central region of the emitted pions.	18
1.6	CM emission angle (θ_1) of π^- meson as a function of the Lab angle (θ_1^L) at antiproton Lab momentum $p_L = 1.9 \text{ GeV}/c$	19
1.7	Feynman diagram for $\bar{p} + p \rightarrow \pi^+ + \pi^-$ (a) and $\pi^- + p \rightarrow \pi^- + p$ (b).	27
1.8	Data for $\bar{p} + p \rightarrow \pi^- + \pi^+$ for π^+ detected forward (black [46] and red [85] empty circles) and for $\pi^- + p \rightarrow \pi^- + p$ (light blue circles, from Ref.[48]). The green circles (from Ref. [86]), and the purple circles (from Ref. [49]) correspond to π^- emission at small t -values (or large u -values).	30
1.9	Data for $\bar{p} + p \rightarrow \pi^- + \pi^+$ for π^- detected forward (black empty circles Ref. [46]), and for $\pi^+ + p \rightarrow \pi^+ + p$ (red solid circles from Ref. [49], and green solid circles from Ref. [47]) corresponding to π^+ emission at small t -values (or large u -values). The π^+p data have been scaled as in the Fig. 1.8 with the same crossing factor 0.589.	30

2.1	Data and modelisation of angular distributions for the reaction $\bar{p} + p \rightarrow \pi^+ + \pi^-$, as a function of $\cos \theta$, for different values of the total energy squared: 3 GeV (open red lozenges, red thick solid line) and 4 GeV (open red crosses, red thick dashed line) from ref. [54]; 6 GeV [53] (black triangles-down); 6.21 GeV [46] (solid circles, black, solid line); 13.5 GeV [47] (open blue circle, blue dash-dotted line); 20.8 GeV [52] (green triangles, green dotted line); 24.3 GeV [69] (cyan square, cyan short-dashed line); upper limits at 30 GeV (yellow open triangles) and 50 GeV (yellow open squares) from [51]. The lines are from the generator [87].	32
2.2	Total cross section for the reaction $\bar{p} + p \rightarrow \pi^+ + \pi^-$, as a function of the beam momentum in Lab system p_L . The data are from: [56] (black, full squares) [55] (black, full circles) [58] (black, full triangle up) [57] (magenta, full triangle down) [59] (black, full circle) [60] (cyan, full cross) [88] (black, open triangle up) [62] (red, full diamond) [64] (grey, full star) [65] (blue, open star) [69] (green, full square). The solid line is the result from the generator, where the transition between the two regimes is visible. The dashed line is the result of the compilation from [24].	33
2.3	Feynman diagrams for the reaction $\bar{p} + p \rightarrow \pi^- + \pi^+$ within effective meson Lagrangian approach.	36
2.4	Diagram for $\Delta \rightarrow N\pi$ decay.	40
2.5	Diagram for ρ decay into a pion pair	43
2.6	Energy dependence (top) and angular distribution (bottom) of form factors (left) and Regge factors (right) for soft (s, solid lines) and hard (h, dashed lines) parameters (see Tables 2.1 and Table 2.2). The notations for nucleon and Δ form factors (left side) are: monopole (black), dipole (red), exponential (green). In the right side the logarithmic function is shown in blue(magenta) for nucleon(Δ). The Regge factor is shown in black(red) for nucleon(Δ).	48
2.7	Angular dependence for the reaction $\bar{p} + p \rightarrow \pi^- + \pi^+$, for $\sqrt{s} = 3.680$ GeV from Ref. [46] (black solid circles) and for $\sqrt{s} = 3.362$ GeV from Ref. [47] (red open circles). The present calculation is shown by a long-dashed red line, and a solid black line at the corresponding energies. The calculation from the constituent interchange model of Ref. [40] is also reported, as a dash-dotted red line, and a dotted black line respectively.	51
2.8	Angular dependence for the reaction $\bar{p} + p \rightarrow \pi^- + \pi^+$ for $\sqrt{s} = 3.627$ GeV [53] (red open circles), and 4.559 GeV [52] (black solid circles). The data from Ref. [53] were excluded from the fit, but they are well reproduced 'a posteriori'. Lines as in Fig. 2.7.	52

2.9	Data from the elastic reactions $\pi + p \rightarrow \pi + p$ at $\sqrt{s} = 3.463$ GeV from Ref. [48] (red open circles), and at $\sqrt{s} = 3.747$ GeV from Ref. [49] (black solid circles). Lines as in Fig. 2.7.	53
2.10	Angular distribution for $\bar{p} + p \rightarrow \pi^- + \pi^+$ for $\sqrt{s} = 3.680$ GeV. The data are from Ref. [46]. The total function (black solid line) and all components are shown in log scale: n exchange (yellow thick short-dashed line) dominates at forward angle, followed by Δ^0 (red thick dotted line) Δ^{++} (green thick dash-dotted line) represents the largest contribution for backward angles, ρ channel (blue thick long-dashed line) has a larger contribution for $\cos \theta \simeq 0$, relatively to the dominant components. The interferences are $n\Delta^0$ (thin black short-dashed line), and $n\Delta^{++}$ (thin red dotted line), visible at forward angles, $\Delta^0\Delta^{++}$ (green thin short dash-dotted line), $n\rho$ (blue thin long-dashed dotted line), $\Delta^0\rho$ (blue thin dash-triple-dotted line), $\Delta^{++}\rho$ (blue thin long-dashed line), contributing at backward angles.	54
2.11	s -dependence for $\bar{p} + p \rightarrow \pi^- + \pi^+$ for $\theta = 90^\circ$. The total function (black solid line), two functions with parameters changed to 110% (black long-dashed line) and 90% (short-dashed line) from the fitted values are shown in log scale, compared with quark counting rules result from Refs. [21, 22] (red triple dot-dashed line).	55
2.12	The collected data for the total cross section for reaction $\bar{p}p \rightarrow \pi^+\pi^-$ as a function of the beam momentum in Lab system p_L (same data as in Fig. 2.2). Three new points (full, purple square) are obtained from the integration of the angular distribution data [47, 46, 52]. The present model with form factor parameters (Listed in Table 2.3) is shown as solid red line. The dashed black line is the modified parametrization from Eq. (2.58) with parameters in Table 2.4 from Ref. [24], the solid black line is from the generator [87].	56
2.13	Angular distribution for $\bar{p} + p \rightarrow K^+ + K^-$ for $\sqrt{s} = 3.680$ GeV. The result of the model (black solid line), as well as the result where the parameters have been overestimated (long dashed line) or underestimated (dotted line) by 10% are shown in log scale. The data are from Ref. [46].	58
3.1	Diagrams of different exchanged particles for reaction $\bar{p} + p \rightarrow \pi^0 + \pi^0$	62
3.2	Diagram for f_0 and f_2 decays into a pion pair.	64
3.3	Angular distribution for the reaction $\bar{p}p \rightarrow \pi^0\pi^0$ in CMS in the energy range $2.911 \text{ GeV} \leq \sqrt{s} \leq 3.686 \text{ GeV}$. From (a) \rightarrow (u), they correspond to the energy $\sqrt{s} = 2.911$ (a), 2.950(b), 2.975(c), 2.979 (d), 2.981(e), 2.985(f), 2.990(g), 2.994(h), 3.005(i), 3.050(j), 3.097(k), 3.524(l), 3.526(m), 3.556(n), 3.591(o), 3.595(p), 3.613(q), 3.616(r), 3.619(s), 3.621(t), 3.686(u) GeV. The data (black circles) are from Ref. [75] and the parameters of the calculation (red line) are given in Table 3.2.	70

3.4	Integrated cross section for the reaction $\bar{p}p \rightarrow \pi^0\pi^0$. The data are obtained by the integration of the partial differential cross section from Ref. [75]. The present calculation (red solid line) covering the range $0 \leq \cos\theta \leq 0.66$ is shown in log scale.	71
3.5	Angular distribution for reaction $\bar{p}p \rightarrow \pi^0\pi^0$ at $\sqrt{s} = 4.274$ GeV [75] with different components. The parameters are listed in Table 3.3. . .	72
3.6	Angular distribution for $\bar{p}p \rightarrow \eta\eta$ (black circle) [75] in the energy range $2.911 \text{ GeV} \leq \sqrt{s} \leq 3.617 \text{ GeV}$. From (a) \rightarrow (m), they correspond to the energy $\sqrt{s} = 2.911$ (a), 2.950(b), 2.975(c), 2.979 (d), 2.981(e), 2.985(f), 2.990(g), 2.994(h), 3.005(i), 3.050(j), 3.526(k), 3.592(l), 3.617(m) GeV. The model calculation (red solid curve) is based on the symmetry of the quark model.	74
3.7	Same as Fig. 3.6, for the reaction $\bar{p}p \rightarrow \eta\pi^0$ in the energy range $2.911 \text{ GeV} \leq \sqrt{s} \leq 3.617 \text{ GeV}$. From (a) \rightarrow (m), they correspond to the energy $\sqrt{s} = 2.911$ (a), 2.950(b), 2.975(c), 2.979 (d), 2.981(e), 2.985(f), 2.990(g), 2.994(h), 3.005(i), 3.050(j), 3.526(k), 3.592(l), 3.617(m) GeV.	75
4.1	Diagram for ep elastic scattering through one photon exchange. . . .	80
4.2	Reaction of $p + \bar{p} \rightarrow e^- + e^+$ in CMS.	81
4.3	Illustration of ep elastic scattering in the Lab system.	82
4.4	The collected data of the proton (left) and neutron (right) form factor ratio $\mu_p G_E/G_M$ by Perdrisat and Punjabi [124]. The data in the left figure from polarized experiments are from Refs. [120, 121] (full circles), Refs. [122, 125] (full squares), and Ref. [123] (full triangles), respectively. The data from unpolarized cross section (green symbols) are: open triangles [126], circles [127], and diamonds [128]. The theoretical predictions are given by Ref. [129] (solid red), Ref. [130] (short-dashed blue), [131] (dash-dot orange), [132] (dash green), and Ref. [133] (short dash-dot magenta). The data in the right figure for neutron FF ratio are from Refs. [134, 135, 136, 137, 138, 139] (red), Refs. [140, 141, 142, 143] (blue), and Refs. [144, 145] (black) and Ref. [146] (green).	84
5.1	Scheme of the reaction $np \rightarrow np(pn)$ in Lab and CM systems.	90
5.2	CMS versus Lab angle for the emitted neutron at different Lab momenta. The corresponding Q^2 for electron scattering is also indicated.	91
5.3	Feynman diagrams for the pole model of $np \rightarrow np(pn)$ scattering. . .	92

5.4	Top figures: data are from Ref. [153], corresponding to different incident beam momenta: $p_L=2.2$ GeV/ c (left), 3.3 GeV/ c (middle), and 4.3 GeV/ c (right). Bottom figures: data are from Ref. [154] and correspond to beam momenta: $p_L= 3.1$ GeV/ c (left), 3.6 GeV/ c (middle), 6.1 GeV/ c (right). The model prediction with Eq. (5.13) from Ref. [152], is also shown (black thick solid line) together with the zero-exchange (red solid line) and charge-exchange (blue dotted line) contributions.	93
5.5	The differential cross sections of the charge-exchange process ($np \rightarrow pn$) at different beam momenta from 2.375 GeV/ c to 8 GeV/ c . The data are from the Refs. [155, 156, 157] and the curves are from the calculation of the pole model with refitted parameters as in Eq. (5.14).	94
5.6	(Left: differential cross section as a function of p_L , according to Eq. (5.9) for $t = 0$. Ref. [152]. Right: total cross section as a function of p_L (black solid thick line), zero-exchange (thin red solid line), and charge-exchange (blue dotted line).	95
5.7	Data (red symbols) of analyzing powers for the charge-exchange process ($np \rightarrow pn$) is from Ref. [151]. The red curves are fitted to the data following Eq. (5.15) and a green asterisk is added to constrain the function passing through zero at zero. The parameters are listed in Table 5.1.	96
5.8	Data (red symbols) of analyzing powers for the zero-exchange process ($np \rightarrow np$) is from Ref. [160]. The red curves are fitted to the data following Eq. (5.15) and a green asterisk is added to constrain the function passing through zero at zero. The parameters are listed in Table 5.2.	98
5.9	$ A_y _{Max}$ for $np \rightarrow np(pn)$ based on the polarization data from charge-exchange (blue dotted line) from Ref. [151] and zero-exchange (red solid line) from Ref. [160] with the parameters as in Table 5.3.	99
5.10	Integrated FoM for $np \rightarrow np(pn)$ based on the fitted result from Fig. 5.9 (upper limit) for charge-exchange (blue dotted line) and zero-exchange (red solid line). The red empty circles are calculated from the Monte-Carlo simulation of JLab proposal PR-09-006 [161].	100
6.1	Physics region, in the plane Temperature as a function of the baryon density, explored at the Nuclotron-based Ion Collider facility (NICA Complex).	104
6.2	The ALPOM2 setup at Nuclotron for polarized neutron experiment.	107
6.3	Quantum numbers of hyperfine structure of deuteron. The quantum numbers of molecular deuterium, electron angular momentum, and the naked deuteron atom angular momentum are presented as F , J and I .	109

6.4	Layout of the ABS (Atomic Beam Source) : pulsed dissociator, beam cooler, sextupoles magnets for focusing, RF (radio-frequency) transition units for polarization, and TOF (time of flight), MS (mass spectrum) from Ref. [170].	110
6.5	Scheme of the radial-symmetric magnetic sextupole that selects atoms by electron spin state. The magnetic field $ B $ increases with r increasing, and r_m is the radius of minimum $ B_m $	110
6.6	The F3 polarimeter (courtesy of Shindin Roman). IC is an ionization chamber. The F3 left, right forward and backward arms have three scintillation counters at the angles a and b with respect to the beam-line.	113
6.7	Correlated angles for the emitted and recoil particles in pp quasi-elastic scattering at the relevant proton momenta: 2.1, 3.75, 4.2 and 7.5 GeV/c.	114
6.8	World data for the $p(d,p)X$ and $C(d,p)X$ reactions for the vector to vector polarization transfer coefficient (K_0) ats a function of the internal proton momentum k from Ref. [179].	115
6.9	The setup of the test run in ALPOM2 experiment during 2015 [180]. $M_{1,2}$: beam monitors. S_1 : scintillator counter, $DC_{0,1,2}$: drift chambers, AT_{1-6} : active target. HCAL: hadron calorimeter.	116
6.10	The Online TDC time spectrum of a wire of a drift chamber during the ALPOM2 expeiment. T_{min} and T_{max} are the drift times.	117
6.11	An example for the reconstruction of a track in the drift chamber of X-Z coordinate from the STRELA experiment [181].	118
6.12	Figures from the test runs by the ALPOM2 group of JINR. Left: dependence of the angular distribution of incident protons and neutrons on 30 cm targets, CH_2 and CH , at 3.75 GeV/c. Right: angular distribution for protons on a 40 cm CH_2 target at 6 GeV/c where the the angular regions for the different processes are highlighted.	119
6.13	Data selection of different processes induced by proton on CH_2 target at 3.75 GeV/c (left) and 6.0 GeV/c (right) as a function of the sum of the energy deposited in the calorimeter (courtesy of the ALPOM2 group of JINR).	121
6.14	One module of the hadron calorimeter: 1. scintillator, 2. iron plates, 3. wavelength-shifting guide, 4. modules container, 5. Photomutiplier, 6. magnetic shield, 7. high-voltage divider, 8. optical connector. The figure is from ALPOM2 proposal [180].	122
6.15	Energy resolution versus kinetic energy for the COMPASS pion data (red) and for 6Li , 4He , deuteron beams (black) during June 2016 test. Open points and yellow curve are the Monte-Carlo simulations and the fit corresponds to protons. The figure is from ALPOM2 proposal [180].	122
6.16	View of the hadron calorimeter setup (left) and of the scintillators in each module (right).	123

6.17	Geometrical layout of hadron calorimeter and its different moduli from ALPOM2 group of JINR.	124
6.18	The setup of ALPOM2 for polarized neutron and proton beams in November 2016 run. $S_{0,1}$ and $S_{up,down}$ are scintillators, corresponding to Table 6.5. DC_0 and $DC_{1,2}$ are the small and large drift chambers before and after the target. The last element downstream is the hadron calorimeter.	125
6.19	The deuteron beam intensity (yellow) and the magnetic field strength of the Nuclotron (green) during the November 2016 run during one spill time.	126
6.20	Counting rate spectra (top) in the left arm of the F3 polarimeter for the 3 beam states (+, 0, -) normalized to the total events recorded by the F3 ion chamber. Left-right asymmetry (bottom) as a function of run number calculated by the F3 polarimeter at proton momentum 3.75 GeV/c. Figures are from F3 polarimeter online system.	127
6.21	The proton (left) and the neutron (right) beam positions in the XY-plane at momentum 3.75 GeV/c (courtesy of the ALPOM2 group of JINR).	129
6.22	Neutron particles interaction in the XZ-(left) and YZ-(right) dimensions at momentum 3.75 GeV/c, reconstructed from the detection of charged particles in forward direction (courtesy of the ALPOM2 group of JINR). The wires of the last plane of the wire chamber are visible.	129
6.23	The (θ, ϕ) distribution for proton (top) and neutron (bottom) on CH2 target at beam momentum 3.75 GeV/c of polarization states "+" and "-".	130
6.24	ϕ asymmetry for proton (right) and neutron (left) at momentum 3.75 GeV/c.	131
6.25	ϕ -asymmetry spectra for proton (left) and neutron (right) at beam momentum 3.75 GeV/c on CH2 target analysis according to Eq. (6.8), integrated in the θ range 0.09 to 0.15.	132
6.26	ϕ -asymmetry spectra for proton (left) and neutron (right) at beam momentum 3.75 GeV/c on CH2 target analysis with Eq. (6.9).	133
6.27	Extracted analyzing power of proton (left) and neutron (right) at beam momentum 3.75 GeV/c with $ P^+ = 0.642$ and $ P^- = 0.511$ on CH2 target following with the two methods, from Eq. (6.8) and Eq. (6.9).	133
6.28	ϕ asymmetry spectra for proton (blue) and neutron (red) at 3.0 GeV/c (left) and 4.2 GeV/c (right) on CH2 target in Eq. (6.9) (courtesy of the ALPOM2 group of JINR).	134

-
- 6.29 Analyzing power A_y as a function of P_{perp} for the reaction $p + CH_2 \rightarrow$ charged particle + X : the full symbols are the results from ALPOM2 experiment for different beam momenta: $p_L = 3$ GeV/c (blue full circles), 3.75 GeV/c (red full squares) and 4.2 GeV/c (green full triangles). The empty symbols are data from ALPOM at beam momenta: 3.8 GeV/c (red empty squares) and 4.5 GeV/c (green empty triangles) [149]. 135
- 6.30 World data for the maximum analyzing power (A_y^{max}) for the reaction $p + CH_2/C \rightarrow$ charged particle + X on different targets CH₂ (red and black symbols), C (cyan symbols)(see text). The results from the present work are shown as blue stars. A linear fit of the corresponding color is also plotted. 137

List of Tables

1.1	Notation of four-momenta in the laboratory (Lab) and Centre of Mass (CMS) reference frames.	15
1.2	(Part I) Collection of experimental data for the reactions: $\bar{p} + p \rightarrow \pi^- + \pi^+, \pi^- + p \rightarrow \pi^- + p, \pi^- + p \rightarrow p + \pi^-$	20
1.3	(Part II) Collection of experimental data for the reactions: $\bar{p} + p \rightarrow \pi^- + \pi^+, \pi^- + p \rightarrow \pi^- + p, \pi^- + p \rightarrow p + \pi^-$	21
1.4	(Part III) Collection of experimental data for the reactions: $\bar{p} + p \rightarrow \pi^- + \pi^+, \pi^- + p \rightarrow \pi^- + p, \pi^- + p \rightarrow p + \pi^-$	22
1.5	Correspondence between variables in the crossed scattering (s) and annihilation (a) channels.	28
2.1	Parameters of the monopole, dipole, exponential form factors for a soft (s) and a hard (h) choice, as well as for Regge parametrization for n and Δ , used for the calculation illustrated in Fig. 2.6.	46
2.2	Summary of the parameters for the logarithmic form factors, Eq. (2.52, 2.56).	46
2.3	Summary table for the parameters for the s -dependent form factor reproducing the total cross section.	57
2.4	Parameters for the modified parametrization formula from Ref. [24].	57
3.1	Parameters for the s -dependent term of the logarithmic form factors for $\bar{p}p \rightarrow \pi^0\pi^0$	68
3.2	Parameters of the f_0NN form factor for $\pi^0\pi^0$ production in the energy range $2.911 \text{ GeV} \leq \sqrt{s} \leq 3.686 \text{ GeV}$	69
3.3	Parameters of form factors for f_0 and f_2 mesons at $\sqrt{s} = 4.274 \text{ GeV}$	71
5.1	Parameters of Eq. (5.15) for the charge-exchange process illustrated in Fig. 5.7.	95
5.2	The parameters for zero-exchange process of Eq. (5.15) corresponding to the data in Fig. 5.8.	97
5.3	Zero-exchange and charge-exchange functions corresponding to Fig. 5.9.	97
6.1	Information on the runs of the ALPOM2 experiment: running time, the beam kinetic energy, the beam type, the beam momentum, and the nature of the target.	105

6.2	Detailed information for the runs in 19-31 November 2016 and 24-27 February 2017: the run number, the target, the beam type and its momentum.	106
6.3	RF units frequency to transfer the atoms states.	109
6.4	The main parameters of Nuclotron.	112
6.5	Online acquisition monitor system. Typical counting rates for the different elements.	128
A.1	(Part I) Differential cross section data for the reactions: $\bar{p} + p \rightarrow \pi^- + \pi^+$	144
A.2	(Part II) Differential cross section data for the reactions: $\bar{p} + p \rightarrow \pi^- + \pi^+$	145
A.3	Collection of differential cross section data for the reaction: $\pi^- + p \rightarrow \pi^- + p$. These data are compared to annihilation into charged pion pair assuming crossing symmetry.	146
A.4	Collection of differential cross section data for the reactions: $\bar{p} + p \rightarrow K^- + K^+$. These data are compared to the model in SU3 symmetry.	147
A.5	Collection of total cross section data for the reactions: $\bar{p} + p \rightarrow \pi^- + \pi^+$. These data are compared to the integration of the model.	148
A.6	(Part I) Collection of angular distribution data for the reaction: $\bar{p} + p \rightarrow \pi^0 + \pi^0$ from Ref. [75].	149
A.7	(Part II) Collection of angular distribution data for the reaction: $\bar{p} + p \rightarrow \pi^0 + \pi^0$ from Ref. [75].	150
A.8	(Part III) Collection of angular distribution data for the reaction: $\bar{p} + p \rightarrow \pi^0 + \pi^0$ from Ref. [75].	151
A.9	(Part IV) Collection of angular distribution data for the reaction: $\bar{p} + p \rightarrow \pi^0 + \pi^0$ from Ref. [75].	152
A.10	(Part V) Collection of angular distribution data for the reaction: $\bar{p} + p \rightarrow \pi^0 + \pi^0$ from Ref. [75].	153
A.11	(Part I) Collection of angular distribution data for the reaction: $\bar{p} + p \rightarrow \eta + \eta$ from Ref. [75].	154
A.12	(Part II) Collection of angular distribution data for the reaction: $\bar{p} + p \rightarrow \eta + \eta$ from Ref. [75].	155
A.13	(Part I) Collection of angular distribution data for the reaction: $\bar{p} + p \rightarrow \pi^0 + \eta$ from Ref. [75].	156
A.14	(Part II) Collection of angular distribution data for the reaction: $\bar{p} + p \rightarrow \pi^0 + \eta$ from Ref. [75].	157
A.15	(Part III) Collection of angular distribution data for the reaction: $\bar{p} + p \rightarrow \pi^0 + \eta$ from Ref. [75].	158
A.16	(Part IV) Collection of angular distribution data for the reaction: $\bar{p} + p \rightarrow \pi^0 + \eta$ from Ref. [75].	159
A.17	Table of the acronyms(left) for the full name(right).	160

Introduction

This work reports on selected aspects in the frame of hadron physics dealing with a phenomenological and an experimental parts. Hadron physics is the branch of physics that investigates the matter at distances smaller than 10^{-15} m, i.e. 1 fermi, the dimension of the nucleon. The nucleons (proton and neutron) are hadrons that are bound by the strong force and are fundamental constituents of the atomic nucleus, which constitutes more than 99 % of the ordinary matter of the Universe. They are the objects that link nuclear and particle physics.

In particle physics, the Standard Model classifies the elementary particles as fermions (spin 1/2 particles) as the quarks and the leptons, and elementary bosons (with integer spin). The quarks are submitted to the strong interaction. There are six types of quarks that differ by flavors: up, down, strange, charm, bottom and top. The leptons are submitted to the electromagnetic interaction. Three leptons: electron, muon and tau are accompanied by the corresponding neutrinos ν_e, ν_μ, ν_τ . Four elementary gauge bosons are the mediators for the four types of fundamental forces, weak (the W and Z bosons) and electromagnetic (the photon), strong (the gluon) and gravitation. Quarks and gluons are the building blocks of the hadrons (baryons and mesons) and obey to Quantum Chromodynamics (the theory of the strong interaction, QCD). QCD is a predictive theory for kinematical conditions where it is possible to define a "hard scale", where the running coupling constant α_s should be small enough to use perturbative methods. At the energy scale of the W boson, 80 GeV, $\alpha_s \simeq 0.12$. In elementary processes involving electrons and/or nucleons, the transferred momentum from the projectile to the target sets the scale. It is related to the range in the nucleon that is probed by the interaction. In the range 1-5 GeV², corresponding to internal distances of 0.1-0.2 fm, quark effects should be dominant. Quarks can not be observed as free particles, confinement is a property of QCD, understood from the statement that the colour force grows with the distance.

The pion is the lightest meson, i.e., a quark - antiquark bound state and the longest range mediator of nuclear forces. Understanding the pion properties will reveal the basic features of colour confinement and chiral symmetry breaking. Adding the strange quark dimension, a new symmetry of the quark model appears, the SU₃ symmetry and the next heavier mesons, the kaons, can be similarly described. We will apply the SU(3) symmetry to meson production extending our model and testing its validity on existing data.

Nucleons are the lightest and the most stable baryons (the lifetime of the proton is longer than 10^{32} years, and neutron, it is less than 15 minutes). The development of particle physics comes along with the understanding of nucleon structure since

they were believed to be elementary particles until the 1960's. Now it is known that they are made of three valence quarks and quark-antiquark pairs and gluons. However, the fundamental properties of the proton and neutron, as the mass, the size, and the origin of the spin still remain not well understood.

The discovery of the Higgs boson [1, 2] tells us the origin of the fermion mass. However, the mass of the light quarks constitutes only few percent of the nucleon mass. Another intrinsic property of a particle, the spin, is object of intensive study. It is known that the proton has spin 1/2, however the experiment showed that only about 30% of the proton spin is carried by the quarks [3] including a very small contribution from the quark-antiquark sea. Efforts have been undertaken to measure the part of the spin that is carried by the gluons, the first results of RHIC (Relativistic Heavy Ion Collider) data until 2008 [4] show that this fraction is close to zero, the preliminary result of gluon polarization from COMPASS (Common Muon Proton Apparatus for Structure and Spectroscopy) is also very small but positive at Bjorken scale $x \sim 0.1$ and the analysis of new world RHIC data [5] and lattice QCD calculation [6] suggest a significant contribution [7] at $x \sim 0.05$. At present, the contribution of the internal orbital angular momentum can not be accessed directly by an experiment, but only through a model. Another puzzle is related to the size of the proton, measuring the charge radius. Recent measurements of the Lamb shift in muonic hydrogen [8] give a smaller value (about 5.5σ) of the proton charge radius than reported in the CODATA 2014 [9] compilation from the weighted average world data of hydrogen spectroscopy and elastic ep scattering. With a precise measurement of the proton electric form factor G_E^p at low momentum transfer, Q^2 , one can extract the root mean squared charge radius as:

$$\langle r_p^2 \rangle = -6 \frac{dG_E^p(Q^2)}{dQ^2} \Big|_{Q^2 \rightarrow 0} .$$

Several low energy experiments aim at a very precise determination of the elastic ep cross section. The PRad experiment [10] was successfully performed in May-June 2016 in the Hall B at JLab (Newport News, USA) at very low Q^2 (10^{-4} - 10^{-1} GeV²) and the collected experimental data is currently under analysis, the MUSE experiment [11] (PSI, Switzerland) will simultaneously measure elastic electron and muon in both charge states scattering on the proton. The low energy ep scattering experiment ProRad is also planned at the PRAE platform [12]. At the Mainz Microtron, following a series of measurements [13, 14], the simultaneous detection of the proton and the electron has recently been proposed [15], with the measurement of the absolute cross section at a per mille absolute precision.

The electromagnetic structure of the nucleon related to the internal dynamics of the electric and magnetic currents, brings unique constrain to nucleon models and it is parametrized in terms of nucleon form factors. Experimentally, nucleon form factors can be accessed through elementary reactions involving electrons and protons, assuming that the interaction occurs through one photon exchange. The reactions

are: polarized and unpolarized electron proton elastic scattering (in the space-like region of the momentum transfer squared), investigated at electron facilities such as JLab and MAMI (Mainz, Germany) and the annihilation reactions (time-like region) $e^+e^- \rightarrow p\bar{p}$ studied by the BaBar (Stanford, USA) and the BES III (Beijing, China) collaborations. The time reversal related reaction $p\bar{p} \rightarrow e^+e^-$, that was investigated at LEAR (Geneva, Switzerland) and FermiLab (Chicago, USA) in the past, will be studied with the PANDA experiment with the antiproton beams of the future Facility for Antiprotons and Ion Research (FAIR) at Darmstadt, Germany.

Electron-hadron or hadron-hadron collisions at small momentum transfer squared are usually considered as soft processes. Understanding the dynamics of the forces at the scale of the nucleon belongs to the domain of “non-perturbative” QCD. However, the situation is not so simple. Even in the high transfer momentum region, the reactions are not purely hard. One usually factorize the process into a hard process which is assumed to be scattering on a quark, and a soft part where the non-perturbative aspects are parametrized in terms of hadron structure functions and fragmentation functions. The phenomenological approaches to describe these processes are based on effective Lagrangian theory. To compute the observables, the effective degrees of freedom relevant to the problem are extracted and the corresponding Lagrangian is built. Parameters as masses and coupling constants are known either from experiment or theory, or are considered as fitting parameters. The electromagnetic channels are very difficult to detect in a hadronic reaction, because hadrons are produced orders of magnitude more copiously than leptons. For the detection of a lepton pair, charged pion pair production is the main background. It is necessary to know precisely the full distribution in energy and angle of the produced pions. The processes involving pions and more generally, mesons, are also interesting by themselves, as they bring stringent tests of fundamental QCD properties.

In the space-like region, precise measurements of proton and neutron electromagnetic form factors have been recently done, through double polarization experiments that need a high intensity, highly (longitudinally) polarized electron beam and the measurement of the recoil nucleon polarization. The method, suggested in the 1970's by A.I. Akhiezer and M.P. Rekalov has allowed precise determination of the form factor ratio up to 9 GeV^2 transferred momentum.

To do such precise measurement, it is necessary to measure the polarization of few GeV protons and neutrons. Dedicated polarimeters have to be built. The best analyzing reaction, i.e., the reaction with the best efficiency and the highest analyzing powers has to be determined at each energy. The measurement of analyzing power is only possible at a polarized proton (neutron) accelerator, in the energy range of interest. Presently, the Nuclotron accelerator complex of the Joint Institute for Nuclear Research (JINR) in Dubna delivers polarized deuterons beams up to $13 \text{ GeV}/c$ momentum, from which polarized neutron and proton beams can be produced.

This thesis concerns on a phenomenological and an experimental work. The outline of the thesis is the following:

The first part is a phenomenological study of the annihilation of $\bar{p}p$ into light meson pairs.

- **Chapter 1:** the kinematic relations for the proton and antiproton annihilation into a light meson pion pair are derived. A general review of the data and the associated literature is detailed. The information on angular distributions and cross sections, necessary for the modelization of the PANDA experiment has been collected. In addition, crossing symmetry has been discussed and the correspondence between elastic scattering and annihilation data is illustrated.
- **Chapter 2:** a model based on tree level Feynman diagrams, has been built to calculate the differential cross section for charged pion pair production. All available sets of angular distribution data have been described within the model, and an extrapolation of the energy dependence of the model is also discussed. According to SU_3 symmetry, the model is also successfully applied to the charged kaon pair channel. A study of different parametrizations of form factors has shown that logarithmic form is preferable. The results of this chapter have been published in Ref. [16] during the preparation of this manuscript.
- **Chapter 3:** the model has been adapted to neutral light meson production $\pi^0\pi^0, \eta\eta, \eta\pi^0$. The content presented here is the object of the work reported in Ref. [17].

The second part reports on my contribution to the experiment ALPOM2, dedicated to the measurement of analyzing powers of protons and neutrons on different targets: C , CH , and CH_2 .

- **Chapter 4:** the history of nucleon form factor measurements based on ep elastic scattering is presented, from the traditional Rosenbluth method to the Akhiezer-Rekalo double polarization method. The extraction of form factors is discussed in the scattering region, as well as in the annihilation region accessible at electron-positron or antiproton-proton colliders.
- **Chapter 5:** polarization experiments require the measurement of the polarization of few GeV protons and neutrons. Hadron polarimetry is based on the measurement of the azimuthal asymmetry in a secondary scattering on a hydrogen rich target.

In case of neutrons, for the pre-experiment of nucleon form factors, two ways of measuring the analyzing power have been compared according to the figure of merit. A pole model is used to estimate the cross section and available data of analyzing powers are collected for the evaluation of ALPOM2 experiment.

Part of this results have been published in Ref. [18] as a contribution to the XXIII International Baldin Seminar on High Energy Physics Problems.

- **Chapter 6:** after an introduction of the history and activity of the joint institute of nuclear research in Dubna where the experiment took place, the production and acceleration of polarized deuteron beams at the Nuclotron accelerator complex are introduced. The ALPOM2 experimental setup, its detectors and targets, are described. Data with polarized proton and neutron beams at 3.0, 3.75 and 4.2 GeV/ c were collected. The preliminary analysis and the results of the analyzing powers are presented.

Part I

Light meson productions in $\bar{p}p$ annihilation

Chapter 1

Annihilation of $\bar{p}p$ into light mesons

1.1 Introduction

Large experimental and theoretical efforts have been going on since decades in order to understand and classify high energy processes. We consider here hadronic reactions and focus in particular to two body processes in the energy range of the PANDA experiment at FAIR [19] (see Fig. 1.1). Let us mention that FAIR will investigate also other domain of physics, where physics communities gathered in four large collaborations: APPA (Atomic Physics, Plasma and Applied sciences), CBM (Compressed Baryonic Matter experiment), NUSTAR (Nuclear structure, Astrophysics and Reactions) and PANDA (Antiproton annihilation at Darmstadt).

The experiment will use antiproton beams created by colliding high intensity protons with a copper target, and then will be collected and pre-cooled in FAIR accelerator complex. The beams will be injected into the High Energy Storage Ring (HESR) and will collide with the fixed target inside the PANDA detector. The beam energy range will be $2.25(1.5) \leq \sqrt{s}(p_L) \leq 5.47(15)$ GeV (GeV/c). The outgoing particles, neutral and charged, will be recorded with a full 4π acceptance high resolution detector.

At the PANDA experiment antimatter and matter will annihilate and produce a fireball of energy in a gluon rich environment according to the Einstein's equivalence between matter and energy. A systematic study of the produced particles will provide a way to understand the secret of mass generation from the strong interaction, and the glueballs purely made of gluons may be observed. The high luminosity antiproton beams on a proton or a nuclear target and a full solid angle acceptance are the main assets of the PANDA experiment. The PANDA collaboration gathered more than 450 physicists from 49 institutions in 17 countries since 2002, and the experiment will collect data after the year 2020.

In this chapter we discuss one reaction of PANDA experiment, antiproton-proton annihilation into two charged pions:

$$\bar{p}(p_1) + p(p_2) \rightarrow \pi^-(k_1) + \pi^+(k_2), \quad (1.1)$$

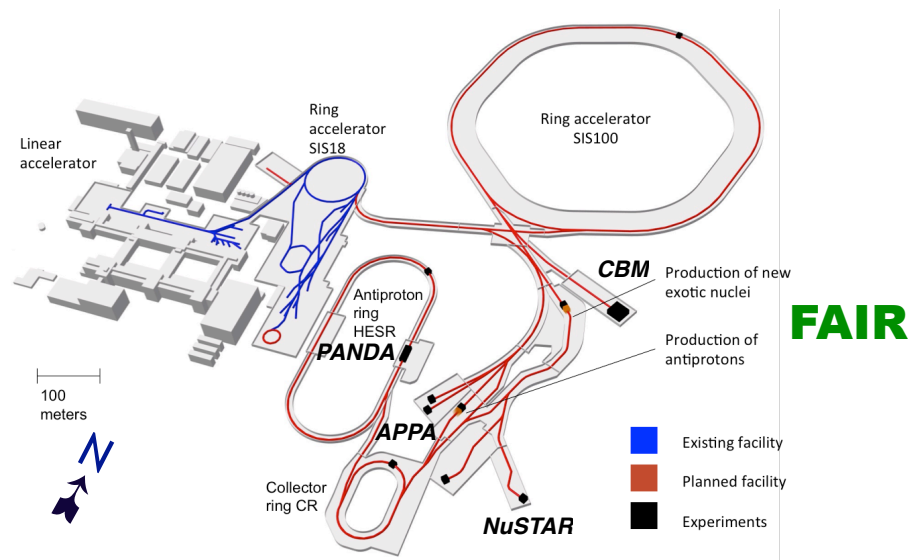


FIGURE 1.1: Illustration of the FAIR Accelerator Complex, including the four collaborations: APPA (Atomic Physics, Plasma and Applied sciences), CBM (Compressed Baryonic Matter experiment), NuSTAR (Nuclear structure, Astrophysics and Reactions) and PANDA (Antiproton annihilation at Darmstadt).

(where the momenta of the particles are indicated in parenthesis) as well as the relation with the crossed reactions of pion-proton elastic scattering

$$\pi^- + p \rightarrow \pi^- + p, \quad (1.2)$$

$$\pi^+ + p \rightarrow p + \pi^+. \quad (1.3)$$

A beam of antiprotons is a very peculiar probe, due to the fact that scattering and annihilation may occur in the same process, with definite kinematical characteristics. This process has been studied in the past, in connection with experiments at Low Energy Antiproton Ring (LEAR) in CERN and FermiLab, where antiproton beams were available. Annihilation occurs mostly through the production of several pions, five pions being the most probable channel. We focus on the annihilation reaction induced by antiprotons on a proton target, with production of two charged pions. At low energies the annihilation into light meson pairs is dominated by a few partial waves and the angular distribution shows a series of oscillations. Experimental data are analyzed with the use of Legendre polynomials [20]. This regime was also studied with the aim to look for resonances in the $\bar{p}p$ system.

A change of behavior appears above $\sqrt{s}=2$ GeV, where the angular distributions become typical for peripheral processes. They are peaked at forward and backward angles, corresponding to small values of t or u , respectively (s , t and u are the Mandelstam variables). The differential cross section, $d\sigma/dt$, and the integrated cross section show a power-law behavior as a function of the energy [21, 22]. At even larger energies, the total cross section becomes asymptotically constant, reaching a regime where $d\sigma/dt$ is function of t only, being independent on s .

According to the foreseen performances of the experiment PANDA, a large amount of data related to light meson pairs production from $\bar{p}p$ annihilation is expected in the future. The best possible knowledge of light meson production is also requested before the experiment takes place, as pions constitute an important background for many other channels. The development of a realistic model working in the few GeV region is necessary, in particular for the program program on time-like form factor measurements [23]. This program requires the detection of a lepton pair, and will benefit from a reliable estimation of the hadronic background. Pion pair production has five or six orders of magnitude larger cross section: pions should be effectively detected and identified [24, 25]. For this aim, the model should reproduce the gross features of the data, and should be expressed in a convenient form to be implemented in MonteCarlo calculations.

For the considered reaction, $\bar{p}p \rightarrow \pi^+\pi^-$, few calculations of cross section and angular distributions exist in the literature, at lower energies than those of interest here. A baryon (N and Δ) t -channel exchange model has applicability below 1 GeV/ c beam momentum [26, 27, 28]. Potential models [29] and sophisticated coupled channel calculations [30] become too involved to be extended to higher energies, among others, due to the opening of several channels and contributions of many resonances [31, 32, 30]. Final state interaction has been discussed in several

works, as [33]. Microscopic quark models were developed to predict relative two-body branching ratios, dynamical selection rules, or consequences of SU(2)/SU(3) symmetry (see, for example [34, 35]). Within a quark model, the authors of Ref. [36] show that relativistic effects accounting for higher partial waves contributions, should be taken into account to reproduce satisfactorily the data from Ref. [37].

The phenomenology added to take into account non-perturbative effects at low energies, is, however, not unique and gave rise to different approaches (for a review, see [38, 39]). The domain of applicability of the above calculations does not exceed 2 GeV.

At high energies, a constituent interchange quark model was developed in Ref. [40]. The energy and angular dependencies can be predicted for large angle scattering and elastic or quasi-elastic processes.

The multi-gluon exchange model of Donnachie and Landshoff [41, 42] describes high-energy elastic scattering in terms of various exchange processes. At small $|t|$ elastic πp scattering is assumed to be driven by single pomeron exchange, with a non-negligible contribution from double pomeron exchange. The pomeron itself represents a multi-gluon exchange between a pair of quarks, and it is described by a combination of Regge theory and the Chou-Yang geometrical model. The pomeron exchange picture provides an adequate description of small t ($|t| \leq 0.7 \text{ GeV}^2$) $\pi^- p$ data at 200 GeV. Large t elastic πp scattering is described in terms of gluon exchange between valence quarks [53] (the multiple scattering model). The leading diagram is found to be a 2 gluon exchange between the pion quarks and two nucleon quarks. One of the latter goes far off-shell and scatters the third nucleon quark via a gluon exchange. The diagram leads asymptotically to the energy-independent behavior as $d\sigma/dt \sim s^{-7}(t/s)^{-7}$. Higher-order QCD corrections could modify the result, and the inclusion of energy dependence cannot be excluded. Moreover, these models can not predict at which values of s and t the gluon exchange mechanism starts to dominate. However these predictions are important, as they give a frame for the comparison with experimental data. Extensive review of testing of QCD manifestations with antiproton beams can be found in Ref. [43].

The Regge model has proved to be very successful in reproducing the gross features of peripheral reactions in the intermediate and high energies domains. The concept of duality comes from the observation that a Regge amplitude, extrapolated into the low energy region, gives a ‘true’ description, in average, of the amplitude. This has been interpreted in the sense that the s -channel resonances are equivalent to t -channel Regge exchanges. A manifestation of duality is that diffractive meson production can be described by multi-peripheral diagrams, where only pions and nucleons appear. The known mesonic and baryonic states can be placed on Regge trajectory, which are approximately linear in the square of the masses.

An effective Lagrangian model was recently developed at larger energies, including meson exchanges in s -channel, which qualitatively reproduces a limited set of angular distributions [44]. Parameters include cut off and normalizations of form factors. It is assumed that Regge poles dominate the small as well as the

particle	Momentum	Lab	CMS
\bar{p}	p_1	(E_L, \vec{p}_L)	(E, \vec{p})
p	p_2	$(M_p, 0)$	$(E, -\vec{p})$
π^-	k_1	$(\varepsilon_1^L, \vec{k}_1^L)$	(ε, \vec{k})
π^+	k_2	$(\varepsilon_2^L, \vec{k}_2^L)$	$(\varepsilon, -\vec{k})$

TABLE 1.1: Notation of four-momenta in the laboratory (Lab) and Centre of Mass (CMS) reference frames.

large $|t|$ regions. An *ad hoc* parametrization of the nucleon Regge trajectory, which saturates at large, negative t , ensures the transition between *soft* and *hard* regimes. However, the authors warn against the application of this approach to neighboring energies, which is possibly related to the specific extrapolation of Regge trajectories in the region $t < 0$.

We have developed a model with meson and baryon exchanges in s , t , and u channels for PANDA experiment. Data are scarce at this region, and do not fill with continuity a large angular or energy range [45, 46, 47]. In order to consolidate the model, we take into account other data sets on the crossed reaction $\pi^\pm p$ elastic scattering and on $\bar{p}p$ annihilation into charged kaons [46] in a comparable energy range [48, 49]. It is known that first order Born diagrams give cross sections much larger than measured, as Feynman diagrams assume point-like particles. Form factors are added in order to take into account the composite nature of the interacting particles at vertexes. Parameters as coupling constants or cutoff are adjusted to reproduce the data. It is straightforward to extend the model to charged kaon pair production, with suitable replacements of the masses of the particles. At the considered energies, one can also rely on SU(3) symmetry, which gives a prescription to connect charged kaon and pion pair production from $\bar{p}p$ annihilation. The comparison of the results with the existing angular distributions and energy dependencies shows that the model successfully reproduces the available data.

1.2 Kinematics of $\bar{p} + p \rightarrow \pi^- + \pi^+$

Let us consider the reaction (1.1). The four momenta are given in Table 1.1. The scheme of the reaction in the laboratory (Lab) and centre of mass (CMS) reference frames is illustrated in Fig. 1.2. In the GeV energy range, one can in principle neglect the pion mass, doing an error of the order of a percent in the kinematical variables. However, let us consider the complete formulas, here, because specificities appear according to the size of the emitted particles.

For convenience the invariant Mandelstam variables are introduced: the total energy s , the momentum transfer from the antiproton to the negative pion (or from the proton to the positive pion) t , and the momentum transfer from the antiproton

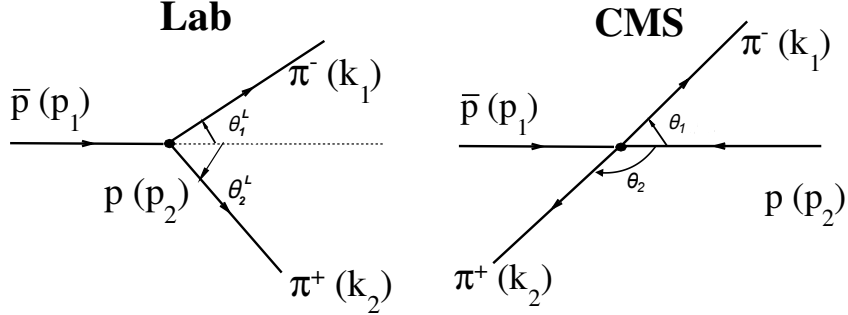


FIGURE 1.2: Scheme of the reaction (1.1) in the Lab and CM systems.

to the positive pion (or from the proton to the negative pion) u . They are calculated in the center of mass (CM) system as:

$$s = (p_1 + p_2)^2 = (k_1 + k_2)^2 = 2M_p^2 + 2p_1 \cdot p_2 = 2M_p^2 + 2E^2 + 2\vec{p}^2 = 4E^2, \quad (1.4)$$

$$u = (p_1 - k_2)^2 = (k_1 - p_2)^2 = M_p^2 + m_\pi^2 - 2E^2(1 + \beta\beta_\pi \cos \theta_1), \quad (1.5)$$

$$t = (p_1 - k_1)^2 = (p_2 - k_2)^2 = M_p^2 + m_\pi^2 - 2E^2(1 - \beta\beta_\pi \cos \theta_1), \quad (1.6)$$

where $\cos \theta_1$ is the cosine of the angle between the momenta of the initial antiproton and the produced π^- , $\beta = \sqrt{1 - M_p^2/E^2}$, and $\beta_\pi = \sqrt{1 - m_\pi^2/\varepsilon^2}$ are the CMS velocities of the (anti)proton and pion, $M_p(m_\pi)$ is the proton(pion) mass. The following relation holds: $s + t + u = 2M_p^2 + 2m_\pi^2$.

Let us note as $\varepsilon_1^{L(+)}$ ($\varepsilon_1^{L(-)}$) of a negative pion emitted forward(backward). From the conservation laws of energy and momentum one finds the relation between the angle and the energy of the emitted π^- meson as:

$$\varepsilon_1^{L(\pm)} = \frac{M_p W^2 \pm \sqrt{p_L^2 \cos^2 \theta_1^L [W^2(M_p^2 - m_\pi^2) + m_\pi^2 p_L^2 \cos^2 \theta_1^L]}}{(W^2 - p_L^2 \cos^2 \theta_1^L)}, \quad (1.7)$$

where $W = E_L + M_p$ is the total energy, $E_L(p_L)$ is the energy (momentum) of the incident antiproton, $\theta_{1,2}^L$ are the angles of the emitted π^- , π^+ , with respect to the direction of the antiproton beam in Lab system. The energy of a pion, ε^L , as a function of its emission angle, θ^L , is illustrated in Fig. 1.3, for $p_L = 1.9$ GeV/ c in the Lab system. The calculation red(green) line, corresponding to the two solutions Eq. (1.7) $\varepsilon_1^{L(+)}$ ($\varepsilon_1^{L(-)}$), is compared to the pion spectra from the FRITIOF (FTF) MonteCarlo generator [50]. This program, often used in high energy experiments, implements the Lund string dynamics model for hadron-hadron, hadron-nucleus and nucleus-nucleus collisions. Here it is only used for illustrative purposes.

The energy of the correlated pion that is emitted at corresponding angles, satisfies energy conservation. The sum of the π^+ and π^- energies is conserved and is equal to the total energy $W = E_L + M_p$. This is illustrated in Fig. 1.4.

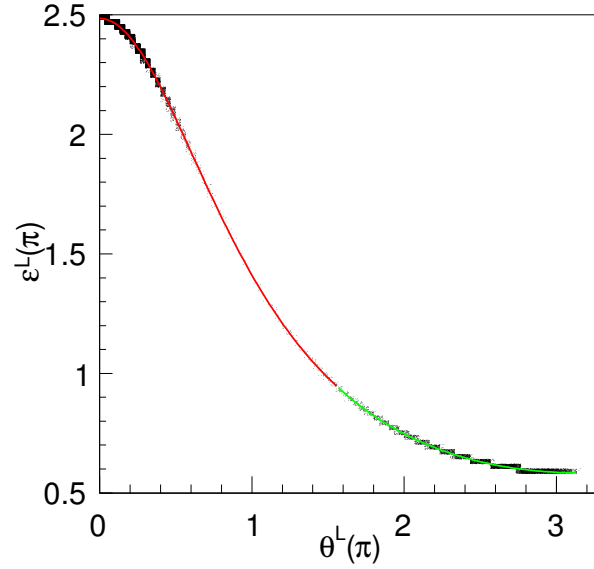


FIGURE 1.3: Energy of the π^\pm meson as a function of the emission angle for $p_L = 1.9 \text{ GeV}/c$ in Lab system. The black points are the events from the FTF generator and the solid line is the result of Eq. (1.7). The red(green) line corresponds to $\varepsilon^{L(+)}$ ($\varepsilon^{L(-)}$).

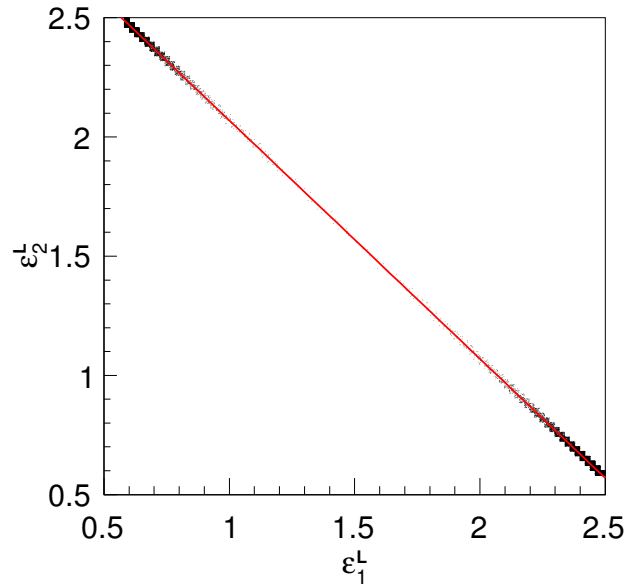


FIGURE 1.4: Energy of π^+ -meson as a function of the energy of π^- -meson for incident momentum $p_L=1.9 \text{ GeV}/c$ in Lab system. The black points are the events from the FTF generator and the solid red line is the calculation of kinematics.

As the final particles have the same mass, the kinematics (and MonteCarlo generator as well) show that the angles of the two emitted particles have a symmetric relation (Fig (1.5)). When one pion is emitted at small forward angle, the other pion can only be detected backward (red part). When the angle increases, both pions run forward (green part). When the angle becomes larger than $\pi/2$, the other pion moves to the forward region (blue part).

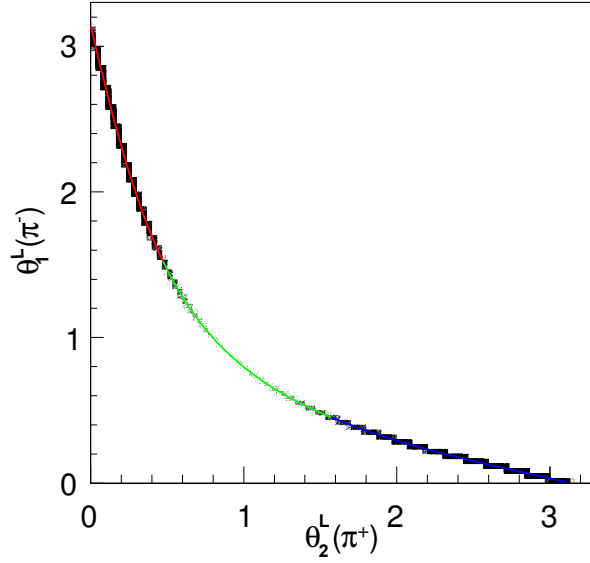


FIGURE 1.5: Correlation between the angles of the π^\pm -mesons for incident momentum $p_L=1.9$ GeV/ c . The black points are the events from the FTF generator. The blue line represents a π^- moving forward (π^+ moving backward), the red line is for the opposite. The green line shows the central region of the emitted pions.

In CMS, the pion pair is emitted back to back and each pion carries half of the total energy. To a pion emitted at a given angle ϑ and with a given CM energy, in the Lab system corresponds a pion of opposite charge emitted at $\pi - \vartheta$, with complementary energy. As in Eq. (1.7), the forward(backward) pion corresponds to $\varepsilon_1^{L(+)}(\varepsilon_1^{L(-)})$.

The correspondance between the CMS (θ_1) and Lab (θ_1^L) angles is:

$$\cos \theta_1 = \frac{E^2 - E\varepsilon_1^{L(\pm)}(1 - \beta_p^L \beta_\pi^L \cos \theta_1^L)}{E^2 \beta_p^L \beta_\pi^L}, \quad (1.8)$$

where $\beta_p^L = \sqrt{1 - M_p^2/E_L^2}$, and $\beta_\pi^L = \sqrt{1 - m_\pi^2/(\varepsilon^L)^2}$ are the Lab velocities of the corresponding particles and it is shown in Fig. 1.6.

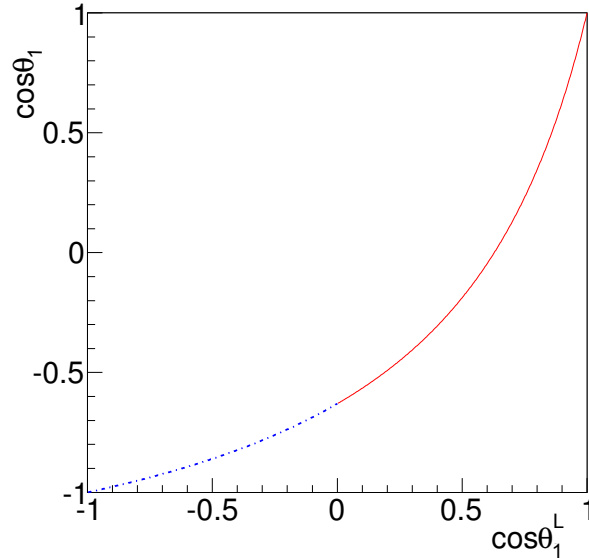


FIGURE 1.6: CM emission angle (θ_1) of π^- meson as a function of the Lab angle (θ_1^L) at antiproton Lab momentum $p_L = 1.9 \text{ GeV}/c$.

1.3 Existing experimental data for $\bar{p} + p \rightarrow \pi^- + \pi^+$

In this section we collect the existing data on $\bar{p}p$ annihilation into pions, or, more generally binary channels, and note the measured observables. We comment the main goals and findings of the experiments. A summary is given in Tables 1.2, 1.3, 1.4.

The two body final state reactions induced by $\bar{p}p$ annihilation have been widely studied at all accelerators delivering antiproton beams, in particular at the cooled antiproton beam of LEAR, constructed in 1982 at CERN.

Antiprotons were produced by focusing 23 GeV/c incident proton beams from the CERN Proton Synchrotron (PS) on a nuclear (Be) target. The LEAR facility provided antiproton beams in the momentum range from 105 MeV/c to 2 GeV/c, with low emittance and momentum spread of $\Delta p/p = 0.1\%$.

1.3.1 Differential cross sections

- Summary of Refs. [51, 72]. The highest energies where the measurement of the angular distribution of reaction (1.1) can be found in Ref. [51]. Upper limits of the cross section at incident momenta of 20 GeV/c, 30 GeV/c and 50 GeV/c measured by the WA7 collaboration at CERN SPS and covering the momentum transfer range $0.5 \text{ GeV}^2 < -t < 8 \text{ GeV}^2$ are reported. The elastic channels

Ref.	Reaction	\sqrt{s} [GeV]	p_L [GeV/c]	Obs.	Comments and Summaries
[45]	$\bar{p}p \rightarrow \pi^- \pi^+$	2.015 - 2.578	0.79-2.43	$\frac{d\sigma}{d\Omega}$	Complete angular distribution.
	$\pi^- p \rightarrow \pi^- p$	1.8955	1.43	$\frac{d\sigma}{d\Omega}$	
[46]	$\bar{p}p \rightarrow \pi^- \pi^+$	3.68	5, 6.21	$\frac{d\sigma}{dt}$	Rapid change with energy. Successful test of crossing symmetry.
[47]	$\bar{p}p \rightarrow \pi^- \pi^+$	3.362	5.0	$\frac{d\sigma}{dt}$	Complete angular distributions. Comparison of annihilation and scattering channels.
	$\pi^- p \rightarrow \pi^- p$	3.207	5.0	$\frac{d\sigma}{dt}$	
[51]	$\bar{p}p \rightarrow \pi^- \pi^+$	7.62	30	$\frac{d\sigma}{dt}$	Similarity between πp and Kp : differential cross sections as geometrical scaling ($ t < 2.8 \text{ GeV}^2$).
	$\pi^- p \rightarrow \pi^- p$	6.198	20	$\frac{d\sigma}{dt}$	
	$\pi^- p \rightarrow \pi^- p$	9.731	50	$\frac{d\sigma}{dt}$	
[52]	$\bar{p}p \rightarrow \pi^- \pi^+$	4.559	10.1	$\frac{d\sigma}{dt}$	Crossing symmetry test. The higher energy points show an energy dependence characteristic of baryon exchange.
	$\pi^- p \rightarrow \pi^- p$				

TABLE 1.2: (Part I) Collection of experimental data for the reactions:
 $\bar{p} + p \rightarrow \pi^- + \pi^+$, $\pi^- + p \rightarrow \pi^- + p$, $\pi^- + p \rightarrow p + \pi^-$.

Ref.	Reaction	\sqrt{s} [GeV]	p_L [GeV/c]	Obs.	Comments and Summaries
[53]	$\bar{p}p \rightarrow \pi^- \pi^+$	3.627	6.0	$\frac{d\sigma}{dt}$	Observation of large dip. Crossing symmetry fails.
[54]	$\bar{p}p \rightarrow \pi^- \pi^+$	2.767	3.0	$\frac{d\sigma}{dt}$	s -dependence compatible with baryon exchange. Drastic change from the s^{-10} dependence observed at low energies.
	$\bar{p}p \rightarrow \pi^- \pi^+$	3.077	4.0	$\frac{d\sigma}{dt}$	
	$\bar{p}p \rightarrow \pi^- \pi^+$	2.767	3.0	$\frac{d\sigma}{dt}$	
	$\bar{p}p \rightarrow \pi^- \pi^+$	3.077	4.0	$\frac{du}{d\sigma}$	
[55]	$\bar{p}p \rightarrow \pi^- \pi^+$	1.92-2.045	0.416-0.888	σ	Ratio between electromagnetic and hadronic channels. 1st extraction of $ G_M $ and $ G_E $.
[56]	$\bar{p}p \rightarrow \pi^- \pi^+$	1.884 - 1.894	0.173-0.266	σ	Low energy total cross section compatible with $1/\beta$ (velocity) dependence.
	$\bar{p}p \rightarrow \pi^- \pi^+$	1.883 - 1.896	0.158-0.275	$\sigma(\cos \theta)$	
[57]	$\bar{p}p \rightarrow \pi^- \pi^+$	1.917 - 1.98	0.403-0.670	σ	Fine search for S-meson.
[58]	$\bar{p}p \rightarrow \pi^- \pi^+$	1.915 - 2.012	0.390-0.780	σ	Complete angular distributions. Search for baryonium state.
	$\bar{p}p \rightarrow \pi^- \pi^+$	1.915-2.015	0.390 -0.790	$\frac{d\sigma}{d\Omega}$	
[59]	$\bar{p}p \rightarrow \pi^- \pi^+$	4.285	8.8	σ	Comparison of annihilation and elastic pp channels.
[60]	$\bar{p}p \rightarrow \pi^- \pi^+$	2.541	2.295-2.345	σ	Bubble-chamber. Topological and individual cross section for multiparticle final states.
[61]	$\bar{p}p \rightarrow \pi^- \pi^+$	1.899	0.28-0.32	σ	Spark chamber. First measurements of cross section into hadron pairs.

TABLE 1.3: (Part II) Collection of experimental data for the reactions:
 $\bar{p} + p \rightarrow \pi^- + \pi^+$, $\pi^- + p \rightarrow \pi^- + p$, $\pi^- + p \rightarrow p + \pi^-$.

Ref.	Reaction	\sqrt{s} [GeV]	p_L [GeV/c]	Obs.	Comments and Summaries
[62]	$\bar{p}p \rightarrow \pi^- \pi^+$	2.257 - 2.735	1.51-2.9	σ	Hydrogen bubble chamber. Search for enhancement in $\bar{N}N$ cross section.
[63]	$\bar{p}p \rightarrow \pi^- \pi^+$	2.534	2.3	σ	Hydrogen bubble chamber. Comparison of five channels with two meson final states.
[64]	$\bar{p}p \rightarrow \pi^- \pi^+$	1.985 - 2.114	0.686-1.098	σ Legn	Hydrogen bubble chamber. No evidence of direct-channel resonances in pion channel, but possible in kaon channel.
[65]	$\bar{p}p \rightarrow \pi^- \pi^+$	2.665	2.69	σ	Hydrogen bubble chamber. Data point consistent with previous result.
[66]	$\bar{p}p \rightarrow \pi^- \pi^+$	1.909	5.9	$\frac{d\sigma}{dt}$	Measurement of cross section for 20 reactions at 90° .
[67]	$\bar{p}p \rightarrow \pi^- \pi^+$	1.909-2.005	0.362-0.760	$\frac{d\sigma(\theta)}{d\Omega} + \frac{d\sigma(\pi-\theta)}{d\Omega}$	Folded angular distribution of π and K pairs.
[68]	$\bar{p}p \rightarrow \pi^- \pi^+$	1.876	0.00	$\frac{\sigma(\pi, K)}{\sigma(X)}$	$\bar{p}p$ annihilation into π and K pairs from atomic states.
[69]	$\bar{p}p \rightarrow \pi^- \pi^+$ $\pi^- p \rightarrow \pi^- p$	4.934 4.107-4.934	12 8, 12	$\frac{d\sigma}{du}, \sigma$ σ	s^{-10} dependence of the differential cross section. Crossing symmetry confirmed.
[70]	$\bar{p}p \rightarrow \pi^- \pi^+$	2.081	1.0	POL	Spark chamber data. Polarization parameter for $\bar{p}p$ annihilation into pion and kaon pairs close to 1.
[71]	$\bar{p}p \rightarrow \pi^- \pi^+$	1.994 - 2.64	0.7-2.4	$\frac{d\sigma}{d\Omega}$	Spark chamber data. Interpretation with Legendre polynomials.

TABLE 1.4: (Part III) Collection of experimental data for the reactions:
 $\bar{p} + p \rightarrow \pi^- + \pi^+, \pi^- + p \rightarrow \pi^- + p, \pi^- + p \rightarrow p + \pi^-$.

$\pi^\pm p$ and Kp (angular and energy dependence) are discussed in terms of geometrical scaling (GS). Assuming that the scattering amplitude is purely imaginary: $\rho = \text{Re}F/\text{Im}F = 0$ at $t = 0$, GS implies that $\text{Im}F(s, t) = \text{Im}F(s, 0)\Phi(\tau)$. $\Phi(\tau)$ should be a universal function for all channels with constant ratio σ_{el}/σ_{tot} and $\tau = -t\sigma_{tot}$ is the scaling variable. If $\sigma_{tot} \sim (\ln s)^2$ the GS behavior can be derived by first principles [72]. GS predicts a universal behavior of the scattering data when plotted as $(1/\sigma_{tot}^2)d\sigma/dt$ versus $-t\sigma_{tot}$. Data of πp and Kp from this experiment exhibit a deviation above $|t| \approx 2.8 \text{ GeV}^2$.

For πp elastic scattering, lowest order QCD predicts a behavior of the differential cross section as $d\sigma/dt \simeq s^{-8}(t/s)^{-7}$ which means a s^{-8} dependence at fixed angle $t/s \simeq (1 - \cos \theta)$. Ref. [51] suggests that the data at 20 GeV/c and at 200 GeV/c exhibit an approximate lowest-order QCD behaviour for $|t| \geq 10 \text{ GeV}^2$ and $|t| \geq 5 \text{ GeV}^2$, respectively, while 50 GeV/c data up to $|t| \simeq 8 \text{ GeV}^2$ have not yet reached a QCD regime. This could be interpreted as a decrease of the QCD t -threshold with increasing energy, a behaviour implying the transition of the 50 GeV/c data to a $|t|^{-7}$ dependence around $|t| = 8 \text{ GeV}^2$.

- Ref. [52] reports on the differential cross section of the reaction (1.1) at 10 GeV/c ($\sqrt{s} = 4.559 \text{ GeV}$) at forward angles, in the range $0.15 \text{ GeV}^2 < -t \leq 1.5 \text{ GeV}^2$. The six measured values show a good agreement with elastic π^+p at backward angle with crossing symmetry. The data can be fitted by a function:

$$\left. \frac{d\sigma}{dt}(s) \right|_{-t=0.3 \text{ GeV}^2} = \text{const} \cdot s^{-\alpha} \quad (1.9)$$

with $\alpha = 4.7 \pm 0.2$ (2.7 ± 0.5) for $p_L < (\geq) 3 \text{ GeV}/c$.

- In Ref. [53], a comparison of the reactions (1.1) and (1.2, 1.3) at 6 GeV/c is given. Precise forward angular distributions are compared. Crossing symmetry is not verified by the forward slopes and the position, shape of the dips. The energy dependence is inconsistent with the Regge model predictions. The paper concludes in failure of line reversal and Regge models.
- In Ref. [46], 23 points are given for the angular distribution of the reaction (1.1) at $p_L=6.21 \text{ GeV}/c$, corresponding to $s = 13.5 \text{ GeV}^2$, in a region near the kinematical limits $-t = 0.063$ and 11.68 GeV^2 .
- Ref. [47] gives 26 points of angular distribution for reaction (1.1) at 5 GeV/c momentum ($s = 11.3 \text{ GeV}^2$). A comparison is made with the results of Ref. [73] and Ref. [74] where πp elastic scattering was measured at similar s values. It concludes in failure of applicability of crossing symmetry for deriving the corresponding matrix elements.

- Ref. [54] reports the values of the differential cross section for the forward and backward πp elastic scattering at incident momenta of 3 and 4 GeV/ c . An evidence for a change of behavior of $d\sigma/du$ from s^{-8} to s^{-2} is highlighted.
- Summaries of Refs. [69, 75, 76, 77]. The highest energy (0.980 TeV) and intensity ($\mathcal{L} = 10^{30} \text{ cm}^{-2} \text{ s}^{-1}$) antiproton source was built at Fermilab. Experiments as E760 [78] and E835 [76, 77], provided data for hadronic and leptonic final channels. In Ref. [69], the backward total cross section at incident antiproton momentum of 12 GeV/ c , in the laboratory system, was measured for different channels. Besides the reactions (1.1,1.2,1.3), elastic $K^- + p \rightarrow p + K^-$ and $\bar{p} + p \rightarrow \bar{p} + p$ scattering was measured at 8 and 12 GeV/ c (corresponding to $\sqrt{s}=4.934 \text{ GeV}$) in the range $-1.5 \text{ GeV}^2 \leq u \leq -0.05 \text{ GeV}^2$. Differential cross sections for two-body neutral final states at $2.911 \text{ GeV} \leq \sqrt{s} \leq 3.686 \text{ GeV}$, in the central angular region, bringing information on resonances which couple to $p\bar{p}$, are reported in Ref. [75].

1.3.2 Total cross sections

- Summaries of Refs. [55, 56]. The annihilation reactions into pions and kaons were measured by the PS170 collaboration, Ref. [55], which primary goal was to collect as high statistics as possible for the measurement of the time-like electromagnetic form factors. Data for the total cross sections in the momentum range $416 \text{ MeV}/c \leq p_L \leq 888 \text{ MeV}/c$ are given, as well as the coefficients of polynomial fit to the known total cross section data between 200 and 1600 MeV. Cross section measurements, including angular distributions and fits with Legendre polynomials for the reaction (1.1) at lower energy (for $158 \text{ MeV}/c \leq p_L \leq 275 \text{ MeV}/c$) can be found in Ref. [56].
- Ref. [57], the total cross section for $\bar{p}p$ annihilation into 2-, 4- and 6-prong topologies, and exclusive charged particles, was measured at Brookhaven National Laboratory (BNL) in the incident momentum range 374 MeV/ c to 680 MeV/ c . A small enhancement of the cross section was observed at 490 MeV/ c corresponding to the S meson mass.
- Ref. [58] reports data for $\bar{p}p$ annihilation into charged pion and kaon pairs at incident momenta of 390, 490, 590, 690, and 780 MeV/ c to search for resonances. An enhancement of cross section was also observed at 490 MeV/ c .
- In Ref. [59], the data for different exclusive annihilation processes for 8.8 GeV/ c $\bar{p}p$ interactions were measured. The comparison between the non-annihilation cross section and pp interaction is discussed. The value of the total cross section of annihilation into $\pi^+\pi^-$ at backward angles ($u = 0$) is given. The cross sections have been normalized assuming a total $\bar{p}p$ annihilation cross section of 55.9 mb.

- In Ref. [60], the $\bar{p}p$ interaction at 2.32 GeV/ c was measured by the POLLY II system. Based on inclusive cross section for annihilation into ρ +pions and the assumption of the equivalence of ρ^+ , ρ^- , ρ^0 states, concludes that most production of charged pions comes from ρ mesons.
- Ref. [62] is dedicated to a system study of $\bar{p}p$ and $\bar{p}d$ interactions between 1.51 and 2.90 GeV/ c . Topological and reaction cross sections are given to study the enhancements at energies of 2190, 2350 and 2375 MeV in the $\bar{N}N$ system.
- In Ref. [63] data for the total cross section of $\bar{p}p$ into meson pairs are collected at 2.3 GeV/ c . The comparison with the dual model shows qualitative agreement.
- Ref. [64] reports on proton-antiproton annihilation into $\pi^+ \pi^-$ and $K^+ K^-$ from 700 to 1100 MeV/ c , with focus on one direct-channel resonances. No evidence of any direct-channel resonances in pion production channel was found but possibly in the kaon channel between 800 and 1000 MeV/ c .
- Ref. [65] presents data on $\pi^+ \pi^-$, $K^+ K^-$ and $\bar{K}^0 + K^0$ final states for the $\bar{p}p$ annihilation at 2.7 GeV/ c .

1.3.3 High energy region

- Summaries of Refs. [51, 41, 42]. The prediction of the $|t|^{-7}$ dependence from the multi-gluon exchange model of Donnachie and Landshoff [41, 42] and the comparison with QCD quark counting rules is discussed in Ref. [51]. The weak t dependence of the 20 and 50 GeV data ($|t|^{-3}$) seems to rule out the gluon exchange diagram as the dominant mechanism at lower energies, while the 200 GeV data do not exclude such a mechanism. The faster fall-off indicated by the 20 GeV data at very large $|t|$ hardly signals the onset of the gluon exchange mechanism, since the fixed angle energy dependence between these data and the extrapolated ($|t|^{-7}$) 200 GeV data is stronger (s^{-8}) than the predicted s^{-7} dependence. The conclusion is that the multi-gluon exchange model applies to $\pi^- p$ data at large t and for energies above 200 GeV.

1.3.4 Low energy region

- In Ref. [45], complete angular distributions for $\bar{p}p$ annihilation into charged pion and kaon pairs between 0.79 GeV/ c and 2.43 GeV/ c are reported. The data are described by Legendre polynomial series. With a Breit-Wigner model including the resonant states and a constituent interchange model plus resonances, three resonances are suggested. They should be confirmed by an experiment measuring polarization observables.

- Summaries of Refs. [38, 39, 79]. The annihilation at rest is object of extensive studies at LEAR by the Obelix collaboration, and summarized in extensive reviews [38, 39]. The most probable number of emitted pions is five, and this number increases with energy for in flight annihilation. Let us mention Ref. [79], with the observations on $\bar{p}d$ annihilation at rest into two pions. The annihilation on a deuterium target brings interesting information of the isotopic properties of the partial waves contributing to the cross section.
- Ref. [80] gives a measurement of the branching ratio $\Gamma(\bar{p}p \rightarrow e^+e^-)/\Gamma(\bar{p}p \rightarrow Total)$ in $\bar{p}p$ annihilation at rest. The annihilation into hadron pair as well as lepton pairs was observed, with the aim of extract proton electromagnetic time-like form factors.
- Summaries of Refs. [67, 81, 82, 64]. Low energy experiments with complete angular distributions in Refs. [67, 81] aimed to search for resonant structures. Other measurements of the cross section for $\pi^+\pi^-$ production at rest are listed in Ref. [68], and a search for the XI(2.2) resonance formation in $\bar{p}p$ can be found in Ref. [82]. The angular distributions for $\bar{p}p$ annihilation into pion and kaon pairs are given, with the description in terms of a Legendre polynomial series (e.g. Ref. [64]).

1.3.5 Polarized experiments

- In Ref. [83] the asymmetries in the differential cross sections for $\bar{p}p \rightarrow \bar{p}p$ and $\bar{p}p \rightarrow \pi^-\pi^+$ at 1.64 GeV/c and 2.55 GeV/c using a polarized proton target were measured at BNL. Differential cross section data are fitted with a partial-wave expansion. The use of a polarized target at LEAR allowed the measurement of analyzing powers at 20 beam momenta from 360 to 1550 MeV/c, for $\bar{p}p$ annihilation into charged pion and kaon pairs. The results show that the analyzing power is close to unity above 1 GeV/c. At lower energies large variations are observed with energy and angle [37].
- In Ref. [70] measurements of one spin polarization parameter for $\bar{p}p$ annihilation into charged pion and kaon pairs with a transversely polarized target, at momentum between 1.0 GeV/c and 2.2 GeV/c at LEAR are presented. The cross section shows large oscillations and the single-spin polarization observable is close to unity for both channels in the studied kinematical range.

1.3.6 Central collisions

- In Ref. [75], two body neutral final channels were reported. Angular distributions show a flattening around 90° CM angle. The s dependence of the cross section was discussed in frame of quark counting rules and Landshoff parametrization, including Sudakov corrections.

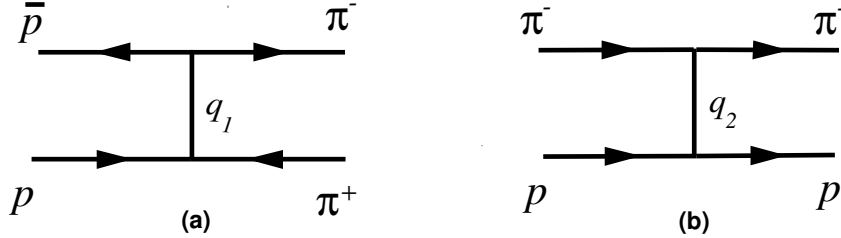


FIGURE 1.7: Feynman diagram for $\bar{p} + p \rightarrow \pi^+ + \pi^-$ (a) and $\pi^- + p \rightarrow \pi^- + p$ (b).

- In Refs. [84, 66], few values of the cross section at $\theta = 90^\circ$ are reported, for several binary reactions, with the AGS antiprotons, in the momentum range 6-10 GeV/ c and discussed in terms of color transparency. In this paper it is noticed that the reactions which allow quark exchange show energy dependence as predicted by quark counting rules. Reactions with mesons in final state which do not go through quark exchange, have cross sections smaller by one order of magnitude than the others. These results were later extensively discussed in Ref. [66], as a test of short distance interaction dynamics. The cross sections at 90° in the CM (large t values) are reported for $3.4 \text{ GeV} \leq \sqrt{s} \leq 3.6 \text{ GeV}$, for 20 exclusive reactions induced by $\bar{p}p$ annihilation. Discussion in terms of valence quark scattering concludes that among the considered mechanisms (gluon exchange, quark-antiquark annihilation followed by pair creation, and quark interchange between hadrons) this last one dominates.

1.4 Relation with the crossed processes

Let us consider the processes of proton-antiproton annihilation into a pion pair Eq. (1.1), Fig. 1.7 and the elastic scattering Eq. (1.2).

The experimental data are often plotted as $d\sigma/dt$ or $d\sigma/du$ as a function of t or u . The conversion factor is: $\frac{d\sigma}{d\cos\theta} = \frac{d\sigma}{dt} \left| \frac{dt}{d\cos\theta} \right| = 2E^2\beta\beta_\pi \frac{d\sigma}{dt}$, and similarly for $d\sigma/du$.

The general expression for the differential cross section of a binary process, in CMS is (see derivation in Section 2.2.1):

$$\frac{d\sigma}{d\Omega} = \frac{|\overline{\mathcal{M}}|^2 |\vec{p}|}{64\pi^2 W^2 |\vec{k}|}, \quad (1.10)$$

Annihilation	Scattering
$\bar{p}(p_1) + p(p_2) \rightarrow \pi^-(k_1) + \pi^+(k_2)$	$\pi^-(-k_2) + p(p_2) \rightarrow \pi^-(k_1) + p(-p_1)$
$s_a = (p_1 + p_2)^2$	$s_s = (-k_2 + p_2)^2$
$t_a = (p_1 - k_1)^2$	$t_s = (-k_2 - k_1)^2$
$u_a = (p_1 - k_2)^2$	$u_s = (p_1 - k_2)^2$
$s_a = 4E^2 = 4(M_p^2 + \vec{p}_a ^2)$	$s_s = m_\pi^2 + M_p^2 + 2E'_2 \varepsilon'_2 + 2 \vec{k}_s ^2$
$\sigma_a = \frac{1}{4} \frac{ \mathcal{M}_a ^2 \vec{k}_a }{64\pi^2 s \vec{p}_a }$	$\sigma_s = \frac{1}{2} \frac{ \mathcal{M}_s ^2 \vec{k}_s }{64\pi^2 s \vec{p}_s }$

TABLE 1.5: Correspondence between variables in the crossed scattering (s) and annihilation (a) channels.

where \mathcal{M} is the matrix element which depends on the reaction and on the dynamics of the process. Here p and k are the momenta in the initial and final channels, respectively, and W is the total energy.

The reactions (1.2,1.3) are the crossed channel of the reaction (1.1). If crossing symmetry holds, their cross sections can be derived from Eq. (1.10) with the replacement $\vec{p} \leftrightarrow \vec{k}$. This means that the amplitudes of the cross processes are the same, but the variables span different regions of the kinematical space, i.e., the matrix element $\mathcal{M}(s, t)$ is the same, at corresponding s and t values.

Many attempts to verify the validity of crossing symmetry were done in the 70's, concluding that in general, one can not drive reliable predictions based on crossing symmetry. The validity of crossing symmetry implies that the underlying reaction mechanism is the same, at corresponding kinematics.

In order to compare scattering and annihilation cross sections, at the same s , one has to find the corresponding incident beam energy or momentum. Let us consider CM system and discuss the meaning of corresponding kinematics. Scattering and annihilation channels are defined as in Table 1.5. In order to apply crossing symmetry, moving from left \leftrightarrow right, a particle becomes antiparticle and its four-momentum changes sign.

Note that the coefficients 1/2 and 1/4 in the cross section formulas are the spin factors: $(2S_\pi + 1)(2S_p + 1)$ and $(2S_{\bar{p}} + 1)(2S_p + 1)$ for the scattering and annihilation channels, respectively, where S_π , S_p and $S_{\bar{p}}$ are the spins of pion, proton and antiproton, i.e., the corresponding initial particles. The incident momentum in the annihilation channel for a given value of the invariant s is: $|\vec{p}_a| = \sqrt{s/4 - M_p^2}$. From the equality $s_a = s_s$, the CMS momentum for $\pi^- p$ scattering, $|\vec{k}_s|$, is evaluated at the same s value:

$$|\vec{k}_s|^2 = \frac{1}{4s} [m_\pi^4 - 2m_\pi^2(M_p^2 + s) + (M_p^2 - s)^2], \quad (1.11)$$

and the amplitudes are assumed to be the same at this point. Then the cross sections for the two crossed processes are related by:

$$\sigma_a = \frac{1}{2} \frac{|\vec{k}_s|^2}{|\vec{p}_a|^2} \sigma_s. \quad (1.12)$$

If the scattering cross section is measured at a value $s_s = s_1$ different from $s_a = s$, at small t values one should rescale the cross section, using the empirical dependence: $\sigma_s \simeq \text{const} \cdot s^{-2}$ [46]. Therefore:

$$\sigma^s(s) = \sigma^s(s_1) \cdot \frac{s^{-2}}{s_1^{-2}}. \quad (1.13)$$

Let us show those data from the compilation above that can be compared as they lie in the similar energy range for annihilation and scattering. As an example we plot in Fig. 1.8 the data from Ref. [46]. The $\pi^- p$ data at 6.73 GeV/ c are compared to the $\bar{p} p$ data at 6.2 GeV/ c . They are first scaled to $s=13.53$ GeV², according to the proportionality and then multiplied with the crossing factor, Eq. (1.12), $f = 0.589$. It appears that the data are qualitatively consistent, in slope and absolute value, for $t \leq 1$ GeV².

Another example is shown in Fig. 1.9. The scattering data for $\pi^- p$ at 5.8 GeV/ c [48] and the annihilation $\bar{p} p$ data for $s = 13.53$ GeV² are compared. According to Eq. (1.12), one finds $f = 0.438$.

We see that the slope is consistent among the sets of data, up to $t = 1$ GeV². Therefore we can state that crossing symmetry works relatively well at low t where one nucleon exchange diagram dominates, but fails at larger t values, where several diagrams as s -channel exchange including the contribution of resonances start to play a role.

These data, however, do help when developing the model, as they fill very forward or backward angles, where annihilation data are scarce. The comparison in this region put constraints on the model parameters.

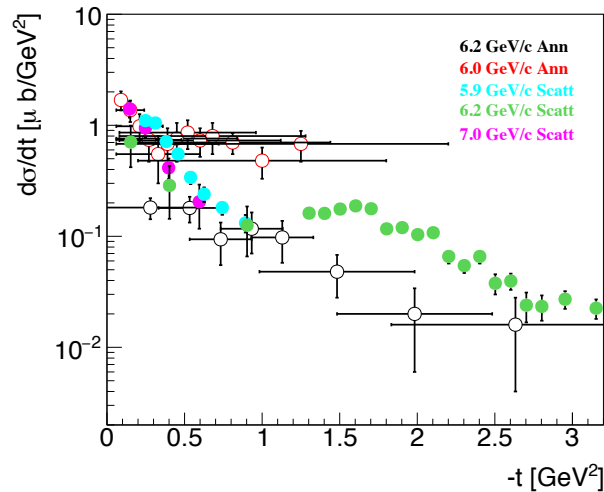


FIGURE 1.8: Data for $\bar{p} + p \rightarrow \pi^- + \pi^+$ for π^+ detected forward (black [46] and red [85] empty circles) and for $\pi^- + p \rightarrow \pi^- + p$ (light blue circles, from Ref. [48]). The green circles (from Ref. [86]), and the purple circles (from Ref. [49]) correspond to π^- emission at small t -values (or large u -values).

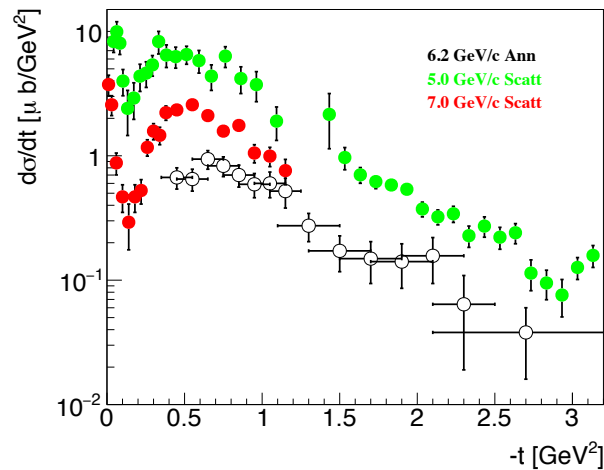


FIGURE 1.9: Data for $\bar{p} + p \rightarrow \pi^- + \pi^+$ for π^- detected forward (black empty circles Ref. [46]), and for $\pi^+ + p \rightarrow \pi^+ + p$ (red solid circles from Ref. [49], and green solid circles from Ref. [47]) corresponding to π^+ emission at small t -values (or large u -values). The π^+p data have been scaled as in the Fig. 1.8 with the same crossing factor 0.589.

Chapter 2

Calculation of $\bar{p}p$ annihilation into charged light meson pairs

2.1 Introduction

From the collection of the experimental data previously presented, one can foresee the difficulty for a coherent description of the annihilation into light mesons.

The difficulties are related to different aspects:

- the most probable reaction mechanism is changing with the energy and the angle;
- data are very scarce not allowing to constrain parameter models;
- model independent considerations based on crossing symmetry or T-invariance, which may help to connect the relevant reactions, can not always be considered as predictive [53].

A generator in frame of PANDARoot, the framework devoted to the PANDA experiment, was built [87] using two different parametrizations. In the “low” energy region, $p_L < 5$ GeV/ c , the parameters of Legendre polynomials up to the order of ten have been fitted to the data from Ref. [45]. In the higher energy region $p_L \geq 5$ GeV/ c , the Regge inspired parametrization from Ref. [44], previously tuned on the data from Refs. [47, 46, 66, 69], was applied. A smooth interpolation connected the two regions. The angular distributions for the reaction (1.1) are shown in Fig. 2.1 for different values of the total energy larger than 2 GeV. The functions used in the pion generator are shown in comparison to the data sample. One can see that a fair agreement is obtained for two data sets [46] (solid circles, black, solid line), and [47] (open blue circle, blue dash-dotted line).

The total cross section can also be calculated and compared to the data. Few points exist in the literature, mainly at lower momenta. The data are shown in Fig. 2.2 as a function of the antiproton momentum, p_L . One can see that the data are scarce over $p_L = 4$ GeV/ c , poorly constraining the generator (red, solid line). The value at $p_L = 12$ GeV/ c from ref. [69] is a measurement of the backward cross section and should be considered a lower limit. For comparison, the parametrization from

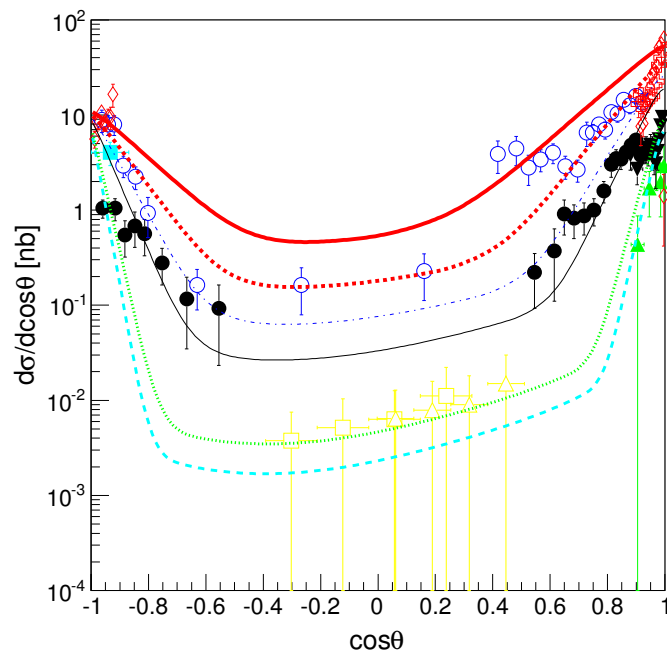


FIGURE 2.1: Data and modelisation of angular distributions for the reaction $\bar{p} + p \rightarrow \pi^+ + \pi^-$, as a function of $\cos\theta$, for different values of the total energy squared: 3 GeV (open red lozenges, red thick solid line) and 4 GeV (open red crosses, red thick dashed line) from ref. [54]; 6 GeV [53] (black triangles-down); 6.21 GeV [46] (solid circles, black, solid line); 13.5 GeV [47] (open blue circle, blue dash-dotted line); 20.8 GeV [52] (green triangles, green dotted line); 24.3 GeV [69] (cyan square, cyan short-dashed line); upper limits at 30 GeV (yellow open triangles) and 50 GeV (yellow open squares) from [51]. The lines are from the generator [87].

the compilation in Ref. [24], which reproduces the low momentum data, is also shown (black, dashed line).

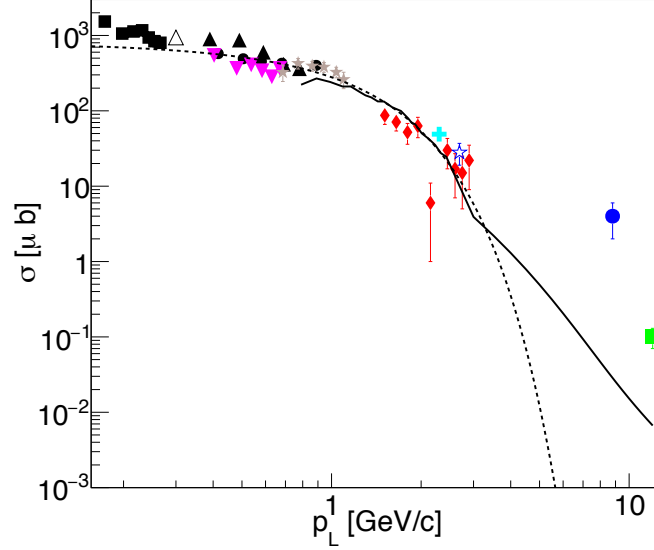


FIGURE 2.2: Total cross section for the reaction $\bar{p} + p \rightarrow \pi^+ + \pi^-$, as a function of the beam momentum in Lab system p_L . The data are from: [56] (black, full squares) [55] (black, full circles) [58] (black, full triangle up) [57] (magenta, full triangle down) [59] (black, full circle) [60] (cyan, full cross) [88] (black, open triangle up) [62] (red, full diamond) [64] (grey, full star) [65] (blue, open star) [69] (green, full square). The solid line is the result from the generator, where the transition between the two regimes is visible. The dashed line is the result of the compilation from [24].

The generator is based on the effective Lagrangian model developed in [44] that considers p and Δ exchanges in t and u channels and ρ -exchange in s channel. Dipole form factors are added at vertices and a specific extrapolation to the time-like region was introduced for the Regge factors. The authors warn about extrapolation outside the considered data sets. As one can see from Fig. 2.2, different parametrization give different results and they are not constrained by the data. Moreover, the results are available only in numerical form.

Therefore it appeared useful to develop an effective meson model, with mesonic and baryonic degrees of freedom in s , t , and u channels that has predictability in a larger kinematical region. This model should have minimal ingredients and calculate the basic features of neutral and charged pion production in the energy range that will be investigated by the future experiment PANDA at FAIR. To get maximum profit from the available data, we consider also existing $\pi^\pm p$ elastic scattering data and apply crossing symmetry in order to compare the predictions based on the

annihilation channel, at least in a limited kinematical range. The main requirement is that the model should be able to reproduce charged pion production from annihilation, and $\pi^\pm p$ elastic scattering without readjustment of the parameters. Moreover, SU(3) symmetry gives a prescription to relate $\bar{p}p$ annihilation into charged kaon and pion pairs. The model should be adapted also to neutral pion production, after suitable changes of the reaction mechanism and of the exchanged particles.

The results presented in this chapter have been published in Ref. [16]. The data used in the analysis are reported in Appendix A.1.

2.2 Formalism for $\bar{p} + p \rightarrow \pi^- + \pi^+$

2.2.1 Derivation of the invariant cross section

We consider the annihilation reaction 1.1 in the center of mass system (CMS). The following notations are used: $q_t = (-p_1 + k_1)$, $q_t^2 = t$, $q_u = (-p_1 + k_2)$, $q_u^2 = u$ and $q_s = (p_1 + p_2)$, $q_s^2 = s$, $s + t + u = 2M_N^2 + 2m_\pi^2$, $M_N(m_\pi)$ is the nucleon(pion) mass. The useful scalar product between four vectors are explicitly written as:

$$\begin{aligned} 2p_1k_2 = 2k_1p_2 &= M_N^2 + m_\pi^2 - u, & 2p_1k_1 = 2k_2p_2 &= M_N^2 + m_\pi^2 - t, \\ 2p_1p_2 &= s - 2M_N^2, & 2k_1k_2 &= s - 2m_\pi^2, \\ p_1^2 = p_2^2 &= M_N^2 = E^2 - |\vec{p}|^2, & k_1^2 = k_2^2 &= m_\pi^2 = \varepsilon^2 - |\vec{k}|^2. \end{aligned} \quad (2.1)$$

The relativistic invariant expression for the cross section of the process (1.1), which holds in any reference system is:

$$d\sigma = \frac{1}{(2S_p + 1)(2S_{\bar{p}} + 1)\mathcal{I}} |\overline{\mathcal{M}}|^2 d\Phi, \quad (2.2)$$

where \mathcal{I} is the flux of colliding particles. With the notations as in Table 1.1, the invariant form for the flux of the binary process (1.1) is:

$$\mathcal{I} = \sqrt{(p_1p_2)^2 - M^2} = 2s\beta_p, \quad \beta = \frac{p}{E} = \sqrt{1 - \frac{4M^2}{s}}. \quad (2.3)$$

It is an invariant expression: it can be evaluated in any reference system. The phase space for the (binary) process (3.1) is:

$$\begin{aligned} d\Phi &= \frac{d^3\vec{k}_1^3}{(2\pi)^3 2\varepsilon_1} \frac{d^3\vec{k}_2^3}{(2\pi)^3 2\varepsilon_2} \delta^4(p_1 + p_2 - k_1 - k_2) (2\pi)^4 \\ &= \frac{1}{(2\pi)^2} \frac{d^3\vec{k}_1^3}{2\varepsilon_1} \frac{d^3\vec{k}_2^3}{2\varepsilon_2} \delta^4(p_1 + p_2 - k_1 - k_2). \end{aligned} \quad (2.4)$$

Using the condition on four momentum conservation $d^4k_2\delta^4(p_1 + p_2 - k_1 - k_2) = 1$:

$$\frac{d^3\vec{k}_2}{2\varepsilon_2} = d^4k_2\delta(k_2^2 - m_\pi^2). \quad (2.5)$$

Using the relations $|\vec{k}_1|^2 = \varepsilon_1^2 - m_\pi^2$, $|\vec{k}_1|^2 d|\vec{k}_1| = 2|\vec{k}_1|d|\vec{k}_1| = 2\varepsilon_1 d\varepsilon_1$, one finds:

$$\frac{d^3\vec{k}_1}{2\varepsilon_1} = \frac{|\vec{k}_1|^2 d|\vec{k}_1| d\Omega}{2\varepsilon_1} = \frac{|\vec{k}_1|}{2} d\varepsilon_1 d\Omega. \quad (2.6)$$

Replacing Eqs. (2.5, 2.6) in Eq.(2.4), the element of phase space becomes:

$$d\Phi = \frac{|\vec{k}_1|}{2(2\pi)^2} d\varepsilon_1 d\Omega \delta(k_2^2 - m_\pi^2). \quad (2.7)$$

Using that $k_2^2 = (p_1 + p_2 - k_1)^2 = s + m_\pi^2 - 4\varepsilon_1 E$

$$\delta(k_2^2 - m_\pi^2) = \delta(s - 4\varepsilon_1 E). \quad (2.8)$$

We may integrate over ε_1 , using the property of δ function, for any function ϕ :

$$\delta\phi(x) = \frac{1}{|\phi'(x_0)|} \delta(x - x_0) \rightarrow \int \delta(s - 4\varepsilon_1 E) dE = \frac{1}{4\varepsilon_1} \delta\left(\varepsilon_1 - \frac{s}{4E}\right) dE, \quad (2.9)$$

from where we find the condition for the energy conservation:

$$\delta\left(\varepsilon_1 - \frac{s}{4E}\right) = 1 \rightarrow \varepsilon_1 = \frac{s}{4E}. \quad (2.10)$$

Finally the phase space for the binary reaction (3.1) has the expression:

$$d\Phi = \frac{1}{2^5\pi^2} \frac{|\vec{k}_1|}{4\varepsilon_1} d\Omega = \frac{1}{2^5\pi^2} \beta_\pi d\Omega, \quad (2.11)$$

and the general expression for the differential cross section is:

$$\frac{d\sigma}{d\Omega} = \frac{1}{2^8\pi^2} \frac{1}{s} \frac{\beta_\pi}{\beta_p} |\overline{\mathcal{M}}|^2, \quad \frac{d\sigma}{d\cos\theta} = \frac{1}{2^7\pi} \frac{1}{s} \frac{\beta_\pi}{\beta_p} |\overline{\mathcal{M}}|^2. \quad (2.12)$$

2.2.2 Calculation of the matrix element

In order to calculate $|\overline{\mathcal{M}}|^2$, one needs to specify a model for the considered reaction. The following contributions to the cross section, Fig. 2.3, are considered:

- baryon exchange:
 - t -channel nucleon (neutron) exchange, Fig. 2.3.a,

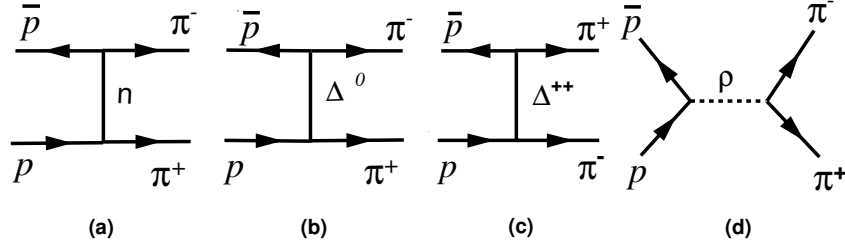


FIGURE 2.3: Feynman diagrams for the reaction $\bar{p}p \rightarrow \pi^+\pi^-$ within effective meson Lagrangian approach.

- t -channel Δ^0 exchange, Fig. 2.3.b,
- u -channel Δ^{++} exchange, Fig. 2.3.c;
- s -channel ρ -meson exchange, Fig. 2.3.d.

We will neglect the difference of masses between the nucleons as well as between different charge states of the pion and of the Δ . Coupling constants are fixed from the known decays of the particles if it is possible, otherwise we use the values from effective potentials as [89]. Masses and widths are taken from [90].

After the calculation of the coupling constant and matrix elements, the total matrix element squared averaged over the spin states of the initial particles, is obtained as the sum of the squared of matrix element for the individual contributions and the interferences among them:

$$\begin{aligned}
 |\mathcal{M}(\bar{p}p \rightarrow \pi^+\pi^-)|^2 &= |\mathcal{M}_n|^2 + |\mathcal{M}_{\Delta^0}|^2 + |\mathcal{M}_{\Delta^{++}}|^2 + |\mathcal{M}_\rho|^2 + \\
 &2\text{Re}[\mathcal{M}_n\mathcal{M}_{\Delta^0}^*] + 2\text{Re}[\mathcal{M}_n\mathcal{M}_{\Delta^{++}}^*] + 2\text{Re}[\mathcal{M}_n\mathcal{M}_\rho^*] + \\
 &2\text{Re}[\mathcal{M}_{\Delta^0}\mathcal{M}_{\Delta^{++}}^*] + 2\text{Re}[\mathcal{M}_{\Delta^0}\mathcal{M}_\rho^*] + 2\text{Re}[\mathcal{M}_\rho\mathcal{M}_{\Delta^{++}}^*].
 \end{aligned} \tag{2.13}$$

Taking into account the phase space and the flux, the expression for the differential cross section is:

$$\frac{d\sigma}{d\Omega}(\bar{p}p \rightarrow \pi^+\pi^-) = \frac{1}{2^8\pi^2} \frac{1}{s(t-M)^2} \frac{\beta_\pi}{\beta_p} |\mathcal{M}(\bar{p}p \rightarrow \pi^+\pi^-)|^2. \tag{2.14}$$

For any binary process, the amplitudes depend on two kinematical variables, for example s, t or E, θ . The relative role of these amplitudes therefore depends on the kinematical region. The dominant contribution in forward direction is N exchange, whereas Δ^{++} mostly contributes to backward scattering. We neglect the difference of masses between the nucleons as well as between different charge states of the pion and of the Δ -resonance. Scattering around $\cos\theta = 0$ is sensitive to s -channel

exchange of vector mesons, with the same quantum numbers as the photon. Although several resonances are present in these region, no one appears to be dominant outside its peak region. Adding resonances brings new parameters and unknown relative phases. Therefore, we limit this contribution to ρ -meson exchange. Assuming ρ as dominant contribution, in our approach is equivalent to give more weight to P-wave. Far from their maximum, all the $L = 1$ resonances give proportional contributions, and one can consider that they are effectively taken into account. The significant test of the contributing L -values is contained in the experimental angular distributions. These are well reproduced by our model. We neglect the difference of masses between the nucleons as well as between different charge states of the pion and of the Δ . Large angle scattering is driven by s-channel exchange of vector mesons, with the same quantum numbers as the photon. We limit our considerations to ρ -meson exchange.

The amplitudes corresponding to the considered diagrams are calculated below, following Feynman rules. The calculation has been done analytically. Sometimes the trace was calculated and/or checked with the help of the FORM program and, if necessary, the resulting expression simplified with the help of MATHEMATICA. Further calculations and graphs are done in frame of C++ and ROOT packages.

The common ingredients are the four-component spinors of the proton, $u(p_2)$, and antiproton, $\bar{v}(p_1)$, which obey the Dirac equation. The corresponding density matrices are

$$\begin{aligned} u_s(p)\bar{u}^s(p) &= p_\mu\gamma^\mu + M_p = \hat{p} + M_p, \\ v_s(p)\bar{v}^s(p) &= \hat{p} - M_p. \end{aligned} \quad (2.15)$$

2.2.3 t -channel neutron exchange

The specific ingredients for the diagram Fig. 2.3.a are:

- the vertex πNN : $-ig_{\pi NN}(i\gamma_5)(2\pi)^4$, where $g_{\pi NN}$ is the pion-nucleon coupling constant and γ_5 is the Dirac matrix, accounting for the pseudoscalar nature of the pion.
- the nucleon propagator, $\frac{i}{(2\pi)^4} \frac{\hat{q}_t + M_p}{q_t^2 - M_p^2}$, where $q_t = -p_1 + k_1 = p_2 - k_2$ is the momentum of the exchanged neutron, with $q_t^2 = t$.

The amplitude is written as:

$$\begin{aligned}
\mathcal{M}_n &= -\frac{i}{(2\pi)^4} \bar{v}(p_1) [-ig_{\pi NN} \gamma_5 (2\pi)^4] \frac{i}{(2\pi)^4} \frac{\hat{q}_t + M_p}{q_t^2 - M_p^2} [-ig_{\pi NN}^2 \gamma_5 (2\pi)^4] u(p_2) \\
&= \frac{g_{\pi NN}^2}{q_t^2 - M_p^2} \bar{v}(p_1) \gamma_5 (\hat{q}_t + M_p) \gamma_5 u(p_2) \\
&= \frac{g_{\pi NN}^2}{q_t^2 - M_p^2} \bar{v}(p_1) (-\hat{q}_t + M_p) u(p_2).
\end{aligned} \tag{2.16}$$

For the matrix element squared we find:

$$|\mathcal{M}_n|^2 = \mathcal{M}_n A^*(a) = \frac{g_{\pi NN}^4}{(q_t^2 - M_p^2)^2} \text{Tr} [(\hat{p}_1 - M_p)(\hat{q} + M_p)^2(\hat{p}_2 + M_p)]. \tag{2.17}$$

Calculating the trace:

$$|\mathcal{M}_n|^2 = 2 \frac{g_{\pi NN}^4}{(t - M_p^2)^2} [-t^2 - t(-2M_p^2 - 2m_\pi^2 + s) - (M_p^2 + 2m_\pi^2) + M_p^2 s], \tag{2.18}$$

or, equivalently,

$$|\mathcal{M}_n|^2 = -2 \frac{g_{\pi NN}^4}{(t - M_p^2)^2} [m^4 + (M_p^2 - t)(M_p^2 - s - t + 2m_\pi)]. \tag{2.19}$$

2.2.4 t -channel Δ^0 exchange

The specific ingredients for Δ exchange (Fig. 2.3.b) are related to the spin 3/2 nature of the Δ -resonance :

- the Δ -spin-vector, U_Δ : we take the expression from book [91], where the density matrix is

$$P_{\mu\nu} = U_\mu^\Delta(p_\Delta) \bar{U}_\nu^{*\Delta}(p_\Delta) = -g_{\mu\nu} + \frac{1}{3} \gamma_\mu \gamma_\nu + \frac{\gamma_\mu P_\nu - \gamma_\nu P_\mu}{3M_\Delta} + \frac{2}{3} \frac{P_\mu P_\nu}{M_\Delta^2}. \tag{2.20}$$

- the vertex $\Delta\pi N$ is written as:

$$-i(2\pi)^4 g_{\Delta\pi N} k_1^\mu, \tag{2.21}$$

- and the Δ -propagator :

$$\frac{i}{(2\pi)^4} \frac{\hat{q}_t + M_\Delta}{q_b^2 - M_\Delta^2} P_{\mu\nu}, \tag{2.22}$$

where $q_t = k_1 - p_1 = p_2 - k_2$, M_Δ is the weighted mass of the Δ resonance, $g_{\Delta\pi N}$ is the coupling constant for the vertex $\Delta \rightarrow \pi N$ (see Eq. (2.25)).

The matrix element for the diagram Fig. 2.3.b is:

$$\begin{aligned}\mathcal{M}_{\Delta^0} &= -\frac{i}{(2\pi)^4}\bar{v}(p_1)[-ig_{\Delta\pi N}^2k_1^\mu(2\pi)^4]\frac{i}{(2\pi)^4}\frac{\hat{q}_t + M_\Delta}{q_t^2 - M_\Delta^2}P_{\mu\nu}(q_t)[-ig_{\Delta\pi N}^2k_2^\nu(2\pi)^4]u(p_2) \\ &= -\frac{g_{\Delta\pi N}^2}{t - M_\Delta^2}\bar{v}(p_1)(\hat{q}_t + M_\Delta)P_{\mu\nu}(q_t)u(p_2)k_1^\mu k_2^\nu.\end{aligned}\quad (2.23)$$

Squaring the amplitude and taking the trace one has

$$\begin{aligned}|\mathcal{M}_{\Delta^0}|^2 &= \frac{g_{\Delta\pi N}^4}{(t - M_\Delta^2)^2}k_1^\mu k_2^\nu k_1^\alpha k_2^\beta \text{Tr}[(\hat{p}_1 - M_p)(\hat{q}_t + M_\Delta)P_{\mu\nu}(q_t) \\ &\quad (\hat{p}_2 + M_p)\tilde{P}_{\alpha\beta}(q_t)(\hat{q}_t + M_\Delta)].\end{aligned}\quad (2.24)$$

which is further processed by FORM giving a lengthy expression of the form: $|\overline{\mathcal{M}_{\Delta^0}}|^2 = f(s, t, M, m, M_\Delta)$.

- The $\Delta N\pi$ coupling constant

The decay width of the Δ in the system where the Δ is at rest (see Fig. 2.4) is given by:

$$\Gamma(\Delta \rightarrow N\pi) = \frac{1}{2M_\Delta}|\mathcal{M}(\Delta \rightarrow N\pi)|^2\Phi_2, \quad \Phi_2 = \frac{|\vec{p}|}{4\pi M_\Delta}, \quad (2.25)$$

where Φ_2 is the integrated phase space for two particle production. In the system where the Δ is at rest the four vectors of the particles are:

$$p_\Delta = (M_\Delta, 0), \quad p_p = (E, \vec{p}), \quad k_\pi = (\varepsilon, \vec{k}), \quad \text{with } M_\Delta = E + \varepsilon,$$

and

$$|\vec{p}| = |\vec{k}| = \frac{\Lambda^{1/2}(M_\Delta^2, M_p^2, m_\pi^2)}{2M_\Delta}, \quad \varepsilon = \frac{M_\Delta^2 - M_p^2 + m_\pi^2}{2M_\Delta}, \quad E = \frac{M_\Delta^2 + M_p^2 - m_\pi^2}{2M_\Delta}. \quad (2.26)$$

Taking the expression of the vertex $\Delta \rightarrow N\pi$ as in Eq. (2.21), the matrix element is

$$\mathcal{M}_{\Delta N\pi} = \bar{u}(p)(-i)(2\pi)^4 g_{\Delta N\pi} k^\mu U_\mu(p_\Delta) \frac{(-i)}{(2\pi)^4} = g_{\Delta N\pi} \bar{u}(p) k^\mu U_\mu(p_\Delta), \quad (2.27)$$

where U_μ is the four-vector describing the Δ spin 3/2 baryon.

Squaring the matrix element and summing over spin states one finds:

$$|\mathcal{M}(\Delta \rightarrow N\pi)|^2 = g_{\Delta N\pi}^2 \bar{u}(p) k^\mu k^\nu \text{Tr}[(\hat{p} + M_p)(\hat{p}_\Delta + M_\Delta)P^{\mu\nu}(q_\Delta)], \quad (2.28)$$

with $P^{\mu\nu}(q_\Delta)$ given by Eq. (2.20).

Calculating the trace after few simplifications, using the following scalar product $(pp_\Delta) = (M_\Delta^2 + M_p^2 - m_\pi^2)/2$ one finds:

$$|\mathcal{M}_{\Delta N\pi}|^2 = \frac{g_{\Delta N\pi}^2}{3M_\Delta^2} \{[(M_\Delta^2 + M_p^2) - m_\pi^2]^2[(M_\Delta^2 - M_p^2) - m_\pi^2]\}. \quad (2.29)$$

The experimental value for M_Δ (mixed charges) is from 1230 to 1234 (≈ 1232) MeV and for the Breit-Wigner full width Γ_Δ (mixed charges) is from 114 to 120 (≈ 117) MeV [92]. The experimental width corresponds to four initial and six final states:

$$\begin{aligned} \Delta^{++} &\rightarrow p + \pi^+, \\ \Delta^+ &\rightarrow p + \pi^0, n + \pi^+, \\ \Delta^0 &\rightarrow p + \pi^-, n + \pi^0, \\ \Delta^- &\rightarrow n + \pi^0, \end{aligned}$$

therefore a factor 3/2 is added in the expression of the full width for an individual state. From

$$\Gamma_\Delta = \frac{3}{2} \frac{\vec{p}}{32\pi M_\Delta^2} |\mathcal{M}(\Delta \rightarrow N\pi)|^2 \quad (2.30)$$

we find $g_{\Delta N\pi} = 15.7 \pm 0.4 \text{ GeV}^{-1}$, or $g_{\Delta N\pi}/m_\pi = 2.18 \pm 0.05$ (dimensionless)¹.

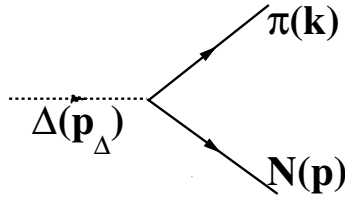


FIGURE 2.4: Diagram for $\Delta \rightarrow N\pi$ decay.

2.2.5 u -channel Δ^{++} exchange

The diagram in Fig. 2.3.c corresponds to π^- emitted at backward angle involves the exchange of Δ^{++} and can be obtained from (Fig. 2.3.b) with the replacements: $t \leftrightarrow u$

¹Note on units: $|\mathcal{M}_{\Delta N\pi}|^2 \rightarrow [\text{GeV}^2]$ implies $g_{\Delta N\pi} \rightarrow [\text{GeV}^{-1}]$.

and $k_1 \leftrightarrow k_2$. Explicitly we write:

$$\mathcal{M}_{\Delta^{++}} = -\frac{g_{\Delta\pi N}^2}{u - M_\Delta^2} \bar{v}(p_1)(\hat{q}_u + M_\Delta)P_{\mu\nu}(q_u)u(p_2)k_2^\mu k_1^\nu, \quad (2.31)$$

with $q_u = k_2 - p_1 = p_2 - k_1$, and $q_u^2 = u$.

2.2.6 s -channel ρ meson exchange

The largest contribution to meson exchange in s -channel, Fig 2.3.d, is given by the ρ -meson. It is an isovector particle, with spin one and negative parity as the photon. Its branching ratio into two pions is $\sim 100\%$.

- The ρ - propagator is

$$-\frac{i}{(2\pi)^4} \left[\frac{g_{\mu\nu} - \frac{q_s^\mu q_s^\nu}{m_\rho^2}}{q_s^2 - m_\rho^2 + i\sqrt{q_s^2}\Gamma_\rho(q_s^2)} \right], \quad (2.32)$$

where $g_{\mu\nu} = \frac{1}{2}[\gamma_\mu\gamma_\nu + \gamma_\nu\gamma_\mu]$ is the metric tensor (symmetric), $q_s = p_1 + p_2 = k_1 + k_2$, $q_s^2 = s$.

- the $\rho\pi\pi$ vertex (see Eq. (2.38)):

$$-ig_{\rho\pi\pi}(k_1 - k_2)^\nu(2\pi)^4, \quad (2.33)$$

where $g_{\rho\pi\pi}$ is the constant for the decay $\rho \rightarrow \pi\pi$;

- the ρNN vertex :

$$-ig_{\rho NN}\Gamma^\mu(q_s)(2\pi)^4, \quad (2.34)$$

where $\Gamma^\mu(q_s)$ includes the proton structure:

$$\Gamma_\mu(q_s) = F_1^\rho(q_s^2)\gamma_\mu(q_s) + \frac{i}{2M_p}F_2^\rho(q_s^2)\sigma_{\mu\nu}q_s^\nu, \quad (2.35)$$

with $\sigma_{\mu\nu} = \frac{i}{2}[\gamma_\mu\gamma_\nu - \gamma_\nu\gamma_\mu]$, antisymmetric tensor. Due to the isovector nature of the ρ , this vertex is similar to the electromagnetic vertex γNN , however the two form factors $F_{1,2}^\rho(q_s^2)$ are different from the proton electromagnetic FFs.

The matrix element is written as:

$$\begin{aligned} \mathcal{M}_\rho &= -\frac{i}{(2\pi)^4} \bar{v}(p_1) [-ig_{\rho NN} \Gamma^\mu(q) (2\pi)^4] u(p_2) \left\{ -\frac{i}{(2\pi)^4} \frac{g_{\mu\nu} - \frac{q_\mu q_\nu}{m_\rho^2}}{[q^2 - m_\rho^2 + i\sqrt{q^2} \Gamma_\rho(q^2)]} \right\} \\ &\quad [-ig_{\rho\pi\pi} (k_1 - k_2)^\nu (2\pi)^4] \\ &= \frac{g_{\rho pp} g_{\rho\pi\pi}}{[s - m_\rho^2 + i\sqrt{s} \Gamma_\rho(s)]} [\bar{v}(p_1) \Gamma^\mu(q) u(p_2)] (k_1 - k_2)^\nu \left\{ g_{\mu\nu} - \frac{q_\mu q_\nu}{m_\rho^2} \right\}. \end{aligned} \quad (2.36)$$

Squaring the amplitude:

$$\begin{aligned} |\mathcal{M}_\rho|^2 &= \frac{g_{\rho NN}^2 g_{\rho\pi\pi}^2}{[s - m_\rho^2 + i\sqrt{s} \Gamma_\rho(s)]^2} (k_1 - k_2)^\mu (k_1 - k_2)^\nu \left(g_{\mu\nu} - \frac{q_\mu q_\nu}{m_\rho^2} \right) \left(g_{\alpha\beta} - \frac{q_\alpha q_\beta}{m_\rho^2} \right) \\ &\quad Tr [(\hat{p}_1 - M_p) \Gamma^\mu(q_s) (\hat{p}_2 + M_p) \Gamma^\alpha(q_s)]. \end{aligned} \quad (2.37)$$

- The $\rho\pi\pi$ coupling constant

The ρ is a spin one meson with mass $m_\rho = 775.26 \pm 0.25$ MeV and full width $\Gamma(\rho) = 149.1 \pm 0.8$ MeV. The branching ratio into two pions is $\approx 100\%$.

The decay width of the ρ meson in the system where it is at rest (see Fig. 2.5) is given by:

$$\Gamma(\rho \rightarrow \pi\pi) = \frac{1}{2m_\rho} |\mathcal{M}(\rho \rightarrow \pi\pi)|^2 \Phi_2, \quad \Phi_2 = \frac{|\vec{k}|}{4\pi m_\rho}, \quad (2.38)$$

where Φ is the integrated phase space, with

$$|\vec{k}| = \frac{\Lambda^{1/2}(m_\rho, m_\pi, m_\pi)}{2m_\rho} = \frac{\sqrt{m_\rho^2 - 4m_\pi^2}}{2}. \quad (2.39)$$

With the vertex $\rho \rightarrow \pi\pi$ as in Eq. (2.33), the matrix element is

$$\mathcal{M}(\rho \rightarrow \pi\pi) = -\frac{(-i)}{(2\pi)^4} (-i) g_{\rho\pi\pi} (k_1 - k_2)^\mu (2\pi)^4 e_\mu = -g_{\rho\pi\pi} (k_1 - k_2)^\mu e_\mu, \quad (2.40)$$

where e_μ is the four-vector describing the spin one ρ -meson. Squaring the matrix element and summing over the spin states:

$$\begin{aligned} |\mathcal{M}_{\rho\pi\pi}|^2 &= -g_{\rho\pi\pi}^2 e_\mu e_\nu^* (k_1 - k_2)^\mu (k_1 - k_2)^\nu = -g_{\rho\pi\pi}^2 g_{\mu\nu} (k_1 - k_2)^\mu (k_1 - k_2)^\nu \\ &= g_{\rho\pi\pi}^2 (k_1^2 + k_2^2 - 2k_1 k_2) = g_{\rho\pi\pi}^2 (m_\rho^2 - 4m_\pi^2), \end{aligned} \quad (2.41)$$

where we used: $m_\rho^2 = (k_1 + k_2)^2$, $2(k_1 k_2) = m_\rho^2 - 2m_\pi^2$. Replacing Eq. (2.41) in (2.38), finally we find for the total width:

$$d\Gamma = \frac{4}{3} \frac{g_{\rho\pi\pi}^2}{16\pi m_\rho^2} (m_\rho^2 - 4m_\pi^2)^{3/2}, \quad (2.42)$$

where we added a factor 4/3 to take into account that the three possible initial states of the ρ meson and the four possible charged decays. Inverting Eq. (3.27), the value

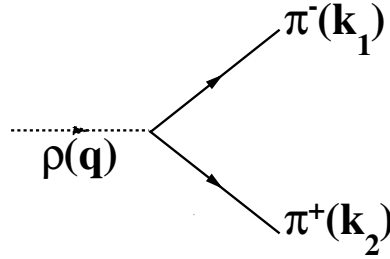


FIGURE 2.5: Diagram for ρ decay into a pion pair

of the coupling constant is $g_{\rho\pi\pi} = 5.175 \pm 0.017$.

The estimated error on is obtained from quadratic error propagation on the errors on the masses and widths as given by PDG. the interferences are given below. The general expressions for the interference are given below. They are further processed with FORM.

2.2.7 The interferences

The matrix element squared (see Eq. (3.31)) contains the coherent sum of the individual amplitudes, i.e., not only the amplitudes square, but also their interferences. Their expressions are listed below.

2.2.7.1 The $\Delta^0 - N$ interference

$$2Re[M_N M_\Delta^0] = 2Re \left\{ \frac{g_{\pi NN}^2 g_{\Delta\pi N}^2}{(t - M_p^2)(t - M_\Delta^2)} \right. \quad (2.43)$$

$$\left. Tr [(\hat{p}_1 + M_p)(-\hat{q}_t + M_p)(\hat{p}_2 + M_p)] \tilde{P}_{\mu\nu}(q_t)(\hat{q}_t + M_\Delta) k_1^\mu k_2^\nu \right\}.$$

2.2.7.2 The $\Delta^{++} - N$ interference

$$2Re[M_N M_{\Delta}^{++}] = 2Re \left\{ \frac{g_{\pi NN}^2 g_{\Delta\pi N}^2}{(u - M_{\Delta}^2)(t - M_p^2)} \right. \quad (2.44)$$

$$\left. Tr [(\hat{p}_1 + M_p)(-\hat{q}_t + M_p)(\hat{p}_2 + M_p)] \tilde{P}_{\mu\nu}(q_u)(\hat{q}_u + M_{\Delta}) k_1^{\nu} k_2^{\mu} \right\}.$$

2.2.7.3 The $\Delta^{++} - \Delta^0$ interference

$$2Re[M_{\Delta}^{*0} M_{\Delta}^{++}] = 2Re \left\{ \frac{g_{\Delta\pi N}^4}{(t - M_{\Delta}^2)(u - M_{\Delta}^2)} \right. \quad (2.45)$$

$$\left. Tr [(\hat{p}_1 - M_p)(\hat{q}_t + M_p) P_{\mu\nu}(q_t)(\hat{p}_2 + M_p) \tilde{P}_{\alpha\beta}(q_u)(\hat{q}_u + M_{\Delta})] k_1^{\mu} k_2^{\nu} k_2^{\alpha} k_1^{\beta} \right\}.$$

2.2.7.4 The $N - \rho$ interference

$$2Re[M_n^* M_{\rho}] = 2Re \left\{ \frac{g_{\pi NN} g_{\rho\pi\pi} g_{\rho NN}^2}{[s - m_{\rho}^2 + i\sqrt{s}\Gamma_{\rho}(s)](t - M_p^2)} \right. \quad (2.46)$$

$$Tr [(\hat{p}_1 - M_p) \Gamma^{\mu}(q_s)(\hat{p}_2 + M_p) \tilde{P}_{\alpha\beta}(q_t)(-\hat{q}_t + M_p)]$$

$$k_1^{\alpha} k_2^{\beta} (k_1 - k_2)^{\nu} \left(g_{\mu\nu} - \frac{q_{\mu} q_{\nu}}{m_{\rho}^2} \right) \left. \right\}.$$

2.2.7.5 The $\Delta^0 - \rho$ interference

$$2Re[M_{\Delta^{*0}} M_{\rho}^*] = 2Re \left\{ \frac{g_{\rho NN} g_{\rho\pi\pi} g_{\Delta\rho N}^2}{[s - m_{\rho}^2 + i\sqrt{s}\Gamma_{\rho}(s)](t - M_{\Delta}^2)} \right. \quad (2.47)$$

$$Tr [(\hat{p}_1 - M_p) \Gamma^{\mu}(q_s)(\hat{p}_2 + M_p) \tilde{P}_{\alpha\beta}(q_t)(-\hat{q}_t + M_{\Delta})]$$

$$k_1^{\alpha} k_2^{\beta} (k_1 - k_2)^{\nu} \left(g_{\mu\nu} - \frac{q_{\mu} q_{\nu}}{m_{\rho}^2} \right) \left. \right\}.$$

2.2.7.6 The $\Delta^{++} - \rho$ interference

$$2Re[M_{\Delta^{*++}} M_{\rho}] = 2Re \left\{ \frac{g_{\rho NN} g_{\rho\pi\pi} g_{\Delta\rho N}^2}{[s - m_{\rho}^2 + i\sqrt{s}\Gamma_{\rho}(s)](u - M_{\Delta}^2)} \right. \quad (2.48)$$

$$Tr [(\hat{p}_1 - M_p) \Gamma^{\mu}(q_s)(\hat{p}_2 + M_p) \tilde{P}_{\alpha\beta}(q_u)(-\hat{q}_u + M_{\Delta})]$$

$$k_1^{\alpha} k_2^{\beta} (k_1 - k_2)^{\nu} \left(g_{\mu\nu} - \frac{q_{\mu} q_{\nu}}{m_{\rho}^2} \right) \left. \right\}.$$

2.2.8 Form factors at vertices

The effects of strong interaction in the initial state, between proton and antiproton, coming from the exchange of vector and (pseudo)scalar mesons are essential. The most simplified structure of meson is considered as a monopole and baryon as a dipole. More physical way is to construct the asymptotic behaviour of baryonic form factors following from the renormalization group. There are two categories of behaviours, one is power law like from the Regge pole theory and one is logarithm like within the Sudakov-type suppression. The Regge theory is valid in the very forward or very backward region $|s| \gg |t|$ where the gluon exchange dominates. Regge factors have been applied to annihilation reactions in PANDA energy region in two recent calculations [44, 93] with *ad-hoc* parameters. For the first time in hadronic reactions, we suggest to use s and t dependent logarithmic behavior. The limit of logarithmic behaviour is that $|t|$ should be large compared with the mass in a large angular region. We make a comparison among these options that can be found in the literature.

2.2.8.1 Angular and energy dependencies of different form factors and Regge factors

The composite nature of the hadrons should be taken into account in the calculation of the diagrams. As different choices for form factors exist in the literature, in order to find the best description of the data in a wide energy and angular ranges, I studied the angular and energy dependencies of different functional forms. In the literature, different functions and parameters may be justified by the scarce knowledge of the non-perturbative structure of the hadrons.

We studied the following dependencies for the form factors:

- Monopole form factor:

$$F_M(x) = \frac{p_M^2}{|p_M^2 - x|}, \quad (2.49)$$

- Dipole form factor:

$$F_D(x) = \frac{p_D^4}{(p_D^2 - x)^2}, \quad (2.50)$$

- Exponential form factor:

$$F_E(x) = e^{-\left| \frac{x - M^2}{p_E^2} \right|}, \quad (2.51)$$

- Logarithmic form factor:

$$F^L(x) = \frac{\mathcal{N} \cdot M_0^4}{\left[(x - \Lambda^2) \log \frac{(x - \Lambda^2)}{\Lambda_{QCD}^2} \right]^2}, \quad M_0 = 3.86, \quad \Lambda_{QCD} = 0.3 \text{ GeV}. \quad (2.52)$$

Factor	parameters	value
$F_{M,D,E}^s(x)$	$p_{M,D,E}^s$	0.8
$F_{M,D,E}^h(x)$	$p_{M,D,E}^h$	1.4
$R_N(x)$	s_0^N, r^N	1, 0.7
$R_\Delta(x)$	s_0^Δ, r^Δ	1.5, 1.4

TABLE 2.1: Parameters of the monopole, dipole, exponential form factors for a soft (s) and a hard (h) choice, as well as for Regge parametrization for n and Δ , used for the calculation illustrated in Fig. 2.6.

Parameter	Value
\mathcal{N}_p	0.361 ± 0.006
\mathcal{N}_Δ	0.041 ± 0.003
Λ_p^2	2.25 ± 0.09
Λ_Δ^2	1.05 ± 0.04

TABLE 2.2: Summary of the parameters for the logarithmic form factors, Eq. (2.52, 2.56).

The monopole, dipole and exponential form factors have been compared for a soft and a hard choice, characterized by a parameter equal to 0.8 and 1.4, respectively.

In the logarithmic function Eq. (2.52), $M_0 = 3.86$ GeV is a scale parameter, that has been inserted to conserve units, $\Lambda_{QCD} = 0.3$ GeV is the QCD scale parameter; $\mathcal{N}_{N,(\Delta)} = 0.361 \pm 0.006(0.041 \pm 0.003)$ is a normalization constant fitted on the data, $\Lambda_{N,(\Delta)} = 2.25 \pm 0.09(1.05 \pm 0.04)$ is a ‘‘slope’’ parameter fitted on the data (in GeV units). A summary of parameters is listed in Table 2.2 for nucleon and Δ exchange.

The effects of the strong interaction in the scattering channel effectively lead to the Regge form of the amplitudes, and to a suppression the t and u diagrams, by applying to the amplitudes a general Regge factor $R(x)$, $x = u, t$, in the following form:

$$R(x) = \left(\frac{s}{s_0}\right)^{2[\alpha(x)-1]}, \quad \alpha(x) = \frac{1}{2} + r \frac{\alpha_s x - M^2}{\pi M^2}, \quad x = t, u; \quad (2.53)$$

where r and s_0 have been chosen from the literature [94]. In the following numerical applications we take $s_0^N \simeq 1$ GeV² and $r^N = r\alpha_s/\pi \simeq 0.7$. This Regge factor incorporates in principle infinite number of resonances, (i.e. $\Delta(1232)$ and others). The trajectory for the Δ resonance is known to be different from the nucleon. The parameters are fixed in this case as: $s_0^\Delta \simeq 1.5$ GeV² and $r^\Delta = r\alpha_s/\pi \simeq 1.4$. The parameters are reported in Table 2.1, $M(M_\Delta)$ is the mass of the nucleon (Δ) and $x = t$ or u . The functions are illustrated in Fig. 2.6 for $s=10$ GeV² as a function of t , and for $\cos\theta=0.1$ as a function of s .

Let us discuss the energy and angular dependence for the chosen set of parameter. Energy dependence

The two upper(lower) inserts of Fig. 2.6 show the $s(\cos\theta)$ -dependence of the functions, the left figures illustrate monopole, dipole and exponential functions, whereas the right inserts concern Regge and logarithmic parametrization. When s increases, the form factors and the Regge factors decrease. The smaller the parameter, the faster they drop. From the formulae and the plots, it is easy to be seen that for the same parameter, the Monopole, Dipole and Exponential parametrization produce, in the order, a larger suppression.

At low energy (< 3 GeV), the hard variants (with parameter 1.4) of the dipole and exponential form factors do not differ essentially. In all the energy region, the monopole and the dipole functions show a smooth decrease with increasing s , and they are not as sensitive as the exponential to the parameter value, that, in this case, appears in the exponent.

As the Regge factor has a power structure, compared to form factors, it falls dramatically when s increases. It can produce a suppression larger than 10^{-10} when $\sqrt{s} \geq 4.5$ GeV. Regge factors comparatively decrease faster with the same parameter and smaller mass, as well as for the same particle and a smaller parameter.

The slope of logarithmic form factor is more mild, between the dipole and the exponential. But the suppression of the logarithmic form factor at small energy (≤ 3.5 GeV) is larger than for the other formulae except the Regge form factor for the nucleon. At large energy, the suppression is smooth.

Angular dependence

From backward to forward angles, the form factors and the Regge factor increase with different slopes and become smaller and smaller at the very forward angle ($\cos\theta = 1$). Around $\cos\theta=0.5$, an inversion takes place between dipole and exponential in the hard form. This also happens for Regge factor between different masses.

The logarithmic form factor shows a milder increase than monopole and dipole, but with a more efficient suppression. Compared with exponential and Regge forms, it has more stable angular dependence and suitable suppression.

The energy and angular dependencies of different form factors, and the Regge factors are shown in Fig. 2.6 with the parameters in Table 2.1 and Table 2.2.

2.2.8.2 The ρNN form factor

The ρNN vertex includes the proton structure in the vector current form with two form factors (FF) $F_{1,2}^\rho$:

$$\Gamma_\mu(q_s) = F_1^\rho(q_s^2)\gamma_\mu(q_s) + \frac{i}{2M_N}F_2^\rho(q_s^2)\sigma_{\mu\nu}q_s^\nu, \quad (2.54)$$

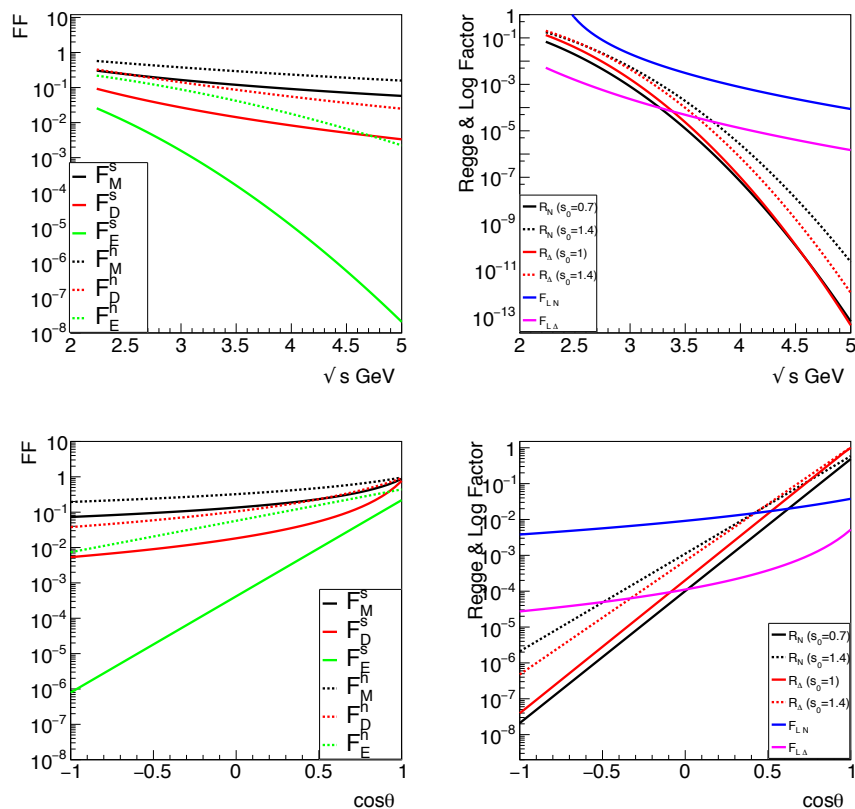


FIGURE 2.6: Energy dependence (top) and angular distribution (bottom) of form factors (left) and Regge factors (right) for soft (s, solid lines) and hard (h, dashed lines) parameters (see Tables 2.1 and Table 2.2). The notations for nucleon and Δ form factors (left side) are: monopole (black), dipole (red), exponential (green). In the right side the logarithmic function is shown in blue(magenta) for nucleon(Δ). The Regge factor is shown in black(red) for nucleon(Δ).

where $\sigma_{\mu\nu} = \frac{i}{2}[\gamma_\mu\gamma_\nu - \gamma_\nu\gamma_\mu]$ is the antisymmetric tensor. Due to the isovector nature of the ρ , the ρNN is similar to the electromagnetic vertex γNN . However the two form factors $F_{1,2}^\rho(q_s^2)$ are different from the proton electromagnetic ones. We do not attempt new parametrization, but prefer to fix the form, the constants and the parameters of $F_{1,2}^\rho(s)$ according to [89, 95, 96] as:

$$F_1^\rho(s) = g_{\rho NN} \frac{\Lambda_\rho^4}{\Lambda_\rho^4 + (s - M_\rho^2)^2}, \quad F_2^\rho(s) = \kappa_\rho F_1^\rho(s), \quad (2.55)$$

with normalization $F_1^\rho(M_\rho^2) = g_{\rho NN}$, where the constant $g_{\rho NN}$ corresponds to the coupling of the vector meson ρ with the nucleon ($g_{\rho NN}^2/(4\pi) = 0.55$), $\kappa_\rho = 3.7$ is the anomalous magnetic moment of the proton with respect to the coupling with ρ , and $\Lambda_\rho = 0.911$ is an empirical cut-off.

To take into account the composite nature of the pion, in principle, a monopole type $\rho\pi\pi$ form factor may be introduced: $F_{\rho\pi\pi} = A_\pi/(s - A_\pi)^2$, where A_π is a parameters to be adjusted on the data. In the present case $F_{\rho\pi\pi}$ was set to one. The ρ amplitude is in principle complex. After a study of the s -dependence of the cross section, a relative phase has been added: $\Phi = e^{i\pi\phi_\rho}$. Finally ϕ_ρ was set to unity. It was not necessary to add or adjust a relative normalization of the ρ diagram.

2.3 Results and comparison with the data

Following different attempts of fitting with different form factors as illustrated above, we found that the best solution in this energy range, is to parametrize the form factors at the $\bar{p}p$ vertices, with the logarithmic function of x (where $x = s$ or t or u) (2.52). This choice is based on a QCD derivation from Refs. [97, 98] that relates the asymptotic behavior of form factors to the quark contents of the participating hadrons. It is also known that a logarithmic dependence of the $\bar{p}p$ cross section reproduces quite well the background for resonant processes [99, 100].

It turns out that the logarithmic function (2.52) acts as a very convenient form factor with the parameters summarized in Table 2.2. The procedure is the following: first we apply the form factor $F_{N,\Delta}^L$ which depends on momentum transfer (t or u) to take into account the composite nature of the particle in the interaction point. Second, we use the factor $F_{N,\Delta}^L(s)$ which effectively takes into account pre-Regge regime excitations of higher resonances in the intermediate state. This leads to an effective form factor as the product:

$$\tilde{F}_{N,\Delta}(s, t) = F_{N,\Delta}^L(s)F_{N,\Delta}^L(t) \text{ (or } \tilde{F}_{N,\Delta}(s, u) = F_{N,\Delta}^L(s)F_{N,\Delta}^L(u)), \quad (2.56)$$

containing the same set of parameters for the s and $t(u)$ dependencies, but different for N and Δ exchanges. The fit does not require independent parameters for s and $t(u)$ dependencies.

2.3.1 Angular distributions

The results for the the $\cos \theta$ dependence of the annihilation reaction $\bar{p} + p \rightarrow \pi^- + \pi^+$ are shown for the available data at four values of the total CMS energy (Laboratory antiproton momentum): $\sqrt{s}(p_L) = 3.362(5)$ GeV(GeV/c) [47], 3.627(6) GeV(GeV/c) [53], 3.680(6.2) GeV(GeV/c) [46], and 4.559 (10.1) GeV(GeV/c) [52]. The calculation from the present model is compared to the predictions from the constituent interchange model of Ref. [40].

In the fitting procedures, only the data taken at the CERN proton synchrotron, from Refs. [46, 47, 52] were included, getting a $\chi^2/ndf = 2.16$ (ndf is the number of degrees of freedom). The data from Ref. [53], taken at the Brookhaven National Laboratory multi particle spectrometer (MPS), were excluded from the fit, due to several neighboring points that bias the fit. The results in this plot are therefore given with the parameters fitted on the other data sets.

The data Ref. [46] (black solid circles) are from Ref. [47] (red open circles) are shown in Fig. 2.7, together with the results of the present calculation for the corresponding energies, solid black line and dashed red line, respectively. The calculation from the constituent interchange model of Ref. [40] is also reported, as a dotted black line and a dash-dotted red line, respectively.

For the two sets of annihilation data, from Ref. [53] and Ref. [52], few points are available at forward angles. For the sake of clarity, a reduced angular region is shown in Fig. 2.8.

The available data from the annihilation reaction do not cover the full θ range, especially in the backward region data are scarce. As the PANDA detector will cover 4π solid angle, we rely on the data from πp elastic scattering with the help of crossing symmetry to fill this region. The results for elastic scattering $\pi + p \rightarrow \pi + p$ are shown in Fig. 2.9. The data correspond to very backward angles of the π emission. No other rearrangement of the parameters was done for the elastic scattering data bringing an additional test of the reliability of the model and of the validity of crossing symmetry, at least in the kinematical region where one diagram dominates. The agreement is very good for all data sets.

The angular distribution for $\sqrt{s} = 3.680$ GeV is shown in Fig. 2.10. The total result (black, solid line) gives a very good description of the data from Ref. [46] (red open circles), that here can be appreciated in log scale. For this single data set $\chi^2/ndf = 1.69$.

All components and their interferences are illustrated in Fig. 2.10. n exchange in t channel dominates at forward angles, followed by Δ^0 exchange. Δ^{++} represent the largest contribution for backward angles. The interferences affect the shape of the angular distribution, some of them being negative in part of the angular region. The ρs -channel exchange is small, but its contribution, as well as the interferences with the other diagrams, help in saturating the cross section around $\cos \theta = 0$, being relatively more important in the region $-0.5 \leq \cos \theta \leq 0.5$.

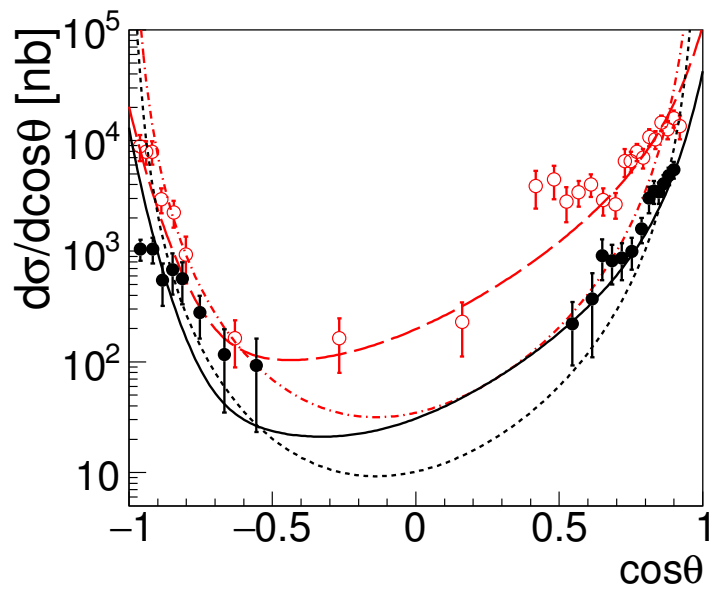


FIGURE 2.7: Angular dependence for the reaction $\bar{p} + p \rightarrow \pi^- + \pi^+$, for $\sqrt{s} = 3.680$ GeV from Ref. [46] (black solid circles) and for $\sqrt{s} = 3.362$ GeV from Ref. [47] (red open circles). The present calculation is shown by a long-dashed red line, and a solid black line at the corresponding energies. The calculation from the constituent interchange model of Ref. [40] is also reported, as a dash-dotted red line, and a dotted black line respectively.

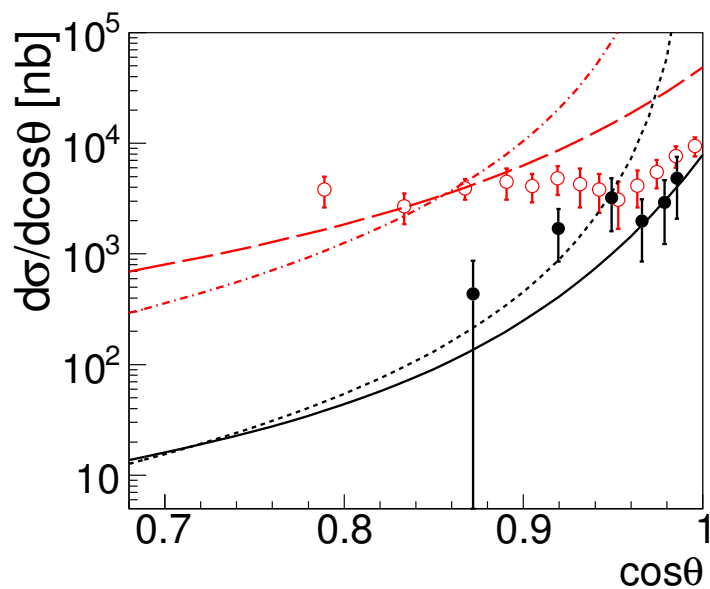


FIGURE 2.8: Angular dependence for the reaction $\bar{p} + p \rightarrow \pi^- + \pi^+$ for $\sqrt{s} = 3.627$ GeV [53] (red open circles), and 4.559 GeV [52] (black solid circles). The data from Ref. [53] were excluded from the fit, but they are well reproduced 'a posteriori'. Lines as in Fig. 2.7.

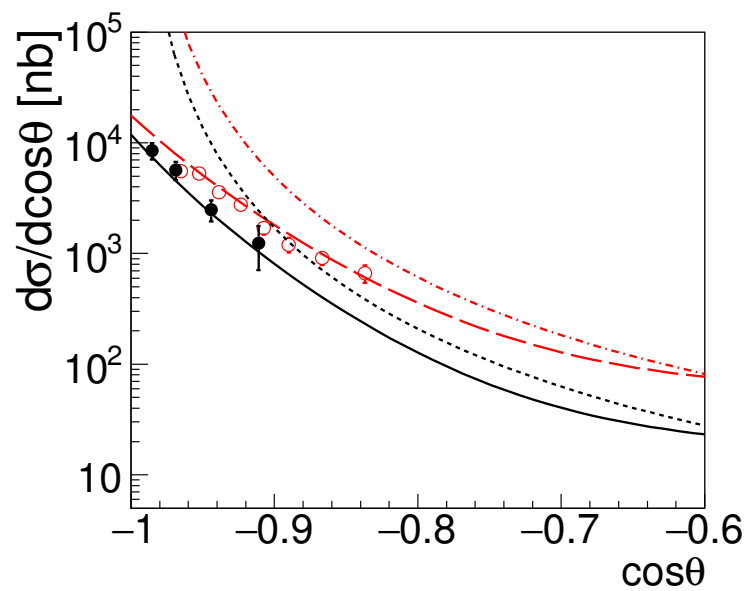


FIGURE 2.9: Data from the elastic reactions $\pi + p \rightarrow \pi + p$ at $\sqrt{s} = 3.463$ GeV from Ref. [48] (red open circles), and at $\sqrt{s} = 3.747$ GeV from Ref. [49] (black solid circles). Lines as in Fig. 2.7.

The necessary number of parameters is very limited: two for the proton and two for the Δ form factor. The phase between the s channel (ρ exchange) and the u, t channels, ϕ_ρ , after fitting, is set to unity. The relative normalization of the ρ diagram is also found consistent with unity and is set to unity.

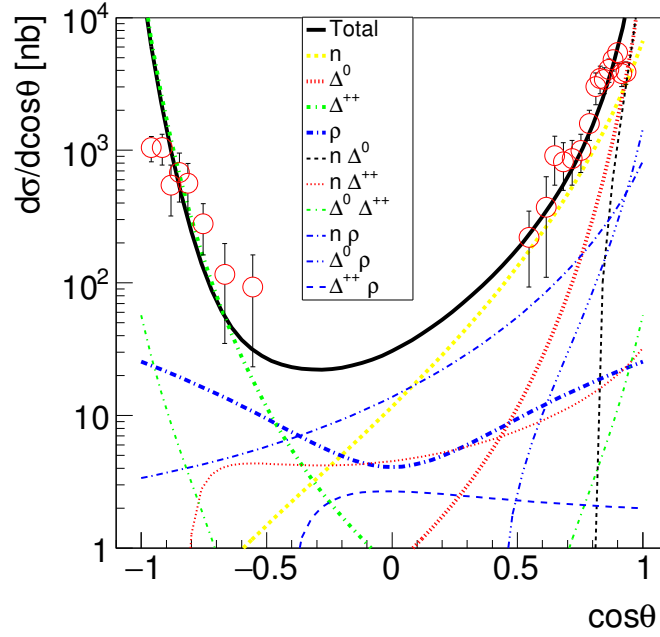


FIGURE 2.10: Angular distribution for $\bar{p} + p \rightarrow \pi^- + \pi^+$ for $\sqrt{s} = 3.680$ GeV. The data are from Ref. [46]. The total function (black solid line) and all components are shown in log scale: n exchange (yellow thick short-dashed line) dominates at forward angle, followed by Δ^0 (red thick dotted line) Δ^{++} (green thick dash-dotted line) represents the largest contribution for backward angles, ρ channel (blue thick long-dashed line) has a larger contribution for $\cos\theta \simeq 0$, relatively to the dominant components. The interferences are $n\Delta^0$ (thin black short-dashed line), and $n\Delta^{++}$ (thin red dotted line), visible at forward angles, $\Delta^0\Delta^{++}$ (green thin short dash-dotted line), $n\rho$ (blue thin long-dashed dotted line), $\Delta^0\rho$ (blue thin dash-triple-dotted line), $\Delta^{++}\rho$ (blue thin long-dashed line), contributing at backward angles.

The dominance of the nucleon and Δ^{++} exchanges in the forward and backward angles, may point out to the presence of nucleon and Δ^{++} poles in the unphysical region. At lower energies, this phenomena is similar to the peak arising from charged pion exchange (pion pole) in the charge exchange neutron-proton scattering (backward peak) and in the proton-antiproton to neutron-antineutron scattering

(forward peak) [101]. At larger energies, the pion pole model has been also successfully applied for neutron proton scattering in Ref. [102].

2.3.2 Energy dependence

We checked that the results are quite stable against a change of the parameters in a reasonable interval. In Fig. 2.11 the s -dependence of the cross section is shown for $\cos\theta = 0$. The long (short) dashed line corresponds to a change of $+(-)10\%$ of the parameters, that increases (decreases) the total function. The sensitivity of the function to these changes is s -dependent, becoming negligible over 4.5 GeV. QCD gives predictions for the cross section of exclusive processes, formulated in terms of quark counting rules [21, 22], that in our case is proportional to s^{-8} . Our model is reasonably consistent with these prediction in the considered energy range.

We may integrate the calculated differential cross section, and give the following values $\sigma(\bar{p} + p \rightarrow \pi^+ + \pi^-) = 4.2 \pm 2.1$ mb at $\sqrt{s} = 3.362$ GeV, $\sigma = 1.4 \pm 0.8$ mb at $\sqrt{s}=3.680$ GeV, and $\sigma = 1.0 \pm 0.5$ mb at $\sqrt{s}=4.559$ GeV, where, for safety, we overestimate the error propagation on the fit parameters by 50%.

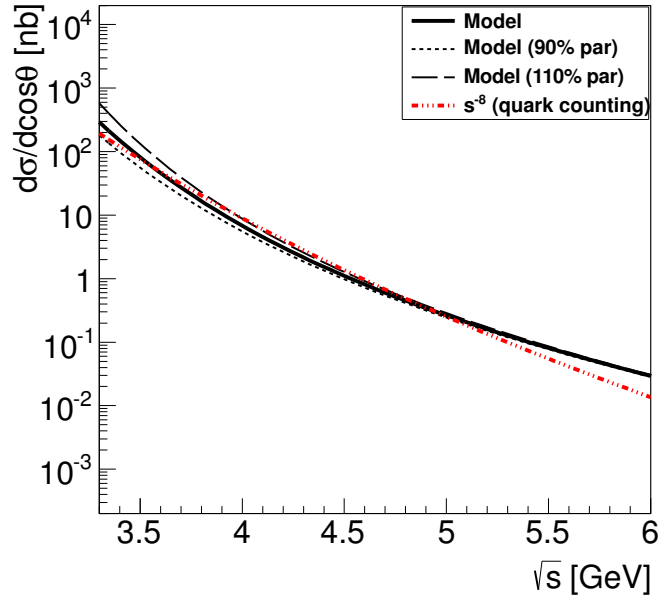


FIGURE 2.11: s -dependence for $\bar{p} + p \rightarrow \pi^- + \pi^+$ for $\theta = 90^\circ$. The total function (black solid line), two functions with parameters changed to 110% (black long-dashed line) and 90% (short-dashed line) from the fitted values are shown in log scale, compared with quark counting rules result from Refs. [21, 22] (red triple dot-dashed line).

2.3.3 Total cross section

As shown above, the differential cross section for $\bar{p}+p \rightarrow \pi^++\pi^-$ is well described by the model based on the t (N and Δ^0), u (Δ^{++}) and s (ρ) diagrams, with logarithmic form factors in the considered energy range. However, the total cross section can not be reproduced in the low energy region ($s \leq 3 \text{ GeV}^2$). The description of the data can be improved by adding an exponential term to s -dependent part of the logarithmic FFs (2.52), where the s dependent part becomes:

$$\begin{aligned} \mathcal{N}(s)_{p,\Delta} &\rightarrow \mathcal{N}(s)_{p,\Delta} - e^{\frac{p_{p,\Delta}^{\mathcal{N}}(s)}{\sqrt{s}}}, \\ \Lambda(s)_{p,\Delta}^2 &\rightarrow \Lambda(s)_{p,\Delta}^2 - e^{\frac{p_{p,\Delta}^{\Lambda}(s)}{\sqrt{s}}}. \end{aligned} \quad (2.57)$$

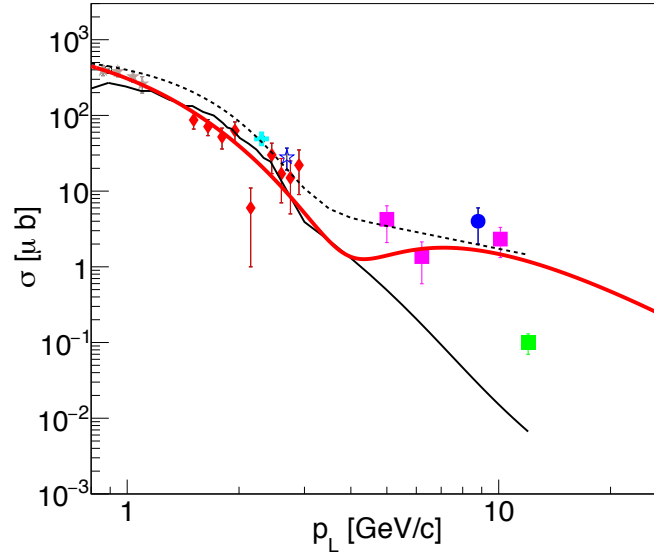


FIGURE 2.12: The collected data for the total cross section for reaction $\bar{p}p \rightarrow \pi^+\pi^-$ as a function of the beam momentum in Lab system p_L (same data as in Fig. 2.2). Three new points (full, purple square) are obtained from the integration of the angular distribution data [47, 46, 52]. The present model with form factor parameters (Listed in Table 2.3) is shown as solid red line. The dashed black line is the modified parametrization from Eq. (2.58) with parameters in Table 2.4 from Ref. [24], the solid black line is from the generator [87].

The parametrization used in Ref. [24] was not constrained in the higher energy region. We may add further constrains by adding three new ‘experimental’ points, estimated by integrating the angular distributions (according to our model). One

Parameter	Value
\mathcal{N}_p	0.361 ± 0.006
\mathcal{N}_Δ	0.197 ± 0.064
Λ_p^2	2.25 ± 0.09
Λ_Δ^2	1.574 ± 0.238
$p_p^{\mathcal{N}}$	-0.260 ± 0.156
$p_\Delta^{\mathcal{N}}$	-5.000 ± 1.083
p_p^Λ	1.378 ± 0.097
p_Δ^Λ	0.788 ± 0.376

TABLE 2.3: Summary table for the parameters for the s -dependent form factor reproducing the total cross section.

Parameter	Value
a	4.848 ± 0.154
b	0.398 ± 0.155
b_1	0.530 ± 0.084
b_0	-4.935 ± 0.090
c	17.306 ± 4.169

TABLE 2.4: Parameters for the modified parametrization formula from Ref. [24].

can modify the parametrization [24], by adding higher order term to the p_L polynomial to describe the region $p_L > 3$ GeV/ c . The suggested parametrization has the form:

$$\sigma = a \cdot e^{-(b \cdot p_L + b_1 \cdot p_L^2 + b_0)} + \frac{c}{p_L}, \quad (2.58)$$

with the parameters as in Table 2.4.

The data and the parametrization are illustrated in Fig. 2.12. We note that the existing model for the PANDARoot generator underestimates the total pion production from momentum p_L about 3 GeV/ c . This is partly due to the difficulty to reproduce backward-forward scattering by the modified Regge parametrization, but, as seen from the angular distributions, Fig. 2.1, the scarce data in the central region are also underestimated by a factor of ($<$) 10. The study of Ref. [25] is based on a rejection factor of 10^{-9} , therefore the conclusions should not be affected. The PANDA experiment will collect a huge amount of data on pion production, and the analysis will be refined on the basis of the developed tools.

2.4 Comparison with the existing data on $\bar{p} + p \rightarrow K^- + K^+$

A similar model, based on corresponding diagrams can be built for charged kaon pair production, changing the mass of the produced and exchanged particle, and replacing the coupling constants. Another possibility is to rely on SU(3) and test its prescription.

Having built the matrix element for $\bar{p} + p \rightarrow \pi^- + \pi^+$, we may calculate the cross section of $\bar{p} + p \rightarrow K^- + K^+$, by applying a global factor, following Ref. [103]:

$$\sigma(\pi^-\pi^+) : \sigma(K^-K^+) = 1 : \frac{4\lambda}{3}, \text{ where } \lambda = 0.4.$$

In the considered energy range, one set of data for the angular distribution exists at $\sqrt{s} = 3.680$ GeV [46]. The results are reported in Fig. 2.13, showing a very good agreement with these data, without need of adjusting the parameters.

We may evaluate the integrated cross section, as

$$\sigma(\bar{p} + p \rightarrow K^+ + K^-) = 2.1 \pm 0.8 \text{ mb at } \sqrt{s}=3.680 \text{ GeV.}$$

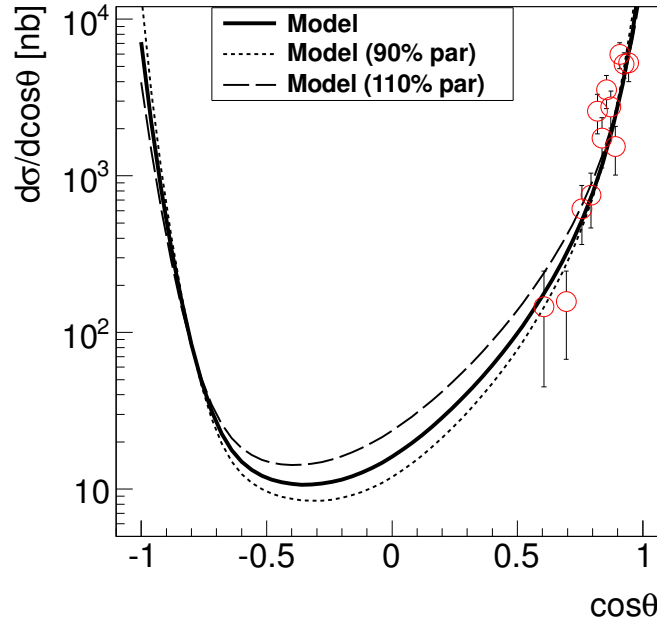


FIGURE 2.13: Angular distribution for $\bar{p} + p \rightarrow K^+ + K^-$ for $\sqrt{s} = 3.680$ GeV. The result of the model (black solid line), as well as the result where the parameters have been overestimated (long dashed line) or underestimated (dotted line) by 10% are shown in log scale. The data are from Ref. [46].

2.5 Summary

We have developed an effective Lagrangian model to describe proton-antiproton annihilation in a charged pion pair. At the PANDA experiment at FAIR, light mesons will be copiously produced in the considered energy range. PANDA will use an antiproton beam on a proton target. One important line of research will be the measurement of time-like form factors through $\bar{p} + p \rightarrow e^+ + e^-$ [23, 24] or $\mu^+ + \mu^-$ [104]. Namely the annihilation into $\pi^+\pi^-$ constitutes the largest background to lepton pair production [105, 25].

A comparison with data from elastic $\pi^\pm p \rightarrow \pi^\pm p$, using crossing symmetry prescriptions shows a good agreement and bring additional constraints at very backward angles. Discussion about validity of crossing symmetry can be found in Refs. [47, 48, 53]. The present results verify that crossing symmetry works at least at backward angles, where one diagram is dominant. Moreover, applying SU(3) symmetry, one recovers the existing data on the angular distribution for $\bar{p} + p \rightarrow K^+ + K^-$ in the corresponding energy range.

The logarithmic expression of the form factors implemented here is typically used for hadron electromagnetic form factors, in the annihilation region. In the scattering region it corresponds to the dipole form, and follows quark counting rules [21, 22] allowing the description of crossed reactions. In recent works it has been suggested that it enters into the early $\bar{q} - q$ pair formation from the quantum vacuum [106, 107]. In the present work it is applied for the first time to fully hadronic reactions, providing the first description of the considered reactions in the FAIR-PANDA energy range.

An application of this work is foreseen to be the implementation into Monte-Carlo simulations for predictions and optimization of the future measurements in PANDA.

Chapter 3

Annihilation into neutral light meson pairs

3.1 Introduction

In this section we give the main lines of the calculation of the reaction $\bar{p}p \rightarrow \pi^0\pi^0$. Although this reaction has cross section ten times less than charged pion pair production, it contributes a large background for several channels and contains the information on different charge states of quark pairs produced in the annihilation.

We consider here the reaction:

$$\bar{p}(p_1) + p(p_2) \rightarrow \pi^0(k_1) + \pi^0(k_2), \quad (3.1)$$

where the notation of four momenta is indicated in the parenthesis. We extend the previous formalism in frame of effective Lagrangian model according to the convenient reaction mechanism. We give the analytical formula and numerical results. The results are compared to the existing data.

3.2 Calculation of the matrix element

The reaction mechanism for neutral pion production takes into account even angular momentum meson exchange in s channel, as it is forbidden from $J=1$ ρ -meson decaying into two identical pions by bosonization.

The following contributions to the cross section, Fig. 3.1, are considered:

- Exchanged particles:
 - nucleon (proton) and Δ^+ exchange, Fig. 3.1a,
 - symmetric exchange of nucleon (proton) and Δ^+ , Fig. 3.1b,
 - f_0, f_2 exchange, Fig. 3.1c.

The total matrix element squared is written as the coherent sum of all the amplitudes. As the produced backward and forward particles are both π^0 that can not be distinguished, we need to add crossed leg diagrams.

$$|\overline{\mathcal{M}}|^2 = \frac{1}{\sqrt{2}} |\mathcal{M}_p + \mathcal{M}_{\Delta^+} + \mathcal{M}_f|^2. \quad (3.2)$$

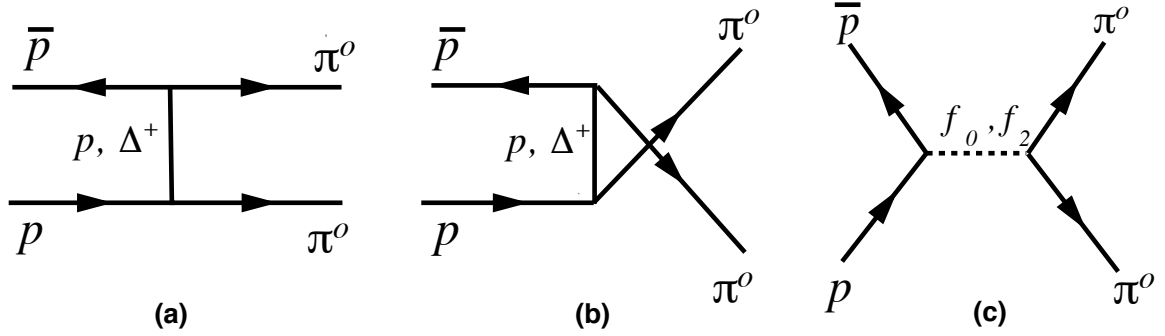


FIGURE 3.1: Diagrams of different exchanged particles for reaction $\bar{p} + p \rightarrow \pi^0 + \pi^0$.

The amplitudes corresponding to the considered diagrams are calculated below, following Feynman rules. The calculation has been done analytically. Sometimes the trace was calculated and/or checked with the help of the FORM program and, if necessary, the resulting expression simplified with the help of MATHEMATICA. Further calculations and graphs are done in frame of C++ and ROOT packages.

The calculation for proton and Delta exchange is the same as for charged pion production. The new part is the scalar meson exchange and its interferences.

3.2.1 s -exchange of neutral scalar mesons: the f_0 contribution

The largest contribution to meson exchange in s -channel, Fig 3.1.c, is given by the scalar particles from Ref. [90], as:

$$\begin{aligned} f_0(500)I^G(J^{PC}) &= 0^+(0^{++}) & M(400 - 550) \text{ MeV}, \Gamma(400 - 700) \text{ MeV} \\ f_0(980)I^G(J^{PC}) &= 0^+(0^{++}) & M(990 \pm 20) \text{ MeV}, \Gamma(40 - 100) \text{ MeV} \\ f_2(1270)I^G(J^{PC}) &= 0^+(2^{++}) & M(1275.5 \pm 0.8) \text{ MeV}, \Gamma(186.7 \pm 2.5) \text{ MeV} \end{aligned} \quad (3.3)$$

Let us start from $f_0(500)$ also called σ meson, the lowest isoscalar scalar particle, with spin zero and positive parity, that decays $\sim 100\%$ into two neutral pions.

- The f_0 - propagator is taken as a Breit-Wigner function

$$\frac{1}{q_s^2 - m_{f_0}^2 + i\sqrt{q_s^2}\Gamma_{f_0}(q_s^2)}, \quad (3.4)$$

$$q_s = p_1 + p_2 = k_1 + k_2, \quad q_s^2 = s.$$

- the $f_0\pi\pi$ vertex $-ig_{f_0\pi\pi}$, where $g_{f_0\pi\pi}$ is the constant for the decay $f_0 \rightarrow \pi\pi$ (See Eq. (3.7));
- the f_0NN vertex : $-ig_{f_0NN}$ where $g_{f_0NN} = 5.0$ GeV is the coupling constant from [89].

The matrix element is written as:

$$\begin{aligned} i\mathcal{M}_{f_0} &= [\bar{v}(p_1)(-ig_{f_0NN})(-i)u(p_2)](i)\frac{1}{q_s^2 - m_{f_0}^2 + i\sqrt{q_s^2}\Gamma_{f_0}(q_s^2)}(-i)g_{f_0\pi\pi} \\ &= -\frac{g_{f_0NN}g_{f_0\pi\pi}}{q_s^2 - m_{f_0}^2 + i\sqrt{q_s^2}\Gamma_{f_0}(q_s^2)}\bar{v}(p_1)u(p_2). \end{aligned} \quad (3.5)$$

Squaring the amplitude:

$$\begin{aligned} |\mathcal{M}_{f_0}|^2 &= \frac{g_{f_0NN}^2 g_{f_0\pi\pi}^2}{|q_s^2 - m_{f_0}^2 + i\sqrt{q_s^2}\Gamma_{f_0}(q_s^2)|^2} \text{Tr}[\bar{v}(p_1)u(p_2)\bar{u}(p_2)v(p_1)] \\ &= \frac{g_{f_0NN}^2 g_{f_0\pi\pi}^2}{|q_s^2 - m_{f_0}^2 + i\sqrt{q_s^2}\Gamma_{f_0}(q_s^2)|^2} 2(s - 4M_p^2). \end{aligned} \quad (3.6)$$

- The $f_0\pi\pi$ coupling constant

The decay width of the f_0 meson in the system where it is at rest is given by :

$$d\Gamma(f_0 \rightarrow \pi\pi) = \frac{1}{2m_{f_0}} |\mathcal{M}(f_0 \rightarrow \pi\pi)|^2 d\Phi_2, \quad (3.7)$$

with the phase space:

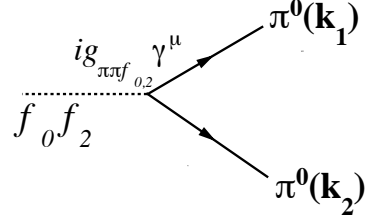
$$d\Phi_2 = \frac{\Lambda^{1/2}(m_{f_0}, m_\pi, m_\pi)}{2^5 \pi^2 m_{f_0}^2} d\Omega, \quad \Lambda^{1/2}(m_{f_0}, m_\pi, m_\pi) = m_{f_0}^2 \sqrt{1 - \frac{4m_\pi^2}{m_{f_0}^2}}. \quad (3.8)$$

Therefore:

$$\Phi_2 = \frac{1}{2^3 \pi} \sqrt{1 - \frac{4m_\pi^2}{m_{f_0}^2}}. \quad (3.9)$$

The matrix element for the decay $f_0 \rightarrow \pi\pi$ is

$$\mathcal{M}(f_0 \rightarrow \pi\pi) = -\frac{(-i)}{(2\pi)^4} (-i)g_{f_0\pi\pi}. \quad (3.10)$$

FIGURE 3.2: Diagram for f_0 and f_2 decays into a pion pair.

The final expression for the width is:

$$\Gamma = \frac{1}{16m_{f_0}\pi} g_{f_0\pi\pi}^2 \sqrt{1 - \frac{4m_\pi^2}{m_{f_0}^2}}. \quad (3.11)$$

Taking the value: $\Gamma = 0.550$ GeV, one finds $g_{f_0\pi\pi} = 4.08 \pm 0.44$ GeV.

3.2.2 The f_0 interferences

The interferences between the N - f_0 and Δ - f_0 channels are listed below.

3.2.2.1 The $N - f_0$ interference

$$2Re[M_N^* M_{f_0}] = 2Re \frac{g_{f_0 NN} g_{f_0\pi\pi} g_{\pi NN}^2}{[s - m_{f_0}^2 - i\sqrt{s}\Gamma_{f_0}(s)](t - M_p^2)} Tr [(\hat{p}_1 - M_p)(-\hat{q}_t + M_p)(\hat{p}_2 + M_p)]. \quad (3.12)$$

3.2.2.2 The $\Delta - f_0$ interference

$$2Re[M_\Delta^* M_{f_0}] = 2Re \frac{g_{f_0 NN} g_{f_0\pi\pi} g_{\Delta NN}^2}{[s - m_{f_0}^2 - i\sqrt{s}\Gamma_{f_0}(s)](t - M_\Delta^2)} Tr [(\hat{p}_1 - M_p)(-\hat{q}_t + M_\Delta) \tilde{P}_{\alpha\beta}(\hat{p}_2 + M_p)] k_1^\alpha k_2^\beta. \quad (3.13)$$

3.2.3 s -exchange of neutral scalar mesons: the f_2 contribution

Let us consider $f_2(1270)$ with spin 2 and positive parity, that decays $\sim 100\%$ into two neutral pions.

- The f_2 - propagator is

$$\frac{\chi_{\mu\nu}\chi_{\alpha\beta}}{[q_s^2 - m_{f_2}^2 + i\sqrt{q_s^2}\Gamma_{f_2}(q_s^2)]}, \quad (3.14)$$

where the width of the f_2 is taken into account by the Breit-Wigner function and the transferred momentum is $q_s = p_1 + p_2 = k_1 + k_2$, $q_s^2 = s$.

- the f_{2NN} vertex : $-ig_{f_{2NN}}$ where $f_{2NN} = 1$ is the coupling constant set to unity. The vertex $f_2 \rightarrow pp$ is written:

$$(-i)g_{f_2pp}\gamma_\mu(p_1 - p_2)_\nu\chi^{\mu\nu}. \quad (3.15)$$

The symmetric tensor $\chi^{\mu\nu}$ has the following properties:

$$\chi_{\mu\nu} = \chi_{\nu\mu}, \quad \chi_{\mu\nu}g^{\mu\nu} = 0, \quad \chi_{\mu\nu}q^\nu = 0; \quad \chi_{\mu\nu}\chi_{\alpha\beta} = \frac{1}{2}(\eta_{\alpha\nu}\eta_{\mu\beta} + \eta_{\mu\beta}\eta_{\nu\alpha}) - \frac{1}{3}\eta_{\mu\nu}\eta_{\alpha\beta}, \quad (3.16)$$

with $\eta_{\mu\nu} = -g_{\mu\nu} + \frac{q_\mu q_\nu}{q^2}$.

The Lagrangian is written as:

$$\mathcal{L}_{f_2\bar{p}p} = g_{f_2pp}\bar{p}(\gamma_\mu i\partial_\nu + \gamma_\nu i\partial_\mu + \frac{2}{3}\eta_{\mu\nu}i\hat{\partial})pT^{\mu\nu}, \quad (3.17)$$

that is equivalent to:

$$\mathcal{L}_{f_2\bar{p}p} = -ig_{f_2pp}g[\gamma_\mu(ip_1 + ip_2)_\nu + i\gamma_\nu(ip_1 + ip_2)_\mu + i\frac{2}{3}\eta_{\mu\nu}(i\hat{p}_1 + i\hat{p}_2)_\nu]T^{\mu\nu}. \quad (3.18)$$

The last term in Eq. (3.18) vanishes as it is the product of an antisymmetric and a symmetric tensor.

- The Lagrangian for the $f_{2\pi\pi}$ vertex is:

$$\mathcal{M}(f_2 \rightarrow \pi\pi) = -\frac{-1}{(2\pi)^4}(-i)g_{f_2\pi\pi}\chi^{\mu\nu}\Theta_{\mu\nu}^\pi, \quad (3.19)$$

where $g_{f_2\pi\pi} = 19 \text{ GeV}^{-1}$ is the constant for the decay $f_2 \rightarrow \pi\pi$ (See Eq. (3.23)), and

$$\Theta_{\mu\nu}^\pi = \frac{1}{2}\eta_{\mu\nu}(\partial_\alpha\pi)^2 - (\partial_\mu\pi)(\partial_\nu\pi), \quad (3.20)$$

which results in:

$$\begin{aligned} & (-i)\frac{1}{2}g_{f_2\pi\pi}\chi^{\mu\nu}\left[2\frac{1}{2}\eta_{\mu\nu}(k_1k_2) - k_{1\mu}k_{2\nu} - k_{1\nu}k_{2\mu}\right] = \\ & \frac{i}{2}g_{f_2\pi\pi}\chi^{\mu\nu}[k_{1\mu}k_{2\nu} + k_{1\nu}k_{2\mu} - (k_1k_2)\eta_{\mu\nu}]. \end{aligned} \quad (3.21)$$

The matrix element for f_2 s -channel exchange in $\bar{p}p \rightarrow \pi^0\pi^0$ is :

$$\begin{aligned} i\mathcal{M}_{f_2} &= [\bar{v}(p_1)(-i)g_{f_2pp}\gamma_\mu(p_2 - p_1)_\nu u(p_2)] \times \\ & i\frac{\chi_{\mu\nu}\chi_{\alpha\beta}}{s - m_{f_2}^2 + i\sqrt{s}\Gamma_{f_2}}\frac{i}{2}g_{f_2\pi\pi}[k_{1\alpha}k_{2\beta} + k_{1\beta}k_{2\alpha} - (k_1k_2)\eta_{\alpha\beta}], \\ \mathcal{M}_{f_2} &= \frac{g_{f_2pp}g_{f_2\pi\pi}}{2}[\bar{v}(p_1)\gamma_\mu(p_2 - p_1)_\nu u(p_2)] \times \\ & \frac{F^{\mu\nu\alpha\beta}}{s - m_{f_2}^2 + i\sqrt{s}\Gamma_{f_2}}[k_{1\alpha}k_{2\beta} + k_{1\beta}k_{2\alpha} - (k_1k_2)\eta_{\alpha\beta}], \\ \mathcal{M}_{f_2}^* &= \frac{g_{f_2pp}g_{f_2\pi\pi}}{2}[\bar{u}(p_2)\gamma_\rho(p_2 - p_1)_\sigma v(p_1)] \times \\ & \frac{F^{\rho\sigma\gamma\delta}}{s - m_{f_2}^2 - i\sqrt{s}\Gamma_{f_2}}[k_{1\gamma}k_{2\delta} + k_{1\delta}k_{2\gamma} - (k_1k_2)\eta_{\gamma\delta}], \end{aligned}$$

where $F^{\mu\nu\alpha\beta} = \chi_{\mu\nu}\chi_{\alpha\beta}$. The matrix element squared is:

$$\begin{aligned} |\mathcal{M}_{f_2}|^2 &= \frac{g_{f_2pp}^2 g_{f_2\pi\pi}^2}{4} \frac{F^{\mu\nu\alpha\beta} F^{\rho\sigma\gamma\delta}}{|s - m_{f_2}^2 + i\sqrt{s}\Gamma_{f_2}|^2} \times \\ & Tr[(\hat{p}_1 - M)\gamma_\mu(p_2 - p_1)_\nu(\hat{p}_2 + M)\gamma_\rho(p_2 - p_1)_\sigma] \times \\ & [k_{1\alpha}k_{2\beta} + k_{1\beta}k_{2\alpha} - (k_1k_2)\eta_{\alpha\beta}][k_{1\gamma}k_{2\delta} + k_{1\delta}k_{2\gamma} - (k_1k_2)\eta_{\gamma\delta}]. \end{aligned} \quad (3.22)$$

- The $f_{2\pi\pi}$ coupling constant

The decay width of the f_2 meson in the system where it is at rest (see Fig. 3.2) is given by :

$$d\Gamma(f_2 \rightarrow \pi\pi) = \frac{1}{2m_{f_2}} |\mathcal{M}(f_2 \rightarrow \pi\pi)|^2 d\Phi_2, \quad (3.23)$$

with the phase space:

$$d\Phi_2 = \frac{\Lambda^{1/2}(m_{f_2}, m_\pi, m_\pi)}{2^5\pi^2 m_{f_2}^2} d\Omega, \quad \Lambda^{1/2}(m_{f_2}, m_\pi, m_\pi) = m_{f_2}^2 \sqrt{1 - \frac{4m_\pi^2}{m_{f_2}^2}}. \quad (3.24)$$

Therefore:

$$\Phi_2 = \frac{1}{2^3\pi} \sqrt{1 - \frac{4m_\pi^2}{m_{f_2}^2}}. \quad (3.25)$$

The matrix element for the decay $f_2 \rightarrow \pi\pi$ is (Fig. 3.2):

$$|\mathcal{M}(f_2 \rightarrow \pi\pi)|^2 = \frac{g_{f_2\pi\pi}^2}{4} \frac{F^{\mu\nu\alpha\beta} F^{\rho\sigma\gamma\delta}}{|s - m_{f_2}^2 + i\sqrt{s}\Gamma_{f_2}|^2} [k_{1\alpha}k_{2\beta} + k_{1\beta}k_{2\alpha} - (k_1k_2)\eta_{\alpha\beta}] \times [k_{1\gamma}k_{2\delta} + k_{1\delta}k_{2\gamma} - (k_1k_2)\eta_{\gamma\delta}]. \quad (3.26)$$

The final expression for the width is:

$$\Gamma = \frac{1}{16m_{f_2}\pi} |\mathcal{M}(f_2 \rightarrow \pi\pi)|^2 \sqrt{1 - \frac{4m_\pi^2}{m_{f_2}^2}}. \quad (3.27)$$

Taking the value: $\Gamma = (0.1867 \pm 0.0025)$ GeV, one finds $g_{f_2\pi\pi} = (19 \pm 0.26)$ GeV⁻¹.

3.2.4 The f_2 interferences

The interferences between the N - f_2 , f_0 - f_2 and Δ - f_2 channels are listed below.

3.2.4.1 The $f_0 - f_2$ interference

$$2Re[\mathcal{M}_{f_0}^* \mathcal{M}_{f_2}] = -Re \frac{g_{f_0NN} g_{f_0\pi\pi} g_{f_2NN} g_{f_2\pi\pi}}{[s - m_{f_0}^2 - i\sqrt{s}\Gamma_{f_0}(s)][s - m_{f_2}^2 + i\sqrt{s}\Gamma_{f_2}(s)]} \times F^{\mu\nu\alpha\beta} (k_{1\alpha}k_{2\beta} + k_{1\beta}k_{2\alpha} - (k_1k_2)\eta_{\alpha\beta}) \times Tr[(\hat{p}_1 - M_p)\gamma_\mu(p_2 - p_1)_\nu(\hat{p}_2 + M_p)]. \quad (3.28)$$

3.2.4.2 The $N - f_2$ interference

$$2Re[\mathcal{M}_{f_2} \mathcal{M}_N^*] = Re \frac{g_{f_2NN} g_{f_2\pi\pi} g_{\pi NN}^2}{[s - m_{f_2}^2 + i\sqrt{s}\Gamma_{f_2}(s)](t - M_p^2)} \times F^{\mu\nu\alpha\beta} (k_{1\alpha}k_{2\beta} + k_{1\beta}k_{2\alpha} - (k_1k_2)\eta_{\alpha\beta}) \times Tr[(\hat{p}_1 - M_p)\gamma_\mu(p_2 - p_1)_\nu(\hat{p}_2 + M_p)(-\hat{q}_t + M_p)]. \quad (3.29)$$

3.2.4.3 The $\Delta - f_2$ interference

$$2Re[\mathcal{M}_\Delta^* \mathcal{M}_{f_2}] = -Re \frac{g_{f_2NN} g_{f_2\pi\pi} g_{\Delta N\pi}^2}{[s - m_{f_2}^2 + i\sqrt{s}\Gamma_{f_2}(s)](t - M_\Delta^2)} \times F^{\mu\nu\alpha\beta} (k_{1\alpha}k_{2\beta} + k_{1\beta}k_{2\alpha} - (k_1k_2)\eta_{\alpha\beta}) \times Tr[(\hat{p}_1 - M_p)\gamma_\mu(p_2 - p_1)_\nu(\hat{p}_2 + M_p)P_{\rho\sigma}(q)(\hat{q}_t + M_\Delta)] k_1^\sigma k_2^\delta. \quad (3.30)$$

Parameters	Value
$p_p^N(s)$	-3.013 ± 0.210
$p_\Delta^N(s)$	-5.959 ± 0.205
$p_p^\Lambda(s)$	4.047 ± 0.019
$p_\Delta^\Lambda(s)$	3.141 ± 0.002

TABLE 3.1: Parameters for the s -dependent term of the logarithmic form factors for $\bar{p}p \rightarrow \pi^0\pi^0$.

3.2.5 The total contribution

After the calculation of the coupling constants and matrix elements, the total matrix element squared averaged over the spin states of the initial particles, is obtained as the sum of the squared of matrix element for the individual contributions and the interferences among them: Explicitly:

$$\begin{aligned}
|\mathcal{M}(\bar{p}p \rightarrow \pi^0\pi^0)|^2 &= |\mathcal{M}_{f_0}(s)|^2 + |\mathcal{M}_{f_2}(s)|^2 + \frac{1}{2} \left\{ |\mathcal{M}_p(t)|^2 + |\mathcal{M}_\Delta(t)|^2 + \right. \\
&\quad |\mathcal{M}_p(u)|^2 + |\mathcal{M}_\Delta(u)|^2 + 2\text{Re}[\mathcal{M}_p(t)^*\mathcal{M}_p(u) + \mathcal{M}_p(t)^*\mathcal{M}_\Delta(t) + \\
&\quad \left. \mathcal{M}_p(t)^*\mathcal{M}_\Delta(u) + \mathcal{M}_p(u)^*\mathcal{M}_\Delta(t) + \mathcal{M}_p(u)^*\mathcal{M}_\Delta(u)] \right\} + \\
&\quad \sqrt{2}\text{Re}[\mathcal{M}_{f_0}^*(s)\mathcal{M}_{f_2}(s) + \mathcal{M}_p(t)\mathcal{M}_{f_0}^*(s) + \mathcal{M}_p(u)\mathcal{M}_{f_0}^*(s) + \\
&\quad \mathcal{M}_\Delta(t)\mathcal{M}_{f_0}^*(s) + \mathcal{M}_\Delta(u)\mathcal{M}_{f_0}^*(s) + \mathcal{M}_p^*(t)\mathcal{M}_{f_2}(s) + \\
&\quad \mathcal{M}_p^*(u)\mathcal{M}_{f_2}(s) + \mathcal{M}_\Delta^*(t)\mathcal{M}_{f_2}(s) + \mathcal{M}_\Delta^*(u)\mathcal{M}_{f_2}(s)]. \quad (3.31)
\end{aligned}$$

Taking into account the phase space and the flux, the expression for the total cross section is:

$$\frac{d\sigma}{d\Omega}(\bar{p}p \rightarrow \pi^0\pi^0) = \frac{1}{2^8\pi^2} \frac{1}{s} \frac{\beta_\pi}{\beta_p} |\mathcal{M}(\bar{p}p \rightarrow \pi^0\pi^0)|^2, \quad (3.32)$$

and

$$\frac{d\sigma}{d\cos\theta}(\bar{p}p \rightarrow \pi^0\pi^0) = \frac{1}{2^7\pi} \frac{1}{s} \frac{\beta_\pi}{\beta_p} |\mathcal{M}(\bar{p}p \rightarrow \pi^0\pi^0)|^2. \quad (3.33)$$

3.3 Results for $\bar{p} + p \rightarrow \pi^0 + \pi^0$

For neutral pion pair production, the first attempt was to apply the same model for the form factors and the same parameters as for the charged pion data. However, the behavior of the total cross section for charged and neutral pion pairs is very different. It turns out that the s -dependent part of the logarithmic form factors needs to be adjusted by adding an energy dependence as in Eq. (2.57). The parameters for the modified parts are fixed as in Table 3.1. The form factors for the f_0NN vertex

Parameters	Value
F_{f_0}	1.17 ± 0.051
χ^2/ndf	109

TABLE 3.2: Parameters of the $f_0 NN$ form factor for $\pi^0\pi^0$ production in the energy range $2.911 \text{ GeV} \leq \sqrt{s} \leq 3.686 \text{ GeV}$.

is taken as:

$$FF_{f_0}(s) = \frac{F_{f_0}^2}{F_{f_0}^2 + (M_{f_0}^2 - s)}, \quad (3.34)$$

with the parameter listed in Table 3.2. In addition, similarly to the charged pion calculation, the phase $\Phi_f = e^{i\pi\phi_f}$ is added for the exchanged meson in s -channel with ϕ_f set to unity.

The fitted plots and data [75] are shown in the Fig. 3.3, in the energy range $2.911 \text{ GeV} \leq \sqrt{s} \leq 3.686 \text{ GeV}$. The data used in the analysis are reported in Appendix A.2. The data were measured in regular intervals; with a gap between 3.097 GeV and 3.524 GeV which separates the data into the ‘lower energy region’ ($2.911 \text{ GeV} \leq \sqrt{s} \leq 3.097 \text{ GeV}$) and ‘higher energy region’ ($3.524 \text{ GeV} \leq \sqrt{s} \leq 3.686 \text{ GeV}$). In the lower energy region, a bump produced by $J \geq 4$ resonances appears around $\cos \theta = 0$. It can not be reproduced by the f_0 and f_2 mesons considered in s -channel, and it disappears at higher energies. Therefore we did not attempt to add higher resonances. The resulting $\chi_L^2/ndf = 218$ for the low energy region is not satisfactory, while in the higher energy region, one obtains $\chi_H^2/ndf = 12$. A global $\chi^2/ndf = 110$ is obtained.

The s -dependence for neutral pion production from 5 GeV to 25 GeV is shown in Fig. 3.4. The data from Ref. [75] are integrated in the available angular range. The calculation is presented with the integration covering the angle from $\cos \theta = 0$ to 0.66, which is the maximum value of the existing data. We notice that the calculation well reproduced the integrated points at the higher energy region, but overestimates the data in the lower region. This can be explained as the data in the lower region have narrower angular distribution (maximum $\cos \theta = 0.48$ at $s = 8.4739 \text{ GeV}^2$) and the very forward and backward regions give very large contribution to the total cross section.

- The higher energy set

The case of the set of data at $\sqrt{s} = 4.274 \text{ GeV}$ is peculiar. The data correspond to the higher energy available, and show a discontinuity with respect to the other sets. In particular the bump for $\cos \theta = 0$ evolves into a dip, and an oscillation appears. To reproduce this dip, the $J = 2$ meson f_2 is added. The form factor of $f_2 NN$ is taken as a monopole, Eq. (3.34), similarly to f_0 and the relative phase is also taken as unity. Concerning the high energy, the contribution from f_0 meson of smaller mass results suppressed by the fitting procedure. The parameters for s -channel are listed in the Table 3.3.

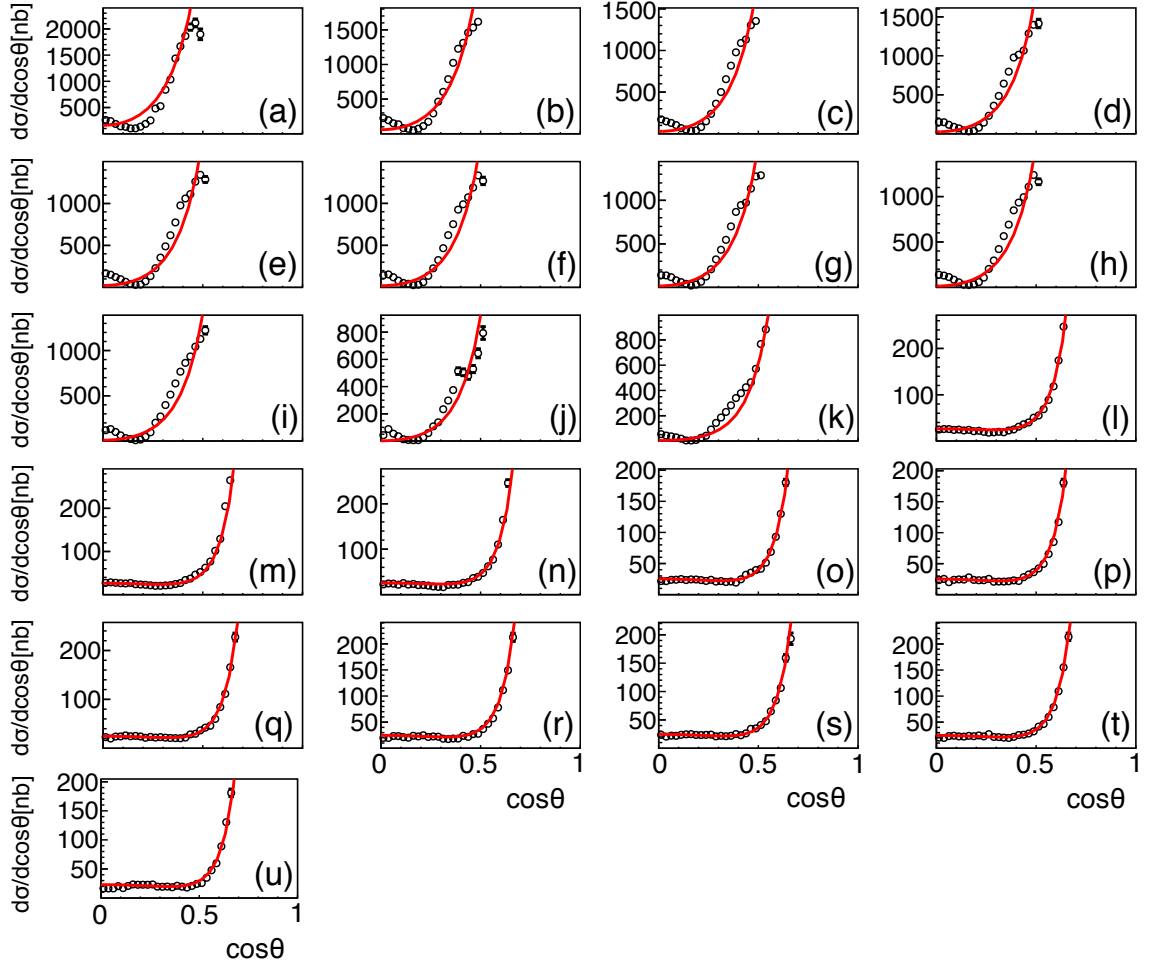


FIGURE 3.3: Angular distribution for the reaction $\bar{p}p \rightarrow \pi^0\pi^0$ in CMS in the energy range $2.911 \text{ GeV} \leq \sqrt{s} \leq 3.686 \text{ GeV}$. From (a) \rightarrow (u), they correspond to the energy $\sqrt{s} = 2.911$ (a), 2.950(b), 2.975(c), 2.979 (d), 2.981(e), 2.985(f), 2.990(g), 2.994(h), 3.005(i), 3.050(j), 3.097(k), 3.524(l), 3.526(m), 3.556(n), 3.591(o), 3.595(p), 3.613(q), 3.616(r), 3.619(s), 3.621(t), 3.686(u) GeV. The data (black circles) are from Ref. [75] and the parameters of the calculation (red line) are given in Table 3.2.

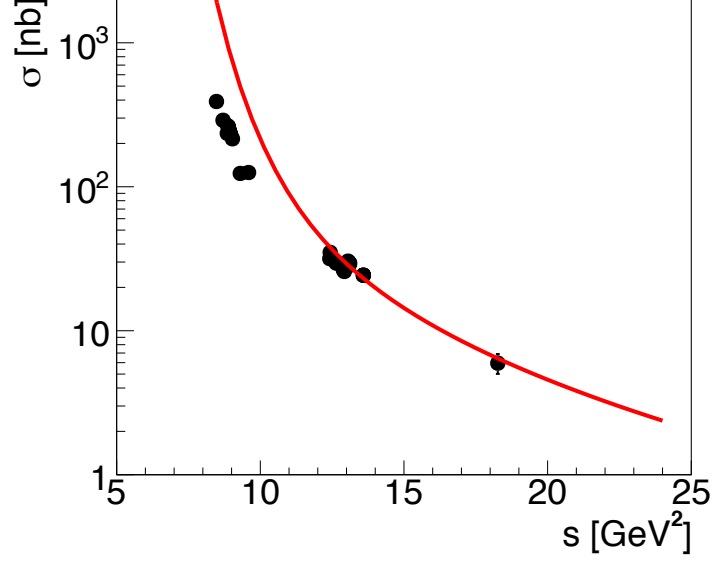


FIGURE 3.4: Integrated cross section for the reaction $\bar{p}p \rightarrow \pi^0\pi^0$. The data are obtained by the integration of the partial differential cross section from Ref. [75]. The present calculation (red solid line) covering the range $0 \leq \cos \theta \leq 0.66$ is shown in log scale.

parameters	Value
F_{f_0}	0.870 ± 0.014
F_{f_2}	0.187 ± 0.001
χ^2/ndf	0.787

TABLE 3.3: Parameters of form factors for f_0 and f_2 mesons at $\sqrt{s} = 4.274$ GeV.

The different components are visible in Fig. 3.5. One can see that the oscillation and the dip can be very well reproduced by the f_2 contribution. The Delta contribution overcomes the Nucleon term. The angular distribution is limited and one can not draw firm conclusions on the t and u channel interplay of the different contribution. A very good agreement is obtained by fitting this set of the data with the present model.

Applying SU(3) symmetry, one can connect other neutral channels. As we see in next section, it works relatively well at all energies except at $\sqrt{s} = 4.274$ GeV.

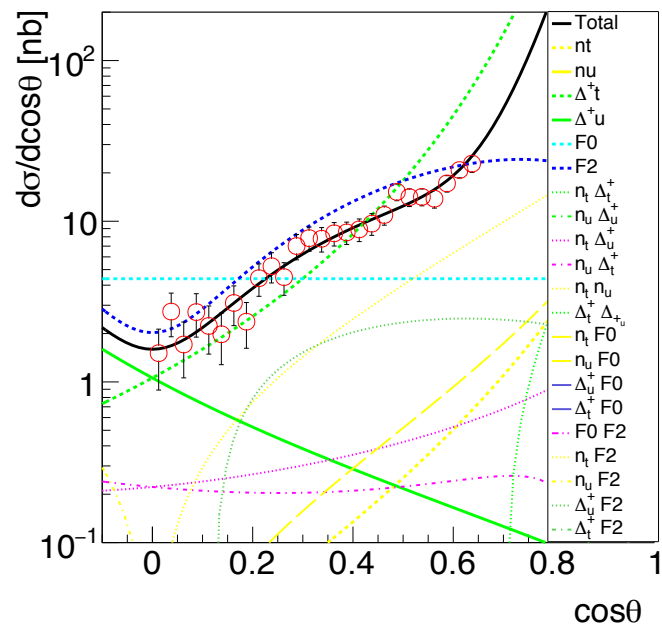


FIGURE 3.5: Angular distribution for reaction $\bar{p}p \rightarrow \pi^0\pi^0$ at $\sqrt{s} = 4.274$ GeV [75] with different components. The parameters are listed in Table 3.3.

3.4 Results for $\bar{p} + p \rightarrow \eta + \eta$ and $\bar{p} + p \rightarrow \eta + \pi^0$

We consider here annihilation reactions at energy \sqrt{s} above 2.9 GeV, and focus on two neutral meson production. We discuss the annihilation reaction of antiproton-proton into $\eta + \eta$, $\pi^0 + \eta$, $\pi^0 + \pi^0$:

$$\bar{p}(p_1) + p(p_2) \rightarrow \pi^0(k_1) + \pi^0(k_2), \quad (3.35)$$

$$\bar{p}(p_1) + p(p_2) \rightarrow \eta(k_1) + \eta(k_2), \quad (3.36)$$

$$\bar{p}(p_1) + p(p_2) \rightarrow \eta(k_1) + \pi^0(k_2), \quad (3.37)$$

where the momenta of the particles are indicated in parenthesis.

The two body channels (3.35, 3.36, 3.37) involve mesons that are related by SU(3) symmetry, as π , η and η' are members of a single nonet. SU(3) allows to predict reactions (3.36, 3.37) from (3.35) using the known quark composition of these mesons:

$$\eta \approx (u\bar{u} + d\bar{d})/\sqrt{2} + s\bar{s}.$$

In principle $\bar{p}p$ does not couple directly to $s\bar{s}$:

$$|q\bar{q}\rangle = \cos\Theta|\eta\rangle + \sin\Theta|\eta'\rangle,$$

$$|s\bar{s}\rangle = -\sin\Theta|\eta\rangle + \cos\Theta|\eta'\rangle,$$

where $q = (u\bar{u} + d\bar{d})/\sqrt{2}$ and $\Theta = 37^\circ$ is the pseudoscalar mixing angle [108].

Having a model that reproduces consistently angular distributions and cross sections for $\pi^0 + \pi^0$, based on s , t , and u channels, the amplitudes for the decay to the channels (3.35, 3.36, 3.37) are related by SU(3), that gives a prescription to renormalize the amplitudes. As an example, replacing π^0 by η , for the decay of a meson M , if $g_{M\pi\pi} = g_1$, then $g_{M\eta\eta}$ is $g_2 \cos^2(\Theta)$ where $g_2 \approx g_1$, and $g_{M\pi\eta}$ is $\approx g_1 \cos(\Theta)$.

Evidently, the kinematics and the masses have to be changed correspondingly. In case of reaction (3.37) the fact that the final state implies a backward forward asymmetry.

In particular the final particles mass-shell conditions fix the energies $E_{1,2}$, the velocity and the modulus of the momentum \vec{k} of the final particles:

$$\begin{aligned} E_{1,2} &= \frac{s + M_{1,2}^2 - M_{2,1}^2}{2\sqrt{s}}, \\ \beta_{1,2} &= \frac{\lambda^{1/2}(s, M_{1,2}^2, M_{2,1}^2)}{s + M_{1,2}^2 - M_{2,1}^2}, \\ |\vec{k}| &= \frac{1}{2\sqrt{s}} \lambda^{1/2}(s, M_1^2, M_2^2), \end{aligned} \quad (3.38)$$

where $\lambda(x, y, z)$ is the so called triangle function:

$$\lambda(x, y, z) = x^2 + y^2 + z^2 - 2xy - 2xz - 2yz. \quad (3.39)$$

Applying SU(3) symmetry and taking into account the kinematics difference due to the masses, without readjusting the parameters, the model is applied in the energy range $2.911 \text{ GeV} \leq \sqrt{s} \leq 3.617 \text{ GeV}$. The result is shown for the reactions (3.36, 3.37) in Fig. 3.6 and Fig. 3.7, respectively. The corresponding tables are reported in Appendix A.2.

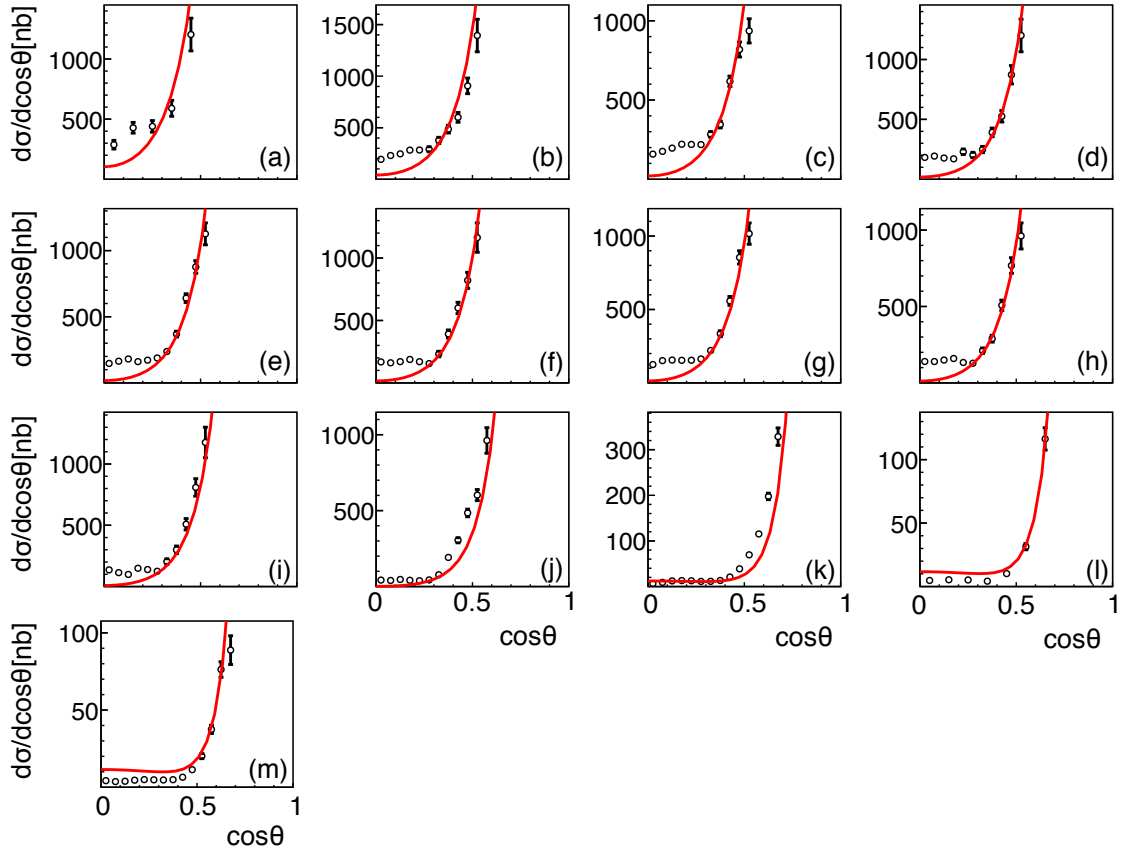


FIGURE 3.6: Angular distribution for $\bar{p}p \rightarrow \eta\eta$ (black circle) [75] in the energy range $2.911 \text{ GeV} \leq \sqrt{s} \leq 3.617 \text{ GeV}$. From (a) \rightarrow (m), they correspond to the energy $\sqrt{s} = 2.911$ (a), 2.950(b), 2.975(c), 2.979 (d), 2.981(e), 2.985(f), 2.990(g), 2.994(h), 3.005(i), 3.050(j), 3.526(k), 3.592(l), 3.617(m) GeV. The model calculation (red solid curve) is based on the symmetry of the quark model.

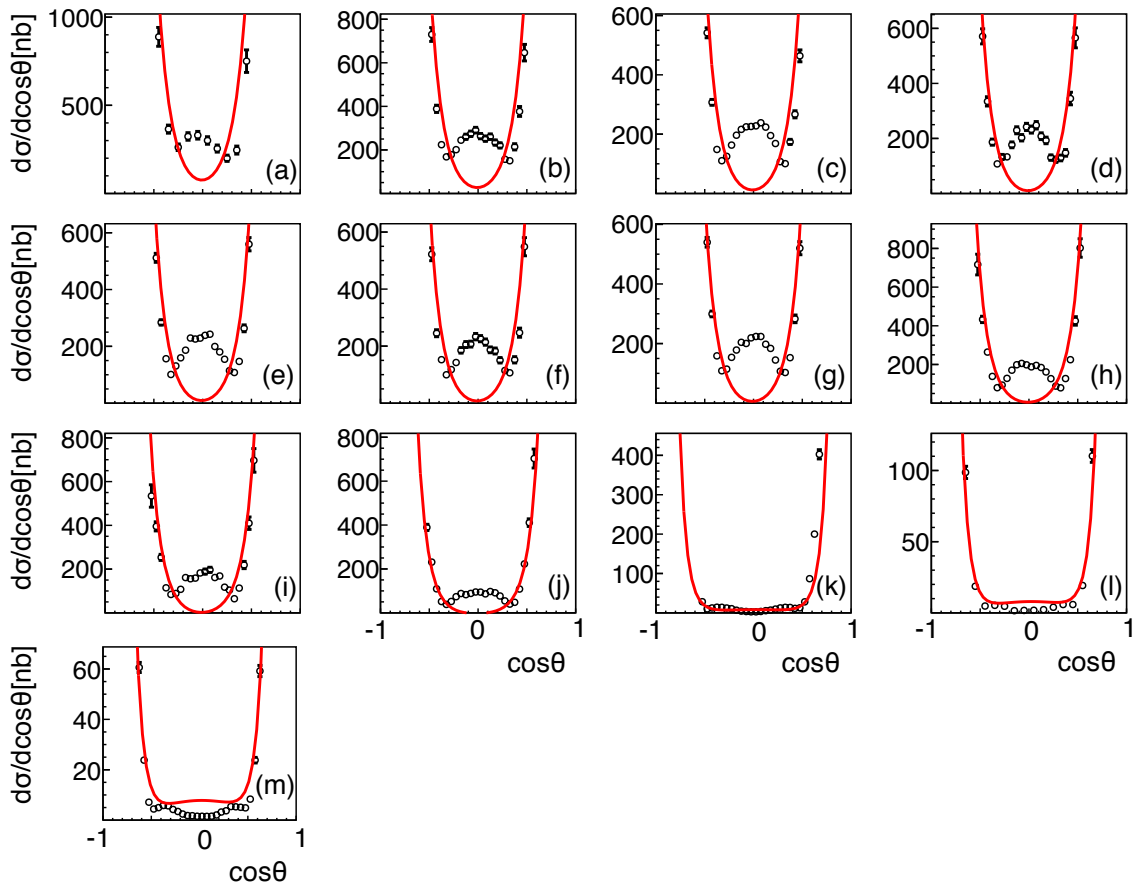


FIGURE 3.7: Same as Fig. 3.6, for the reaction $\bar{p}p \rightarrow \eta\pi^0$ in the energy range $2.911 \text{ GeV} \leq \sqrt{s} \leq 3.617 \text{ GeV}$. From (a) \rightarrow (m), they correspond to the energy $\sqrt{s} = 2.911$ (a), 2.950(b), 2.975(c), 2.979 (d), 2.981(e), 2.985(f), 2.990(g), 2.994(h), 3.005(i), 3.050(j), 3.526(k), 3.592(l), 3.617(m) GeV.

The model is able to reproduce the data in the backward and forward regions. Similarly to $\pi^0\pi^0$ it is expected that the bump in the central region is missed by the model.

For the higher energy $\sqrt{s} = 4.274$ GeV, the data of $\eta\eta$ and $\eta\pi^0$ have large error bars and few points are measured. Precise data are expected from the PANDA experiment to fill this region.

Part II

Proton and neutron analyzing power measurements

Chapter 4

Introduction on electromagnetic form factors

In 1933, Otto Stern measured the proton magnetic moment and found it anomalously larger than a point-like particle which indicates that proton is not an elementary particle [109], $\mu_p = 2.792847356(23)\mu_N$. 20 years later, in a series of electron nucleon scattering experiments [110] (Robert Hofstadter shared the Nobel Prize in Physics in 1961 “for his pioneering studies of electron scattering in atomic nuclei and for his thereby achieved discoveries concerning the structure of the nucleons”), the elastic ep cross section was measured and form factors (FFs) were extracted according to the method suggested by M.N. Rosenbluth [111]. It consists in the measurement of the unpolarized cross section at fixed momentum transfer, Q^2 , and at different angles of the scattered electron.

Polarization observables contain unique and precise information on the reaction mechanism and on the underlying interaction, as they are sensitive to interferences of the amplitudes and their relative phases. One important achievement of polarization techniques was, for example, to prove the Parity violation in weak decays. The experiment was led by Ms. Wu in 1956 [112], and consisted in the measurement of γ rays and electron angular distribution from polarized ^{60}Co decaying by electromagnetic and weak interaction into the ground state of ^{60}Ni .

We are concerned here by the recoil polarization method in ep elastic scattering. It was suggested by A.I. Akhiezer and M.P. Rekalov [113, 114]. It allows to extract the electric and magnetic form factors by the measurement of the recoil proton polarization in elastic ep scattering, using a longitudinally polarized electron beam.

In a semi-classical framework, from quantum mechanic considerations, the initial incident particle and the final scattered particle are represented by plane waves. When this plane wave scatters on a charge object at some point it generates spherical waves which can be observed as a plane wave at a large distance. The cross section can be factorized in two terms: the Mott cross section for the scattering on a point-like object and a term that contains the structure of the composite particle, expressed in terms of form factors. From a Parity and Time invariant theory, the necessary number of form factors is decided by the spin (S) of the particle. A particle with spin S is described by $2S+1$ form factors. Schematically, for small values of

momentum transfer, form factors probe the size of the hadron and give information on the nucleon radius. At large momentum transfer, form factors contain the information of the short distance interaction, driven by the quarks and gluons inside the hadron.

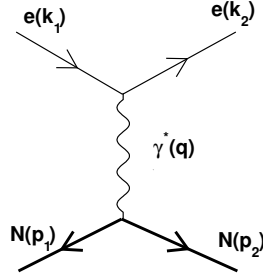


FIGURE 4.1: Diagram for ep elastic scattering through one photon exchange.

Under the assumption of one virtual photon exchange, the ep elastic scattering process (shown in Fig. 4.1) contains the electron vertex $ee\gamma$, the propagator of the virtual photon of four momentum q^2 , and the $pp\gamma$ vertex, that can be written in terms of F_1 and F_2 , the Dirac and Pauli form factors. In the most general case, the nucleon electromagnetic current at the proton vertex is described by two independent spin structures.

The amplitude corresponding to the diagram (4.1) \mathcal{M} is explicitly written as:

$$\begin{aligned}\mathcal{M} &= \frac{e^2}{q^2} \ell^\mu J_\mu, \\ \ell^\mu &= \bar{u}(k_2) \gamma^\mu u(k_1), \\ j^\mu &= \bar{u}(p_2) \left[F_1(q^2) \gamma_\mu - \frac{\sigma_{\mu\nu}}{2M} F_2 \right] u(p_1),\end{aligned}\tag{4.1}$$

where $\sigma_{\mu\nu} = \frac{\gamma_\mu \gamma_\nu - \gamma_\nu \gamma_\mu}{2}$ (γ are the Dirac matrices), ℓ^μ , j^μ correspond to the electron and nucleon currents, respectively, and \bar{u} (u) is the spinor describing each external line in the diagram (4.1). It is convenient to introduce the Sachs form factors, the electric G_E and the magnetic G_M . They are linear combinations of F_1 and F_2 form factors (4.2):

$$\begin{aligned}G_M &= F_1 + F_2, \\ G_E &= F_1 - \tau F_2, \text{ with } \tau = -\frac{q^2}{4M_p^2}.\end{aligned}\tag{4.2}$$

In the Breit frame (defined as a system where the initial and final nucleon energies are the same) G_E and G_M can be interpreted as Fourier transforms of electric charge and magnetization spatial densities.

Form factors can be accessed in both the Time-like (TL) and the Space-like (SL) region of the momentum transfer squared, by suppress elementary annihilation and scattering experiments. The TL region, where $q^2 > 0$, is presently investigated by the running experiment BESIII, at the BEPCII collider (Beijing), using the reaction $e^- + e^+ \rightarrow p + \bar{p}$ [115] and in the next future, by the PANDA experiment at FAIR, Darmstadt, which will make use of antiproton beam and will measure $p + \bar{p} \rightarrow e^- + e^+$ [23, 116, 25] and study this process from different time directions of the annihilation reactions. In the SL region where $q^2 < 0$ ($Q^2 = -q^2 > 0$), experiments are planned and ongoing with high intensity, highly polarized electron beam at the Jefferson Laboratory (JLab) at large momentum transfer, and at MAMI in Mainz at lower beam energy, measuring polarized and unpolarized cross section in ep elastic scattering. Using crossing symmetry, and assuming that form factors are analytical function, one can in principle connect SL and TL regions.

4.1 Form factors in the time-like region

In TL region, two annihilation channels $e^- + e^+ \rightarrow p + \bar{p}$ and $p + \bar{p} \rightarrow e^- + e^+$ contain the same $\gamma^* NN$ vertex, under the one-photon exchange assumption. The unpolarized cross section depends on the moduli squared of form factors, as form factors are complex functions due to unitarity. The expression of the total cross section is [117]:

$$\sigma(e^- e^+ \rightarrow p\bar{p}) = \beta^2 \sigma(p\bar{p} \rightarrow e^- e^+) = \frac{4\pi^2 \alpha^2 \beta}{3q^2} \left(\frac{1}{\tau} |G_E|^2 + 2|G_M|^2 \right), \quad (4.3)$$

where $\beta = \sqrt{1 - 1/\tau}$.

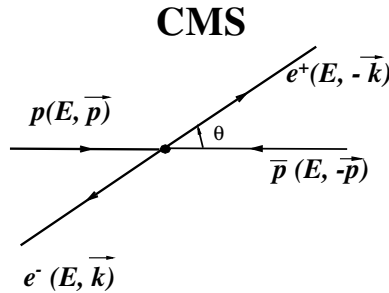


FIGURE 4.2: Reaction of $p + \bar{p} \rightarrow e^- + e^+$ in CMS.

The CMS is more convenient for expressing the annihilation differential cross section ([117]):

$$\frac{d\sigma}{d\cos\theta}(pp \rightarrow \bar{e}^- e^+) = \frac{\pi\alpha^2}{2q^2\beta} [(1 + \cos^2\theta)|G_M|^2 + \frac{1}{\tau} \sin^2\theta|G_E|^2], \quad (4.4)$$

corresponding to the reaction illustrated in Fig. 4.2, from where one can see that a precise measurement of the angular distribution allows the individual extraction of G_E and G_M . Other annihilation channels into heavier leptons, like μ and τ pairs, assuming lepton universality, also contain the same physical information on the hadron structure, but, taking into account the lepton mass, the cross sections contains extra terms, as for example a particle mass fourth power term. In TL region, form factors are complex, therefore polarization phenomena are particularly important: for example, a single spin observables as the analyzing power contain information on the relative phase of form factors [118].

4.2 Form factors in the space-like region

In SL region, form factors can be extracted from two sorts of experiments. One way is from the measurement of the differential cross section in unpolarized ep scattering at fixed q^2 . This method is traditionally called the Rosenbluth separation. The calculation of the unpolarized cross section, squaring the matrix element (4.2), summing over the initial particle polarization and averaging over the final particle polarizations leads to the Rosenbluth formula [111]. The differential cross section $d\sigma/d\Omega_{\theta_e}$ (4.5) is factorized in the cross section for a point-like particle $d\sigma_M/d\Omega_{\theta_e}$ (Mott cross section) and a term that contains the proton structure parametrized in terms of form factors that are functions only of q^2 . The differential cross section for elastic ep scat-

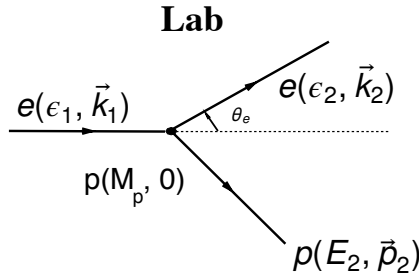


FIGURE 4.3: Illustration of ep elastic scattering in the Lab system.

tering, illustrated in Fig. 4.3 in the Lab system, is written as:

$$\begin{aligned} \frac{d\sigma}{d\Omega_{\theta_e}} &= \frac{d\sigma_M}{d\Omega_{\theta_e}} \left[2\tau G_M^2 \tan^2(\theta_e/2) + \frac{G_E^2 + \tau G_M^2}{1 + \tau} \right], \\ \frac{d\sigma_M}{d\Omega_{\theta_e}} &= \frac{\alpha^2}{-q^2} \left(\frac{\epsilon_2}{\epsilon_1} \right)^2 \frac{\cos^2(\theta_e/2)}{\sin^2(\theta_e/2)}, \end{aligned} \quad (4.5)$$

where $\epsilon_{1,2}$ is the energy of the incident and outgoing electrons in Lab system, θ_e is the electron scattering angle and $\alpha = e^2/4\pi \simeq 1/137$ is the electromagnetic fine

structure constant. It is convenient to define a reduced cross section σ_{red} as:

$$\sigma_{red}(\theta_e, q^2) = \tau G_M^2 + \varepsilon G_E^2, \quad (4.6)$$

where $\varepsilon = [1 + 2(1 + \tau) \tan^2(\theta_e/2)]^{-1}$.

From Eq. (4.6), it appears that the reduced cross section at the fixed transfer momentum Q^2 and at different scattering angles θ_e , is a linear function of ε only. The slope of the reduced cross section is the electric FF, G_E , and the intercept is related to the magnetic FF, G_M . When $\theta_e = \pi$ or at large Q^2 the magnetic FF saturates the cross section. One big limitation of this method is the precision for the extraction of G_E in these conditions. At large transferred momentum Q^2 , τ becomes large, and as a consequence, the electric contribution to the cross section becomes proportionally very small. Then the experiment will give very large error bars for the electric FF. In the neutron case, as it has smaller magnetization and is a neutral particle, the Rosenbluth separation even at small Q^2 can not be obtained with the same precision as for the proton.

An alternative method, first suggested by A.I. Akhiezer and M.P. Rekalo [113, 114], requires double polarization experiments: a longitudinally polarized electron beam on an unpolarized target and the measurement of the polarization of the recoil protons, or with a transverse polarized target measuring the asymmetry induced by the polarization of the beam [119]. Recent experiments prove that the method with $\bar{e}^- + p \rightarrow e^- + \vec{p}$ allows to reach larger values of Q^2 , due to the fact that a polarized target can not sustain high intensity beam for a long time.

Under the assumption of one-photon exchange, as form factors are real in the SL region, the single polarization observables vanish (this is not true in TL region, where form factors are complex). The ratio of form factors is related to the ratio of the longitudinal and transverse polarization of the scattered proton, when the electron beam is longitudinally polarized:

$$\frac{P_{t=x}}{P_{\ell=z}} = -2 \cot(\theta_e/2) \frac{M_p}{\epsilon_1 + \epsilon_2} \frac{G_E}{G_M}. \quad (4.7)$$

The double polarized technique gives more precise results than the unpolarized method, because measuring the ratio of the two polarization components reduces the systematic uncertainties, as it is (at the first order) independent on the electron polarization and on the analyzing powers of the polarimeter.

The world data of the form factors ratio with two methods are compared in Fig. 4.4. The data from the double polarization experiments are presented as full symbols and the unpolarized data are in open symbols (green). Double polarized experiments were made possible by the development of highly polarized and intense electron beams, hadron polarimeters in the GeV range, polarized targets and large acceptance spectrometers. Since then several experiments have been performed at JLab following the Akhiezer-Rekalo method, to measure the form factors ratio, first up to $Q^2 = 3.5 \text{ GeV}^2$, then extended to 5.6 and 8.5 GeV^2 [120, 121, 122, 123].

Before polarization experiments became possible, the common understanding of G_E and G_M for the proton was that they had a similar dependence on Q^2 , following the dipole behavior $G_D = [1 + Q^2[\text{GeV}^2]/0.71]^{-2}$, as well as the neutron magnetic FF, whereas the neutron electric FF was considered to be equal to zero. It is clearly accepted that the polarized data are more precise. To describe the FF ratio, several models have been developed to reproduce the linear decreasing of Q^2 . One of the interesting questions for protons is if the FF ratio will become negative with the transferred momentum growing. For neutron, the behaviours of the models are very different above 4 GeV^2 . All these phenomena motivate the experimentalists to explore the FF structures to the higher Q^2 regions of the proton and the neutron.

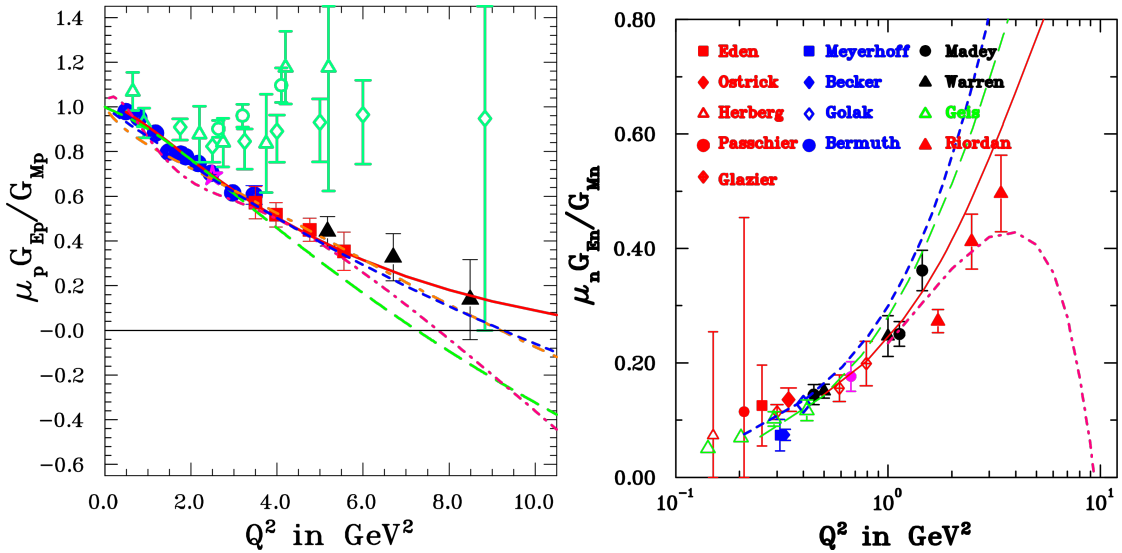


FIGURE 4.4: The collected data of the proton (left) and neutron (right) form factor ratio $\mu_p G_E/G_M$ by Perdrisat and Punjabi [124]. The data in the left figure from polarized experiments are from Refs. [120, 121] (full circles), Refs. [122, 125] (full squares), and Ref. [123] (full triangles), respectively. The data from unpolarized cross section (green symbols) are: open triangles [126], circles [127], and diamonds [128]. The theoretical predictions are given by Ref. [129] (solid red), Ref. [130] (short-dashed blue), [131] (dash-dot orange), [132] (dash green), and Ref. [133] (short dash-dot magenta). The data in the right figure for neutron FF ratio are from Refs. [134, 135, 136, 137, 138, 139] (red), Refs. [140, 141, 142, 143] (blue), and Refs. [144, 145] (black) and Ref. [146] (green).

The upgrade of JLab, doubling the maximum beam energy from 6 to 12 GeV (11 GeV Halls A, B, C, and 12 GeV Hall D) allows future experiments with polarized beams for measuring proton and neutron form factors. Indeed, several experiments

are planned at JLab to measure all four nucleon form factors up to the highest momentum: proton, neutron, electric and magnetic. For example in Hall A a new spectrometer, the Super Bigbite Spectrometer (SBS) will have a very large acceptance and a new polarimeter. This experiment is expected to reach $Q^2 = 15 \text{ GeV}^2$, and needs a large investment to guarantee a detection covering the whole focal plane, including a polarimeter that supports a large background particle rate [147].

In order to optimize the measurements, different analyzer materials at different thicknesses are being investigated. Measurements of the polarization of protons had been taken in Saclay, using the Saturne accelerator up to the available highest momentum, 3.2 GeV/c and a Carbon or a CH₂ target with different thicknesses (for more details see Ref. [148] and references therein). At larger momenta, the Dubna Synchrotron at the JINR-VBLHE (Dubna) allowed the measurements of the analyzing powers with a CH₂ target at the proton momenta $p_p = 3.8, 4.5$ and 5.3 GeV/c [149], with different target thicknesses, indicating that CH₂ provides larger analyzing powers than carbon. More precise measurements are required in the known energy region as well as their extension to higher momenta.

Polarization measurements are even more important for neutron, as the electric neutron form factor is expected to be small. The analyzing reaction has to be carefully optimized. We denote elastic scattering the reaction $np \rightarrow np$ meaning that the neutron is detected forward and charge exchange the reaction $np \rightarrow pn$ meaning that a proton is detected forward. Both reactions are considered for polarimetry. Analyzing powers strongly depend on the energy and angle of the detected particle. When the incident neutron momentum increases, it appears that analyzing powers decrease (increase) for a neutron detected forward (backward). In present work, we investigate the energy range where each reaction is more favorable. Moreover, different targets have been used as no measurement exists for heavier targets than hydrogen.

Chapter 5

Calculation of cross sections, analyzing powers, efficiency and figure of merit

The results presented in this chapter have been published in Ref. [18]. Hadron polarimetry in the GeV region is requested for modern experiments. As it will be explained in detail later, a polarization measurement consists in the measurement of the azimuthal asymmetry in a secondary scattering on a polarimeter target. Therefore the set up needs to measure precisely the incident and outgoing trajectories, in order to reconstruct the azimuthal distribution. For unpolarized particles, this distribution is flat, for polarized particles it contains an asymmetry (the left-right asymmetry is sensitive to the normal polarization, the up-down asymmetry is sensitive to transverse polarization. The longitudinal polarization can be measured only deflecting the particle in the vertical plane.) The quantity that allows to measure and compare the performance of a polarimeter is the Figure of Merit (FoM). Two ingredients need to be known:

- the polarimeter efficiency,
- the analyzing powers.

The secondary reaction (the polarimeter target as well as the detection) is chosen according to the following criteria: maximize the polarimeter efficiency and the analyzing powers. The polarimeter efficiency is defined as the number of useful events over the number of the incident events. Useful events means events issued from a reaction that carries a polarization information, i.e., very sensitive to the spin dependent terms of the interaction, that translates into large analyzing powers. For example, events issued from multiple scattering, or non-interacting events (that are the majority) do not carry polarization information.

Proton polarimetry has revealed to be a unique way to access the electric to magnetic proton form factor ratio, as the G_E/G_M ratio can be directly measured from the ratio of the transverse to longitudinal polarization of the recoil proton in the scattering of longitudinally polarized electrons [113, 114]. In particular at JLab the GEp collaboration measured this ratio up to $q^2 \simeq 8.5 \text{ GeV}^2$ ([123] and references therein)

shown in Fig. 4.4). It is planned to extend proton and neutron FF measurements up to the largest Q^2 following the 11 GeV² upgrade of the JLab accelerator. The measurement of proton analyzing powers was done by ALPOM at beam momentum 1.75 to 5.3 GeV/c [149]. In Dubna, presently, it is possible to extend this measurement to 7.5 GeV/c.

In case of neutrons, the polarization method is mandatory due to the smallness of the neutron electric FF. To study the neutron analyzing power, elastic np scattering has been used as polarizing reaction up to momenta of 3 GeV/c [150]. It appears that the neutron analyzing power becomes smaller and smaller at forward angles with increasing energy, whereas it becomes large and negative when the outgoing neutron is detected at backward angles [151]. The latter situation corresponds to charge exchange reactions and gives a new opportunity to extend neutron polarimetry to high energies. In Dubna, a neutron beam momentum up to 4.2 GeV/c is available.

The purpose of this chapter is to give an estimation of the expected FoM of a polarimeter based on the reactions:

- $n + p \rightarrow n + p$: this elastic reaction is described by t-channel exchange of a neutral pion, so it will be denoted ‘zero-exchange’, meaning zero charge exchange.
- $n + p \rightarrow p + n$: this reaction is described by t-channel exchange of a charged pion, so it will be denoted ‘charge-exchange’.

In the final channel the detected particle is written first. Note that for a neutron detected forward the diagram for zero-exchange is dominant, whereas for a proton detected forward the charge-exchange diagram is dominant. The two reactions can be considered contributing both to the cross section, and their balance depends on the scattering angle of the detected particle.

This study is based on the calculation from Ref. [152], tuned on existing data, with the aim to determine at which incident momentum elastic and charge-exchange reactions become competitive in terms of FoM.

5.1 Performance of a polarimeter

The performance of a polarimeter is expressed in terms of the total FoM square, \mathcal{F}^2 . For a given configuration, *i.e.*, target thickness and acceptance, it is defined as:

$$\mathcal{F}^2 = \int_{\theta} \varepsilon(\theta) A_y^2(\theta) d\theta, \quad (5.1)$$

where the integration is performed over the angular range where the polarimeter is efficient. In Eq. (5.1), $\varepsilon(\theta)$ is the differential efficiency of polarimeter for different processes, defined as the differential cross section for the useful reaction over the total cross section, σ_{tot} . The polarimeter efficiencies for the considered processes are

calculated from the cross sections, assuming an ideal system with 100% efficiency of detectors, as the ratio of the relevant cross section, $\sigma_i(\theta)$ over the total cross section:

$$\varepsilon(\theta) = \frac{\sigma_i(\theta)}{\sigma_{tot}}. \quad (5.2)$$

The notation $A_y(\theta)$ is used for the analyzing power, the single spin polarization observable when the beam is polarized. The total np cross section in the energy range of interest is quite constant and it is taken as $\sigma(N + N \rightarrow anything) \simeq 40$ mb. We can estimate the cross section on a CH2 target as follows:

$$\sigma_{tot}(N + CH2 \rightarrow anything) = 2\sigma(N + N) + A^{2/3}\sigma(N + N) \simeq (80 + 200) \text{ mb} = 280 \text{ mb}. \quad (5.3)$$

The statistical error on the polarization, ΔP , is related to \mathcal{F}^2 as:

$$\Delta P = \sqrt{\frac{2}{N_{inc}\mathcal{F}^2}} \quad (5.4)$$

The knowledge of FoM allows to estimate the number of incident events, N_{inc} , necessary to obtain a given error ΔP on the polarization measurement. It allows to estimate the duration of the experiment. The larger is the FoM, the shorter is the running time to get the same error on the polarization. Typically, a number of incident particle equal to 10^6 can be obtained (including 40% experimental inefficiency) with a beam intensity of 10^4 particle per second during a spill of 4 s each 10 s measuring for one hour per beam polarization state (total 3 hours). In these conditions, typical for the ALPOM2 setup, an error on the polarization equal to 0.02 can be obtained with $\mathcal{F}^2=0.0049$.

5.1.1 Kinematics of np scattering

The zero-exchange and charge-exchange reactions with four momenta in Lab and CM systems as in Fig. 5.1, are defined as:

$$\begin{aligned} n(k_1) + p(k_2) &\rightarrow n(k_3) + p(k_4) \text{ zero-exchange}, \\ n(k_1) + p(k_2) &\rightarrow p(k_4) + n(k_3) \text{ charge-exchange}. \end{aligned} \quad (5.5)$$

The Mandelstam variables are defined in terms of four momenta as:

$$\begin{aligned} t &= (k_1 - k_3)^2 = (k_2 - k_4)^2, \\ u &= (k_1 - k_4)^2 = (k_2 - k_3)^2, \\ s &= (k_1 + k_2)^2 = (k_3 + k_4)^2. \end{aligned} \quad (5.6)$$

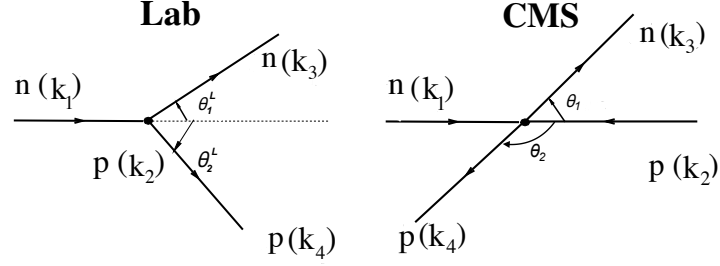


FIGURE 5.1: Scheme of the reaction $np \rightarrow np(pn)$ in Lab and CM systems.

Here we use the same mass for neutron and proton $M_n = M_p = M$. The following relation holds:

$$s + t + u = 4M^2. \quad (5.7)$$

In the Lab system, defining the kinetic energy as $T = E_L - M$, where E_L is the total energy of the incident particles ($s = 2M(E_L + M)$), we get the relations:

$$s = 4M^2 + 2TM, \quad T = \frac{s - 4M^2}{2M} = \sqrt{p_L^2 - M^2} - M. \quad (5.8)$$

Then we get:

$$\begin{aligned} E_L^2 &= p_L^2 + M^2, \\ E_L + M &= E_3 + E_4, \\ \vec{P}_L &= \vec{k}_3 + \vec{k}_4, \\ |\vec{P}_L| &= |\vec{k}_3| \cos \theta_1^L + |\vec{k}_4| \cos \theta_2^L. \end{aligned}$$

As we do not distinguish neutron and proton, and according to energy momentum conservation, no neutrons going to backward directions in the Lab system. The kinematical relation between the angles in CM and Lab systems is shown in Fig. 5.2 for different momenta: 3 GeV/c, 3.75 GeV/c, 4.2 GeV/c, 5.3 GeV/c, 7.5 GeV/c. In the legend, the transferred momentum Q^2 for eN elastic scattering necessary to obtain the same nucleon momentum is also shown. The maximum detection angle for the ALPOM2 experiment is $\theta_2^L < 17^\circ$. It corresponds to a CMS angle $\theta_2 < 49^\circ$ (70°) for beam momentum equal to 3 (7.5) GeV/c.

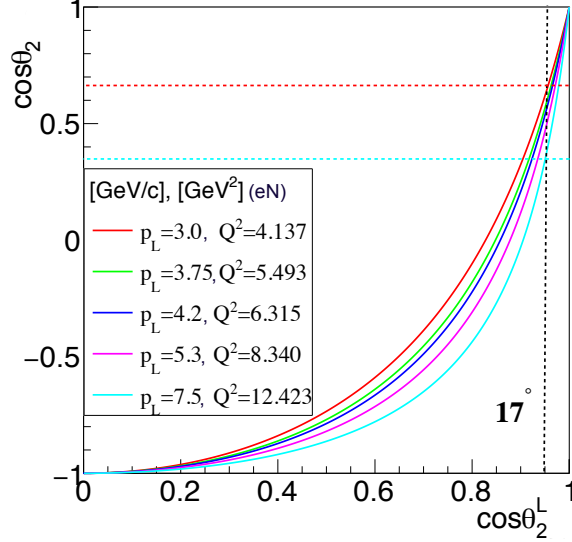


FIGURE 5.2: CMS versus Lab angle for the emitted neutron at different Lab momenta. The corresponding Q^2 for electron scattering is also indicated.

5.1.2 Angular distributions of np scattering

The pole model for $np \rightarrow np(pn)$ scattering, illustrated in Fig. 5.3, was derived in Ref. [152].

The t -dependent differential cross section is:

$$\frac{d\sigma}{dt} = \frac{1}{64\pi s q^2} (|\mathcal{M}_\pi(u) + \mathcal{M}_\rho(u)|^2 + \frac{1}{4} |\mathcal{M}_\pi(t) + \mathcal{M}_\rho(t)|^2 + |\mathcal{M}_P(t)|^2), \quad (5.9)$$

where $q^2 = s/4 - M^2$ and $\mathcal{M}_{\pi/\rho,P}$ are the amplitudes corresponding to π , ρ , and pomeron-like exchanges respectively. This formula assumes that the reaction $np \rightarrow np$ where the neutron emitted forward is predominantly driven by the diagram Fig. 5.3.a, whereas if the proton is detected forward the diagram Fig. 5.3.b dominates. As the two diagrams act in two different kinematic regions, their interferences are neglected. The matrix element square is parametrized as:

- for the charge exchange reaction, Fig. 5.3(a):

$$|\mathcal{M}_{CE}(u)|^2 = \left(F_u \frac{u A_\pi}{u - m_\pi^2} F_u \right)^2 + \left| F_u \frac{u A_\rho e^{i\varphi}}{u - m_\rho^2} F_u \right|^2 + 2 \left(F_u \frac{u A_\pi}{u - m_\pi^2} F_u \right) \left(F_u \frac{u A_\rho e^{-i\varphi}}{u - m_\rho^2} F_u \right), \quad (5.10)$$

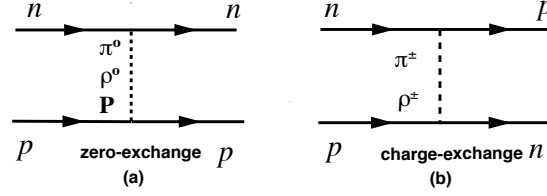


FIGURE 5.3: Feynman diagrams for the pole model of $np \rightarrow np(pn)$ scattering.

- for the elastic scattering (zero-exchange), Fig. 5.3(b):

$$|\mathcal{M}_{ZE}(t)|^2 = \frac{1}{4} \left[\left(F_t \frac{tA_\pi}{t - m_\pi^2} F_t \right)^2 + \left| F_t \frac{tA_\rho e^{i\varphi}}{t - m_\rho^2} F_t \right|^2 + 2 \left(F_t \frac{tA_\pi}{t - m_\pi^2} F_t \right) \left(F_t \frac{tA_\rho e^{-i\varphi}}{t - m_\rho^2} F_t \right) \right] + (A_P e^{-b|t|})^2, \quad (5.11)$$

A monopole form factor at each vertex has been introduced, with the replacement $t \leftrightarrow u$ corresponding to zero-exchange or charge-exchange:

$$F_t = \frac{\Lambda}{\Lambda + |t|}, \quad F_u = \frac{\Lambda}{\Lambda + |u|}, \quad (5.12)$$

where Λ is a cutoff parameter. In Ref. [152], Λ is taken equal to the nucleon mass squared as $\Lambda = M^2 = 0.88 \text{ GeV}^2$, and the masses of ρ and π mesons are, $m_\rho = 0.775 \text{ GeV}$, $m_\pi = 0.1396 \text{ GeV}$.

The s -dependent amplitudes corresponding to the exchanged particles A_ρ , A_π and the pomeron-like particle A_P are (Ref. [152]):

$$\begin{aligned} A_\pi &= -111.1 + 102.8\sqrt{s}, \quad A_\rho = -34.4 + 71.3\sqrt{s}, \quad \varphi = 0.91 + 0.44\sqrt{s}, \\ A_P &= -1008.4 + 568.0\sqrt{s}, \quad b = 3.713[1 - e^{-2.258(\sqrt{s}-1.792)}], \end{aligned} \quad (5.13)$$

where the parameters are fitted on the data as illustrated in Fig. 5.4, for zero-exchange reaction at different incident neutron beam momenta. The pole model gives a good description for all values of the beam momentum at small t , but starts to deviate at large t . In order to reproduce the charge-exchange process, we refitted the data and we found the parameters of Eq. (5.13) to be:

$$\begin{aligned} A_\pi &= 99.6 - 65.4\sqrt{s}, \quad A_\rho = -100.2 + 72.3\sqrt{s}, \quad \varphi = 0.53 + 0.52\sqrt{s}, \\ A_P &= -1408.4 + 568.0\sqrt{s}, \quad b = 10[1 - e^{-7.371(\sqrt{s}-0.076)}]. \end{aligned} \quad (5.14)$$

The results are illustrated in Fig. 5.5 for the data from charge-exchange process.

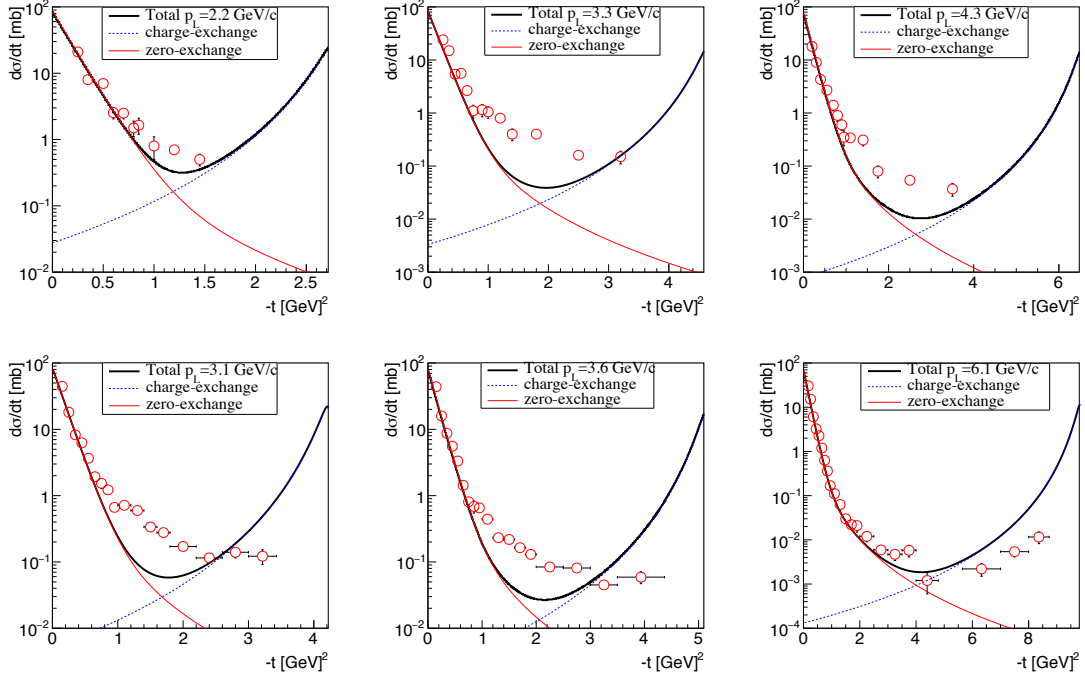


FIGURE 5.4: Top figures: data are from Ref. [153], corresponding to different incident beam momenta: $p_L=2.2$ GeV/ c (left), 3.3 GeV/ c (middle), and 4.3 GeV/ c (right). Bottom figures: data are from Ref. [154] and correspond to beam momenta: $p_L= 3.1$ GeV/ c (left), 3.6 GeV/ c (middle), 6.1 GeV/ c (right). The model prediction with Eq. (5.13) from Ref. [152], is also shown (black thick solid line) together with the zero-exchange (red solid line) and charge-exchange (blue dotted line) contributions.

The zero-exchange process is dominant at forward angles, while the charge-exchange is dominant for backward angle. This is also seen in Fig. 5.7 where the s -dependence of the cross section calculated for $t = 0$ is illustrated (left). The total cross section, integrated over all the angular range, is shown in Fig. 5.7 (right).

The plot at $t = 0$ gives larger value in a smaller p_L region compared to Fig. 5.7 of Ref. [152]. However our Fig. 5.4 shows that the model is consistent with the data at small t . Concerning the total cross section (right plot), the difference with the original paper comes from the contribution of charge-exchange reaction for $p_L \geq 6$ GeV, but from the the plot corresponding to $p_L = 6.12$ GeV, in Fig. 5.4, one can see that the calculation reproduces the experimental data fairly well. We can also see from Fig. 5.7, that, as the total cross section decreases when the momentum increases, the difference of the charge-exchange and zero-exchange contributions

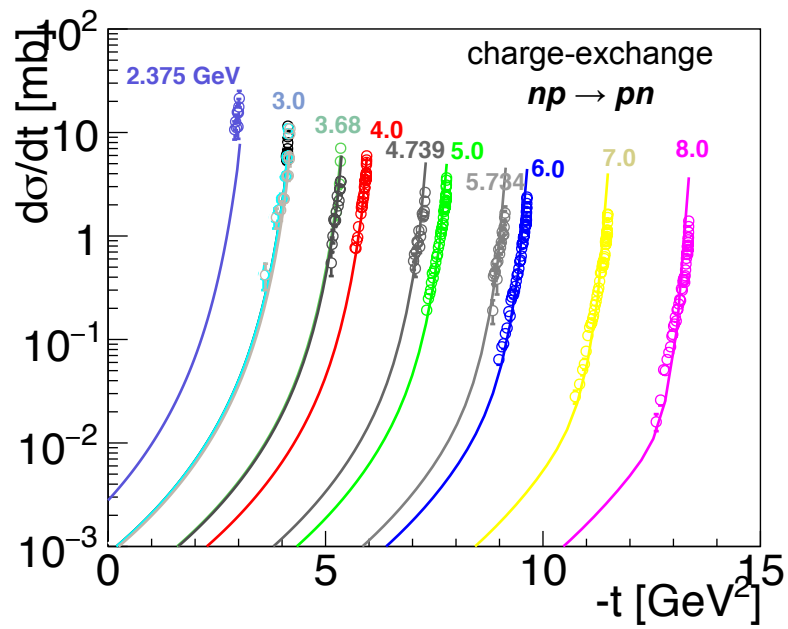


FIGURE 5.5: The differential cross sections of the charge-exchange process ($np \rightarrow pn$) at different beam momenta from 2.375 GeV/ c to 8 GeV/ c . The data are from the Refs. [155, 156, 157] and the curves are from the calculation of the pole model with refitted parameters as in Eq. (5.14).

becomes larger and larger. This means that charge-exchange reactions become far more difficult to detect than elastic scattering at high energy.

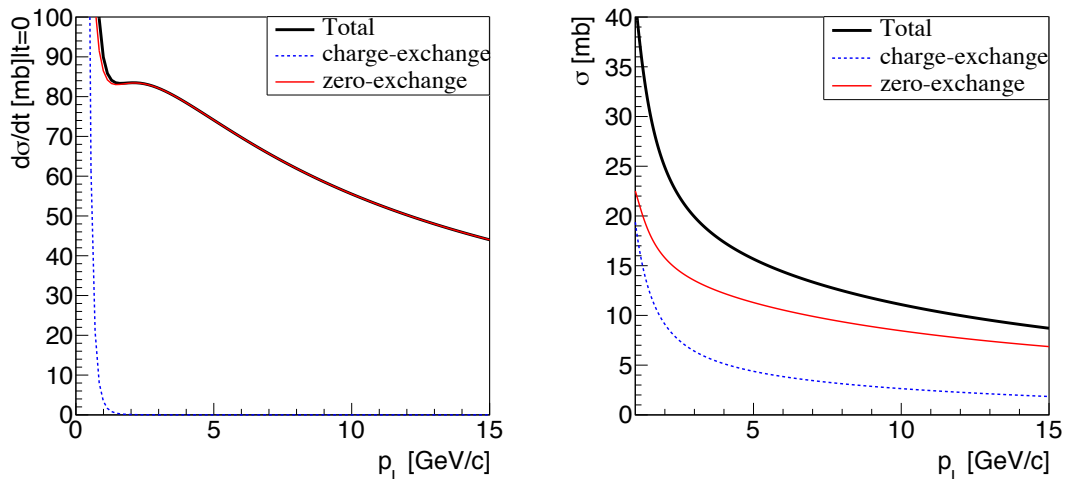


FIGURE 5.6: (Left: differential cross section as a function of p_L , according to Eq. (5.9) for $t = 0$. Ref. [152]. Right: total cross section as a function of p_L (black solid thick line), zero-exchange (thin red solid line), and charge-exchange (blue dotted line).

5.1.3 Analyzing powers

Analyzing powers have been measured in Ref. [151] for the interesting kinematical range of charge-exchange process, for neutron beam incident momenta from 2 to 12 GeV/c and neutron detection in the range $0.01 \leq |t| \leq 1.0$ GeV². We have fitted the points with a series of polynomials:

$$A_y = a(p)t + b(p)t^2 + c(p)t^3, \quad (5.15)$$

with the parameters indicated in Table 5.1. The data only cover a small range of an-

p_L [GeV/c]	a	b	c
3 ± 1	-1.964	1.910	4.749
5 ± 1	-1.60	2.122	0
7 ± 1	-2.482	4.363	-2.384
9 ± 1	-2.086	1.846	0
11 ± 1	-2.627	9.161	5.251

TABLE 5.1: Parameters of Eq. (5.15) for the charge-exchange process illustrated in Fig. 5.7.

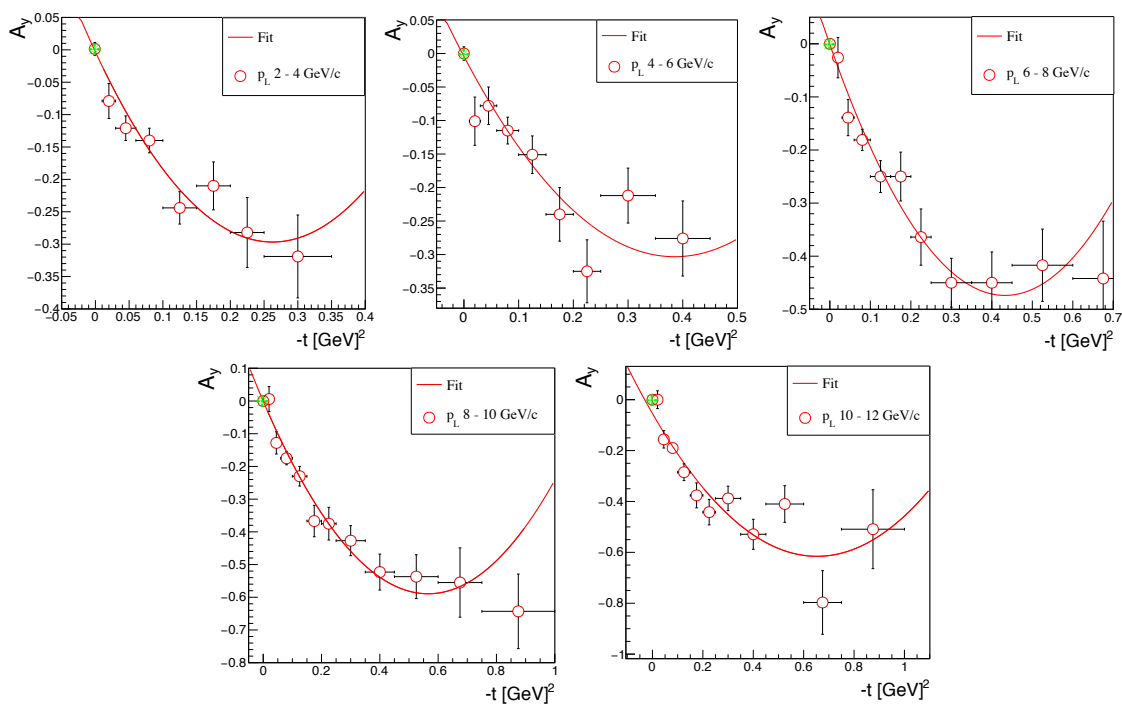


FIGURE 5.7: Data (red symbols) of analyzing powers for the charge-exchange process ($np \rightarrow pn$) is from Ref. [151]. The red curves are fitted to the data following Eq. (5.15 and a green asterisk is added to constrain the function passing through zero at zero. The parameters are listed in Table 5.1.

p_L [GeV/c]	a	b	c
2	2.861	-8.161	6.209
3	1.047	-2.374	1.345
4	6.129	-1.097	3.252
6	2.879	-7.448	3.885

TABLE 5.2: The parameters for zero-exchange process of Eq. (5.15) corresponding to the data in Fig. 5.8.

charge-exchange	$y = 0.141 + 0.045x$
zero-exchange	$y = 0.365 - 0.061x$

TABLE 5.3: Zero-exchange and charge-exchange functions corresponding to Fig. 5.9.

gles. From these data at the same t value, with the incident momentum increasing, the absolute value of the analyzing power of charge-exchange process increases. Analyzing powers for the zero-exchange process can be found in Ref. [158, 159]. They are plotted in Fig. 5.8 where the lines are the results from Eq. (5.15) with parameters as in Table 5.2. Differently from charge-exchange, when the momentum increases, the analyzing power shows a decreasing behaviour.

To compare the analyzing powers of charge-exchange and zero-exchange reactions, in Fig. 5.9 we plot the maximum absolute value of the analyzing powers as a function of the incident momentum, and assume a linear function to extrapolate to the higher momentum region. The results have to be considered upper limits. With increasing momentum, the maximum analyzing powers for zero-exchange and charge-exchange have an opposite behavior. While the zero-exchange analyzing power decreases with increasing momentum, the charge-exchange analyzing power increases, which may compensate the cross section contribution of the charge-exchange reaction.

5.2 Calculation of polarimeter efficiency and maximum figure of merit

We define the maximum differential FoM squared ($\mathcal{F}_{(Max)}$) (for charge-exchange and zero-exchange reactions) as:

$$\mathcal{F}_{(Max)}^2 = \int_{\theta=0^\circ}^{\theta=17^\circ} A_{y_{(Max)}}^2 \cdot \varepsilon(\theta) d\theta. \quad (5.16)$$

We calculate the integrated FoM (see Fig. 5.10) for the angular acceptance of

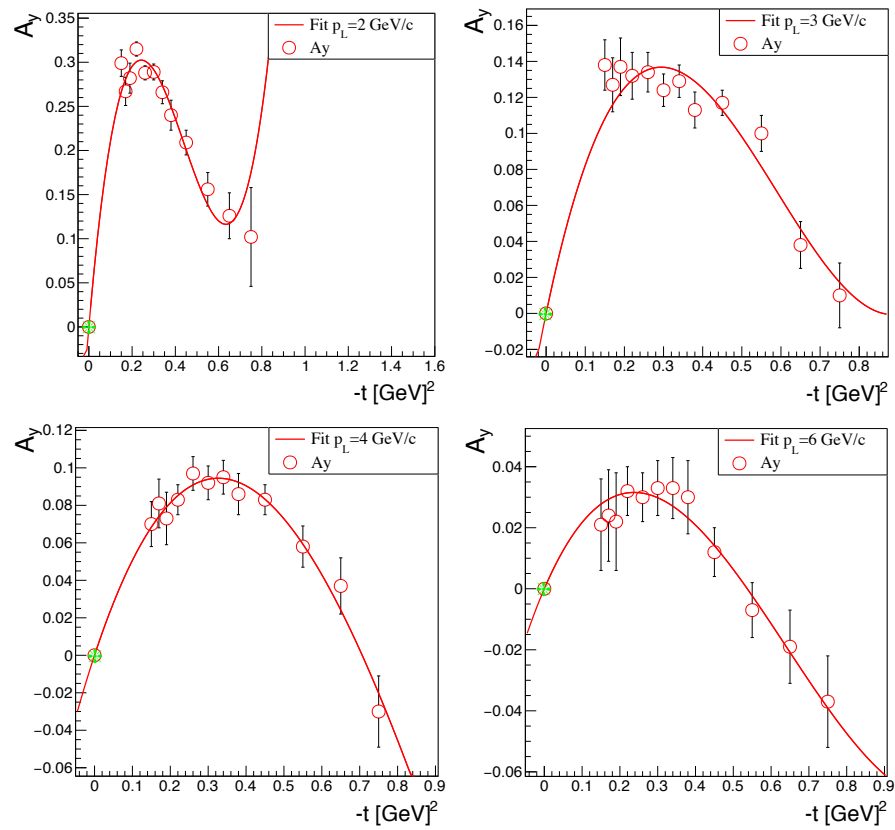


FIGURE 5.8: Data (red symbols) of analyzing powers for the zero-exchange process ($np \rightarrow np$) is from Ref. [160]. The red curves are fitted to the data following Eq. (5.15) and a green asterisk is added to constrain the function passing through zero at zero. The parameters are listed in Table 5.2.

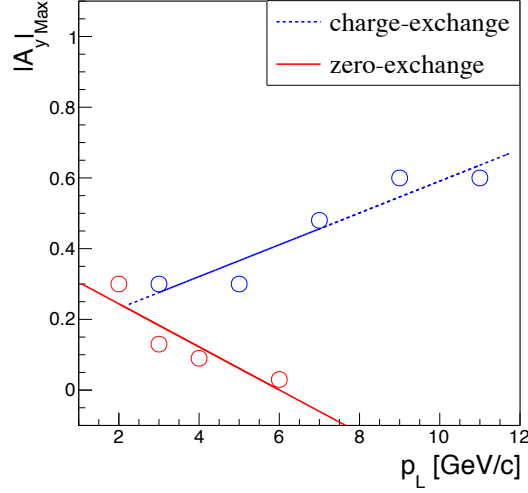


FIGURE 5.9: $|A_y|_{Max}$ for $np \rightarrow np(pn)$ based on the polarization data from charge-exchange (blue dotted line) from Ref. [151] and zero-exchange (red solid line) from Ref. [160] with the parameters as in Table 5.3.

ALPOM2 within 17° in Lab. As discussed above, the cross section of both reactions decreases with increasing momentum, but charge-exchange is less probable than zero-exchange in the low momentum region, and the analyzing powers can not compensate this effect. So, in this momentum region, zero-exchange has larger FoM. For p_L larger than 4.8 GeV/c, the analyzing power has a more important role compared to the cross section. Then, the charge-exchange reaction gives larger FoM, which is more effective for polarimetry. For the same running time, the measurement will be more precise, having smaller errors. In Fig. 5.10 the red empty circles are reported from the MonteCarlo simulation of JLab proposal PR-09-006 [161].

Quantitatively, for ALPOM2, at momenta of 3.75 GeV and higher, with number of incident particle $\geq 10^6$, the uncertainty of the polarization (ΔP) can be estimated to 0.045 (zero-exchange) and 0.030 (charge-exchange), in spite of the fact that the total cross section for zero-exchange is larger than for charge-exchange. With increasing beam momentum, FoM of zero-exchange decreases dramatically while charge-exchange stays about constant, then the charge-exchange becomes preferable, under the present assumptions of an ideal experimental environment. However our calculation is reliable for elastic scattering only up to 6 GeV/c, as elastic analyzing powers have been measured only up to 6 GeV/c.

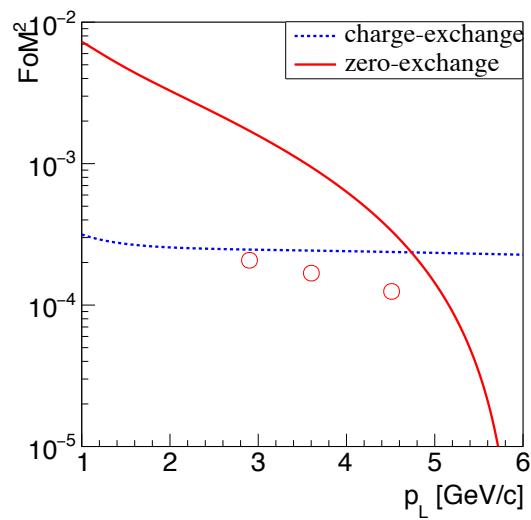


FIGURE 5.10: Integrated FoM for $np \rightarrow np(pn)$ based on the fitted result from Fig. 5.9 (upper limit) for charge-exchange (blue dotted line) and zero-exchange (red solid line). The red empty circles are calculated from the MonteCarlo simulation of JLab proposal PR-09-006 [161].

Chapter 6

The ALPOM2 Experiment at Nuclotron accelerator of the Joint Institute for Nuclear Research

6.1 Introduction

This chapter describes the experiment ALPOM2 that takes place at the Nuclotron complex accelerator of the Joint Institute for Nuclear Research in Dubna and aims to measure analyzing powers for protons and neutrons useful for polarimetry in the GeV energy range. After a brief discussion of the JINR and its history, and a brief focus on a major project in high energy physics that is under construction, NICA, I'll describe the experimental setup starting from the polarized deuteron source put in operation for this experiment, the different elements of ALPOM2, the data taking procedure as well as the data analysis. My participation includes help in the preparation of the experiment, in data taking, and in the analysis and interpretation of the data. Moreover, as shown above, I collected existing data and predicted, with the help of a pole model, the cross section and the analyzing power for elastic and charge exchange neutron-proton reactions. The analyzing powers measured in this experiment will be very useful for electron scattering experiments planned at Jefferson Laboratory to measure proton and neutron electromagnetic form factors.

6.2 Short presentation of the Joint Institute for Nuclear Research

This historical introduction is aimed to describe the laboratory where the experiment took place. I want to stress two aspects: the discoveries and the role that the institute played since its foundation, and the present availability of the polarized deuteron beam up to 13 GeV. This beam is unique in the world, and it is necessary for the experiment described here. The opportunity of the deuteron beam is results from the funding of a major project, the NICA project, which is supposed to gather large parts of the physics community in next future.

Dubna, as well as the JINR were built at the end of the World War II. The aim of the institute, when it was established, was -similarly to CERN- to federate the scientific and material potentials of the Member States for investigations of the fundamental properties of matter. JINR consists of eight laboratories, including the largest theoretical institute in the world, the Bogoliubov Laboratory of Theoretical Physics (BLTP), the Veksler and Baldin Laboratory of High Energies (VBLHE) where our experiment is performed, and a University centre.

Nowadays, the main activities of JINR are theoretical and experimental studies in elementary particle physics, nuclear physics, condensed matter physics, biology and computing technologies. The research policy of JINR is advised by the Scientific Council, which consists of eminent scientists from 18 Member States as well as known researchers from world institutions. More than 800 scientific centers and universities in 62 countries are involved in collaborative work. Since the Institute was built, many important discoveries were recognized in different fields of physics. I mention few of them:

- Discovery of super-heavy elements with atomic mass 262. A team from JINR first reported to have produced this element, later baptized Dubnium in 1967. In 1970, the Russian team together with a team from Lawrence Berkeley National Laboratory confirmed the discovery [162]. The existence of four new elements was confirmed in January 2016 and they were named Nihonium, Moscovium, Tennessine and Oganesson.
- High energy neutron pairs exchange (1998) [163]: Observation of two-neutron exchange in the ${}^6\text{He} + {}^4\text{He}$ reaction, searching for the "di-neutron" configuration of ${}^6\text{He}$.
- World recognized advances in ultra-cold neutrons (1975) [164].
- Quark counting rules in QCD (1973) [21].

Among the outstanding personalities who spent most of their career in Dubna and are well known, we can mention Bruno Pontecorvo, N.N. Bogolyubov and A. M. Baldin, who is the founder of the Nuclotron accelerator.

The NICA project

The NICA project [165] (see Fig. 6.2) includes the upgraded accelerator Nuclotron, that will provide variety of beam species ranging from protons and polarized deuterons to very massive gold ions. Two collision points in a new ring are foreseen at NICA: one for heavy-ion studies with the MultiPurpose detector (MPD) detector and another one for polarized beams for the Spin Physics Detector (SPD) experiment.

The accelerated beams and their characteristics are as follows:

- Polarized proton $p\uparrow p\uparrow$ at $\sqrt{s_{pp}}=12 \div 27$ GeV (5 \div 12.6 GeV kinetic energy).
- Polarized deuteron $d\uparrow d\uparrow$ at $\sqrt{s_{NN}}=4 \div 13$ GeV (2 \div 5.5 GeV kinetic energy).
- Heavy ions will be accelerated up to kinetic energy of 4.5 GeV per nucleon.
- The average luminosity will be $L_{average} \approx 1 \times 10^{32} \text{ cm}^{-2}\text{s}^{-1}$.

To accelerate polarized beams (proton and deuteron) the following elements of the collider will be operated:

- SPI (Polarized ion source) \rightarrow LU - 20 (light ion linear accelerator) \rightarrow Nuclotron \rightarrow NICA collider.

Out of the Linac, the injection energy for the protons is 20 MeV and for the deuteron is 5 MeV/ u [166].

The accelerated polarized deuterons, $d\uparrow$ can reach up to 5.6 GeV/ u without undergoing depolarization by spin resonances in the ring. They have been produced in the past by the Synchrophasotron with the polarized source POLARIS (the first depolarizing resonance is above 10 GeV/ c momentum). Polarized proton beams $p\uparrow$, can not be accelerated due to depolarizing resonances, but polarized proton and neutron beams have been obtained from deuteron break-up. To produce $p\uparrow$ beams up to 13.5 GeV, it will be necessary to add a dynamic solenoid (Siberian Snake) in the Nuclotron, to accelerate the protons first up to 5 - 6 GeV, then to transfer them to the collider ring for storage and stochastic cooling to be accelerated up to 13.5 GeV. The critical field of the Nuclotron magnet is $B = 2$ T, with $dB/dt = 4$ T/s. The physics of the NICA project is based on the search for a particular state of nuclear matter, the 'mixed phase', Fig. 6.1. The suggestions for the physical program are collected in a white physics book, based on the contributions of the world community [165]. They investigate fundamental physics problems:

- The strong interaction between the elementary constituents (quarks and gluons) within the Standard Model;
- Phase transition between hadronic matter, QGP, and new phases of baryonic matter;
- Basic properties of vacuum and QCD symmetries in strong interactions.

The specificity of NICA is to access a region of the phase diagram with high density and low temperature where quarks, meson and baryons are predicted to coexist. Moreover, it will be a unique world facility for polarized particles and light ions in the GeV range.

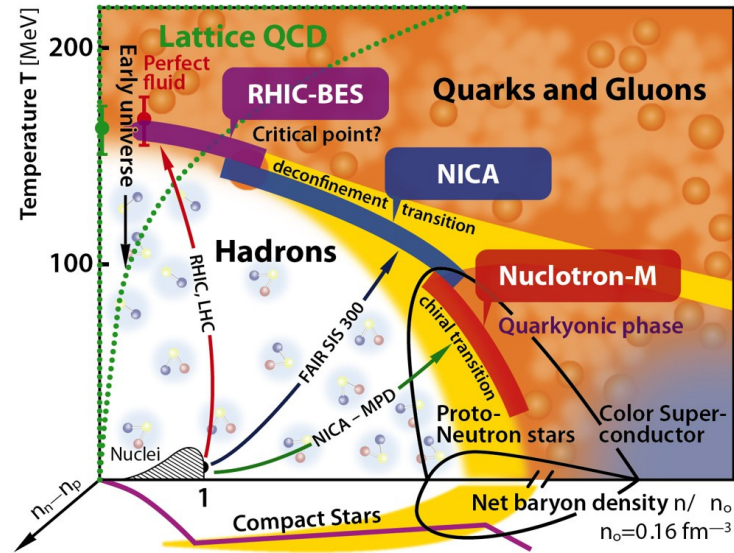


FIGURE 6.1: Physics region, in the plane Temperature as a function of the baryon density, explored at the Nuclotron-based Ion Collider facility (NICA Complex).

6.3 Description of the experiment

The experiment ALPOM2 follows the upgrade of ALPOM [149], which was a polarimeter located on the ALPHA beam line of the Nuclotron accelerator. ALPOM was built as the upgrade of part of the POMME polarimeter moved from Saclay, after closing Saturne (1997) [167].

The main goal of the ALPOM2 experiment is to measure analyzing powers for neutron and proton induced reactions in the GeV energy range in view of optimizing polarimetry for experiments in hadron and electromagnetic physics. For protons, it is planned to measure the reaction $\vec{p} + CH_2 \rightarrow \text{one charge particle} + X$ using a polarized proton beam at momentum 5.3 GeV/c and 7.5 GeV/c on a target with high hydrogen content: CH₂. For neutrons, beam momenta of 3.0, 3.75, 4.2 and 5.3 GeV/c, and a CH and/or an active scintillator target are used and the relevant reactions are elastic scattering and charge exchange.

Polarized neutron and proton beams are produced from the breakup of polarized deuterons after the acceleration and extraction from the Nuclotron accelerator. The beams hit the polarimeter target and the outgoing particles are detected. Their azimuthal distributions for each beam polarization state are analyzed. The asymmetry is directly related to the product of the analyzing powers (that are extracted) and the beam polarization that is measured in a dedicated polarimeter.

Before the main beam time, two test runs have been done to check the quality of the beam, the beam line and the setup. The first test run of the ALPOM2 experiment

was done in February 2015. At that time only unpolarized beam was available. This allowed to tune the beam line at the relevant momenta, to study the efficiency of the apparatus, the acceptable counting rates, as well as eventual experimental asymmetries. The second test run was done in June 2016, as a commissioning of the new polarized source and of the injection beam line. In November 2016 a polarized proton beam up to 4.2 GeV/c and a neutron beam up to 4.2 GeV/c were available. The experiment received 2 weeks of data taking. The information on the experimental runs is summarized in Table 6.1 and in Table 6.2, which include the details of the beam types, running time, beam momentum, and the information on the target.

Date	Nucleon kinetic energy [GeV]	beam on target (p_L) [GeV/c]	target [cm]
2015.02.16 unpolarized	2.94	$p_D = 7.5 \text{ GeV}/c$ $p_N = 3.75$ $p_P = 3.75$	CH, 6 x 5 CH2, 20-40
2015.02.25 unpolarized	5.15	$p_{N,P} = 6 - 7.2$	CH2, 40
2016.06.25-27 unpolarized	2.94	$p_P = 3.75$ $p_N = 3.75$	CH2, CH, p CH
2016.11.19-30 polarized	2.20	$p_{P,N} = 3.0$	CH2 30 - 40
	2.94	$p_{P,N} = 3.75$	CH2, C 30
	3.36	$p_{P,N} = 4.2$	CH 6 x 5
2017.02.24-27 polarized	2.94	$p_{P,N} = 3.75$	CH2, C 30, Cu

TABLE 6.1: Information on the runs of the ALPOM2 experiment: running time, the beam kinetic energy, the beam type, the beam momentum, and the nature of the target.

6.3.1 The experimental setup

6.3.1.1 The beam

Essential to the experiment are the polarized proton and neutron beams. They are produced from the breakup of a deuteron beam produced from the Cooler Injector Polarized IOn Source (CIPIOS), preaccelerated in a potential of 100-150 keV LU-20 injector, and accelerated by the Nuclotron (See Fig. 6.2).

The source of polarized deuterons - CIPIOS

The polarized deuterons necessary for the ALPOM2 experiment are produced from a new source called CIPIOS, received from Bloomington (Indiana, USA) and

run No. Nov. 2016	Target	proton [GeV/c]	neutron [GeV/c]
38-47	CH2	3.75	
50-57	CH2	3.75	
58-67	CH2		3.75
68-84	C		3.75
85-98	CH2		3.75
100-138	CH		3.75
140-159	CH2		3.75
164-176	CH2	3.0	
177-197	CH2		3.0
199-213	CH2	4.2	
214-228	C	4.2	
229-251	CH2		4.2
Feb. 2017			
5-10	CH2	3.75	
39-45	CH2	3.75	
55-61	CH2	3.75	
62-65	Cu	3.75	
66-76	C	3.75	
77-78	C		3.75
80-86	Cu		3.75
88-98	CH2		3.75
99-112	Cu	3.75	

TABLE 6.2: Detailed information for the runs in 19-31 November 2016 and 24-27 February 2017: the run number, the target, the beam type and its momentum.

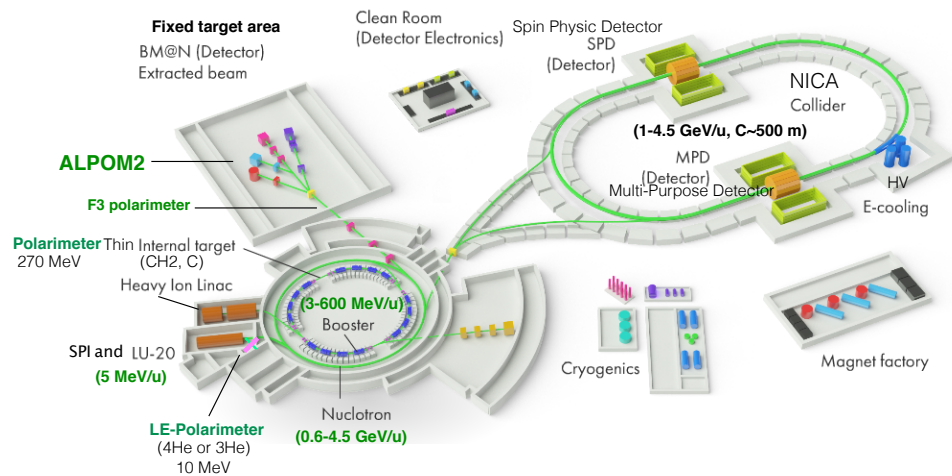
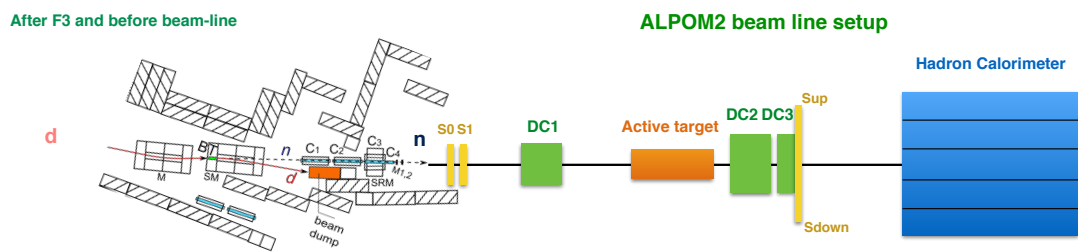


FIGURE 6.2: The ALPOM2 setup at Nuclotron for polarized neutron experiment.

recently upgraded. The existing source of polarized deuterons (0.4 mA D^+ cryogenic source POLARIS) cannot satisfy the requirements of intensity and polarization. CIPIOS is a pulsed, cold nozzle atomic beam polarized ion source with a plasma (H, D) charge-exchange ionizer.

Polarization Method

The principle to polarize particles through adiabatic transitions between two hyperfine structure levels was established by A. Abragam [168, 169]. The Hamiltonian of the system can be decomposed in three parts: the kinetic energy, potential energy, and the angular kinetic energy. For deuteron atoms, the angular kinetic part induces six hyperfine structure states. The quantum numbers of the molecular deuterium (F), of the electron angular momentum (J) and of the naked deuteron atom angular momentum (I) are illustrated in Fig. 6.3, together with the substates, as a function of the magnetic field. They can be separated by applying different strengths of the magnetic field. In a radially-symmetric magnetic field B , increasing with the distance in the perpendicular direction with respect to the beam line, the deuteron energy of the $m_J = +1/2$ states increases, so the particles feel a focusing strength towards the beam line. On the opposite, the deuterons in the $m_J = -1/2$ states are pushed away from the beam line direction.

The Atomic Beam Source (ABS), Fig. 6.4, provides high-intensity beams of hydrogen or deuterium atoms with high degree of polarization [170]. The different elements are described here:

1. Dissociator: the dissociator breaks-up the chemical bond of deuterium molecules to produce deuteron atoms.

2. Cooler: the nozzle cooler to cool down the newly produced deuteron atoms. The cooling system for atomic beams is called the cryo-cooler.

3. 1st set of permanent Sextupoles: it is a set of radially-symmetric $|B|$ strength magnets (see Fig. 6.5). The magnetic field is $|B| = B_m (\frac{r}{r_m})^2$. As shown in Fig. 6.3, the energies of deuteron atoms in the six different states are separated into two groups. The atoms with electron spin $m_J = -1/2$ will be stripped away from the axis of beam direction. On the contrary, the atoms of state $m_J = +1/2$ will be focused to the beam line. Finally the three ($m_J = +1/2$) states are selected out of six.

4. Radio-frequency transition units: three units of different frequencies (Table. 6.3) can transfer the three ($m_J = +1/2$) states to the deuteron tensor or vector polarization states with different frequency.

5. 2nd sextupoles: a conventional electromagnet sextupole is set as an analyzing device to tune the states. Then the positive hydrogen and the neutrally polarized deuteron meet up at the resonant charge-exchange ionizer (the polarized ions are formed at resonant charge-exchange of the polarized atoms and unpolarized ions in plasma).

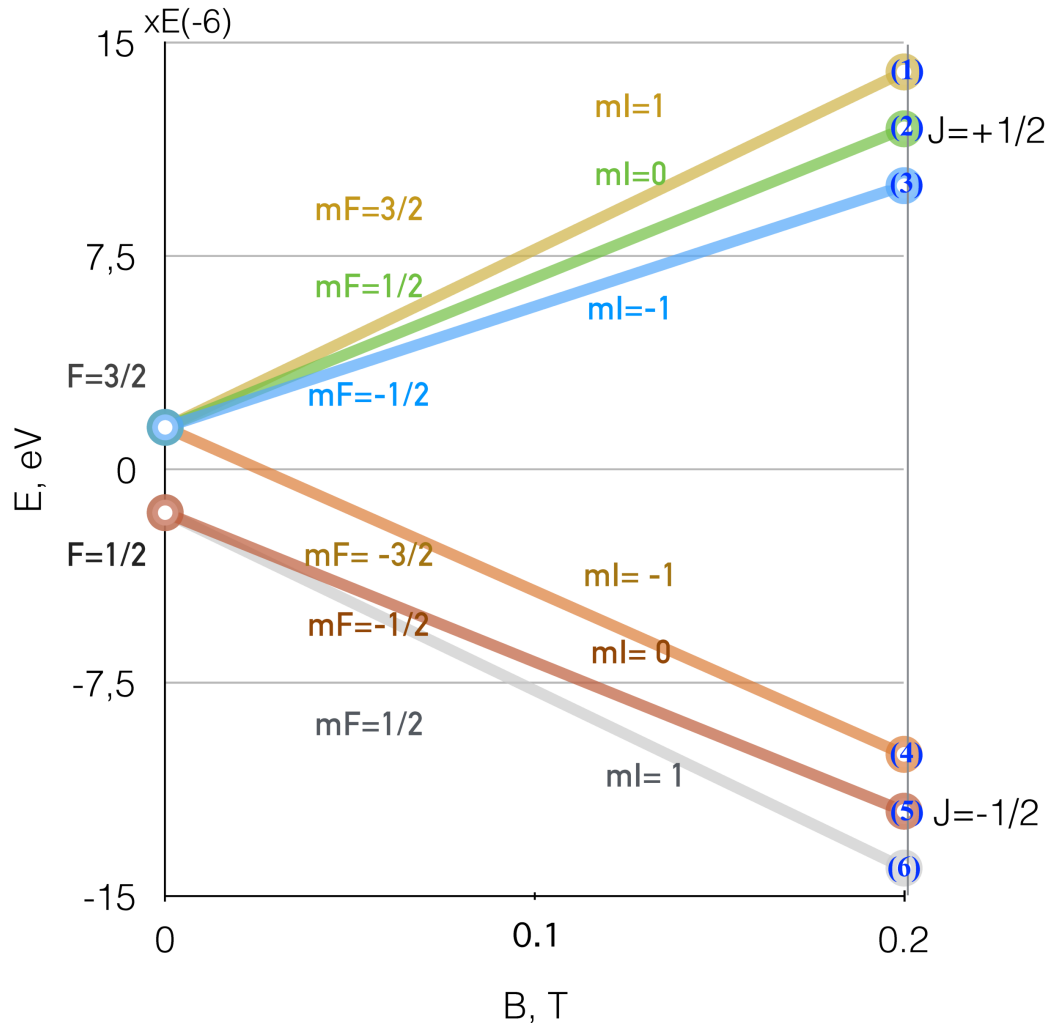


FIGURE 6.3: Quantum numbers of hyperfine structure of deuterium. The quantum numbers of molecular deuterium, electron angular momentum, and the naked deuterium atom angular momentum are presented as F , J and I .

Frequency	m_J	m_I		m_J	m_I
10.8 Hz	1/2	+1	(1) → (4)	-1/2	-1
	1/2	0	(2) → (3)	1/2	-1
	-1/2	0	(5) → (6)	-1/2	1
343 Hz	1/2	0	(2) → (5)	-1/2	0
	1/2	-1	(3) → (6)	-1/2	1
415 Hz	1/2	0	(2) → (6)	-1/2	1

TABLE 6.3: RF units frequency to transfer the atoms states.

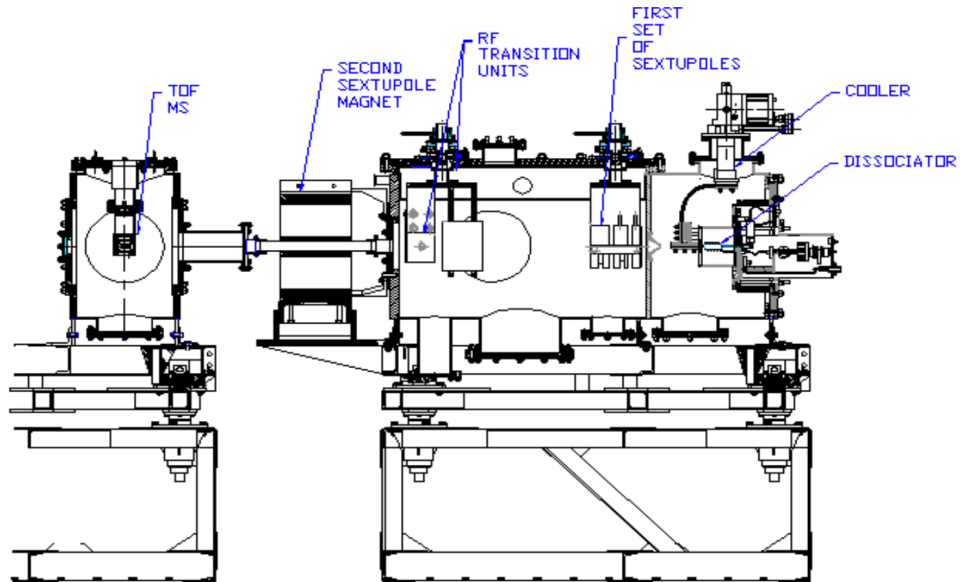


FIGURE 6.4: Layout of the ABS (Atomic Beam Source) : pulsed dissociator, beam cooler, sextupoles magnets for focusing, RF (radio-frequency) transition units for polarization, and TOF (time of flight), MS (mass spectrum) from Ref. [170].

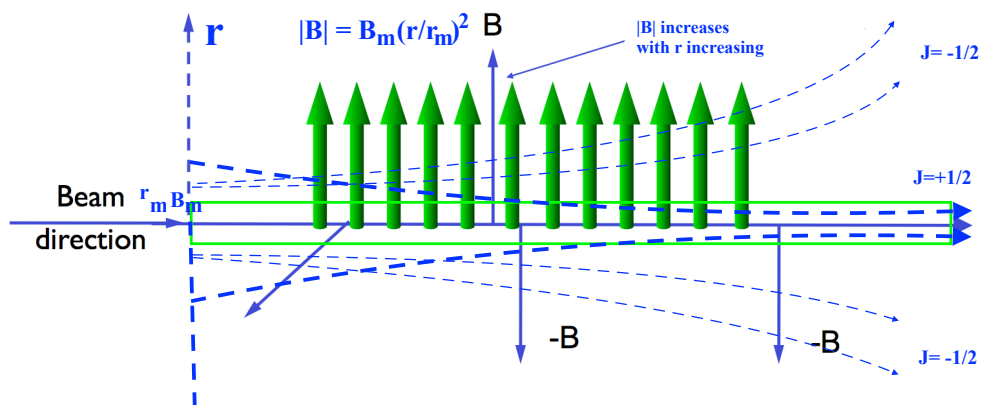
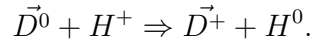


FIGURE 6.5: Scheme of the radial-symmetric magnetic sextupole that selects atoms by electron spin state. The magnetic field $|B|$ increases with r increasing, and r_m is the radius of minimum $|B_m|$.

The positive polarized deuteron particles of CIPIOS are produced through the process:



The CIPIOS source is expected to produce high-quality polarized deuteron beams with intensity 10 mA and energy up to 5 GeV/u. The maximal values of the vector (+1,-1) and tensor (+1,-2) polarizations will be approached. It is planned to increase the beam intensity up to 10^{10} deuterons/pulse after the first stage of operation. In order to increase intensity of polarized beams of D^+ and H^+ , reducing the background current of the H_2^+ ions, a storage cell will be used.

Negatively charged polarized deuterons are also planned to be produced in order to enhance the beam intensity. It can be expected only after the stripping injection to be developed.

Modernized linac LU-20

After SPI, an Alvarez-type DTL (drift-tube linac) linear accelerator LU-20 [166] is used as an injector for the Nuclotron. It was first built as a proton injector for the Synchrotron with output energy of 20 MeV in 1974. Now it is operated as an injector of light ions, polarized protons and deuterons of 20 MeV energy and 5 MeV/u energy, respectively.

Along the beam direction, the LU-20 consists in a pre-injector, a buncher, a resonator, a debuncher, followed by the transport channel.

1. A high voltage electrostatic pre-injector with uniformly space quadrupole focusing has been designed, manufactured and successfully launched in May 2016 [171]. It allows to decrease the potential in the high-voltage platform to minimize the beam losses on the residual gas. It provides proton and light ion beam acceleration at currents up to 10 mA up to energy 150 KeV/nucleon with the subsequent injection to the existing linac LU-20 and the Nuclotron.

2. Buncher: increases the accelerated beam intensity.

3. LU-20 resonator: is the main part to accelerate the beam prior to the main ring.

4. Debuncher: is used to decrease the dispersion of the beam before the injection into Nuclotron.

5. Transport channels with bending magnets are added to change the beam direction. Vertically polarized beams are injected to the Nuclotron.

Later on it is planned to replace LU-20 by a new superconducting linac accelerator [172]. The new accelerator is expected to reach the energy 25 MeV for protons and up to 7.5 MeV/u for deuterium. It usually uses RF cavities to charge the cylindrical conductor. The conductor should change the charge positive and negative alternately, in order to increase the velocity of the particles. The solenoids or quadrupoles magnets will be located between cavities to focus the beam. Unlike the old LU-20, the superconducting cavities will be phase independent within the allowed phase slipping value.

The Nuclotron accelerator The Nuclotron, a superconducting synchrotron, was constructed during the years 1987-1992, to accelerate light nuclei and multi-charged heavy ions [173].

The principle of the synchrotron is a time variation of the magnetic field strength based on the circulation time of the charged particles, avoiding beam energy losses, in order to accelerate the particles in the same ring. It usually has two separated parts, the injection and the booster. It is composed of radio frequency cavities for direct acceleration, dipole magnets (bending magnets) for deflection of particles (to close the path), and quadrupole / sextupole magnets for beam focusing.

The perimeter of the accelerator is 251.5 m. The ring comprises 96 dipole magnets (1.5 m long), 64 quadrupole lenses (0.45 m long), 28 multipole correctors (0.31 m long) with 3 or 4 types of windings in each, twelve 6 kA helium-cooled current leads, 234 leads of 100 A current for correcting windings and special-purpose magnets, 32 special units for beam injection, acceleration, diagnostics, and extraction, and also about 600 sensors of cryogenic temperatures.

The main parameters of the Nuclotron are listed in the Table 6.4 [173].

Parameters	Designed	Obtained
Accelerated particles	$1 < Z < 92$	$1 < Z < 36$
Energy, GeV/amu	6 (A/Z=2)	4.2
Magnetic field, B	2.0	1.5
Injection energy, MeV/amu	5	5
Vacuum pressure, Torr	$1 \cdot 10^{-10}$	$1 \cdot 10^{-10}$
Repetition rate, Hz	0.5	0.2
Velocity of the field increase, Tl/s stand testing	4	4.1
in the ring	2	1.0
Intensity (d \uparrow)	$3 \cdot 10^{10}$	$3 \cdot 10^7$

TABLE 6.4: The main parameters of Nuclotron.

6.3.1.2 On-line beam polarimeters

The accurate measurement of the beam polarization is very important, as its value will be directly used in the extraction the analyzing power in ALPOM2. The error on the beam polarization is the main source of the systematic error on the analyzing power.

The polarized beam is tagged with its three polarization states, up (plus, +), down (minus, -), and unpolarized (zero, 0). As we are interested in proton and neutron (spin 1/2 particles) analyzing power, we consider only vector polarized deuterons.

Several beam polarimeters are set along the beam line in order to measure the deuteron beam polarization and to control the eventual depolarization during the transmission and the acceleration.

A low energy polarimeter at the exit of the source has measured deuteron vector and tensor polarization at energy of 10 MeV in 2016 [174].

During the acceleration, at the internal target station, a polarimeter, based on d, p elastic scattering can be used [175]. It can not be used during the run, as it needs a specific beam focussing.

During the ALPOM2 experiment, mainly the high energy polarimeter F3 (Fig. 6.6) was used, as the information can be recorded on line, for each beam burst, and collected together with the data, insuring a continuous relative monitoring of the beam polarization.

F3 is an on-line beam polarimeter to monitor the vector polarization of the deuteron beam after the accelerator and before the breakup target. The measurement of the vector deuteron polarization is based on the asymmetry of the quasi-elastic pp reaction with vector beam polarization [176]. The scattered and recoil particles from the reaction on hydrogen in a polyethylene (CH₂) or carbon targets are measured symmetrically in left and right arms. The layout of the F3 polarimeter is shown in Fig.

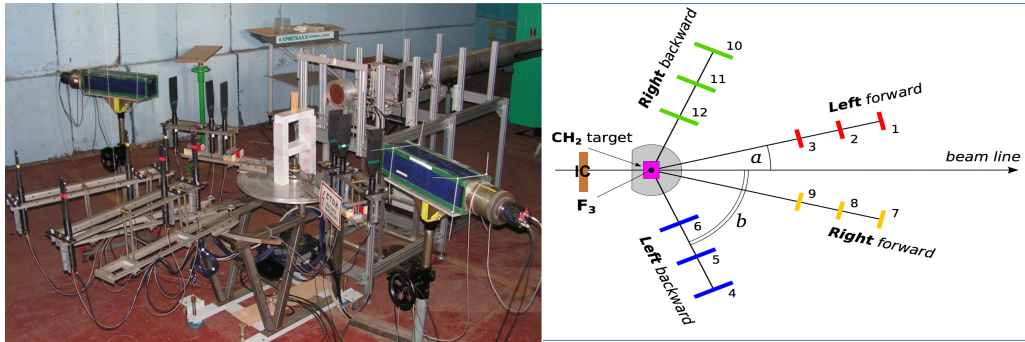


FIGURE 6.6: The F3 polarimeter (courtesy of Shindin Roman). IC is an ionization chamber. The F3 left, right forward and backward arms have three scintillation counters at the angles a and b with respect to the beam-line.

6.6. An ionization chamber (IC) is set as a beam intensity monitor for normalization. F3 has two arms, left and right. Each arm has three sets of scintillator counters at $\theta=10.8^\circ$ with respect to the beam-line, and a bigger size scintillator at $\theta=60^\circ$. A coincidence between the two arms and IC is also used as a trigger of the data acquisition system. The counting rates (N_L^\pm and N_R^\pm) of the scattered particles are recorded by the left and right arms. The numbers of events are related to the beam polarization P and analyzing power A by:

$$\begin{aligned} N_L^\pm &= N_L^0(1 + P^\pm \cdot A(\cos \theta)), \\ N_R^\pm &= N_R^0(1 - P^\pm \cdot A(\cos \theta)). \end{aligned}$$

The superscript \pm is corresponding to the beam polarization states “+1” and “-1”. The analyzing power depends on the amplitudes of the reaction, which, in turn, depends on incident energy and scattering angles. The detectors should be set at the angles where the analyzing power of pp elastic scattering for a given energy is maximum. The relation between the maximum analyzing power and the angle at high momentum (1.45 - 4.5 GeV/ c) can be found from a summary of previous experiments [177], and parameterized into a simple function,

$$A(p_L, t) = a \cdot \sqrt{-t} \cdot (1 + b \cdot t + c \cdot t^2), \quad (6.1)$$

where a , b , and c are functions of the beam momentum with parameters fitted from data (detail in Ref. [176]), and t is the Mandelstam variable. According to the func-

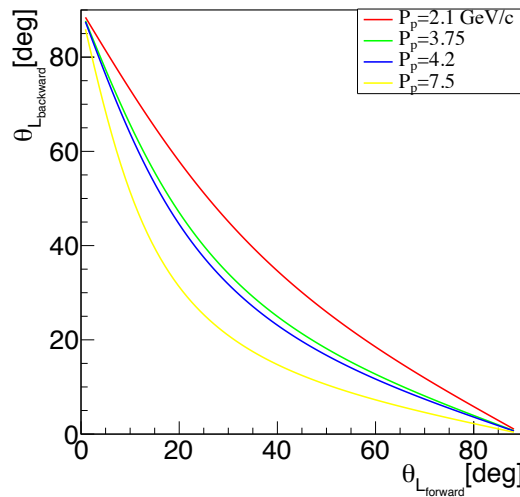


FIGURE 6.7: Correlated angles for the emitted and recoil particles in pp quasi-elastic scattering at the relevant proton momenta: 2.1, 3.75, 4.2 and 7.5 GeV/ c .

tion (Eq. 6.1), adjusted to the experimental data, the maximum analyzing power for a proton momentum in the range 2-6 GeV/ c is around 10° , changing slightly with increasing momentum. So the forward scintillator counters are set at about 10° . The scintillator detecting the recoil particle in coincident is set at around 60° , that is the corresponding angle from the pp elastic kinematic, as shown in Fig. 6.7, in order to maximize the coincidence counting rate.

The largest analyzing power and angles at each momentum can be known from previous experiments [178]. From the counting rates of the detectors, we derive with the help of Eq. (6.1) the polarization of the d , (and consequently of the n , p) beams. We assume pp elastic scattering, after correction for the carbon content of the target, and 100% transfer of polarization from the deuteron to the proton or neutron.

6.3.1.3 Deuteron breakup

The deuteron beam undergoes a breakup reaction in a 25(30) cm thick CH₂(C) target for protons(neutrons), installed upstream of the ALPOM2 polarimeter separately. The protons and neutrons produced by the deuteron breakup reaction have the same polarization as the deuteron beam as shown in Fig. 6.8 when the momentum is half of the deuteron beam momentum. The breakup reactions are

$$\begin{aligned} dp &\rightarrow (pp)n \text{ (charge exchange breakup),} \\ dp &\rightarrow (pn)p \text{ (charge retention breakup),} \end{aligned}$$

the last one corresponding to charge exchange in the deuteron. The polarization of the deuteron is almost fully transferred to the fragments. From previous measurements [179] it is known that the polarization transfer coefficient (K_0) equals to 1 until $k = 0.15$ GeV/c as illustrated in Fig. 6.8. k is the internal momentum of proton inside the deuteron, which is defined as,

$$k = \sqrt{\frac{m^2}{4\alpha(1-\alpha)} - m^2},$$

with

$$\alpha = \frac{E_p + p_{\parallel}}{E_d + p_d},$$

where E_p and p_{\parallel} are the energy and longitudinal momentum of proton. E_d, p_d are deuteron beam energy and momentum. m is the nucleon mass.

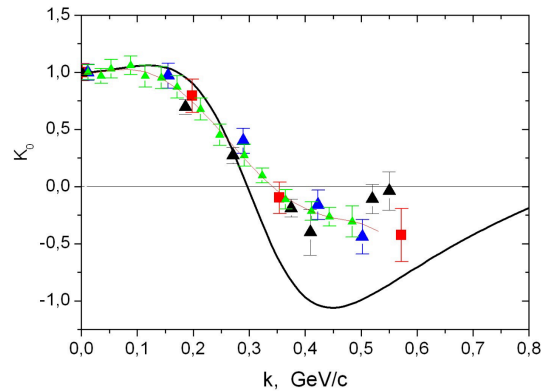


FIGURE 6.8: World data for the $p(d, p)X$ and $C(d, p)X$ reactions for the vector to vector polarization transfer coefficient (K_0) at a function of the internal proton momentum k from Ref. [179].

The break-up protons emitted at zero angle from the deuteron beam are separated by two dipoles of the beam transport line [180]. The neutron beam is selected

by bending the charged particles in another direction with a magnetic field. A magnet switched on/off allows to deviate or not the particles and inject them in the ALPOM2 line: a proton or a neutron beam. Then the beam is focused on the polarimeter target. The acceptance of the beam transfer line is about $\Delta\Omega \sim 10^{-4}$ sr, and $\Delta P_p/P_p \sim 3\%$. The elements of the ALPOM2 beam line do not change the proton or neutron polarizations up to the target.

6.3.2 Setup for the test run

The detectors of the ALPOM2 setup are mainly scintillator counters and drift chambers. An active target, described below, is used also as a detector for neutron. The

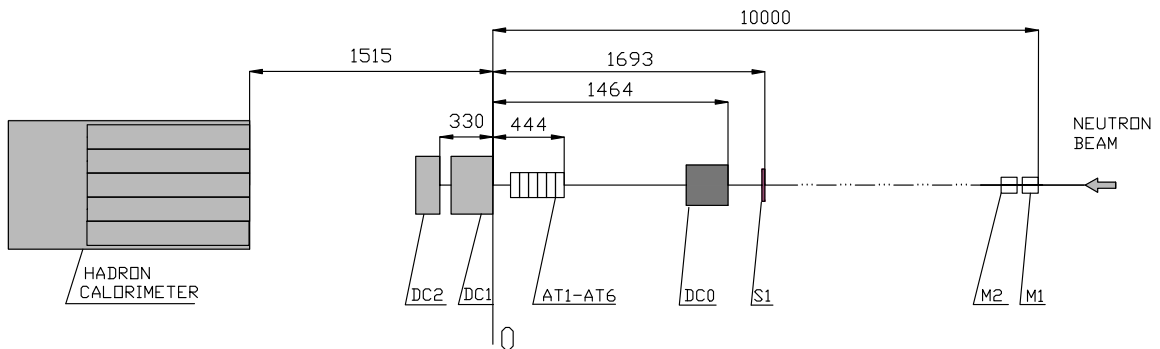


FIGURE 6.9: The setup of the test run in ALPOM2 experiment during 2015 [180]. $M_{1,2}$: beam monitors. S_1 : scintillator counter, $DC_{0,1,2}$: drift chambers, AT_{1-6} : active target. HCAL: hadron calorimeter.

beam hits first the scintillator counter, which gives a very fast response signal. This signal is used as a trigger: it decides if the signal from the chambers will be recorded or not.

6.3.2.1 Drift Chamber

The drift chambers are taken from the STRELA experiment [181]. As seen in Fig. 6.9, there are two series of drift chambers ($DC_{0,1,2}$) of different sizes. Two small size modules DC_0 , of dimensions 12.5×12.5 cm², are located upstream of the target and two large chambers of dimensions 25×25 cm² $DC_{1,2}$ are located downstream of the target. Each module of small or large sizes, consists of X and Y coordinates planes in one gas enclosure. The small DC_0 have 4 planes (2X and 2Y), and the large $DC_{1,2}$ have 8 planes (4X and 4Y). Each plane has five signal wires spaced by 4.2 cm, and the contiguous planes are shifted by half of a space. The shift of wire space helps to remove the left-right ambiguity in the reconstruction of the particle tracks. The total

material, considering the eight planes, is 0.141 g/cm^2 and the sensitive area is 0.008 radiation lengths.

To determine the position of the particle going through the chamber, one measures the drift time differences between two wires. The time difference depends not only on the position but also on the velocity of the electron through the gas in the chamber. This is mainly related to the components of the gas and the pressure, the strength of electric field, as well as to the temperature of the experimental environment and the geometry design [182].

In ALPOM2, each chamber contains a two-component gas mixture of Argon-Methane (Ar_2CH_4), which allows a mode of constant electron drift velocity and a high linear dependence of the drift time on the track coordinate throughout the chamber at an electric field strength of 1.5 kV/cm . The signals are collected by the wires of each chamber. Chip cards amplify, shape, and discriminate the input signals given by the signal wires. Then the analogic signals go to time to digital converter (TDC) modules and convert to digital signals. The drift velocity can be expressed as:

$$v_d(t) = \frac{R}{N_{tot}} \cdot \frac{dN}{dt},$$

where R is the length of the drift gap (21 mm), and N_{tot} is the total number of events. The TDC time spectrum of the channel No. 72 is shown in Fig. 6.10. The minimum

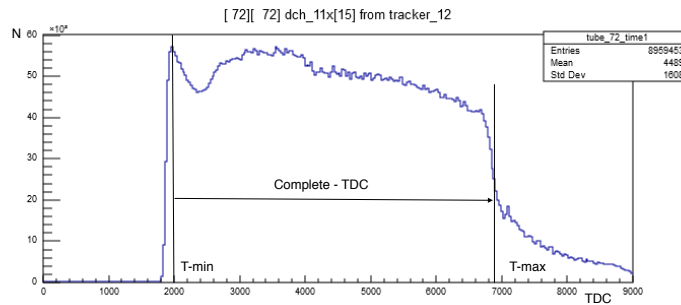


FIGURE 6.10: The Online TDC time spectrum of a wire of a drift chamber during the ALPOM2 experiment. T_{min} and T_{max} are the drift times.

and maximum drift time for each channel (a wire) are T_{min} and T_{max} . Integrating the drift velocity on the drift time, we convert the drift time to a distance $r(t)$ which

is the position with respect to the center:

$$r(t) = \int_{T_{min}}^{T_{max}} v_d(t') dt' = \frac{R}{N_{tot}} \int_{T_{min}}^{T_{max}} \frac{dN}{dt'} dt'. \quad (6.2)$$

6.3.2.2 Track reconstruction

Each wire gives the position of the crossing particle, in one coordinate. Then, the information from the wires of all the planes allow to trace the track of the particle. In order to reconstruct a trajectory, one event must have three hits or more, *i.e.*, three planes at least, must fire. The track of the particle at each plane can be decomposed in xz coordinates as illustrated in Fig. 6.11. The track in a plane perpendicular to

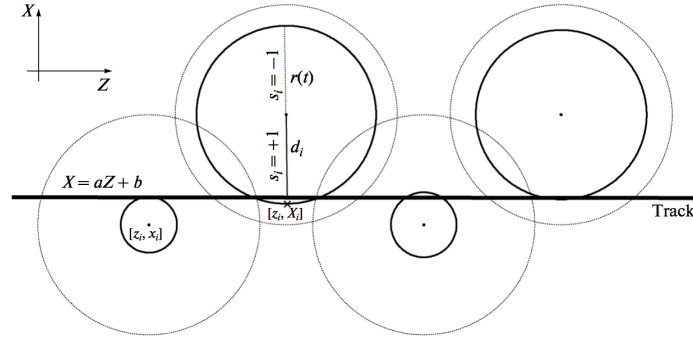


FIGURE 6.11: An example for the reconstruction of a track in the drift chamber of X-Z coordinate from the STRELA experiment [181].

the wires of one drift module can be parameterized as a linear function:

$$X = aZ + b, \quad (6.3)$$

where a and b are parameters. We assume the incident particle has hit N wires, and the distance d_i of the i th wire can be written as:

$$d_i = \frac{az_i - x_i + b}{\sqrt{1 + a^2}}. \quad (6.4)$$

The values of a and b are obtained by minimizing the χ^2 function:

$$\chi^2 = \frac{1}{N-2} \sum_i^N [|d_i| - s_i r_i]^2, \quad (6.5)$$

where $s_i = \pm 1$ according to the relative position between the track and the wire, and r_i is the distance (6.2) of the i th wire.

During this experiment, all drift chambers have been tested under beam. It has been found that the spatial resolution is less than 0.1 mm which guarantees an angular resolution better than 0.4 mrad.

6.3.2.3 Polarimeter target

In order to optimize the analyzer of the experiment, different materials and thicknesses of the polarimeter target were used for different analyzing processes, at different beam momenta of protons and neutrons.

The angular distribution of the emitted protons and neutrons with CH₂ and CH targets at 3.75 GeV/c are shown in Fig. 6.12 (left). The plot shows that the number of the detected particles for a neutron beam with a CH₂ target is larger than for the CH target. It indicates that higher hydrogen content material, CH₂, corresponds to a larger efficiency.

With the same target material, the neutron beam has a larger number of events than the proton beam in the region $\theta = 0.02$ to 0.16 rad which is the sensitive region for the analyzing power measurement. This is the region where the proton beam has nuclear interactions with the active target, as shown in Fig. 6.12 (right). In a cone around the beam line with opening $\theta < 0.02$ rad the neutron beam produces more events than protons, that go through the target directly without scattering with the nuclei of the materials.

The number of events decreases when θ increases from 0.02 to 0.16 rad, when the beam scatters off carbon and hydrogen nuclei. If the beam momentum increases to 7.5 GeV/c, even less particles undergo a nuclear reaction with the target.

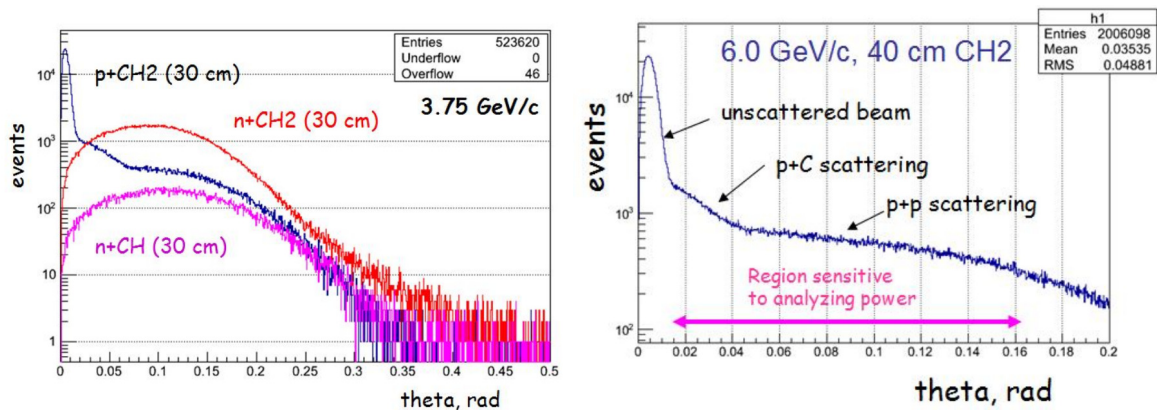


FIGURE 6.12: Figures from the test runs by the ALPOM2 group of JINR. Left: dependence of the angular distribution of incident protons and neutrons on 30 cm targets, CH₂ and CH, at 3.75 GeV/c. Right: angular distribution for protons on a 40 cm CH₂ target at 6 GeV/c where the angular regions for the different processes are highlighted.

For a proton beam, the polarimeter analyzer (CH₂ target) consists of 11 blocks of polyethylene of dimension $300 \times 300 \times 51 \text{ mm}^3$. The density of the material is $\rho = 0.919 \pm 0.002 \text{ g/cm}^2$. Increasing the beam momentum, the average interaction point corresponds to a larger path of the beam particle in the target. The acceptance angle of the outgoing particles corresponding to the geometry may change from 120 to 240 mrad.

For a neutron beam, the polarimeter analyzer (active target CH) consists of 8 blocks of scintillators of dimension $500 \times 150 \times 50 \text{ mm}^3$. This material has density $\rho = 1.032 \text{ g/cm}^3$. Two photomultipliers, connected directly to the scintillator collect and amplify the signal. They participate to the trigger in coincidence to sign the neutron interaction with the scintillator material.

6.3.2.4 Hadron calorimeter

The reason to add a hadron calorimeter in ALPOM2, is primarily to decrease the trigger rates by selecting the useful events. The events corresponding to a proton beam scattering on a CH₂ target can be classified in four types (Fig. 6.13), according to the number of produced charged particle: no interaction with the target, no charged particle ($1 \rightarrow 0$), one charged particle ($1 \rightarrow 1$), and two charged particles ($1 \rightarrow 2$). The most suitable reaction to measure the proton analyzing power involves one charged particle production, protons or pions ($1 \rightarrow 1$).

When the proton beam momentum increases from $3.75 \text{ GeV}/c$ to $6 \text{ GeV}/c$, the proportion of one charged particle events decreases dramatically. Other processes, like unscattered events coming from the beam and events with two or more charged particles decrease by less than one half, which decreases the total asymmetry. The neutron induced reactions have a similar behavior when the beam momentum increases. The hadron calorimeter helps identifying the useful reaction. This is shown in Fig. 6.13, where the number of events corresponding to each type is shown as a function of the sum of the energy deposited in the calorimeter, at $3.75 \text{ GeV}/c$ (left) and $6.0 \text{ GeV}/c$ (right) for a CH₂ target. Such study is particularly important for the forthcoming JLab experiments. The new large acceptance spectrometer built for the future GEp-V experiment at high transfer momenta (up to 15 GeV^2) will have extremely large particle rates [147].

Moreover, as the analyzing power becomes smaller and smaller when the momentum increases, the calorimeter can be used to select the leading protons at smallest angles, which has the effect to increase the analyzing power. The hadron calorimeter makes it possible to select high momentum particles through their energy deposit.

The hadron calorimeter consists of 28 modules, built in Dubna for the COMPASS experiment at CERN and made available for the present experiment [183, 184]. It is located downstream the polarimeter. It is a sampling calorimeter composed of

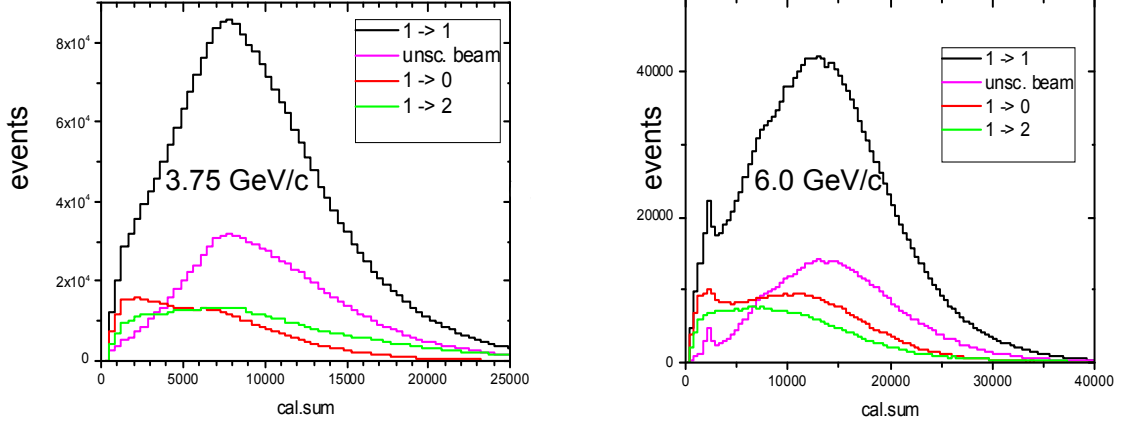


FIGURE 6.13: Data selection of different processes induced by proton on CH_2 target at 3.75 GeV/c (left) and 6.0 GeV/c (right) as a function of the sum of the energy deposited in the calorimeter (courtesy of the ALPOM2 group of JINR).

interleaved plates of plastic scintillator and iron. As the particles should lose all their energy in the detector, the iron plates are used to slow down the hadrons, allowing to have a compact detector.

The strong interaction in the iron plates should be taken into account in the reconstruction of the energy of the particles. The hadronic interactions undergo two stages: 1. hard collision between the primary hadrons and nuclei which mainly depends on the incident hadron type, 2. spallation of the nucleus with absorption of the fast hadrons, which mainly depends on the binding energy of the nucleus. During these stages a number of secondary particles can be produced by the primary particles. Parts of these secondary, even tertiary, nuclear reactions compose the hadronic cascade.

One module of a sampling calorimeter is shown in Fig. 6.14 [183, 184]. It is composed of scintillator and iron plates which are contained in a module container. The produced photons are transported through a shifter, a light guide, and amplified by the photomultiplier. The collected signal gives information on the energy (amplitude) and time, that is recorded for further analysis.

The main characteristics of the calorimeter to be studied are:

1. The energy resolution $\frac{\sigma}{E}$ for pions from Dubna and COMPASS are shown in Fig. 6.15. The spatial resolution $\sigma_{x,y}$ strongly depend on the production technology of the scintillators, on the wavelength-shifting light guide to the PM, and high voltage dividers;

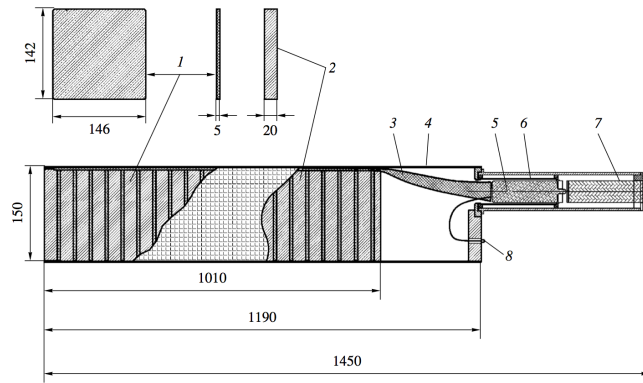


FIGURE 6.14: One module of the hadron calorimeter: 1. scintillator, 2. iron plates, 3. wavelength-shifting guide, 4. modules container, 5. Photomultiplier, 6. magnetic shield, 7. high-voltage divider, 8. optical connector. The figure is from ALPOM2 proposal [180].

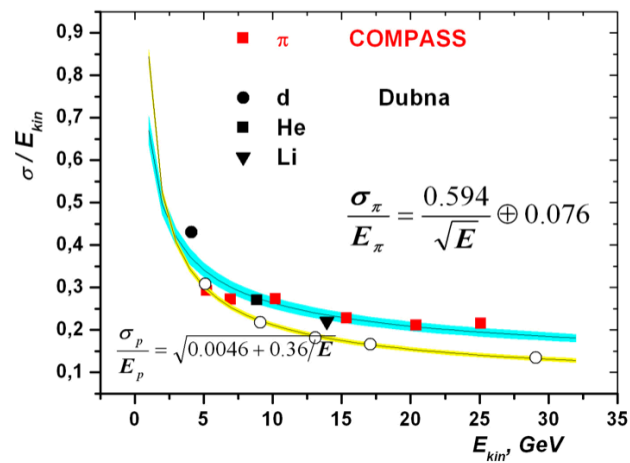


FIGURE 6.15: Energy resolution versus kinetic energy for the COMPASS pion data (red) and for ${}^6\text{Li}$, ${}^4\text{He}$, deuteron beams (black) during June 2016 test. Open points and yellow curve are the Monte-Carlo simulations and the fit corresponds to protons. The figure is from ALPOM2 proposal [180].

2. e/π ratio of response between electron-induced and pion-induced shower amplitudes;
3. the cross section and thickness of iron and scintillator plates, which should be sufficient to guarantee the full absorption of the hadron energy.

The scintillator plates absorb a portion of the cascade particles, convert into photons to be detected by a photomultiplier tube. The amplitude of a PMT pulse is proportional to the energy deposit in the scintillator. The pulse heights are recorded by the analog-to-digital convert system. Through coefficients that calibrate the amplitudes of the module signals, the amplitude spectra are converted into energy spectra. The energy spectra of pions are typically Gaussian distributions.



FIGURE 6.16: View of the hadron calorimeter setup (left) and of the scintillators in each module (right).

The total weight of the calorimeter is 2.5 t. Fig. 6.16 shows the moduli of the hadron calorimeter and the structure, which are composed of different material and are of different geometries. The calorimeter is designed with moduli of different size and composition at a different distance around the beam axis, as shown in Fig. 6.17. The geometry is optimized to have similar counting rates in each modulus, as most of the particles hit the central moduli and less particles are scattered at larger angles. The angular and energy distributions follow an almost cylindrical symmetry, so the calorimeter employs the same material at the same distance from centre.

- In the centre there are 4 moduli which are composed by $4 \times 75 \times 75 \text{ mm}^2$ blocks. Each modulus has 50 layers of 10 mm Pb + 10 mm scintillator.
- In the intermediate part around the central part, there are $8 \times 150 \times 150 \text{ mm}^2$ moduli with two components. The first part is constituted of 18 layers with 10 mm lead and 10 mm scintillator, the second part has 20 layers (20mm Fe+10 mm scintillator + 1 reserve).

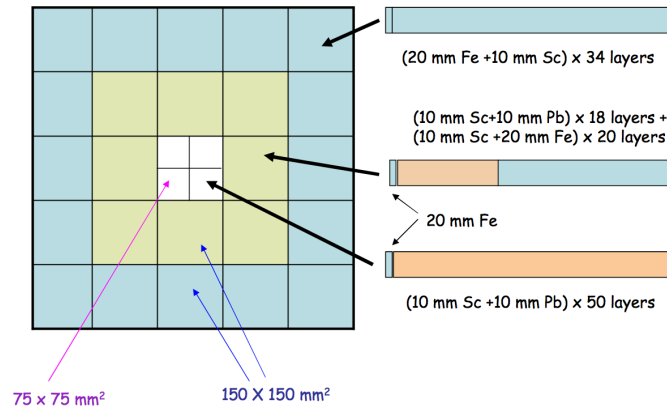


FIGURE 6.17: Geometrical layout of hadron calorimeter and its different moduli from ALPOM2 group of JINR.

- In the peripheral region there are $16 \times 150 \times 150 \text{ mm}^2$ moduli. Each of them has 34 layers (20 mm Fe + 10 mm scintillator), and the total length is $34 \times (20+10)=102 \text{ mm}$.

6.3.3 Online data acquisition system and analysis

The results presented here were mostly collected during the beam time attributed to ALPOM2 in November 19-30, 2016. A polarized deuteron beam was available at 6.0, 7.5 and 8.4 GeV/ c momentum. A beam time of few days took place in Feb. 2017 with neutron beam at 3.75 GeV/ c . It was mostly devoted to different checks of the beam and the apparatus as well as to a measurement of neutron analyzing powers on a Cu target. The intensity in the accelerator was $2-5 \times 10^8$ particles per spill and was reduced by a factor of 3 after the extraction. The beam spill structure was of 4 s every 12 s. Following the deuteron break-up on the beryllium target, the recorded number of trigger of protons and neutrons (at about half deuteron momentum) impinging on the target was around 7000/spill. The polarization was different for the two states, for one state around +70%, and for the other -25%.

The setup of the experiment in the November 2016 run with polarized beams is shown in Fig. 6.18. Compared to the test run, a pair of up-down counters was set before the HCAL as the trigger for neutron beam.

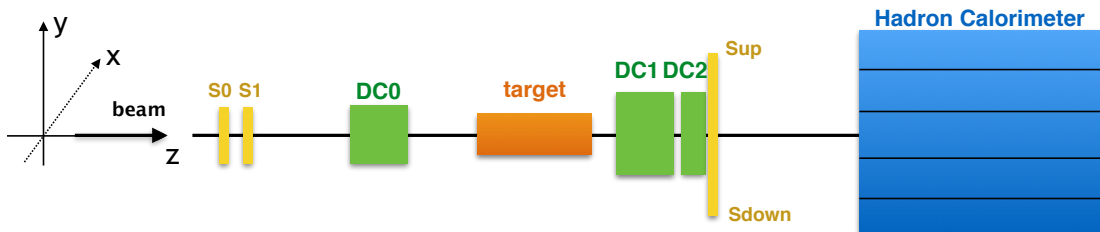


FIGURE 6.18: The setup of ALPOM2 for polarized neutron and proton beams in November 2016 run. $S_{0,1}$ and $S_{up,down}$ are scintillators, corresponding to Table 6.5. DC_0 and $DC_{1,2}$ are the small and large drift chambers before and after the target. The last element downstream is the hadron calorimeter.

The data acquisition (DAQ) system of ALPOM2 setup is adapted from the STRELA experiment [181]. It is based on the VMEbus standard, which assumes high speed modular computing systems on a unified bus and has a high versatility and extendibility [185].

The system consists of 8 modules of 4 types, Trigger (TRIG), Time-to-Digital Converter (TDC), MSC, and TQDC. The TDC modules are used to convert (digitize) the time of shaped pulse signals from the drift chambers. The online system records the raw time of all hits. The TQDC is a multi-hit time-stamping TDC, and a waveform digitizer. It is used to measure the arrival time, the charge, and the shape of the pulse.

Trigger: The wait time of per spill is 0.001 s, the duration is 5.000 s and the repetition time is 2.000 s. The TRIG signal shaper time is 3×50 ns with internal trigger generator pulser 100 Hz. The trigger logic is based on the LEMO method.

The read out triggers in the TRIG event statistics (410 out 411) is about 99.76 %, and the trigger bits of 6 LEMO in 410 read out triggers is 100 %.

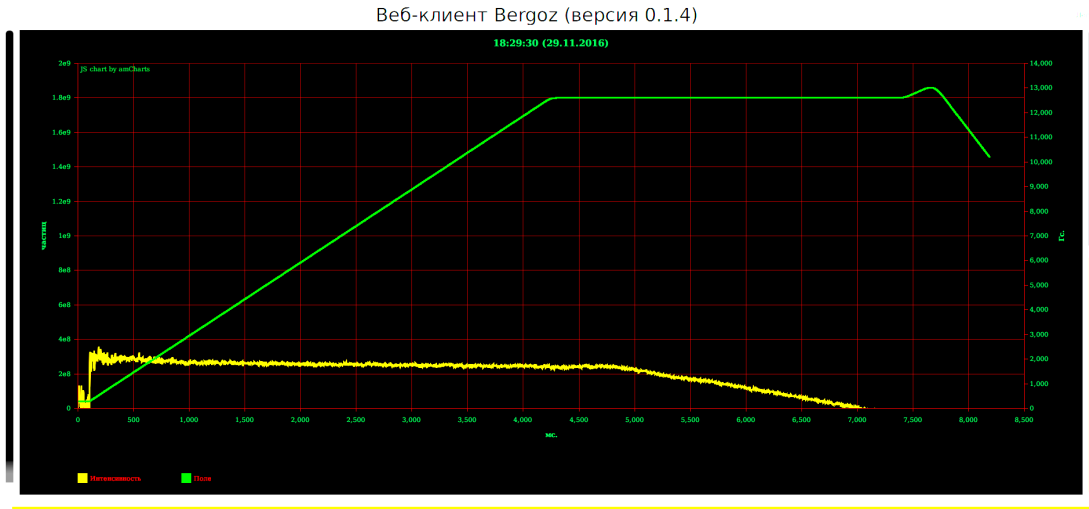


FIGURE 6.19: The deuteron beam intensity (yellow) and the magnetic field strength of the Nuclotron (green) during the November 2016 run during one spill time.

Important elements for controlling and event detection for this beam run are:

1. **Beam Monitor:** to check the accelerated field, beam intensity, polarization, stability, duration, momentum. The accelerated field is monitored. In Fig. 6.19 the magnetic field and the beam intensity in the Nuclotron accelerator are shown.

The intensity of the extracted deuteron beam is measured at the level of the F3 polarimeter, with the ionization chamber as a monitor. The beam polarization is visualised and checked online from the F3 polarimeter. The counting rates are illustrated in Fig. 6.20 for the left arm of the polarimeter, corresponding to a deuteron beam momentum of 7.5 GeV/c. The reaction of interest here is pp elastic scattering at momentum 3.75 GeV/c. In the bottom of Fig. 6.20 the left-right asymmetry calculated by the F3 polarimeter at proton momentum 3.75 GeV/c is shown as a function of run number. One can see that the asymmetry is different in the two polarization states, moreover a residual asymmetry lower than 2 % remains in the unpolarized state. According to the value of analyzing power $A_y=0.2$ with 8 % uncertainty from Ref. [186] and Eq. (6.1) the beam polarizations are estimated as

$$\begin{aligned} P^+ &= 0.642 \pm 0.005, \\ P^- &= -0.511 \pm 0.006. \end{aligned}$$

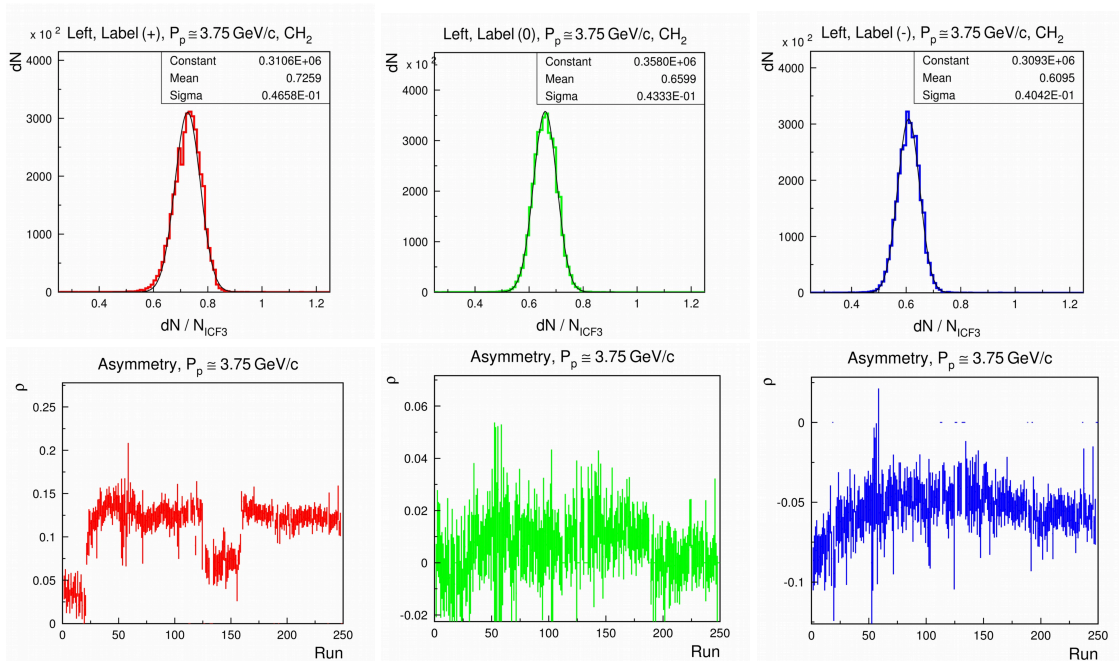


FIGURE 6.20: Counting rate spectra (top) in the left arm of the F3 polarimeter for the 3 beam states (+, 0, -) normalized to the total events recorded by the F3 ion chamber. Left-right asymmetry (bottom) as a function of run number calculated by the F3 polarimeter at proton momentum 3.75 GeV/c. Figures are from F3 polarimeter online system.

2. **Tracking and reconstruction system:** in Table 6.5, typical counting rates for

Online Monitors		
1	S_0	647
2	S_1	503
3	S_{up}	3867
4	S_{down}	5102
5	$F3_{left}$	468
6	$F3_{right}$	370
7	F3 IC	603
8	Trigger	2874
11	Monitor1	3268
12	Monitor2	3102

TABLE 6.5: Online acquisition monitor system. Typical counting rates for the different elements.

the different elements are reported. S_0 , S_1 are the triggers for proton beam which determine the acceptance of the setup and produce a signal that opens the time window that collects the signals from the drift chambers and starts the DAQ system. For neutrons, an active target and an up-down counter which is set behind the drift chambers are used in coincidence for the trigger system. The beam positions for proton (left) and neutrons (right) at the level of the two triggers are shown in the Fig. 6.21. in the XY-plane. The Z-axis corresponds to the longitudinal direction along the beam, the X- and Y-axis are in the horizontal and vertical plane respectively and form an orthonormal system. The zero of the Z-axis is fixed at the S_1 scintillator. The proton beam appears slightly vertically decentered, while the neutron beam is better centered. This may be due to the magnet field in the dipole set after the deuteron beam breakup to separate the charge and neutral particles. A possible angular misalignment has been checked in the February 2017 run. The effect has been studied and the correction for the track reconstruction has been implemented.

The neutron beam interaction with the target as reconstructed from the detected charged emitted particles in forward region is shown in Fig. 6.22. The first interaction region corresponds to the 30 cm CH_2 target. From the XZ and YZ - axis contours, the interaction does not occur preferentially in the central region. This effect on the asymmetry of the ϕ distribution will be reduced when normalized to the unpolarized state. The interactions on the wires of the last plane of the chamber are also visible.

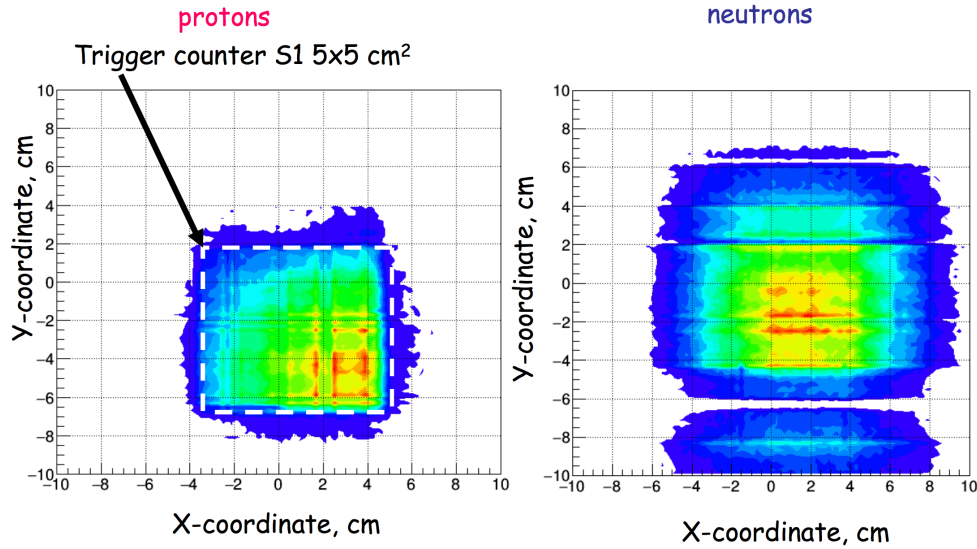


FIGURE 6.21: The proton (left) and the neutron (right) beam positions in the XY-plane at momentum 3.75 GeV/c (courtesy of the ALPOM2 group of JINR).

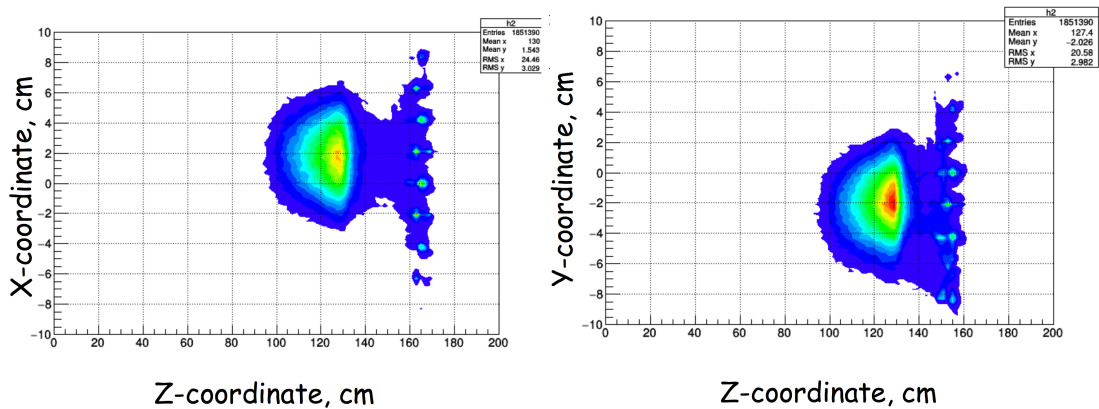


FIGURE 6.22: Neutron particles interaction in the XZ-(left) and YZ-(right) dimensions at momentum 3.75 GeV/c, reconstructed from the detection of charged particles in forward direction (courtesy of the ALPOM2 group of JINR). The wires of the last plane of the wire chamber are visible.

6.4 Extraction of analyzing powers

In this section, we select data corresponding to one track at beam momentum of 3.75 GeV/ c as a sample of events to extract the analyzing power.

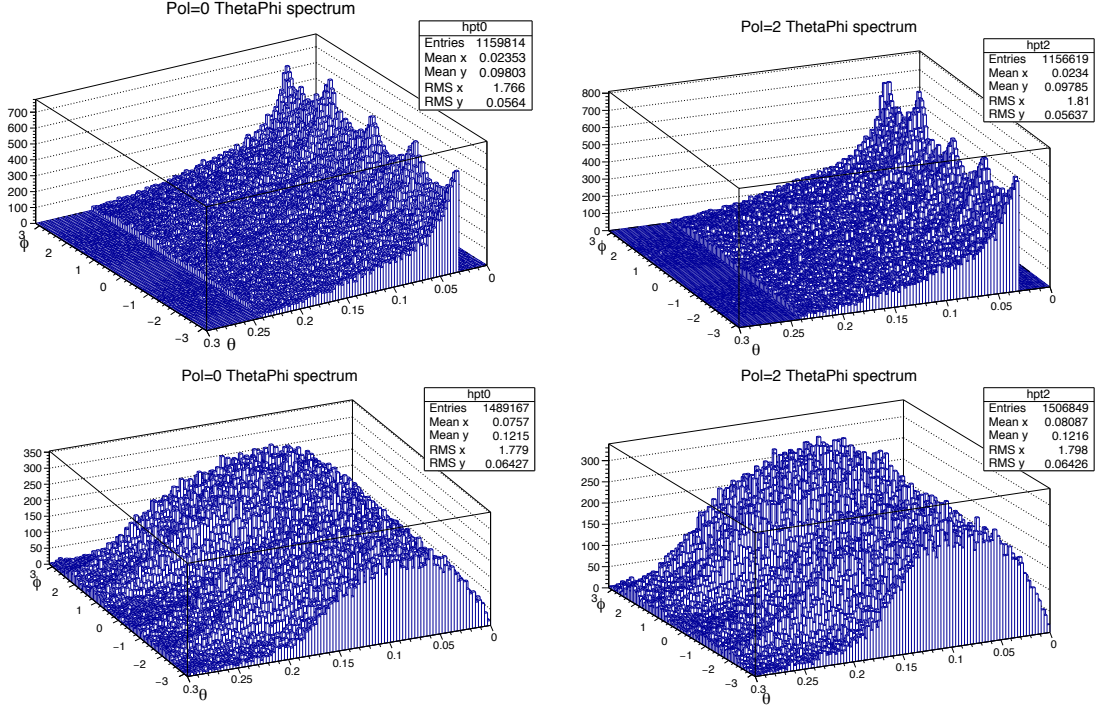


FIGURE 6.23: The (θ, ϕ) distribution for proton (top) and neutron (bottom) on CH2 target at beam momentum 3.75 GeV/ c of polarization states "+" and "-".

The ingoing and outgoing trajectories are reconstructed from the small and large chambers, as described in Sec. 6.3.2.2. The azimuthal and polar angles are calculated and their histograms are built. The (θ, ϕ) distribution of proton and neutron on CH2 target at beam momentum 3.75 GeV/ c for the polarization states "+" and "-" are shown in Fig. 6.23. The difference in asymmetry appears after normalizing the polarized spectrum to the unpolarized one. The number of events detected in a unit solid angle around the direction of the scattered particle, for beam polarization states "+" and "-", $N^\pm(\theta, \phi)$, is:

$$N^\pm(\theta, \phi) = N_0(\theta, \phi)(1 + P_y^\pm A_y(\theta) \cos \phi). \quad (6.6)$$

The azimuthal spectra in the two beam polarization states normalized to the counts in the unpolarized state are shown in Fig. 6.24. They correspond to polarized proton beam at 3.75 GeV/ c on a CH2 target, with the detection of one forward charged particle.

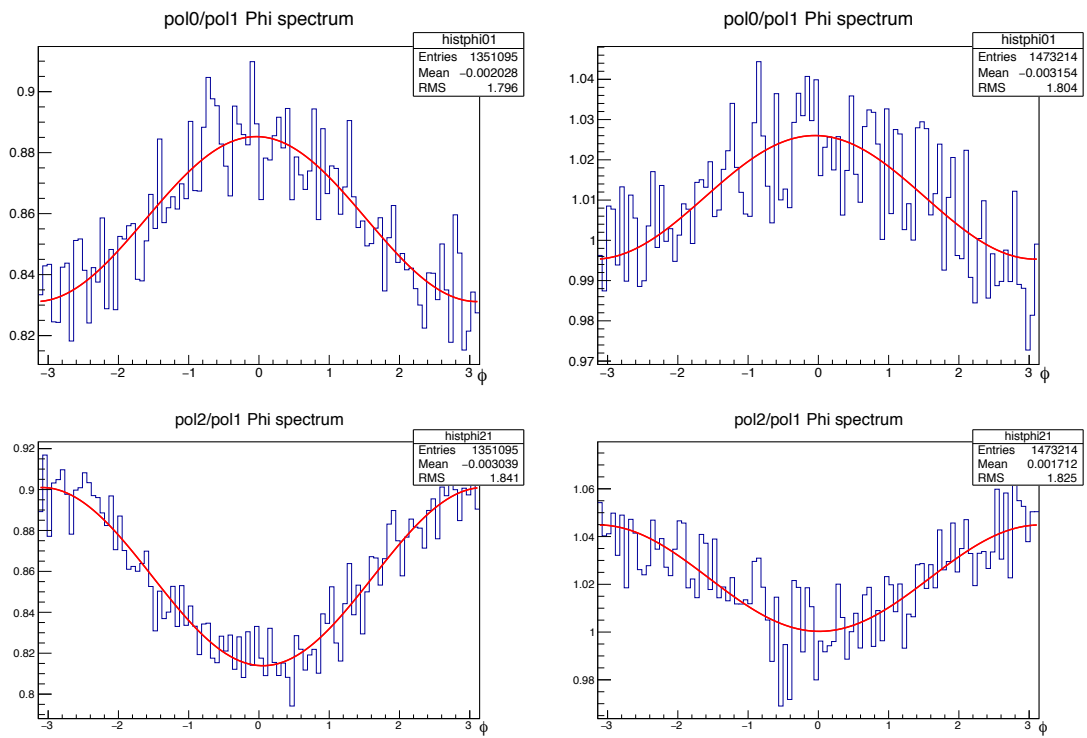


FIGURE 6.24: ϕ asymmetry for proton (right) and neutron (left) at momentum 3.75 GeV/c.

I extracted the asymmetry following two methods.

1. If we had the same value for the up and down polarizations, $|P^+| = |P^-| = P$, we could write for the counting rates:

$$\begin{aligned} N^+(\theta, \phi) &= N_0(\theta, \phi)(1 + PA(\theta) \cos \phi), \\ N^-(\theta, \phi) &= N_0(\theta, \phi)(1 - PA(\theta) \cos \phi), \end{aligned}$$

and find:

$$\begin{aligned} N^+(\theta, \phi) + N^-(\theta, \phi) &= 2N_0(\theta, \phi), \\ N^+(\theta, \phi) - N^-(\theta, \phi) &= 2N_0(\theta, \phi)A(\theta)P \cos \phi. \end{aligned}$$

Integrating on the relevant θ domain (or choosing a specific θ bin), one can extract the asymmetry $\epsilon = AP \cos \phi$ from a fit on a $\cos \phi$ distribution, where A is the average analyzing power (or $A(\theta)$ for a specific bin):

$$\frac{N^+ - N^-}{N^+ + N^-} = AP \cos \phi = \epsilon, \quad (6.7)$$

If $|P^+| \neq |P^-|$, the asymmetry ϵ becomes:

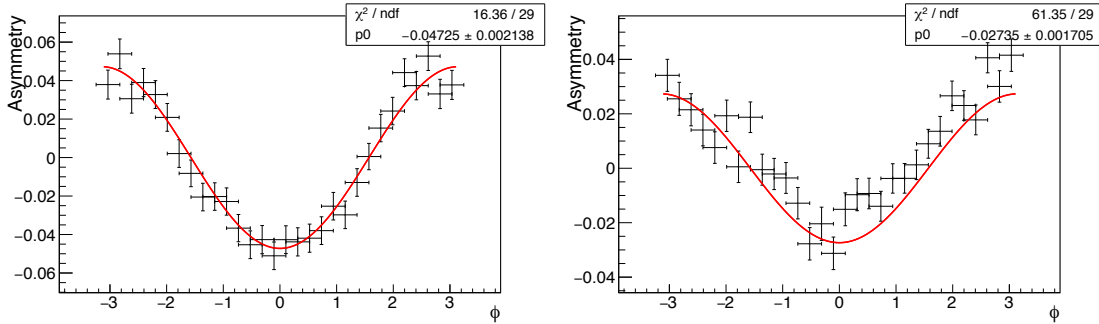


FIGURE 6.25: ϕ -asymmetry spectra for proton (left) and neutron (right) at beam momentum 3.75 GeV/c on CH2 target analysis according to Eq. (6.8), integrated in the θ range 0.09 to 0.15.

$$\epsilon = \frac{A \cos \phi (|P^+| + |P^-|)}{2 + A \cos \phi (|P^+| - |P^-|)}, \quad (6.8)$$

and the results are plotted in Fig. 6.25. Propagating the statistical error on the counting rate, one finds $\Delta\epsilon \simeq 1/\sqrt{N}$. For 10^6 collected events, this means a 10^{-3} statistical error, to be compared to the expected asymmetries that are of the order of few percent in the high energy range. It appears that the largest source of error is the systematic error. The main systematics are related to experimental asymmetries, that can be evaluated from the data, and to the error

on the beam polarization, that is typically 2 or 3%. Such error affects globally the distribution, therefore it enters in the absolute value of the analyzing power, not in the extraction of the asymmetry.

2. In our case the beam polarization is quite different in the two polarized beam states. We may normalize the spectra corresponding to P^\pm to the unpolarized spectrum to take into account spill by spill, the eventual instabilities of the beam:

$$\frac{N^+ - N^-}{N_0} = A(|P^+| + |P^-|) \cos \phi = \epsilon, \quad (6.9)$$

In this way, we cancel the experimental asymmetries due to the setup or the beam misalignment, that are equally present in all the beam states. The results are plotted in Fig. 6.26.

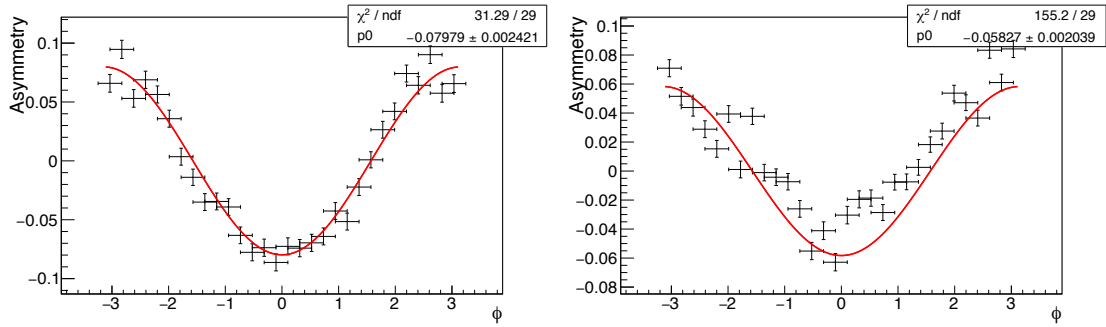


FIGURE 6.26: ϕ -asymmetry spectra for proton (left) and neutron (right) at beam momentum 3.75 GeV/c on CH2 target analysis with Eq. (6.9).

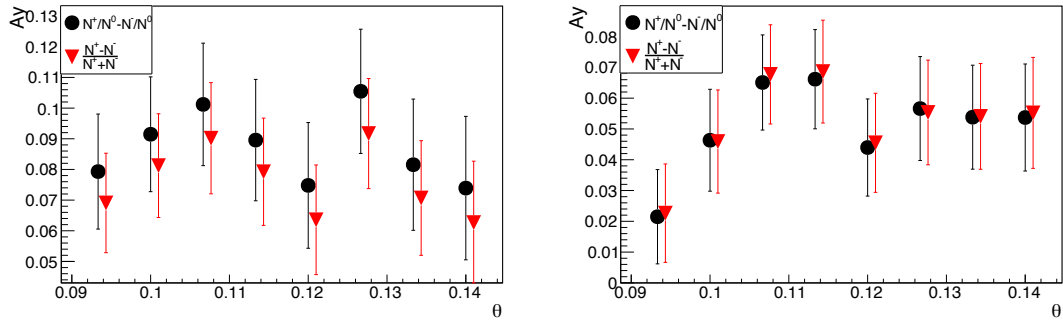


FIGURE 6.27: Extracted analyzing power of proton (left) and neutron (right) at beam momentum 3.75 GeV/c with $|P^+| = 0.642$ and $|P^-| = 0.511$ on CH2 target following with the two methods, from Eq. (6.8) and Eq. (6.9).

Comparing the analyzing powers obtained from Eq. (6.8) and Eq. (6.9), we find results that are compatible within the errors (see Fig. 6.27). The errors are similar as they reflect the statistics only.

With the same procedure as for the beam momentum 3.75 GeV/*c* and Eq. (6.9), the asymmetry of proton and neutron at 3.0 GeV/*c* and 4.2 GeV/*c* are obtained and presented in Fig. 6.28.

As discussed in the previous section, there is no large difference between the different methods of the asymmetry calculation. Thus, here we only show the results from Eq. (6.9).

In order to derive the analyzing powers, the beam polarization has to be known from the F3 polarimeter. For beam momentum at 3 GeV/*c*, the analyzing power is taken as $A_y = 0.25 \pm 0.02$ at the scattering angle of 10.5° while the recoil particle is emitted at an angle of 68° . The beam polarization for the two states "+" and "-" is $P^+ = 0.652 \pm 0.004 \pm 0.052$ and $P^- = -0.343 \pm 0.005 \pm 0.027$.

For the beam momentum at 4.2 GeV/*c*, the analyzing power is taken as $A_y = 0.179$ with 8% uncertainty at a scattering angle of 8° while the coincident recoil particle angle is 67.5° . Then the beam polarization for the two states "+" and "-" are $P^+ = 0.538 \pm 0.005 \pm 0.043$ and $P^- = -0.298 \pm 0.005 \pm 0.024$.

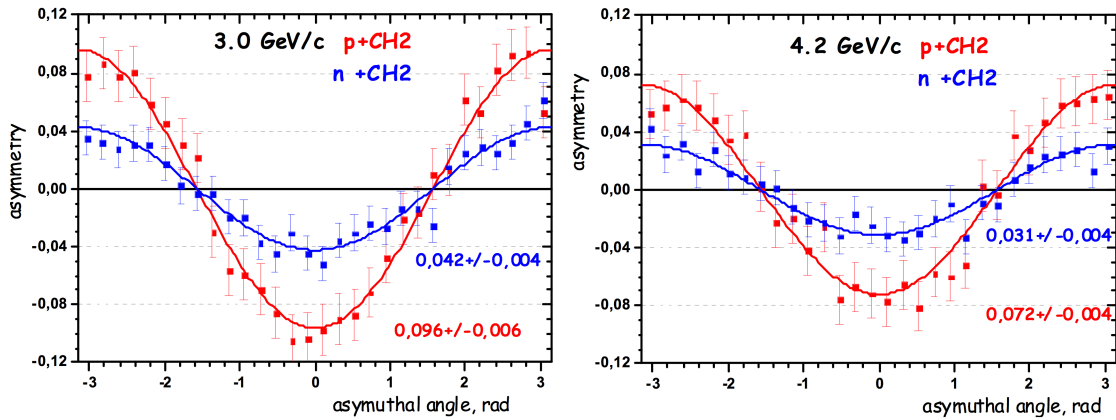


FIGURE 6.28: ϕ asymmetry spectra for proton (blue) and neutron (red) at 3.0 GeV/*c* (left) and 4.2 GeV/*c* (right) on CH2 target in Eq. (6.9) (courtesy of the ALPOM2 group of JINR).

Following Eq. (6.9), we can estimate that the average of the proton (neutron) analyzing powers corresponding to Fig. 6.28 is 0.0965 (0.0422) and 0.0861(0.0371) for the momentum 3 GeV/*c* and 4.2 GeV/*c*. Such values for proton are consistent with the existing data, and for neutron it is the first time that has been able to extend to 4.2 GeV/*c*.

The collective data of proton analyzing powers for 3.0, 3.75 and 4.2 GeV/*c* as a function of the $P_{perp} = p_L \cdot \sin \theta$ are shown in Fig. 6.29 with full symbols. The data from the previous ALPOM experiment at 3.8 and 4.5 GeV/*c* are also plotted (empty

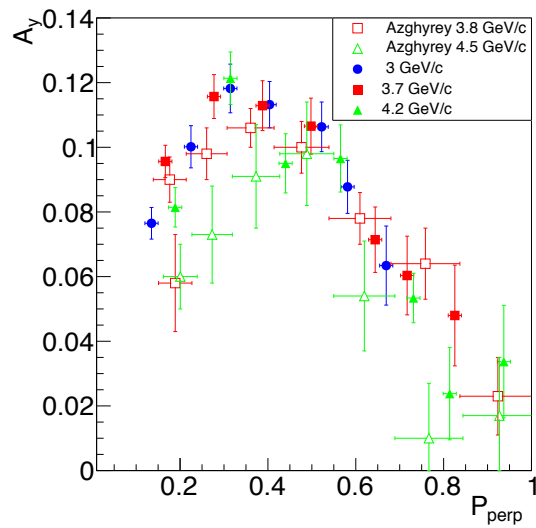


FIGURE 6.29: Analyzing power A_y as a function of P_{perp} for the reaction $p + CH_2 \rightarrow \text{charged particle} + X$: the full symbols are the results from ALPOM2 experiment for different beam momenta: $p_L = 3$ GeV/c (blue full circles), 3.75 GeV/c (red full squares) and 4.2 GeV/c (green full triangles). The empty symbols are data from ALPOM at beam momenta: 3.8 GeV/c (red empty squares) and 4.5 GeV/c (green empty triangles) [149].

symbols). It is clear that the present data are more precise and have better systematic consistency.

In Fig. 6.30 the world data for proton analyzing powers on different targets are shown as a function of the inverse of the incident momentum. It was previously observed that the maximum analyzing power follows an almost linear behavior decreasing as a function of this variable [187]. The present data are shown as full blue stars and fit well in the existing systematics.

The data in Fig. 6.29 were collected in series of measurements during several years. The first complete study and optimization of the target thickness for a C target was done in Saturne National Laboratory, with the POMME polarimeter and reported in Ref. [188]. The data are collected in Ref. [148] for a similar measurement at higher energies. After closing Saturne, the polarimeter POMME was moved to Dubna, where the polarized deuterons were available from the Synchrophasotron and set at the ALPHA set up. The data on CH_2 from Ref. [149] have been obtained in the first ALPOM experiment. Low energy data on Carbon are from Ref. [189]. At JLab, although no hadron beam is available, from the recoil polarization experiments one may assume that the proton polarization is known, and extract the effective analyzing powers of the polarimeter. The data from [190, 121, 125] have been obtained in this way. This may explain that in particular the data from the PhD thesis [125] are systematically higher than the other data on CH_2 . This tendency is underline by the linear fit by the corresponding color. From the figure it appears that a target with high hydrogen content as CH_2 is preferable, although the difference should disappear at high energies where quasi free pp scattering dominates. One can confirm that polarization measurement are doable for the JLab12 proposed measurements, with $A_y \simeq 5\%$.

6.5 Summary of experimental results

The possibility to accelerate polarized deuterons up to 13 GeV at the Dubna Nuclotron accelerator complex opens unique opportunity to have polarized proton and neutron beams. This allows, as discussed in this work, to optimize proton and neutron polarimetry at higher energies, what is necessary for the new form factor experiments at the upgraded JLab facility. Optimization includes the choice of the most efficient secondary reaction, producing the largest analyzing powers.

In the ALPOM2 experiment with polarized proton and neutron beam at 3.0, 3.75 and 4.2 GeV/ c in November 2016 the data were taken for 12 days on different targets, C , CH_2 , CH and Cu . The proton analyzing powers up to 3.75 GeV/ c have been measured. I have presented a preliminary analysis on part of the collected data.

This analysis already shows that the present data are more precise and consistent with the data previously measured. It is known that the semi-inclusive reaction $p + C, CH_2 \rightarrow 1 \text{ charge particle} + X$, that was used at lower energies due to its detection simplicity, is not ideal when the proton momentum increases. One reason is

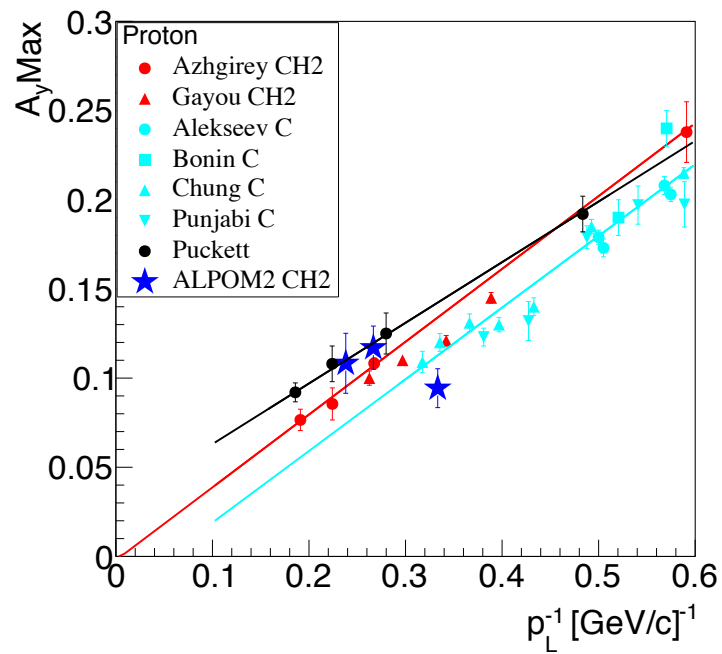


FIGURE 6.30: World data for the maximum analyzing power (A_y^{max}) for the reaction $p + CH_2/C \rightarrow \text{charged particle} + X$ on different targets CH_2 (red and black symbols), C (cyan symbols)(see text). The results from the present work are shown as blue stars. A linear fit of the corresponding color is also plotted.

that the proportion of one charged particle events decreases dramatically with increasing momentum. In order to identify the useful reaction, a hadron calorimeter was added, and it was indeed observed that the analyzing power changes when a selection of the energy deposit in the calorimeter is done.

The neutron analyzing power has been first measured on heavy targets. The new idea for neutron polarimetry was to compare charge exchange reactions to elastic scattering. It is known, for $\vec{n}p \rightarrow np$, that when the momentum increases, the analyzing power decreases at forward angles, while becoming negative and increases at backward angles. The analyzing powers for neutrons on different targets, have been measured up to 4.2 GeV for the first time, confirming the feasibility of neutron form factor proposal [161].

Chapter 7

Conclusion

The first part of this work is devoted to a phenomenological description of the antiproton-proton annihilation reactions into light meson pairs in the energy domain that will be explored by the PANDA collaboration. No existing model attempted to reproduce the full set of existing data and can be extrapolated at higher energies in a reliable way.

We have built an effective Lagrangian model including mesonic and baryonic degree of freedom, with Born level s, t, u channel Feynman diagrams. A logarithmic parametrization of the form factors takes into account the structure of baryons and shows to be very effective in this non-perturbative domain where the Regge parametrization does not apply consistently.

Coupling constants and necessary parameters are fixed on existing data. As data are scarce in this energy region, we collected annihilation and elastic πp scattering data. The kinematic relations of the proton and antiproton annihilation into a light meson pion pair were derived in terms of invariants. This helped to find the corresponding results on πp from crossing symmetry. These data were useful to fill the incomplete angular distributions for very forward or backward angles, and constrain the model, in a region where the cross section is the largest. Our conclusion on crossing symmetry is that it can be safely applied when one diagram is dominant.

The comparison with four sets data measured at the same accelerator, the CERN proton synchrotron, gives a $\chi^2/ndf \simeq 2.16$ that reduces to $\chi^2/ndf = 1.69$ for one individual set corresponding to the most complete angular distribution at $\sqrt{s} = 3.680$ GeV. Not only the angular distribution is well reproduced, but also the energy dependence is naturally consistent with quark counting rules. Compared with a quark exchange model, the description of the data is more satisfactory, also considering the very limited number of parameters. We checked that the model has a reasonable stability while a parameter change of $\pm 10\%$ larger. Within the SU(3) symmetry of the quark model, our calculation is applicable to charged kaon pair production. Adding a smooth s -dependence of the form factors parameters, the $\pi^0\pi^0$ channel can be reasonably described. SU(3) symmetry helps to extend successfully the model to other neutral meson pair productions: $\eta\eta, \eta\pi^0$.

Besides, to understand the hadron structure and reaction mechanism in the non-perturbative region is also intrinsic interest of this reaction. Our model, that is derived in analytical form, can be used in MonteCarlo generator, for comparison with

the large amount of data expected from PANDA. We stress that hadronic reactions are orders of magnitude larger than electromagnetic channels, therefore they constitute the largest background for electromagnetic channels. In particular the extraction of electromagnetic channels that contain the information on electromagnetic proton form factors in the time-like region, as $\bar{p}p \rightarrow e^+e^-$ and $\bar{p}p \rightarrow \mu^+\mu^-$, will benefit from the deep understanding of the meson production channels. The data collected and used in this part are all from Durham HEPDATA Database.

The second part reports on my participation and on the results of the experiment ALPOM2, on the measurement of analyzing powers for proton and neutron on different targets: C , CH , and CH_2 . The experimental contribution is devoted to optimization of hadron polarimetry at the high energies, requested for the form factor program at the upgraded Jefferson Laboratory accelerator facility.

The possibility to accelerate high energy polarized deuteron beams at the Nuclotron accelerator complex in Dubna, gives unique opportunity to measure the proton and neutron analyzing powers on different targets and with different configurations.

Based on a pole model, we compared the figure of merit of two reactions, the elastic $\vec{n} + p \rightarrow n + p$ (with a forward neutron detected) and the charge exchange reaction $\vec{n} + p \rightarrow p + n$ (with a forward proton detected). We defined the energy region where the reactions are competitive and shown that for $p_L > 5$ GeV/ c the charge exchange reaction becomes more favorable.

In the ALPOM2 experiment with polarized proton and neutron beam at 3.0, 3.75 and 4.2 GeV/ c in November 2016 the data were taken for 12 days on different targets, C , CH_2 , CH and Cu . I participated to three runs: the first with unpolarized beams, was useful to check the experimental set up, calibrate the hadron polarimeter, and align the transport beam line. One run was mostly devoted to commissioning of the new source and new injector line. The last run was dedicated to polarization measurements. The original request will be completed in a future run. Polarization measurements have been based on the measurement of the azimuthal asymmetry in a secondary scattering, choosing the most efficient reaction, but simple for the detection. At high energies the final channel 'one charged particle +X' becomes proportionally very low, compared to multitrack events. In the present experiment a hadron calorimeter was added, to allow selection on the energy deposit of the final particles. From a preliminary analysis, it appears that this information is useful to increase the effective analyzing power.

The proton analyzing powers up to 3.75 GeV/ c have been measured and are consistent to the data previously measured. The neutron analyzing power has been first measured on heavy targets.

The preliminary analysis, based on one track events, shows that an asymmetry of several percent is indeed observed, and the conclusion can be drawn that the polarization method can be extrapolated to higher energies.

The data presented here are preliminary. The following corrections should be agreed in the collaboration and implemented before making the data finals.

- We gave an average number for the beam polarization. As it is monitored burst by burst, a more refined correction can be done with the data collected from the F3 polarimeter.
- The efficiency, in particular in the neutron case will have to be evaluated, taking into account the number of the incident deuterons (known from the IC of the F3 polarimeter) and the acceptance of the line. For this aim, in the February 2017 run, dedicated measurements were taken with the beam impinging on the ALPOM line with different angles.
- The study of multiple track events should be performed. Part of these events may be included in the final analysis if it is proved that they have large analyzing powers, further increasing the figure of merit.
- The experimental asymmetries may reach 15%. They are mostly due to a misalignment of the beam. They are canceled in the measurement of the analyzing power, by the normalization with the unpolarized beam. An effect could however still be present at the percent level.

This will allow to give a more reliable figure of merit and to conclude definitely if heavy targets as Cu are more convenient in neutron polarimetry.

Further measurements for proton at higher energies are expected in near future. The comparison of different targets suggests that at 4.2 GeV/ c a Cu target, that is more compact and easily handable could be used and give similar analyzing powers as hydrogen-rich targets, showing that the most probable reaction is on a quasi-free nucleon.

During this work I had the opportunity to participate to different faces of the work of a physicist. During the phenomenological work, carried in collaboration with Yury Bystritsky, from the JINR -BLTP Institute, I learned the basics of relativistic kinematics, Feynman diagrams and traces calculations. I also learned things beyond physics itself, for example the methodology and the methods to progress, in particular in the fields where I did not have enough background, due to the fact that my Master degree was focussed on nuclear physics. It made me realize how important it is to have clear ideas of the result to be reached and of the goals to be achieved, otherwise one can never reach the destination. The opportunity to participate to an experiment at an accelerator forced me to look deeply in every step of the experiment, not only to the data analysis, that was the part where I took the main role.

I understand that the difficulty of hadron physics is related to the complexity of the nucleon, in the intermediate energy domain, where the relevant degrees of freedom should be first understood. For the experiment, the relevant reactions and observables should be first calculated, simulated and compared.

Appendix A

Collection of experimental data

A.1 Charged meson pair production

Differential cross section of the reaction $\bar{p} + p \rightarrow \pi^- + \pi^+$ (I)									
Ref. [47], $\sqrt{s}=3.362$ GeV				Ref. [53], $\sqrt{s}=3.627$ GeV					
$-t$ [GeV ²]	$d\sigma/dt$ [nb/GeV ²]			$-t$ [GeV ²]	$-t_{min}$	$-t_{max}$	$d\sigma/dt$ [nb/GeV ²]		
0.45	2.9	±	0.7	0.09	0.03	0.15	1.69	±	0.33
0.55	3.4	±	0.6	0.15	0.09	0.21	1.37	±	0.30
0.65	2.7	±	0.5	0.21	0.15	0.27	0.98	±	0.28
0.75	3.1	±	0.5	0.27	0.21	0.33	0.74	±	0.27
0.85	2.2	±	0.4	0.33	0.27	0.39	0.55	±	0.25
0.95	2.3	±	0.4	0.39	0.33	0.45	0.68	±	0.26
1.05	1.5	±	0.3	0.45	0.39	0.51	0.76	±	0.29
1.15	1.7	±	0.3	0.52	0.44	0.60	0.86	±	0.25
1.25	1.4	±	0.3	0.6	0.52	0.68	0.73	±	0.21
1.35	1.4	±	0.4	0.68	0.60	0.76	0.80	±	0.25
1.5	0.57	±	0.15	0.81	0.63	0.99	0.70	±	0.15
1.7	0.62	±	0.17	1.00	0.80	1.20	0.48	±	0.15
1.9	0.86	±	0.20	1.25	0.95	1.55	0.68	±	0.21
2.1	0.73	±	0.19	Ref. [52], $\sqrt{s}=4.551$ GeV					
2.3	0.60	±	0.21						
2.5	0.95	±	0.32	Ref. [52], $\sqrt{s}=4.551$ GeV					
2.8	0.83	±	0.31						
4.0	0.049	±	0.025	0.175	0.150	0.200	0.51	±	0.29
6.0	0.035	±	0.018	0.24	0.20	0.28	0.31	±	0.18
7.7	0.035	±	0.016	0.36	0.28	0.44	0.21	±	0.12
8.5	0.20	±	0.09	0.52	0.44	0.60	0.34	±	0.17
8.7	0.48	±	0.13	0.80	0.60	1.00	0.18	±	0.09
8.9	0.63	±	0.16	1.25	1.00	1.50	0.046	±	0.046
9.05	1.7	±	0.4	Ref. [52], $\sqrt{s}=4.551$ GeV					
9.15	1.7	±	0.4						
9.25	1.9	±	0.5						

TABLE A.1: (Part I) Differential cross section data for the reactions: $\bar{p} + p \rightarrow \pi^- + \pi^+$.

$\bar{p} + p \rightarrow \pi^- + \pi^+$ (II)				
Ref. [46], $\sqrt{s}=3.68$ GeV				
$-t$ [GeV ²]	$-t_{min}$	$-t_{max}$	$d\sigma/dt$ [nb/GeV ²]	
0.65	0.55	0.75	0.94	± 0.16
0.75	0.65	0.85	0.83	± 0.15
0.85	0.75	0.95	0.70	± 0.14
0.95	0.85	1.05	0.59	± 0.13
1.05	0.95	1.15	0.60	± 0.14
1.15	1.05	1.25	0.52	± 0.14
1.3	1.1	1.5	0.274	± 0.070
1.5	1.3	1.7	0.172	± 0.055
1.7	1.5	1.9	0.149	± 0.055
1.9	1.7	2.1	0.141	± 0.055
2.1	1.9	2.3	0.157	± 0.063
2.3	2.1	2.5	0.064	± 0.045
2.7	2.1	3.3	0.038	± 0.022
9.1	8.3	9.9	0.016	± 0.012
9.75	9.25	10.25	0.020	± 0.014
10.25	9.75	10.75	0.048	± 0.020
10.6	10.4	10.8	0.097	± 0.040
10.8	10.6	11.0	0.117	± 0.047
11.0	10.8	11.2	0.094	± 0.039
11.2	11.0	11.4	0.180	± 0.047
11.45	11.15	11.75	0.180	± 0.039

TABLE A.2: (Part II) Differential cross section data for the reactions:
 $\bar{p} + p \rightarrow \pi^- + \pi^+$.

Elastic scattering: $\pi^- + p \rightarrow \pi^- + p$					
Ref. [49], $\sqrt{s}=3.747$ GeV					
$-t$ [GeV ²]	$-t_{min}$	$-t_{max}$	$d\sigma/dt$ [mb/GeV ²]		
0.15	0.05	0.025	2.4	±	0.4
0.25	0.15	0.35	1.6	±	0.3
0.40	0.20	0.60	0.70	±	0.15
0.60	0.40	0.80	0.35	±	0.15
Ref. [48], $\sqrt{s}=3.463$ GeV					
0.893	0.737	1.049	0.218	±	0.03924
0.743	0.599	0.887	0.300	±	0.042
0.626	0.536	0.716	0.396	±	0.0594
0.539	0.455	0.623	0.56100	±	0.07293
0.458	0.380	0.536	0.9100	±	0.0819
0.382	0.309	0.455	1.1800	±	0.0944
0.312	0.245	0.379	1.7300	±	0.1211
0.248	0.187	0.309	1.8200	±	0.1274

TABLE A.3: Collection of differential cross section data for the reaction: $\pi^- + p \rightarrow \pi^- + p$. These data are compared to annihilation into charged pion pair assuming crossing symmetry.

Differential cross section $\bar{p} + p \rightarrow K^- + K^+$				
Ref. [46], $\sqrt{s}=3.68$ GeV				
$-t$ [GeV ²]	$-t_{min}$	$-t_{max}$	$d\sigma/dt$ [nb/GeV ²]	
0.35	0.25	0.45	0.940	± 0.230
0.45	0.35	0.55	0.920	± 0.170
0.55	0.45	0.65	1.060	± 0.200
0.65	0.55	0.75	0.274	± 0.094
0.75	0.65	0.85	0.490	± 0.130
0.85	0.75	0.95	0.630	± 0.150
0.95	0.85	1.05	0.310	± 0.110
1.05	0.95	1.15	0.460	± 0.130
1.20	1.00	1.40	0.134	± 0.051
1.40	1.20	1.60	0.110	± 0.045
1.75	1.25	2.25	0.028	± 0.016
2.25	1.75	2.75	0.026	± 0.018

TABLE A.4: Collection of differential cross section data for the reactions: $\bar{p} + p \rightarrow K^- + K^+$. These data are compared to the model in SU3 symmetry.

Total cross section $\bar{p} + p \rightarrow \pi^- + \pi^+$							
Ref.	p_L [GeV]	σ	$\delta\sigma$ [mb]	Ref.	p_L [GeV]	σ	$\delta\sigma$ [mb]
[55]	0.416	0.574	0.009	[63]	2.3	0.049	0.004
	0.505	0.491	0.007	[64]	0.686	0.325	0.080
	0.581	0.453	0.007		0.772	0.427	0.068
	0.681	0.428	0.008		0.861	0.394	0.059
	0.888	0.401	0.010		0.943	0.381	0.057
[56]	0.173	1.530	0.200		1.037	0.326	0.052
	0.198	1.060	0.16		1.098	0.261	0.064
	0.216	1.130	0.16	[68]	2.69	0.028	0.009
	0.231	1.170	0.16	[69]	12.0	0.00010	0.00003
	0.243	0.940	0.14	[59]	8.8	0.004	0.002
	0.266	0.800	0.10	[60]	2.32	0.049	0.004
				[80]	0.3	0.94	0.18
[58]	0.390	0.899	0.054	[62]	1.51	0.087	0.021
	0.490	0.868	0.035		1.65	0.071	0.017
	0.590	0.599	0.026		1.8	0.052	0.016
	0.690	0.416	0.021		1.95	0.063	0.019
	0.780	0.362	0.025		2.15	0.006	0.005
[57]	0.403	0.543	0.059		2.45	0.030	0.013
	0.480	0.366	0.044		2.6	0.017	0.01
	0.537	0.407	0.046		2.75	0.015	0.01
	0.584	0.340	0.047		2.9	0.022	0.013
	0.630	0.283	0.041				
	0.670	0.365	0.049				

TABLE A.5: Collection of total cross section data for the reactions: $\bar{p} + p \rightarrow \pi^- + \pi^+$. These data are compared to the integration of the model.

A.2 Neutral meson pair production

$\bar{p} + p \rightarrow \pi^0 + \pi^0$ (I)									
$\cos \theta_1$	$d\sigma/d\cos \theta$ [nb]								
	$\sqrt{s}=2.911$ GeV		$\sqrt{s}=2.950$ GeV		$\sqrt{s}=2.975$ GeV		$\sqrt{s}=2.979$ GeV		
0.0125	262.48	± 18.61	225.17	± 8.76	172.11	± 5.31	149.72	± 7.40	
0.0375	240.52	± 16.48	194.89	± 8.07	148.17	± 4.85	147.35	± 7.69	
0.0625	186.43	± 14.43	150.23	± 6.85	129.85	± 4.54	114.60	± 6.64	
0.0875	140.74	± 12.96	136.6	± 6.71	103.82	± 3.98	88.20	± 5.49	
0.1125	131.70	± 12.18	80.37	± 4.84	67.34	± 3.17	68.76	± 4.99	
0.1375	102.38	± 10.19	71.20	± 4.52	50.08	± 2.68	42.24	± 3.70	
0.1625	102.96	± 10.00	49.88	± 3.54	34.89	± 2.19	30.10	± 3.04	
0.1875	135.32	± 12.46	72.26	± 4.53	40.07	± 2.31	37.18	± 3.33	
0.2125	187.29	± 14.54	111.08	± 5.74	79.53	± 3.38	77.30	± 5.18	
0.2375	254.03	± 16.61	172.77	± 7.04	149.22	± 4.77	142.61	± 7.12	
0.2625	481.14	± 24.15	293.3	± 9.3	238.54	± 5.96	230.68	± 9.10	
0.2875	525.95	± 25.13	463.10	± 12.06	360.85	± 7.34	359.37	± 11.35	
0.3125	838.84	± 31.86	604.53	± 13.79	500.44	± 8.83	485.18	± 13.60	
0.3375	1035.52	± 35.15	787.60	± 15.75	654.99	± 9.96	643.04	± 15.44	
0.3625	1435.23	± 43.79	1023.72	± 18.37	817.64	± 11.30	796.47	± 17.29	
0.3875	1667.79	± 47.75	1226.85	± 20.81	977.88	± 12.73	977.87	± 20.08	
0.4125	1864.32	± 52.94	1311.65	± 21.75	1089.53	± 13.79	1014.17	± 20.80	
0.4375	2034.9	± 60.75	1459.26	± 24.27	1131.32	± 14.36	1067.47	± 21.84	
0.4625	2113.91	± 75.31	1532.84	± 28.8	1303.57	± 17.49	1285.92	± 27.19	
0.4875	1897.16	± 102.29	1616.50	± 37.81	1353.97	± 21.95	1397.69	± 35.10	
0.5125							1414.55	± 54.81	

TABLE A.6: (Part I) Collection of angular distribution data for the reaction: $\bar{p} + p \rightarrow \pi^0 + \pi^0$ from Ref. [75].

$\bar{p} + p \rightarrow \pi^0 + \pi^0$ (II)				
$\cos \theta_1$	$d\sigma/d\cos \theta$ [nb]			
	$\sqrt{s}=2.981$ GeV	$\sqrt{s}=2.985$ GeV	$\sqrt{s}=2.990$ GeV	$\sqrt{s}=2.994$ GeV
0.0125	167.49 ± 5.65	144.95 ± 6.89	140.51 ± 4.27	139.55 ± 5.46
0.0375	150.99 ± 5.44	154.17 ± 7.37	136.77 ± 4.38	129.83 ± 5.39
0.0625	122.40 ± 4.67	120.04 ± 6.25	117.11 ± 3.99	112.99 ± 5.07
0.0875	97.53 ± 4.12	80.14 ± 4.89	80.64 ± 3.18	84.66 ± 4.13
0.1125	66.85 ± 3.47	52.68 ± 3.90	59.93 ± 2.72	55.51 ± 3.33
0.1375	40.61 ± 2.61	42.32 ± 3.49	40.19 ± 2.20	28.78 ± 2.25
0.1625	29.52 ± 2.08	26.21 ± 2.53	20.71 ± 1.45	25.06 ± 2.11
0.1875	33.16 ± 2.14	31.48 ± 2.79	31.97 ± 1.85	32.94 ± 2.38
0.2125	71.45 ± 3.42	61.18 ± 4.18	64.01 ± 2.81	58.06 ± 3.35
0.2375	133.94 ± 4.78	137.05 ± 6.43	123.90 ± 3.96	107.16 ± 4.62
0.2625	228.63 ± 6.23	226.95 ± 8.44	207.40 ± 5.14	203.04 ± 6.48
0.2875	354.74 ± 7.88	325.05 ± 9.95	321.41 ± 6.33	296.14 ± 7.64
0.3125	489.14 ± 9.48	466.64 ± 12.15	432.05 ± 7.49	421.49 ± 9.41
0.3375	621.29 ± 10.58	621.95 ± 14.22	545.99 ± 8.40	564.29 ± 10.92
0.3625	774.10 ± 11.76	752.67 ± 15.47	700.25 ± 9.50	690.83 ± 12.13
0.3875	977.09 ± 13.88	925.67 ± 17.88	866.98 ± 10.99	848.53 ± 13.89
0.4125	1059.71 ± 14.60	989.42 ± 18.95	945.52 ± 11.72	934.08 ± 14.94
0.4375	1111.99 ± 15.46	1072.81 ± 20.27	973.21 ± 12.16	993.25 ± 15.71
0.4625	1260.93 ± 18.34	1188.49 ± 23.56	1134.76 ± 14.51	1108.17 ± 18.23
0.4875	1342.39 ± 23.28	1333.10 ± 30.54	1274.57 ± 18.87	1237.84 ± 23.34
0.5125	1286.67 ± 35.10	1267.93 ± 44.31	1287.62 ± 27.53	1163.08 ± 32.10

TABLE A.7: (Part II) Collection of angular distribution data for the reaction: $\bar{p} + p \rightarrow \pi^0 + \pi^0$ from Ref. [75].

$\bar{p} + p \rightarrow \pi^0 + \pi^0$ (III)				
$\cos \theta_1$	$d\sigma/d\cos \theta$ [nb]			
	$\sqrt{s}=3.005$ GeV	$\sqrt{s}=3.050$ GeV	$\sqrt{s}=3.097$ GeV	$\sqrt{s}=3.524$ GeV
0.0125	118.81 ± 6.77	42.89 ± 6.06	54.09 ± 3.04	24.79 ± 0.50
0.0375	131.63 ± 7.40	87.51 ± 10.61	42.86 ± 2.60	25.86 ± 0.48
0.0625	99.60 ± 6.18	53.67 ± 7.17	36.76 ± 2.43	25.79 ± 0.49
0.0875	62.15 ± 4.57	34.65 ± 5.48	28.74 ± 2.14	23.84 ± 0.50
0.1125	32.22 ± 2.87	12.85 ± 2.87	18.33 ± 1.60	24.63 ± 0.47
0.1375	22.04 ± 2.45	7.48 ± 1.76	4.29 ± 0.58	22.78 ± 0.43
0.1625	8.3 ± 1.1	5.98 ± 2.12	3.97 ± 0.60	24.07 ± 0.47
0.1875	15.77 ± 1.94	6.38 ± 2.60	8.00 ± 0.92	21.08 ± 0.45
0.2125	46.71 ± 3.74	26.84 ± 4.82	25.52 ± 1.89	22.17 ± 0.42
0.2375	96.09 ± 5.76	58.18 ± 7.33	41.38 ± 2.36	19.75 ± 0.39
0.2625	202.14 ± 8.81	107.38 ± 10.06	90.67 ± 3.85	17.92 ± 0.38
0.2875	271.01 ± 9.84	137.16 ± 11.63	143.08 ± 4.81	18.75 ± 0.40
0.3125	397.38 ± 12.38	233.43 ± 15.46	185.72 ± 5.38	19.82 ± 0.41
0.3375	512.76 ± 14.10	297.59 ± 18.28	229.83 ± 5.99	18.79 ± 0.39
0.3625	636.28 ± 15.77	374.42 ± 20.40	282.20 ± 6.83	22.62 ± 0.49
0.3875	766.29 ± 17.48	513.77 ± 24.63	339.67 ± 7.51	24.95 ± 0.54
0.4125	863.65 ± 19.29	505.10 ± 25.13	378.08 ± 7.98	30.94 ± 0.62
0.4375	934.48 ± 20.42	477.79 ± 24.54	424.89 ± 8.67	36.25 ± 0.76
0.4625	1042.69 ± 23.26	528.94 ± 26.38	464.32 ± 9.29	40.07 ± 0.86
0.4875	1127.80 ± 29.09	645.03 ± 33.49	570.94 ± 10.98	50.36 ± 0.97
0.5125	1222.92 ± 41.34	793.88 ± 46.94	766.99 ± 15.24	55.18 ± 1.14
0.5375			882.73 ± 21.92	68.75 ± 1.39
0.5625				88.79 ± 1.58
0.5875				118.08 ± 2.03
0.6125				174.09 ± 2.19
0.6375				247.08 ± 1.58

TABLE A.8: (Part III) Collection of angular distribution data for the reaction: $\bar{p} + p \rightarrow \pi^0 + \pi^0$ from Ref. [75].

$\bar{p} + p \rightarrow \pi^0 + \pi^0$ (IV)								
$\cos \theta_1$	$d\sigma/d\cos \theta$ [nb]							
	$\sqrt{s}=3.556$ GeV		$\sqrt{s}=3.591$ GeV		$\sqrt{s}=3.595$ GeV		$\sqrt{s}=3.613$ GeV	
0.0125	22.50	\pm 1.33	21.84	\pm 1.25	23.47	\pm 1.34	22.76	\pm 1.17
0.0375	24.55	\pm 1.48	21.69	\pm 1.32	25.41	\pm 1.48	19.90	\pm 1.11
0.0625	24.14	\pm 1.47	23.76	\pm 1.40	20.03	\pm 1.34	23.97	\pm 1.28
0.0875	21.82	\pm 1.33	23.96	\pm 1.37	23.88	\pm 1.42	24.22	\pm 1.24
0.1125	25.42	\pm 1.47	25.04	\pm 1.38	24.54	\pm 1.43	26.26	\pm 1.27
0.1375	22.02	\pm 1.40	23.43	\pm 1.38	24.27	\pm 1.46	24.53	\pm 1.25
0.1625	23.52	\pm 1.45	24.45	\pm 1.39	27.86	\pm 1.57	25.33	\pm 1.27
0.1875	20.93	\pm 1.31	24.31	\pm 1.37	23.78	\pm 1.41	24.08	\pm 1.20
0.2125	21.16	\pm 1.32	23.39	\pm 1.32	23.19	\pm 1.37	21.41	\pm 1.11
0.2375	19.84	\pm 1.31	21.96	\pm 1.31	23.25	\pm 1.41	23.23	\pm 1.20
0.2625	17.90	\pm 1.21	23.83	\pm 1.35	25.46	\pm 1.48	21.87	\pm 1.15
0.2875	16.96	\pm 1.12	21.00	\pm 1.21	20.79	\pm 1.28	22.77	\pm 1.16
0.3125	16.41	\pm 1.13	21.78	\pm 1.23	21.10	\pm 1.27	21.73	\pm 1.10
0.3375	21.39	\pm 1.33	20.24	\pm 1.24	21.07	\pm 1.33	20.95	\pm 1.13
0.3625	21.67	\pm 1.32	21.09	\pm 1.23	21.56	\pm 1.33	20.78	\pm 1.12
0.3875	21.98	\pm 1.29	19.33	\pm 1.13	22.98	\pm 1.30	20.46	\pm 1.06
0.4125	25.97	\pm 1.46	24.62	\pm 1.35	22.01	\pm 1.32	21.81	\pm 1.12
0.4375	27.42	\pm 1.5	31.95	\pm 1.54	28.19	\pm 1.52	28.40	\pm 1.31
0.4625	36.32	\pm 1.66	35.30	\pm 1.55	32.53	\pm 1.58	29.59	\pm 1.31
0.4875	39.35	\pm 1.83	39.47	\pm 1.66	36.21	\pm 1.69	36.59	\pm 1.45
0.5125	47.81	\pm 2.00	41.59	\pm 1.74	42.27	\pm 1.86	42.19	\pm 1.60
0.5375	62.30	\pm 2.28	51.37	\pm 1.89	49.68	\pm 1.96	46.03	\pm 1.62
0.5625	77.13	\pm 2.66	68.77	\pm 2.31	65.54	\pm 2.35	60.09	\pm 1.89
0.5875	110.37	\pm 3.32	92.95	\pm 2.78	84.94	\pm 2.79	84.27	\pm 2.40
0.6125	164.49	\pm 4.54	129.89	\pm 3.47	117.05	\pm 3.46	111.30	\pm 2.84
0.6375	245.61	\pm 7.41	180.27	\pm 5.15	180.75	\pm 5.45	165.65	\pm 4.23
0.6625							227.43	\pm 8.16

TABLE A.9: (Part IV) Collection of angular distribution data for the reaction: $\bar{p} + p \rightarrow \pi^0 + \pi^0$ from Ref. [75].

$\bar{p} + p \rightarrow \pi^0 + \pi^0$ (V)							
$\cos \theta_1$	$d\sigma/d\cos \theta$ [nb]						
	$\sqrt{s}=3.616$ GeV	$\sqrt{s}=3.619$ GeV	$\sqrt{s}=3.621$ GeV	$\sqrt{s}=3.686$ GeV	$\sqrt{s}=3.686$ GeV	$\sqrt{s}=3.686$ GeV	$\sqrt{s}=3.686$ GeV
0.0125	19.87 ± 1.16	23.59 ± 1.77	20.37 ± 1.06	16.65 ± 1.21			
0.0375	19.73 ± 1.18	20.48 ± 1.63	19.73 ± 1.06	16.48 ± 1.19			
0.0625	23.46 ± 1.32	22.21 ± 1.68	23.33 ± 1.21	16.49 ± 1.18			
0.0875	23.25 ± 1.30	21.87 ± 1.69	24.07 ± 1.19	20.46 ± 1.36			
0.1125	21.24 ± 1.19	23.70 ± 1.73	22.71 ± 1.15	17.03 ± 1.23			
0.1375	20.22 ± 1.18	24.56 ± 1.76	22.38 ± 1.14	20.74 ± 1.31			
0.1625	23.90 ± 1.31	24.88 ± 1.83	23.77 ± 1.20	23.40 ± 1.41			
0.1875	22.64 ± 1.25	23.50 ± 1.73	23.08 ± 1.18	22.80 ± 1.45			
0.2125	24.83 ± 1.27	23.29 ± 1.68	24.51 ± 1.17	22.89 ± 1.38			
0.2375	21.62 ± 1.22	23.59 ± 1.73	22.74 ± 1.17	22.76 ± 1.36			
0.2625	22.63 ± 1.24	24.00 ± 1.75	27.04 ± 1.27	23.34 ± 1.41			
0.2875	22.13 ± 1.21	20.95 ± 1.59	21.63 ± 1.11	19.56 ± 1.30			
0.3125	18.36 ± 1.07	21.89 ± 1.59	21.43 ± 1.07	19.30 ± 1.25			
0.3375	17.59 ± 1.07	21.18 ± 1.63	20.39 ± 1.08	19.69 ± 1.24			
0.3625	18.63 ± 1.10	21.93 ± 1.64	19.73 ± 1.06	18.49 ± 1.24			
0.3875	18.55 ± 1.05	25.00 ± 1.69	21.93 ± 1.08	21.07 ± 1.32			
0.4125	23.81 ± 1.23	22.93 ± 1.65	25.30 ± 1.18	19.58 ± 1.22			
0.4375	21.77 ± 1.18	26.22 ± 1.80	26.01 ± 1.22	18.00 ± 1.18			
0.4625	27.04 ± 1.30	34.17 ± 2.02	28.24 ± 1.23	20.81 ± 1.29			
0.4875	27.72 ± 1.30	34.97 ± 2.04	32.34 ± 1.31	24.30 ± 1.38			
0.5125	36.82 ± 1.54	40.95 ± 2.28	41.50 ± 1.55	25.68 ± 1.39			
0.5375	46.95 ± 1.73	47.75 ± 2.39	46.44 ± 1.61	34.78 ± 1.71			
0.5625	57.33 ± 1.95	65.12 ± 2.86	59.95 ± 1.86	47.74 ± 1.96			
0.5875	78.09 ± 2.40	84.32 ± 3.43	78.72 ± 2.23	59.80 ± 2.30			
0.6125	111.28 ± 2.99	106.29 ± 4.01	109.35 ± 2.73	88.88 ± 3.02			
0.6375	149.25 ± 4.22	159.21 ± 5.95	155.16 ± 3.93	130.39 ± 4.07			
0.6625	212.49 ± 7.89	193.04 ± 10.17	213.72 ± 7.16	180.87 ± 6.51			

TABLE A.10: (Part V) Collection of angular distribution data for the reaction: $\bar{p} + p \rightarrow \pi^0 + \pi^0$ from Ref. [75].

$\bar{p} + p \rightarrow \eta + \eta$ (I)												
$\cos \theta_1$	$d\sigma/d\cos \theta$ [nb]											
	$\sqrt{s}=2.950$ GeV			$\sqrt{s}=2.975$ GeV			$\sqrt{s}=2.979$ GeV			$\sqrt{s}=2.981$ GeV		
0.025	193.12	±	18.01	158.74	±	11.31	182.41	±	19.44	147.10	±	10.93
0.075	230.23	±	19.96	176.09	±	12.04	193.42	±	20.28	163.81	±	11.55
0.125	246.47	±	20.76	196.39	±	12.92	177.14	±	19.21	180.71	±	12.21
0.175	282.37	±	22.54	220.93	±	13.95	170.62	±	19.08	160.57	±	11.56
0.225	283.60	±	23.31	219.63	±	14.33	229.78	±	23.21	171.87	±	12.15
0.275	290.78	±	24.66	218.71	±	14.85	202.50	±	22.36	188.12	±	13.37
0.325	376.97	±	30.18	283.18	±	17.95	248.42	±	26.19	237.59	±	16.09
0.375	485.65	±	37.25	345.39	±	21.80	391.53	±	36.20	368.88	±	21.97
0.425	600.43	±	47.62	618.08	±	32.99	525.96	±	48.01	640.66	±	33.17
0.475	905.62	±	76.00	818.67	±	47.34	872.67	±	76.54	876.45	±	47.60
0.525	1393.89	±	157.83	936.16	±	76.44	1200.29	±	135.91	1126.67	±	83.06
$\cos \theta_1$	$\sqrt{s}=2.985$ GeV			$\sqrt{s}=2.990$ GeV			$\sqrt{s}=2.994$ GeV			$\sqrt{s}=3.005$ GeV		
0.025	167.80	±	16.78	124.97	±	9.50	140.00	±	12.47	135.82	±	16.23
0.075	161.01	±	16.61	151.64	±	10.75	139.74	±	12.50	113.17	±	14.99
0.125	170.08	±	17.01	155.45	±	10.65	149.47	±	12.91	98.49	±	14.07
0.175	187.62	±	17.81	153.74	±	10.84	159.55	±	13.53	148.79	±	17.78
0.225	169.69	±	17.32	154.19	±	11.31	133.47	±	12.73	138.36	±	17.43
0.275	154.57	±	16.77	162.88	±	11.88	128.63	±	12.99	124.40	±	17.25
0.325	231.27	±	22.05	220.53	±	15.18	210.86	±	17.76	203.51	±	23.19
0.375	391.62	±	32.63	335.00	±	20.39	289.22	±	22.38	299.89	±	30.77
0.425	600.45	±	45.65	558.20	±	30.54	507.61	±	34.07	508.31	±	46.40
0.475	821.20	±	64.32	854.50	±	45.42	767.85	±	51.30	808.86	±	71.49
0.525	1163.81	±	117.56	1016.55	±	72.80	961.70	±	85.34	1176.03	±	124.66

TABLE A.11: (Part I) Collection of angular distribution data for the reaction: $\bar{p} + p \rightarrow \eta + \eta$ from Ref. [75].

$\bar{p} + p \rightarrow \eta + \eta$ (II)											
$\sqrt{s}=3.097$ GeV				$\sqrt{s}=3.526$ GeV				$\sqrt{s}=3.617$ GeV			
$\cos \theta_1$	$d\sigma/d\cos \theta$ [nb]			$\cos \theta_1$	$d\sigma/d\cos \theta$ [nb]			$\cos \theta_1$	$d\sigma/d\cos \theta$ [nb]		
0.025	42.30	±	4.64	0.025	6.58	±	0.57	0.025	4.25	±	0.57
0.075	39.79	±	4.59	0.075	9.06	±	0.68	0.075	3.65	±	0.52
0.125	46.39	±	4.94	0.125	12.26	±	0.79	0.125	3.86	±	0.53
0.175	41.18	±	4.63	0.175	13.02	±	0.82	0.175	4.56	±	0.59
0.225	37.99	±	4.54	0.225	12.60	±	0.81	0.225	4.93	±	0.63
0.275	43.37	±	5.08	0.275	11.10	±	0.76	0.275	4.79	±	0.63
0.325	77.42	±	7.25	0.325	11.33	±	0.80	0.325	4.70	±	0.64
0.375	191.65	±	12.40	0.375	13.19	±	0.89	0.375	4.87	±	0.68
0.425	304.63	±	17.08	0.425	20.82	±	1.18	0.425	6.47	±	0.81
0.475	484.60	±	25.33	0.475	38.71	±	1.75	0.475	11.35	±	1.13
0.525	602.23	±	36.72	0.525	69.45	±	2.62	0.525	20.16	±	1.67
0.575	961.94	±	84.37	0.575	115.25	±	4.02	0.575	37.45	±	2.66
				0.625	197.53	±	7.15	0.625	76.24	±	5.03
				0.675	328.57	±	19.20	0.675	88.80	±	9.31
$\sqrt{s}=2.911$ GeV				$\sqrt{s}=3.592$ GeV							
0.05	287.44	±	36.21	0.05	4.76	±	0.63				
0.15	428.42	±	44.67	0.15	5.32	±	0.67				
0.25	439.82	±	48.28	0.25	5.18	±	0.67				
0.35	589.90	±	66.37	0.35	4.22	±	0.64				
0.45	1203.85	±	136.31	0.45	10.18	±	1.09				
				0.55	31.40	±	2.44				
				0.65	116.34	±	8.82				

TABLE A.12: (Part II) Collection of angular distribution data for the reaction: $\bar{p}+p \rightarrow \eta+\eta$ from Ref. [75].

$\bar{p} + p \rightarrow \pi^0 + \eta$ (I)									
$\cos \theta_1$	$d\sigma/d\cos \theta$ [nb]								
	$\sqrt{s}=2.950$ GeV		$\sqrt{s}=2.975$ GeV		$\sqrt{s}=2.979$ GeV		$\sqrt{s}=2.981$ GeV		
-0.475	730.04	± 31.74	541.67	± 16.93	571.02	± 27.41	511.62	± 15.91	
-0.425	388.63	± 16.77	307.20	± 9.91	334.72	± 16.91	284.20	± 9.44	
-0.375	223.91	± 11.49	148.31	± 6.21	186.55	± 11.19	156.38	± 6.38	
-0.325	168.10	± 9.55	110.40	± 5.91	107.46	± 8.44	100.94	± 5.02	
-0.275	178.03	± 9.73	125.03	± 5.61	132.57	± 9.40	130.98	± 5.70	
-0.225	201.10	± 10.47	163.07	± 6.48	132.98	± 9.27	159.60	± 6.37	
-0.175	244.69	± 11.41	196.40	± 7.22	176.72	± 10.68	186.47	± 6.94	
-0.125	260.33	± 12.12	216.11	± 7.67	229.61	± 12.82	229.26	± 7.85	
-0.075	274.07	± 12.52	224.68	± 7.75	202.52	± 11.73	225.75	± 7.84	
-0.025	290.65	± 13.14	225.83	± 7.95	241.82	± 13.17	228.91	± 7.91	
0.025	263.27	± 12.34	227.88	± 7.92	232.19	± 12.86	238.78	± 8.09	
0.075	251.74	± 12.31	238.33	± 8.42	247.84	± 13.64	242.72	± 8.41	
0.125	260.76	± 12.82	223.65	± 8.12	208.10	± 12.35	199.49	± 7.43	
0.175	233.82	± 12.14	195.19	± 7.64	192.75	± 12.07	180.31	± 7.25	
0.225	220.66	± 12.11	168.40	± 7.37	130.37	± 9.83	154.57	± 6.77	
0.275	157.05	± 10.45	107.12	± 5.69	122.81	± 9.80	114.50	± 6.04	
0.325	150.24	± 10.81	100.47	± 5.65	129.00	± 10.50	107.88	± 5.99	
0.375	214.19	± 14.41	173.87	± 8.68	147.55	± 12.21	146.95	± 7.60	
0.425	376.64	± 22.75	266.88	± 12.08	345.02	± 22.90	263.46	± 12.18	
0.475	646.67	± 38.04	463.97	± 20.13	565.58	± 36.28	559.55	± 23.40	

TABLE A.13: (Part I) Collection of angular distribution data for the reaction: $\bar{p}+p \rightarrow \pi^0+\eta$ from Ref. [75].

$\bar{p} + p \rightarrow \pi^0 + \eta$ (II)				
$\cos \theta_1$	$d\sigma/d\cos \theta$ [nb]			
	$\sqrt{s}=2.985$ GeV	$\sqrt{s}=2.990$ GeV	$\sqrt{s}=2.994$ GeV	$\sqrt{s}=3.005$ GeV
-0.525			716.65 ± 53.57	534.22 ± 51.17
-0.475	522.18 ± 22.64	539.90 ± 16.28	432.96 ± 16.55	395.36 ± 20.87
-0.425	245.24 ± 12.32	299.40 ± 9.69	264.06 ± 10.71	253.56 ± 14.07
-0.375	152.42 ± 8.79	158.67 ± 6.61	138.28 ± 7.26	114.40 ± 8.60
-0.325	99.48 ± 6.86	108.62 ± 5.27	79.99 ± 5.29	84.04 ± 7.34
-0.275	117.69 ± 7.76	114.23 ± 5.37	93.39 ± 5.60	88.56 ± 7.28
-0.225	142.51 ± 8.27	153.74 ± 6.31	128.24 ± 6.67	107.60 ± 7.87
-0.175	185.2 ± 9.77	178.28 ± 6.67	170.49 ± 7.71	161.27 ± 10.06
-0.125	205.56 ± 10.53	204.16 ± 7.39	198.51 ± 8.62	155.87 ± 10.00
-0.075	207.08 ± 10.39	200.25 ± 7.35	205.47 ± 8.88	158.82 ± 10.27
-0.025	233.18 ± 11.31	219.12 ± 7.80	198.16 ± 8.67	182.44 ± 11.00
0.025	226.21 ± 10.9	223.73 ± 7.97	187.67 ± 8.38	188.63 ± 11.70
0.075	214.13 ± 11.09	223.68 ± 8.02	195.16 ± 8.65	196.65 ± 11.88
0.125	186.98 ± 10.25	197.73 ± 7.55	184.32 ± 8.58	161.45 ± 10.49
0.175	182.93 ± 10.56	183.72 ± 7.46	161.35 ± 8.06	168.55 ± 11.26
0.225	150.36 ± 9.53	144.71 ± 6.72	126.68 ± 7.17	117.31 ± 9.25
0.275	114.52 ± 8.24	107.09 ± 5.89	88.23 ± 6.00	103.98 ± 9.23
0.325	106.52 ± 8.56	102.82 ± 6.01	79.24 ± 5.83	64.54 ± 6.92
0.375	152.05 ± 11.09	152.65 ± 8.17	127.18 ± 8.54	113.17 ± 10.37
0.425	247.17 ± 16.06	282.95 ± 12.97	224.68 ± 12.82	218.68 ± 16.67
0.475	548.61 ± 31.83	520.04 ± 22.00	425.16 ± 22.07	409.81 ± 28.48
0.525			802.27 ± 47.77	696.90 ± 53.93

TABLE A.14: (Part II) Collection of angular distribution data for the reaction: $\bar{p} + p \rightarrow \pi^0 + \eta$ from Ref. [75].

$\bar{p} + p \rightarrow \pi^0 + \eta$ (III)						
$\cos \theta_1$	$d\sigma/d\cos \theta$ [nb]					
	$\sqrt{s}=3.097$ GeV		$\sqrt{s}=3.526$ GeV		$\sqrt{s}=3.617$ GeV	
-0.675						60.60 \pm 2.01
-0.625						23.82 \pm 1.01
-0.525	389.29	\pm 14.17	28.31	\pm 0.82	7.12	\pm 0.49
-0.475	231.15	\pm 7.63	10.13	\pm 0.46	4.42	\pm 0.36
-0.425	109.47	\pm 4.72	12.49	\pm 0.52	4.97	\pm 0.41
-0.375	51.52	\pm 3.03	14.31	\pm 0.55	5.82	\pm 0.42
-0.325	38.38	\pm 2.65	14.07	\pm 0.54	5.69	\pm 0.43
-0.275	51.90	\pm 3.05	12.29	\pm 0.50	4.24	\pm 0.37
-0.225	73.64	\pm 3.61	10.61	\pm 0.48	3.44	\pm 0.34
-0.175	88.08	\pm 4.10	6.73	\pm 0.38	2.42	\pm 0.26
-0.125	82.78	\pm 3.95	4.41	\pm 0.30	1.83	\pm 0.22
-0.075	88.51	\pm 4.18	3.45	\pm 0.26	1.76	\pm 0.24
-0.025	94.98	\pm 4.30	2.64	\pm 0.23	1.55	\pm 0.22
0.025	94.39	\pm 4.36	2.61	\pm 0.22	1.54	\pm 0.21
0.075	86.45	\pm 4.10	3.57	\pm 0.27	1.50	\pm 0.20
0.125	97.22	\pm 4.47	5.52	\pm 0.33	1.57	\pm 0.22
0.175	91.33	\pm 4.32	7.03	\pm 0.38	2.05	\pm 0.24
0.225	76.82	\pm 4.11	9.63	\pm 0.45	3.22	\pm 0.33
0.275	54.50	\pm 3.41	12.63	\pm 0.53	3.72	\pm 0.34
0.325	39.77	\pm 3.00	14.01	\pm 0.55	5.40	\pm 0.42
0.375	48.00	\pm 3.50	13.67	\pm 0.57	5.29	\pm 0.42
0.425	108.53	\pm 5.92	11.45	\pm 0.52	5.10	\pm 0.42
0.475	222.83	\pm 10.15	12.81	\pm 0.58	4.88	\pm 0.42
0.525	410.95	\pm 17.44	27.97	\pm 0.92	8.34	\pm 0.59
0.575	703.08	\pm 43.19	86.77	\pm 1.97	23.80	\pm 1.12
0.625			200.01	\pm 3.91	59.19	\pm 2.23
0.675			402.65	\pm 11.82		

TABLE A.15: (Part III) Collection of angular distribution data for the reaction: $\bar{p} + p \rightarrow \pi^0 + \eta$ from Ref. [75].

$\bar{p} + p \rightarrow \pi^0 + \eta$ (IV)					
$\sqrt{s}=2.911$ GeV			$\sqrt{s}=3.592$ GeV		
$\cos \theta_1$	$d\sigma/d\cos \theta$ [nb]		$\cos \theta_1$	$d\sigma/d\cos \theta$ [nb]	
-0.45	888.33	± 53.47	-0.65	98.66	± 4.30
-0.35	364.91	± 23.03	-0.55	18.68	± 0.91
-0.25	262.13	± 18.77	-0.45	4.80	± 0.41
-0.15	323.37	± 21.61	-0.35	5.29	± 0.42
-0.05	330.18	± 21.96	-0.25	4.65	± 0.40
0.05	300.48	± 21.52	-0.15	1.53	± 0.22
0.15	254.71	± 20.26	-0.05	1.72	± 0.23
0.25	199.68	± 17.86	0.05	1.82	± 0.24
0.35	246.02	± 22.84	0.15	2.23	± 0.27
0.45	750.50	± 63.89	0.25	3.94	± 0.37
			0.35	5.85	± 0.46
			0.45	5.85	± 0.51
			0.55	19.22	± 1.03
			0.65	110.20	± 4.49

TABLE A.16: (Part IV) Collection of angular distribution data for the reaction: $\bar{p} + p \rightarrow \pi^0 + \eta$ from Ref. [75].

A.3 Table of acronyms

Acronyms	Full name
CM	Centre of Mass
Lab/L	Laboratory
IC	Ionization Chamber
DC	Drift Chamber
A_y	Analyzing power
FoM	Figure of Merit
SL	Space-Like
TL	Time-Like
FFs	Form Factors

TABLE A.17: Table of the acronyms(left) for the full name(right).

Bibliography

- [1] G. Aad et al. Observation of a new particle in the search for the Standard Model Higgs boson with the ATLAS detector at the LHC. *Phys. Lett. B*, 716(1):1–29, 2012.
- [2] S. Chatrchyan et al. Observation of a new boson at a mass of 125 GeV with the CMS experiment at the LHC. *Phys. Lett. B*, 716(1):30–61, 2012.
- [3] J.J. Aubert et al. The ratio of the nucleon structure functions F_2^N for iron and deuterium. *Phys. Lett. B*, 123:275, 1983.
- [4] E. C. Aschenauer et al. The RHIC SPIN program: achievements and future opportunities. *arXiv:1304.0079*, 2013.
- [5] D. de Florian, R. Sassot, M. Stratmann, and W. Vogelsang. Evidence for polarization of gluons in the proton. *Phys. Rev. Lett.*, 113(1):012001, 2014.
- [6] Y.B. Yang et al. Glue spin and helicity in proton from lattice QCD. *Phys. Rev. Lett.*, 118(10):102001, 2017.
- [7] C.A. Aidala, S.D. Bass, D. Hasch, and G.K. Mallot. The spin structure of the nucleon. *Rev. Mod. Phys.*, 85:655–691, 2013.
- [8] A. Antognini et al. Proton structure from the measurement of 2S-2P transition frequencies of muonic hydrogen. *Science*, 339(6118):417–420, 2013.
- [9] P.J. Mohr, D.B. Newell, and B.N. Taylor. CODATA recommended values of the fundamental physical constants: 2014. *Journal of Physical and Chemical Reference Data*, 45(4):043102, 2016.
- [10] A.H. Gasparian. The New Proton Radius Experiment at Jefferson Lab. *JPS Conf. Proc.*, 13:020052, 2017.
- [11] E.J. Downie. The Proton Radius Puzzle. *EPJ Web Conf.*, 113:05021, 2016.
- [12] D. Marchand. A new platform for research and applications with electrons: the PRAE project. In *EPJ Web Conf.*, volume 138, page 01012, 2017.
- [13] J.C. Bernauer et al. High-precision determination of the electric and magnetic form factors of the proton. *Phys. Rev. Lett.*, 105:242001, 2010.

- [14] J.C. Bernauer. Proton Charge Radius and Precision Tests of QED. In *34th International Symposium on Physics in Collision Bloomington, Indiana, United States*, 2014.
- [15] A. Vorobyev. Proton radius: status and perspectives. In *7th Workshop on Hadron Structure and QCD: From Low to High Energies*, 2016.
- [16] Y. Wang, Yu. M. Bystritskiy, and E. Tomasi-Gustafsson. Antiproton-proton annihilation into charged light meson pairs within effective meson theory. *Phys. Rev. C*, 95:045202, 2017.
- [17] Y. Wang, Yu. M. Bystritskiy, A.I. Ahmadov, and E. Tomasi-Gustafsson. Antiproton-proton annihilation into light neutral meson pairs within an effective meson theory. *arXiv:1706.00205*, 2017.
- [18] Y. Wang, D. Marchand, N. Piskunov, and E. Tomasi-Gustafsson. Neutron polarimetry in the momentum range 1-6 gev. *EPJ Web Conf.*, 138:01023, 2017.
- [19] W. Erni et al. Physics performance report for panda: strong interaction studies with antiprotons. *arXiv:0903.3905*, 2009.
- [20] A.A. Carter, M. Coupland, E. Eisenhandler, C. Franklyn, W.R. Gibson, et al. Measurement of the polarization parameter for antiproton-proton annihilation into charged pion and kaon pairs between 1.0 and 2.2 GeV/c. *Nucl. Phys. B*, 127(2):202 – 241, 1977.
- [21] V.A. Matveev, R.M. Muradyan, and A.N. Tavkhelidze. Automodelity in strong interactions. *Teor. Mat. Fiz.*, 15:332–339, 1973.
- [22] S.J. Brodsky and G.R. Farrar. Scaling Laws at Large Transverse Momentum. *Phys. Rev. Lett.*, 31:1153–1156, 1973.
- [23] E. Tomasi-Gustafsson and M.P. Rekalo. New possibility for further measurements of nucleon form factors at large momentum transfer in time-like region: $\bar{p} + p \rightarrow \ell^+ + \ell^-$, $\ell = e$ or μ . *arXiv:0810.4245*, 2008.
- [24] A. Dbeyssi. *Study of the internal structure of the proton with the PANDA experiment at FAIR*. PhD thesis, Université Paris-sud, 2013.
- [25] B. Singh et al. Feasibility studies of time-like proton electromagnetic form factors at PANDA at FAIR. *Eur. Phys. J.*, A52(10):325, 2016.
- [26] B. Moussallam. $\bar{p}p \rightarrow \pi\pi$ in a baryon exchange potential model. *Nucl. Phys.*, A429:429–444, 1984.
- [27] B. Moussallam. Antinucleon-nucleon annihilations into two mesons. *Nucl. Phys.*, A407:413–428, 1983.

- [28] B. Moussallam. Prospects for resonances below 2.1 GeV in $\bar{p}p \rightarrow \pi\pi$ and $\bar{p}p \rightarrow \bar{K}K$. In *Proceedings, 3rd LEAR Workshop: Physics with Antiprotons at LEAR in the ACOL Era.: Tignes (Savoie), France, January 19-26*, pages 203–207, 1986.
- [29] B. Loiseau. $\bar{N}N$ interaction theoretical models. *Nucl. Phys.*, A543:33C–48C, 1992.
- [30] G.Q. Liu and F. Tabakin. Coupled channels study of anti-proton proton reactions. *Phys. Rev.*, C41:665–679, 1990.
- [31] Y. Yan and R. Tegen. Role of tensor meson pole and Δ exchange diagrams in $p\bar{p} \rightarrow \pi^+\pi^-$. *Phys. Rev. C*, 54(3):1441–1450, 1996.
- [32] Y. Yan, R. Tegen, T. Gutsche, and A. Faessler. Neutron proton high-energy charge exchange scattering. *arXiv preprint hep-ph/0112168*, 2001.
- [33] V. Mull, K. Holinde, and J. Speth. Role of final state interactions in the $p\bar{p} \rightarrow \pi^+\pi^-$ annihilation process. *Phys. Lett.*, B275:12–18, 1992.
- [34] M. Kohno and W. Weise. Quark Model Description of Low-energy Proton - Anti-proton Annihilation Into Two Mesons. *Phys. Lett.*, B152:303–307, 1985.
- [35] U. Hartmann, E. Klempt, and J.G. Korner. SU(3) analysis of anti-proton proton annihilation into two mesons. *Phys. Lett.*, B155:163–166, 1985.
- [36] B. El-Bennich and W.M. Kloet. Relativistic treatment of pion wave functions in the annihilation $p\bar{p} \rightarrow \pi^-\pi^+$. *Phys. Rev. C*, 70:034001, 2004.
- [37] A. Hasan et al. Differential cross-sections and analyzing powers for $p\bar{p} \rightarrow \pi^-\pi^+$ and K^-K^+ from 360 MeV/c to 1550 MeV/c. *Nucl. Phys.*, B378:3–51, 1992.
- [38] C.B. Dover, T. Gutsche, M. Maruyama, and A. Faessler. The physics of nucleon - antinucleon annihilation. *Prog. Part. Nucl. Phys.*, 29:87–174, 1992.
- [39] E. Klempt, C. Batty, and J.M. Richard. The antinucleon-nucleon interaction at low energy: annihilation dynamics. *Phys. Rept.*, 413:197–317, 2005.
- [40] J.F. Gunion, S.J. Brodsky, and R. Blankenbecler. Large-angle scattering and the interchange force. *Phys. Rev. D*, 8(1):287, 1973.
- [41] A. Donnachie and P.V. Landshoff. Elastic Scattering and Diffraction Dissociation. *Nucl. Phys.*, B244:322, 1984.
- [42] A. Donnachie and P.V. Landshoff. Multi - Gluon Exchange in pp Elastic Scattering. *Phys. Lett.*, B123:345, 1983.

- [43] S.J. Brodsky. Testing quantum chromodynamics with antiprotons. *Riv. Nuovo Cim.*, 29N9:1–74, 2006. 345(2004).
- [44] J. Van de Wiele and S. Ong. Regge description of two pseudoscalar meson production in antiproton-proton annihilation. *Eur. Phys. J.*, A46:291–298, 2010.
- [45] E. Eisenhandler, W.R. Gibson, C. Hojvat, P.I.P. Kalmus, L.C.Y. Lee, et al. Measurement of differential cross sections for antiproton proton annihilation into charged pion and kaon pairs between 0.79 GeV/c and 2.43 GeV/c. *Nucl. Phys.*, B96:109, 1975.
- [46] T. Buran, A. Eide, P. Helgaker, P. Lehmann, A. Lundby, et al. Anti-proton-proton annihilation into $\pi^+\pi^-$ and K^+K^- at 6.2 GeV/c. *Nucl. Phys.*, B116:51, 1976.
- [47] A. Eide, P. Lehmann, A. Lundby, C. Baglin, P. Briandet, et al. Elastic scattering and two-body annihilations at 5 GeV/c. *Nucl. Phys.*, B60:173–220, 1973.
- [48] D.P. Owen, F.C. Peterson, J. Orear, A.L. Read, D.G. Ryan, et al. High-energy elastic scattering of π^\pm , K^- , and \bar{p} on hydrogen at c.m. angles from 22° to 180° . *Phys. Rev.*, 181:1794–1807, 1969.
- [49] W. F. Baker et al. Elastic forward and backward scattering of π^- and K^- mesons at 5.2 and 7.0 GeV/c. *Nucl. Phys. B*, 25(2):385 – 410, 1971.
- [50] P. Hong. An event generator for interactions between hadrons and nuclei - FRITIOF version 7.0. *Comp. Phys. Comm.*, 71(3):173–192, 1992.
- [51] Z. Asad et al. Elastic Scattering of Charged Mesons, Anti-protons and Protons on Protons at Incident Momenta of 20 GeV/c, 30 GeV/c and 50 GeV/c in the Momentum Transfer Range $0.5\text{GeV}/c^2 < -t < 8\text{GeV}/c^2$. *Nucl. Phys.*, B255:273, 1985.
- [52] A. Berglund, T. Buran, P.J. Carlson, C.J.S. Damerell, I. Endo, et al. A Study of the Reaction $\bar{p}p \rightarrow \pi^-\pi^+$ at 10 GeV/c. *Nucl. Phys.*, B137:276–282, 1978.
- [53] N.A. Stein et al. Comparison of the line reversed channels $\bar{p}p \rightarrow \pi^-\pi^+$ and $\pi^+p \rightarrow p\pi^+$ at 6 GeV/c. *Phys. Rev. Lett.*, 39:378–381, 1977.
- [54] A. Brabson, G. Calvelli, S. Cittolin, P. De Guio, F. Gasparini, et al. A measurement of $\bar{p}p \rightarrow \pi^+\pi^-$ and $\bar{p}p \rightarrow K^+K^-$ for small values of t and u at 3 and 4 GeV/c. *Phys. Lett.*, B42:287–290, 1972.
- [55] G. Bardin, G. Burgun, R. Calabrese, G. Capon, R. Carlin, et al. Determination of the electric and magnetic form-factors of the proton in the timelike region. *Nucl. Phys.*, B411:3–32, 1994.

- [56] G. Bardin, G. Burgun, R. Calabrese, G. Capon, R. Carlin, et al. A Measurement of the $\bar{p}p \rightarrow \pi^+\pi^-$ Reaction for $158 \text{ MeV}/c \leq p(\bar{p}) \leq 275 \text{ MeV}/c$. *Phys. Lett.*, B192:471, 1987.
- [57] F. Sai, S. Sakamoto, and S.S. Yamamoto. Measurement of $\bar{p}p$ annihilation cross-sections into charged particles in the momentum range $374 \text{ MeV}/c - 680 \text{ MeV}/c$. *Nucl. Phys.*, B213:371, 1983.
- [58] T. Tanimori, T. Fujii, T. Kageyama, K. Nakamura, F. Sai, et al. Observation of an enhancement in $\bar{p}p \rightarrow \pi^+\pi^-$, $\bar{p}p \rightarrow K^+K^-$ cross sections at \bar{p} momentum of approximately $500 \text{ MeV}/c$. *Phys. Rev. Lett.*, 55:1835–1838, 1985.
- [59] D.R. Ward, A.J. Simmons, R.E. Ansorge, C.N. Booth, J.R. Carter, et al. Exclusive annihilation processes in 8.8 GeV $\bar{p}p$ interactions and comparisons between $\bar{p}p$ nonannihilations and pp interactions. *Nucl. Phys.*, B172:302, 1980.
- [60] C.K. Chen, T. Fields, D.S. Rhines, and J. Whitmore. $\bar{p}p$ Interactions at $2.32 \text{ GeV}/c$. *Phys. Rev.*, D17:42, 1978.
- [61] G. Bassompierre et al. Measurement of the antiproton-proton annihilation cross-section into $\pi^+\pi^-$ or K^+K^- at $300 \text{ MeV}/c$. *Lettere Al Nuovo Cimento Series 2*, 20(1):29–33, 1977.
- [62] P.S. Eastman et al. A formation study of n anti-n interactions between 1.51 and $2.90 \text{ GeV}/c$. (I). topological and reaction cross-sections. *Nucl. Phys.*, B51:29–56, 1973.
- [63] T. Fields, W.A. Cooper, D.S. Rhines, J. Whitmore, and W.W.M. Allison. Comparison of new data on $\bar{p}p \rightarrow \pi^-\pi^+$ and other two meson states at $2.3 \text{ GeV}/c$. *Phys. Lett.*, B40:503–506, 1972.
- [64] M.A. Mandelkern, R.R. Burns, P.E. Condon, and J. Schultz. Proton-antiproton annihilation into $\pi^+\pi^-$ and K^+K^- from 700 to $1100 \text{ MeV}/c$. *Phys. Rev.*, D4:2658–2666, 1971.
- [65] V. Domingo, G.P. Fisher, L. Marshall Libby, and R. Sears. Two meson final states in interactions of $2.7 \text{ GeV}/c$ $\bar{p}p$. *Phys. Lett. B*, 25(7):486 – 488, 1967.
- [66] C. White, R. Appel, D. S. Barton, G. Bunce, A. S. Carroll, et al. Comparison of 20 exclusive reactions at large t . *Phys. Rev.*, D49:58–78, 1994.
- [67] T. Tanimori, S. Ishimoto, K. Nakamura, K.H. Tanaka, M. Sudou, et al. Experimental Study of the Reactions $\bar{p}p \rightarrow \pi^-\pi^+$ and K^-K^+ Between $360 \text{ MeV}/c$ and $760 \text{ MeV}/c$. *Phys. Rev.*, D41:744, 1990.
- [68] M. Doser et al. $\bar{p}p$ Annihilation Into $\pi^+\pi^-$ and K^+K^- From Atomic p States. *Nucl. Phys.*, A486:493, 1988.

- [69] T.A. Armstrong et al. Backward scattering in $\pi^- p \rightarrow p\pi^-$, $\bar{p}p \rightarrow \pi^+\pi^-$, $K^- p \rightarrow pK^-$ and $\bar{p}p \rightarrow p\bar{p}$ at 8 GeV/c and 12 GeV/c. *Nucl. Phys.*, B284:643, 1987.
- [70] A.A. Carter et al. Measurement of the Polarization Parameter for anti-Proton-Proton Annihilation Into Charged Pion and Kaon Pairs Between 1.0 GeV/c and 2.2 GeV/c. *Nucl. Phys.*, B127:202, 1977.
- [71] H. Nicholson et al. Antiproton-Proton Annihilation into Charged Pion and Kaon Pairs from 0.7 to 2.4 GeV/c. *Phys. Rev. D*, 7:2572–2590, 1973.
- [72] G. Auberson, T. Kinoshita, and A. Martin. Violation of the pomeranchuk theorem and zeros of the scattering amplitudes. *Phys. Rev. D*, 3:3185–3194, 1971.
- [73] W.F. Baker, P.J. Carlson, V. Chabaud, A. Lundby, J. Banaigs, et al. Anti-proton-proton elastic scattering at 3.55 GeV/c. *Nucl. Phys.*, B12:5–8, 1969.
- [74] C.W. Akerlof, P.K. Caldwell, C.T. Coffin, P. Kalbaci, D.I. Meyer, et al. Measurement of the double-charge-exchange reactions $\pi^- p \rightarrow K^+\Sigma^-$ and $K^- p \rightarrow \pi^+\Sigma^-$. *Phys. Rev. Lett.*, 27:539–542, 1971.
- [75] T.A. Armstrong et al. Two-body neutral final states produced in $\bar{p}p$ annihilations at $2.911 \text{ GeV} \leq \sqrt{s} \leq 3.686 \text{ GeV}$. *Phys. Rev.*, D56:2509–2531, 1997.
- [76] M. Ambrogiani et al. Measurements of the magnetic form-factor of the proton in the timelike region at large momentum transfer. *Phys. Rev.*, D60:032002, 1999.
- [77] M. Andreotti, S. Bagnasco, W. Baldini, D. Bettoni, G. Borreani, et al. Measurements of the magnetic form-factor of the proton for timelike momentum transfers. *Phys. Lett.*, B559:20–25, 2003.
- [78] T.A. Armstrong et al. Measurement of the proton electromagnetic form-factors in the timelike region at 8.9 GeV^2 – 13 GeV^2 . *Phys. Rev. Lett.*, 70:1212–1215, 1993.
- [79] L. Gray, T. Papadopoulou, E. Simopoulou, A. Vayaki, T. Kalogeropoulos, and J. Roy. Observations on $\bar{p}d$ annihilations at rest into two pions. *Phys. Rev. Lett.*, 30:1091–1094, 1973.
- [80] G. Bassompierre, G. Binder, P. Dalpiaz, P.F. Dalpiaz, G. Gissinger, et al. Measurement of the Branching Ratio $\Gamma(\bar{p}p \rightarrow e^+e^-)/\Gamma(\bar{p}p \rightarrow \text{Total})$ in anti-Proton-Proton Annihilation at Rest. *Phys. Lett.*, B64:475, 1976.
- [81] Y. Sugimoto, M. Sudou, T. Fujii, Y. Fujii, S. Homma, et al. Search for Structures in the $\bar{p}p \rightarrow \pi^+\pi^-$ and $\bar{p}p \rightarrow K^+K^-$ Cross-sections Between 360 MeV/c and 760 MeV/c. *Phys. Rev.*, D37:583, 1988.

- [82] J.H. Christenson, G.A. Kreiter, P. Nemethy, J. Sculli, and P. Yamin. A search for the XI(2.2) in $\bar{p}p$ formation. *BNL-38385, CONF-860701-7, Print-86-1291 (NYU)*, 1986.
- [83] R.D. Ehrlich, A. Etkin, P. Glodis, V.W. Hughes, K. Kondo, et al. Measurements of the symmetries in the differential cross sections for $\bar{p}p \rightarrow \bar{p}p$ and $\bar{p}p \rightarrow \pi^- \pi^+$ using polarized protons. *Phys. Rev. Lett.*, 28:1147–1150, 1972.
- [84] S. Heppelmann, J.Y. Wu, R. Appel, D.S. Barton, G. Bunce, et al. Hard exclusive hadron nucleon scattering and color transparency. *Nucl. Phys.*, A527:581C–583C, 1991.
- [85] N.A. Stein et al. Comparison of the line-reversed channels $\bar{p}p \rightarrow \pi^- \pi^+$ and $\pi^+ p \rightarrow p \pi^+$ at 6 GeV/c. *Phys. Rev. Lett.*, 39:378–381, 1977.
- [86] T. Buran, Å. Eide, et al. $\pi^- p$ and $K^- p$ elastic scattering at 6.2 GeV/c. *Nucl. Phys. B*, 111(1):1–19, 1976.
- [87] M. Zambrana et al. Analysis of time-like form factor measurements at panda. Technical report, HIM Mainz, 2014.
- [88] G. Bassompierre et al. First Determination of the Proton Electromagnetic Form-Factors at the Threshold of the Timelike Region. *Phys. Lett.*, B68:477, 1977.
- [89] R. Machleidt. High-precision, charge-dependent Bonn nucleon-nucleon potential. *Phys. Rev. C*, 63:024001, 2001.
- [90] K.A. Olive et al. Review of Particle Physics. *Chin. Phys.*, C38:090001, 2014.
- [91] A.I. Akhiezer and M.P. Rekalov. *Hadron Electrodynamics*. Naukova Dumka, Kiev, 1977.
- [92] J. Beringer et al. Review of Particle Physics (RPP). *Phys. Rev.*, D86:010001, 2012.
- [93] J. Guttmann and M. Vanderhaeghen. Theoretical analysis of the $p\bar{p} \rightarrow \pi^0 e^+ e^-$ process within a Regge framework. *Phys. Lett. B*, 719(1):136–142, 2013.
- [94] A.B. Kaidalov. Regge poles in QCD. *arXiv preprint hep-ph/0103011*, 2001.
- [95] E. A. Kuraev, Yu. M. Bystritskiy, V. V. Bytev, A. Dbeyssi, and E. Tomasi-Gustafsson. Annihilation of $\bar{p} + p \rightarrow e^+ + e^- + \pi^0$ and $\bar{p} + p \rightarrow \gamma + \pi^0$ through ω -meson intermediate state. *J. Exp. Theor. Phys.*, 115:93–104, 2012.
- [96] C. Fernandez-Ramirez, E. Moya de Guerra, and J. M. Udias. Effective Lagrangian approach to pion photoproduction from the nucleon. *Annals Phys.*, 321:1408–1456, 2006.

- [97] V.L. Chernyak and A.R. Zhitniskii. Asymptotic form of hadronic form factors in the quark model. *JETP Lett*, 25(11), 1977.
- [98] G.P. Lepage and S.J. Brodsky. Exclusive processes in quantum chromodynamics: the form factors of baryons at large momentum transfer. *Phys. Rev. Lett.*, 43(8):545, 1979.
- [99] M. Ablikim et al. Study of $e^+e^- \rightarrow p\bar{p}$ in the vicinity of $\Lambda(3770)$. *Phys. Lett.*, B735:101–107, 2014.
- [100] B. Aubert. Study of $e^+e^- \rightarrow p\bar{p}$ using initial state radiation with BABAR. *Phys. Rev. D*, 73:012005, 2006.
- [101] W. N. Cottingham, M. Lacombe, B. Loiseau, J. M. Richard, and R. Vinh Mau. Nucleon nucleon interaction from pion nucleon phase shift analysis. *Phys. Rev.*, D8:800–819, 1973.
- [102] Yu.A. Troyan, M. Kh. Anikina, A.V. Belyaev, A.P. Ierusalimov, and A.Yu. Troyan. Elastic $np \rightarrow np(pn)$ scattering at intermediate energies. *Phys. Part. Nucl. Lett.*, 11:101–108, 2014.
- [103] V.V. Anisovich. The resonance $f_0(1500)$: Is it a scalar glueball? *Phys. Lett. B*, 364(3):195 – 198, 1995.
- [104] A. Dbeyssi, E. Tomasi-Gustafsson, G.I. Gakh, and M. Konchatnyi. Proton-antiproton annihilation into massive leptons and polarization. *Nucl. Phys.*, A894:20–40, 2012.
- [105] A. Dbeyssi and E. Tomasi-Gustafsson. Classification of $\bar{p}p$ induced reactions. *Prob. Atomic Sci. Technol.*, 2012N1:84–87, 2012.
- [106] A. Bianconi and E. Tomasi-Gustafsson. Phenomenological analysis of near threshold periodic modulations of the proton timelike form factor. *Phys. Rev. C*, 93(3):035201, 2016.
- [107] A. Bianconi and E. Tomasi-Gustafsson. Periodic interference structures in the timelike proton form factor. *Phys. Rev. Lett.*, 114(23):232301, 2015.
- [108] J.P. Singh, F.X. Lee, and L. Wang. Eta-nucleon coupling constant in QCD with SU(3) symmetry breaking. *Int. J. Mod. Phys.*, A26:947–963, 2011.
- [109] R. Frisch and O. Stern. Über die magnetische ablenkung von wasserstoffmolekülen und das magnetische moment des protons. i. *Zeitschrift für Physik*, 85(1):4–16, 1933.
- [110] R. Hofstadter. Electron scattering and nuclear structure. *Rev. Mod. Phys.*, 28:214–254, 1956.

- [111] M.N. Rosenbluth. High Energy Elastic Scattering of Electrons on Protons. *Phys. Rev.*, 79:615–619, 1950.
- [112] C.S. Wu, E. Ambler, R.W. Hayward, D.D. Hoppes, and R.P. Hudson. Experimental test of parity conservation in beta decay. *Phys. Rev.*, 105:1413–1415, 1957.
- [113] A.I. Akhiezer and M.P. Rekalo. Polarization phenomena in electron scattering by protons in the high energy region. *Sov. Phys. Dokl.*, 13:572, 1968.
- [114] A.I. Akhiezer and M.P. Rekalo. Polarization effects in the scattering of leptons by hadrons. *Sov. J. Part. Nucl.*, 4:277, 1974.
- [115] M. Ablikim et al. Measurement of the cross section for $e^+e^- \rightarrow p\bar{p}$ at center-of-mass energies from 2.0 GeV to 3.07 GeV. *Phys. Lett.*, B630:14–20, 2005.
- [116] M. Sudol, M.C. Mora Espi, E. Becheva, J. Boucher, T. Hennino, et al. Feasibility studies of the time-like proton electromagnetic form factor measurements with PANDA at FAIR. *Eur. Phys. J.*, A44:373–384, 2010.
- [117] T. Massam and A. Zichichi. A one-parameter fit to the electromagnetic form factors of the nucleon. *Il Nuovo Cimento A (1965-1970)*, 43(4):1137–1148, 1966.
- [118] A.Z. Dubnickova, S. Dubnicka, and M.P. Rekalo. Investigation of the nucleon electromagnetic structure by polarization effects in $e^+e^- \rightarrow N\bar{N}$ processes. *Nuovo Cim.*, A109:241–256, 1996.
- [119] N. Dombey. Scattering of polarized leptons at high energy. *Rev. Mod. Phys.*, 41:236–246, 1969.
- [120] M. K. Jones et al. G_{Ep}/G_{Mp} ratio by polarization transfer in $\vec{e}p \rightarrow e\vec{p}$. *Phys. Rev. Lett.*, 84:1398–1402, 2000.
- [121] V. Punjabi, C.F. Perdrisat, K.A. Aniol, F.T. Baker, J. Berthot, et al. Proton elastic form-factor ratios to $Q^2 = 3.5 \text{ GeV}^2$ by polarization transfer. *Phys. Rev. C*, C71:055202, 2005.
- [122] O. Gayou et al. Measurement of G_{Ep}/G_{Mp} in $\vec{e}p \rightarrow e\vec{p}$ to $Q^2 = 5.6 \text{ GeV}^2$. *Phys. Rev. Lett.*, 88:092301, 2002.
- [123] A.J.R. Puckett, E.J. Brash, M.K. Jones, W. Luo, M. Meziane, et al. Recoil Polarization Measurements of the Proton Electromagnetic Form Factor Ratio to $Q^2 = 8.5 \text{ GeV}^2$. *Phys. Rev. Lett.*, 104:242301, 2010.
- [124] C. Perdrisat and V. Punjabi. Nucleon form factors. *Scholarpedia*, 5(8):10204, 2010. revision 143981.

- [125] A.J.R. Puckett, E.J. Brash, O. Gayou, M.K. Jones, L. Pentchev, et al. Final Analysis of Proton Form Factor Ratio Data at $Q^2 = 4.0, 4.8$ and 5.6 GeV^2 . *Phys. Rev. C*, 85:045203, 2012.
- [126] M.E. Christy et al. Measurements of electron proton elastic cross-sections for $0.4 < Q^2 < 5.5 \text{ (GeV/c)}^2$. *Phys. Rev.*, C70:015206, 2004.
- [127] I.A. Qattan, J. Arrington, R.E. Segel, X. Zheng, K. Aniol, et al. Precision Rosenbluth measurement of the proton elastic form-factors. *Phys. Rev. Lett.*, 94:142301, 2005.
- [128] L. Andivahis, Peter E. Bosted, A. Lung, L.M. Stuart, J. Alster, et al. Measurements of the electric and magnetic form-factors of the proton from $Q^2 = 1.75 \text{ GeV/c}^2$ to 8.83 GeV/c^2 . *Phys. Rev.*, D50:5491–5517, 1994.
- [129] E. L. Lomon. Effect of recent R(p) and R(n) measurements on extended Gari-Krumpelmann model fits to nucleon electromagnetic form-factors. *Phys. Rev. C*, 66:045501, 2002.
- [130] M. Guidal, M.V. Polyakov, A.V. Radyushkin, and M. Vanderhaeghen. Nucleon form-factors from generalized parton distributions. *Phys. Rev.*, D72:054013, 2005.
- [131] J.P.B.C. de Melo, T. Frederico, E. Pace, S. Pisano, and G. Salme. Time- and Space-like Nucleon Electromagnetic Form Factors beyond Relativistic Constituent Quark Models. *Phys. Lett.*, B671:153–157, 2009.
- [132] F. Gross, G. Ramalho, and M. T. Pena. Pure S-wave covariant model for the nucleon. *Phys. Rev. C*, 77(1):015202, 2008.
- [133] I. C. Cloët, G. Eichmann, B. El-Bennich, T. Klähn, and C. D. Roberts. Survey of nucleon electromagnetic form factors. *Few-Body Systems*, 46(1):1–36, 2009.
- [134] T. Eden, R. Madey, W.M. Zhang, B.D. Anderson, H. Arenhovel, et al. Electric form factor of the neutron from the ${}^2\text{H}(\vec{e}, e'\vec{n}){}^1\text{H}$ reaction at $Q^2=0.255 \text{ (GeV/c)}^2$. *Phys. Rev. C*, 50:1749–1753, 1994.
- [135] M. Ostrick, C. Herberg, H.G. Andresen, J.R.M. Annand, K. Aulenbacher, et al. Measurement of the Neutron Electric Form Factor $G_{E,n}$ in the Quasifree ${}^2\text{H}(\vec{e}, e'\vec{n})p$ Reaction. *Phys. Rev. Lett.*, 83:276–279, 1999.
- [136] C. Herberg, M. Ostrick, H.G. Andresen, J.R.M. Annand, K. Aulenbacher, et al. Determination of the neutron electric form-factor in the D(e,e' n)p reaction and the influence of nuclear binding. *Eur.Phys.J.*, A5:131–135, 1999.

- [137] I. Passchier, R. Alarcon, T.S. Bauer, D. Boersma, J.F.J. van den Brand, et al. Charge Form Factor of the Neutron from the Reaction ${}^2\vec{H}(\vec{e}, e'n)p$. *Phys. Rev. Lett.*, 82:4988–4991, 1999.
- [138] D.I. Glazier, M. Seimetz, J.R.M. Annand, H. Arenhovel, M. Ases Antelo, et al. Measurement of the electric form-factor of the neutron at $Q^2 = 0.3$ (GeV/c) 2 to 0.8 (GeV/c) 2 . *Eur. Phys. J.*, A24:101–109, 2005.
- [139] S. Riordan, S. Abrahamyan, B. Craver, A. Kelleher, A. Kolarkar, et al. Measurements of the Electric Form Factor of the Neutron up to $Q^2 = 3.4$ GeV 2 Using the Reaction ${}^3\vec{He}(\vec{e}, e'n)pp$. *Phys. Rev. Lett.*, 105(26):262302, 2010.
- [140] M. Meyerhoff, D. Eyl, A. Frey, H.G. Andresen, J.R.M. Annand, et al. First measurement of the electric form-factor of the neutron in the exclusive quasielastic scattering of polarized electrons from polarized He-3. *Phys. Lett.*, B327:201–207, 1994.
- [141] J. Becker, H.G. Andresen, J.R.M. Annand, K. Aulenbacher, K. Beuchel, et al. Determination of the neutron electric form-factor from the reaction ${}^3\vec{He}(\vec{e}, e'n)$ at medium momentum transfer. *Eur.Phys.J.*, A6:329–344, 1999.
- [142] J. Golak, G. Ziemer, H. Kamada, H. Witala, and W. Gloeckle. Extraction of electromagnetic neutron form-factors through inclusive and exclusive polarized electron scattering on polarized He-3 target. *Phys. Rev. C*, 63:034006, 2001.
- [143] J. Bermuth et al. The Neutron charge form-factor and target analyzing powers from ${}^3\vec{He}(\vec{e}, e'n)$ scattering. *Phys. Lett.*, B564:199–204, 2003.
- [144] R. Madey et al. Measurements of G_E^n/G_M^n from the ${}^2\text{H}(\vec{e}, e' \vec{n}){}^1\text{H}$ Reaction to $Q^2 = 1.45$ (GeV/c) 2 . *Phys. Rev. Lett.*, 91(12):122002, 2003.
- [145] G. Warren et al. Measurement of the Electric Form Factor of the Neutron at $Q^2 = 0.5$ and 1.0 GeV $^2/c^2$. *Phys. Rev. Lett.*, 92:042301, 2004.
- [146] E. Geis, M. Kohl, V. Ziskin, T. Akdogan, H Arenhövel, et al. Charge Form Factor of the Neutron at Low Momentum Transfer from the ${}^2\vec{H}(\vec{e}, e'n){}^1\text{H}$ Reaction. *Phys. Rev. Lett.*, 101(4):042501, 2008.
- [147] E. Brash, E. Cisbani, M. Jones, M. Khandaker, N. Liyanage, L. Pentchev, C.F. Perdrisat, V. Punjabi, and B. Wojtsekhowski. Large Acceptance Proton Form Factor Ratio Measurements up to 14.5 GeV 2 Using Recoil-Polarization Method. *JLab proposal 12-07-109*, 2009.
- [148] N. E. Cheung et al. Calibration of the polarimeter POMME at proton energies between 1.05 GeV and 2.4 GeV. *Nucl. Instrum. Meth.*, A363:561–567, 1995.

- [149] L.S. Azhgirey et al. Measurement of analyzing powers for the reaction $\vec{p} + CH_2$ at $p_p = 1.75 \text{ GeV}/c - 5.3 \text{ GeV}/c$. *Nucl. Instrum. Methods*, 538(1):431–441, 2005.
- [150] T. Eden, R. Madey, et al. Electric form factor of the neutron from the ${}^2H(\vec{e}, e'\vec{n}){}^1H$ reaction at $Q^2=0.255 \text{ (GeV}/c)^2$. *Phys. Rev. C*, 50:R1749–R1753, 1994.
- [151] M. A. Abolins, M. T. Lin, R. C. Ruchti, J. G. Horowitz, R. C. Kammerud, N. W. Reay, et al. Measurement of the Polarization Parameter in np Charge-Exchange Scattering from 2 to 12 GeV/c. *Phys. Rev. Lett.*, 30:1183–1185, 1973.
- [152] Yu. A. Troyan, M. Kh. Anikina, A. V. Belyaev, A. P. Ierusalimov, and A. Yu. Troyan. Elastic $np \rightarrow np(pn)$ scattering at intermediate energies. *Phys. Part. Nucl. Lett.*, 11:101–108, 2014.
- [153] M. N. Kreisler, F. Martin, M. L. Perl, M. J. Longo, and S. T. Powell. Neutron-Proton Elastic Scattering from 1 to 6 GeV. *Phys. Rev. Lett.*, 16:1217–1220, 1966.
- [154] B. G. Gibbard et al. Neutron-Proton Elastic Scattering from 8 to 30 GeV/c. *Phys. Rev. Lett.*, 24:22–25, 1970.
- [155] E. L. Miller, M. Elfield, N. W. Reay, N. R. Stanton, M. A. Abolins, M.T. Lin, and K. W. Edwards. Neutron-Proton Charge-Exchange Scattering 3-12 GeV/c. *Phys. Rev. Lett.*, 26(16):984, 1971.
- [156] H. Palevsky, J. A. Moore, R. L. Stearns, H. R. Muether, R. J. Sutter, R. E. Chrien, A. P. Jain, and K. Otnes. np Elastic Charge Exchange in the BeV Energy Region. *Phys. Rev. Lett.*, 9(12):509, 1962.
- [157] S.T. Powell. *Elastic neutron-proton charge exchange scattering between 1.75 GeV/c and 7.20 GeV/c*. PhD thesis, The University of Michigan, 1970.
- [158] P. Adlarson et al. Neutron-proton scattering in the context of the $d^*(2380)$ resonance. *Phys. Rev. C*, 90:035204, 2014.
- [159] J. Ball et al. Angular dependence of analyzing power in np elastic scattering between 0.312 and 1.10 GeV. *Nucl. Phys. A*, 559(4):489 – 510, 1993.
- [160] R. Diebold, D. S. Ayres, S. L. Kramer, A. J. Pawlicki, and A. B. Wicklund. Measurement of the Proton-Neutron Elastic-Scattering Polarization from 2 to 6 GeV/c. *Phys. Rev. Lett.*, 35:632–635, 1975.
- [161] B.D. Anderson, J. Arrington, S. Kowalski, R. Madey, B. Plaster, and A.Yu. Semenov. The Neutron Electric Form Factor at Q^2 up to 7 $(\text{GeV}/c)^2$ from the Reaction ${}^2H(\vec{e}, e'\vec{n}){}^1H$ via Recoil Polarimetry. *Proposal*, 2011.

- [162] N.D. Sergey et al. Chemical identification of dubnium as a decay product of element 115 produced in the reaction $^{48}\text{Ca} + ^{243}\text{Am}$. *Mendelevov Communications*, 15(1):1–4, 2005.
- [163] G.M. Ter-Akopian et al. Two-neutron exchange observed in the $^6\text{He} + ^4\text{He}$ reaction Search for the di-neutron configuration of ^6He . *Phys. Lett. B*, 426(3):251–256, 1998.
- [164] R. Golub and J. M. Pendlebury. Ultra-cold neutrons. *Reports on Progress in Physics*, 42(3):439, 1979.
- [165] D. Blaschke et al. Exploring strongly interacting matter at high densities - NICA White Paper. *Eur. Phys. J. A*, 52(8):267, 2016.
- [166] A. N. Govorov et al. Linac LU-20 as injector of Nuclotron. *Conf. Proc.*, C9608262:349–351, 1996.
- [167] P.Ed. Fiala. Proton-proton data measured by the nucleon-nucleon collaboration at Saturne II. Technical report, Czech Technical University in Prague, 2000.
- [168] A. Abragam. *The Principles of Nuclear Magnetism*. Number 32. Oxford University Press, 1961.
- [169] S. Oh. The adiabatic transitions in a polarized deuteron source. *Nucl. Instrum. Meth.*, 82:189–197, 1970.
- [170] V. V. Fimushkin et al. Development of polarized ion source for the JINR accelerator complex. volume 678, page 012058, 2016.
- [171] S. Polozov et al. Commissioning of New Proton and Light Ion Injector for Nuclotron-NICA. In *7th International Particle Accelerator Conference (IPAC 16)*, Busan, Korea, pages 94–943. JACOW, Geneva, Switzerland, 2016.
- [172] S. Polozov et al. The Perspective of JINR Lu-20 Replacement by a Superconducting Linac. In *7th International Particle Accelerator Conference (IPAC 16)*, Busan, Korea, pages 944–946. JACOW, Geneva, Switzerland, 2016.
- [173] N.N. Agapov, A. D. Kovalenko, and A. I. Malakhov. Nuclotron: main results and development plans. *Atomnaya Ehnergiya*, 2002.
- [174] M. Janek, V. P. Ladygin, V. V. Avdeichikov, et al. Investigation of reactions using polarized and unpolarized deuteron beam at nuclotron: current status and perspectives. In *EPJ Web Conf.*, volume 138, page 01028, 2017.
- [175] P. K. Kurilkin et al. The 270 MeV deuteron beam polarimeter at the Nuclotron Internal Target Station. *Nucl. Instrum. Meth.*, A642:45–51, 2011.

- [176] L.S. Azhgirey et al. Intermediate-energy polarimeter for the measurement of the deuteron and proton beam polarization at the JINR synchrotron. *Nucl. Instrum. Meth. A*, 497:340–349, 2003.
- [177] V. P. Ladygin. Analyzing power of pp and np elastic scattering at momenta between 2000 and 6000 MeV/c and polarimetry at LHE. Technical Report E13-99-123, Joint Inst. Nucl. Res., Dubna, 1999.
- [178] J. Bystricky and F. Lehar. Nucleon-nucleon scattering data. *Fachinformationszentrum Karlsruhe*, 11, 1981.
- [179] V. Punjabi, R. Abegg, S. Belostotsky, M. Boivin, A. Boudard, et al. Measurement of polarization transfer κ_0 and tensor analyzing power T_{20} in the backward elastic dp scattering. *Phys. Lett.*, B350:178–183, 1995.
- [180] V.P. Balandin, A.E. Baskakov, S.N. Basilev, E. Brash, Yu.P. Bushuev, O.P. Gavrishchuk, et al. Measurement of analyzing power for the reaction $\vec{p} + \text{CH}_2$ at polarized proton momentum of 7.5 GeV/c (ALPOM2 proposal). *Physics of Particles and Nuclei*, 45(1):330–332, 2014.
- [181] V.V. Glagolev et al. STRELA Experimental Setup for studying Charge-Exchange Processes. *Nucl. Exp. Tech.*, 56:387–397, 2013.
- [182] V.D. Peshekhonov. Wire gaseous coordinate detectors and their applications in biomedical research. *Sov. J. Particles Nucl. (Engl. Transl.); (United States)*, 17:5, 1986.
- [183] N. V. Vlasov et al. A calorimeter for detecting hadrons with energies of 10-100 GeV. *Instrum. Exp. Tech.*, 49(1):41–55, 2006.
- [184] Ph. Abbon, E. Albrecht, V. Yu. Alexakhin, Yu. Alexandrov, G.D. Alexeev, M.G. Alekseev, A. Amoroso, H. Angerer, V.A. Anosov, B. Badefek, et al. The COMPASS experiment at CERN. *Nucl. Instrum. Meth. A*, 577(3):455–518, 2007.
- [185] C.F. Parkman. VMEbus at CERN: a brief review. Technical Report CERN-DD-85-28, CERN, Geneva, 1985.
- [186] J. Bystricky, J. Derégel, F. Lehar, A. de Lesquen, L. van Rossum, J.M. Fontaine, F. Perrot, C.A. Whitten, T. Hasegawa, C.R. Newsom, et al. A proton and neutron beam polarimeter at SATURNE II. *Nuclear Instruments and Methods in Physics Research Section A: Accelerators, Spectrometers, Detectors and Associated Equipment*, 239(2):131–138, 1985.
- [187] I. M. Sitnik. Optimum target thickness for polarimeters. *Nucl. Instrum. Meth.*, A527:278–283, 2004.

-
- [188] B. Bonin et al. Measurement of the Inclusive pC Analyzing Power and Cross-section in the 1 GeV Region and Calibration of the New Polarimeter POMME. *Nucl. Instrum. Meth. A*, 288:379, 1990.
- [189] I. G. Alekseev et al. Measurement of the carbon analyzing power for the momenta range 1.35 GeV/ c to 2.02 GeV/ c . *Nucl. Instrum. Meth.*, A434:254–260, 1999.
- [190] O. Gayou. *Proton form factors, measurement of the proton form factors ratio $\mu_p G_E$* . PhD thesis, Université Blaise Pascal, 2003.

Titre : Etude des réactions d'annihilation proton-antiproton et contribution expérimentale à la polarimétrie hadronique

Mots clés : physique hadronique, phénoménologie, polarimétrie

Résumé : Ce travail de thèse s'inscrit dans le cadre de la physique hadronique et consiste en des études phénoménologiques et expérimentales dédiées à la structure interne des nucléons et reliées aux mesures des facteurs de forme des hadrons dans les régions temps et espace.

Un programme expérimental dont le but est la mesure des facteurs de forme électromagnétiques du proton dans la région temps est prévu auprès du détecteur de grande acceptance PANDA (anti-Proton Annihilation at Darmstadt) à partir des réactions d'annihilation $\bar{p}p \rightarrow e^+e^-$ dans l'intervalle en énergie $2.25(1.5) < \sqrt{s}(pL) < 5.47(15)$ GeV (GeV/c). Un modèle effectif de mésons a été développé pour évaluer la section efficace d'annihilation $\bar{p}p$ en une paire de pions légers, dans le domaine en énergie d'intérêt. Un facteur de forme logarithmique a été introduit pour modéliser la nature composite des hadrons en interaction. Ce modèle s'applique aussi à la diffusion élastique pion proton, par symétrie de croisement, et à la production d'une paire de kaons chargés, suivant la symétrie SU(3). Le modèle a été ensuite étendu à différentes voies neutres telles $\pi^0\text{-}\pi^0$, $\eta\text{-}\eta$, $\pi^0\text{-}\eta$. Les résultats obtenus sont présentés et comparés aux données existantes.

Dans la région espace, j'ai contribué à l'expérience ALPOM2 (JINR Dubna, Russie), la seule expérience actuellement capable de mesurer les pouvoirs d'analyse protons et neutrons pour les mesures à JLab avec plusieurs types de cibles. Expérimentalement, un faisceau polarisé de protons ou de neutrons de 3.0, 3.75 et 4.2 GeV/c est obtenu par cassure du faisceau de deutons polarisés du Nuclotron et les fragments chargés issus des collisions avec les cibles de C, CH₂, CH et Cu sont mesurés. Les résultats expérimentaux de l'analyse préliminaire sont présentés.

Title : Study of antiproton-proton annihilation reactions and experimental contribution to hadron polarimetry

Keywords : Hadronic physics, phenomenology, polarimetry

Abstract : This thesis work, set in the framework of hadron physics, reports on a phenomenological and an experimental studies dedicated to nucleon internal structure, both related to hadron electromagnetic form factor measurements in the time-like and in the space-like regions.

An experimental program aiming to determine the proton electromagnetic form factors in the time-like region is planned with the PANDA (anti-Proton Annihilation at Darmstadt) large acceptance detector through the annihilation reaction $\bar{p}p \rightarrow e^+e^-$ in the energy range $2.25(1.5) < \sqrt{s}(pL) < 5.47(15)$ GeV (GeV/c). An effective meson model has been developed to evaluate the cross section of $\bar{p}p$ annihilation into light meson pairs, in the energy domain relevant to the PANDA experiment. A logarithmic form factor is introduced to account for the composite nature of the interacting hadrons. The model was also applied to πp elastic scattering, using crossing symmetry, and to charged kaon pair production, on the basis of SU(3) symmetry. The model has then been extended to different neutral channels $\pi^0\text{-}\pi^0$, $\eta\text{-}\eta$, $\eta\text{-}\pi^0$ relying on SU(3) symmetry. In the range $3.362(5) < \sqrt{s}(pL) < 4.559(10.1)$ GeV (GeV/c), the results obtained are presented and compared to existing data.

In the space-like region, I contributed to the ALPOM2 experiment (JINR Dubna, Russia), the only experiment right now able to measure proton and neutron analyzing powers in the momentum range of interest for Jefferson Lab measurements and allowing considering different types of target. Experimentally, in the framework of ALPOM2, from the Nuclotron polarized deuteron beam, polarized proton and neutron beams at 3.0, 3.75 and 4.2 GeV/c were obtained by deuteron break-up and the charged fragments from the collisions with C, CH₂, CH and Cu targets were measured.



